



## Determination of Color Properties of Dyed Textile Products Using Different Mordanting Methods

Adem ÖNAL\* , Neslihan ÖZBULAT , Sama NACHED , Miray YILMAZ 

Tokat Gaziosmanpaşa University, Tokat, Türkiye.

**Abstract:** In this research, we investigated the dyestuff properties of dwarf elderberry (*Sambucus ebulus*), which has many pharmacological functions. Dyeing of cotton fabrics and wool yarns was carried out using *Sambucus ebulus* L. fruit extracts. Textile products were processed to pre-, meta-, and post-mordanting methods in the presence of iron sulfate ( $\text{FeSO}_4$ ), copper sulfate ( $\text{CuSO}_4$ ) and alum ( $\text{AlK}(\text{SO}_4)_2$ ) mordants. Color analyses of dyed textile products were performed and, the results were examined in terms of washing, rubbing, and light fastness. According to the results, it was determined that wool yarns showed better dyeing potential than that of cotton fabrics in terms of washing fastness. While the highest K/S value was measured as 6.55 in cotton fabrics with the pre-mordanting method, the highest K/S value was measured as 14.90 in wool yarns. In addition, the highest color strength values were obtained in each three mordanting methods. While gray, beige, and cream color tones were obtained in dyeing cotton fabrics, beige, green, and gray color tones were obtained in dyeing wool yarns.

**Keywords:** *Sambucus ebulus*, dwarf elderberry, dyestuff, natural dyes, textile products.

**Submitted:** February 16, 2023. **Accepted:** May 03, 2023.

**Cite this:** Önal, A., Özbulat, N., Nached, S., & Yılmaz, M. (2023). Determination of Color Properties of Dyed Textile Products Using Different Mordanting Methods. *Journal of the Turkish Chemical Society, Section B: Chemical Engineering*, 6(2), 27–32. **DOI:** <https://doi.org/10.58692/jotcsb.1251980>.

\*Corresponding author. E-mail: [adem.onal@gop.edu.tr](mailto:adem.onal@gop.edu.tr).

### 1. INTRODUCTION

*Sambucus ebulus* L. is one of the medicinal plants known since ancient times (Jabbari et al., 2017). *Sambucus ebulus* L., commonly called dwarf elder, elderberry, or danewort, belongs to the Adoxaceae family. It is known to have about 190 species and grows mainly in southern and central Europe, northwest Africa and southwest Asia (Shokrzadeh and Saravi, 2010). *Sambucus ebulus* L. has been reported to have anti-ulcerogenic, anti-microbial, anti-inflammatory, anti-parasitic, anti-viral, and anti-oxidant properties (Cumhur 2022; Jiménez et al., 2015; Salehzadeh et al., 2014; Yesilada et al., 2014). Plant extracts are used in many fields due to their versatile applications as well as their important biological activities. Extracts obtained from various parts of plants are widely used in dyeing textile products (Önal et al., 2021a; Önal et al. 2021b). Since natural products are environmentally-friendly, biodegradable, non-allergenic, non-toxic, they can be considered as a very important alternative to synthetic dyes (Önal et al., 2020).

Metal salts that strongly bind the dyestuff to the fiber are called mordant. Mordants are metal salts used to derive more than one color. Generally, mordants such as  $\text{FeSO}_4$ ,  $\text{CuSO}_4$ , and  $\text{AlK}(\text{SO}_4)_2$  are widely used. Mordants have been used in natural dyeing since ancient times, as plants have low affinity for fiber in dyeing (Önal, 1996).

In the literature, it has been reported that the compound with dyestuff properties in *Sambucus ebulus* L. is (*S*)-sambunigrin (Figure 1) (Kayabası and Etikan 1998). It is known that the fruits and leaves of the elderberry plant are used as natural dyes (Özdemir, 2018). In this study, cotton fabrics and wool yarn were dyed using three different mordanting methods by using extracts from elderberry fruits. Color analyses of dyed textile products were performed.

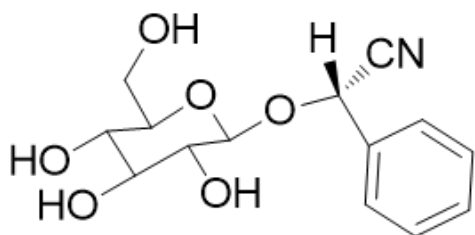


**Figure 1:** Structure of (S)-sambunigrin.

## 2. EXPERIMENTAL SECTION

### 2.1. Chemicals and Apparatus

*Sambucus ebulus* L. fruits were collected in July from the Tokat province, Türkiye.  $\text{CuSO}_4 \cdot 5\text{H}_2\text{O}$ ,  $\text{FeSO}_4 \cdot 7\text{H}_2\text{O}$ ,  $\text{AlK}(\text{SO}_4)_2 \cdot 12\text{H}_2\text{O}$  were obtained from Sigma Aldrich. Textile products were obtained from Toga Textile Ltd. company, Tokat province, Türkiye. The color properties of the dyed samples were evaluated by Premier Colorscan SS 6200A Spectrophotometer in terms of CIELab values ( $L^*$ ,  $a^*$ ,  $b^*$ ,  $C^*$ ) and color strength (K/S) values. Color codes were determined by Pantone Color Guide. The light fastness, washing fastness, and rubbing fastness values of all dyed samples were determined according to ISO 105-C06 and International Color Standardization (CIS) were tested with Atlas weather-ometer, Launder-ometer and 255 model crock-meter, respectively (Eser et al., 2015).

### 2.2. Methods

Extraction was carried out using cold press method. 100 g of fresh fruits of *Sambucus ebulus* L. were pressed and diluted with distilled water up to 2 liters. This procedure was continued until it reached 4 liters, and finally all of extracts were collected to get stable color tone (Önal et al., 2021a; Önal et al. 2021b). All dyeing processes were applied as in our previous studies ( Eser et al., 2015; Önal et al., 2021a).

#### 2.2.1. Pre-mordanting

The cotton fabric/wool yarn was heated in 0.1 M mordant solution for 1h at 70 °C. After cooling of the sample, it was rinsed with distilled water and put into dye-bath solution (100 mL). It was heated at 70 °C for 1h. The dyed material was rinsed with distilled water and dried.

#### 2.2.2. Meta-mordanting

Mordant (in solid state which is equivalent to 0.1 M mordant solution), dyestuff solution and cotton fabric/wool yarn was put into the flask and heated at 70 °C for 1 h. After cooling, it was rinsed and dried.

#### 2.2.3. Post-mordanting

The cotton fabric/wool yarn was first treated with the dyestuff solution for 1h at 70 °C. After cooling, it was rinsed with distilled water and put into 0.1 M mordant solution and heated for 1h at 70 °C. Finally, the dyed material was rinsed with distilled water and dried.

## 3. RESULTS AND DISCUSSION

### 3.1. Dyeing Mechanism

Mordants provide better bonding of the dyestuff to the fiber molecule. In this study, color properties were investigated by using three different mordants ( $\text{CuSO}_4$ ,  $\text{FeSO}_4$ , and  $\text{AlK}(\text{SO}_4)_2$ ). Metal cations in mordants can form stable complexes. The complex between dyestuffs and metal cations can be explained as follows:

- Metal cations form complexes between the free amino ( $-\text{NH}_2$ ) and carboxyl groups ( $-\text{COOH}$ ) of the wool yarn and the  $-\text{OH}$  molecules of the dyestuff ((S)-sambunigrin), thus displaying dyestuff properties (Figure 2).

- The metal complex formed between the  $-\text{CH}_2\text{O}$  groups in the cellulose molecules in the cotton fabric and the  $-\text{OH}$  groups in the dyestuff ((S)-sambunigrin) shows dyestuff properties (Figure 3).

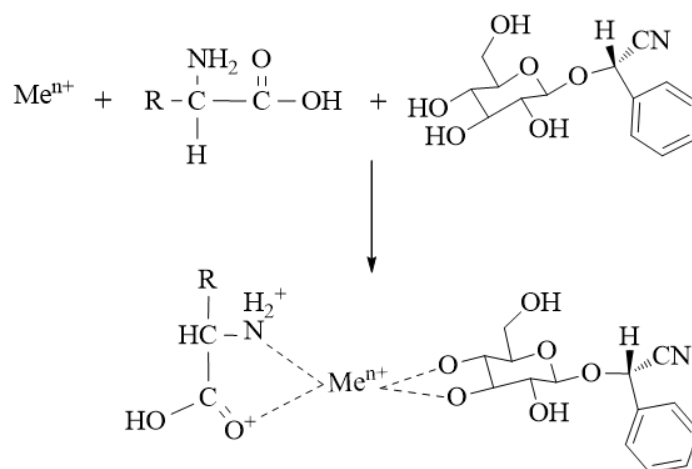


**Figure 2:** Proposed dyeing mechanism of wool yarn with (S)-sambunigrin ( $\text{M}^{n+}$ :  $\text{Cu}^{2+}$ ,  $\text{Fe}^{2+}$ ,  $\text{Al}^{3+}$ ).

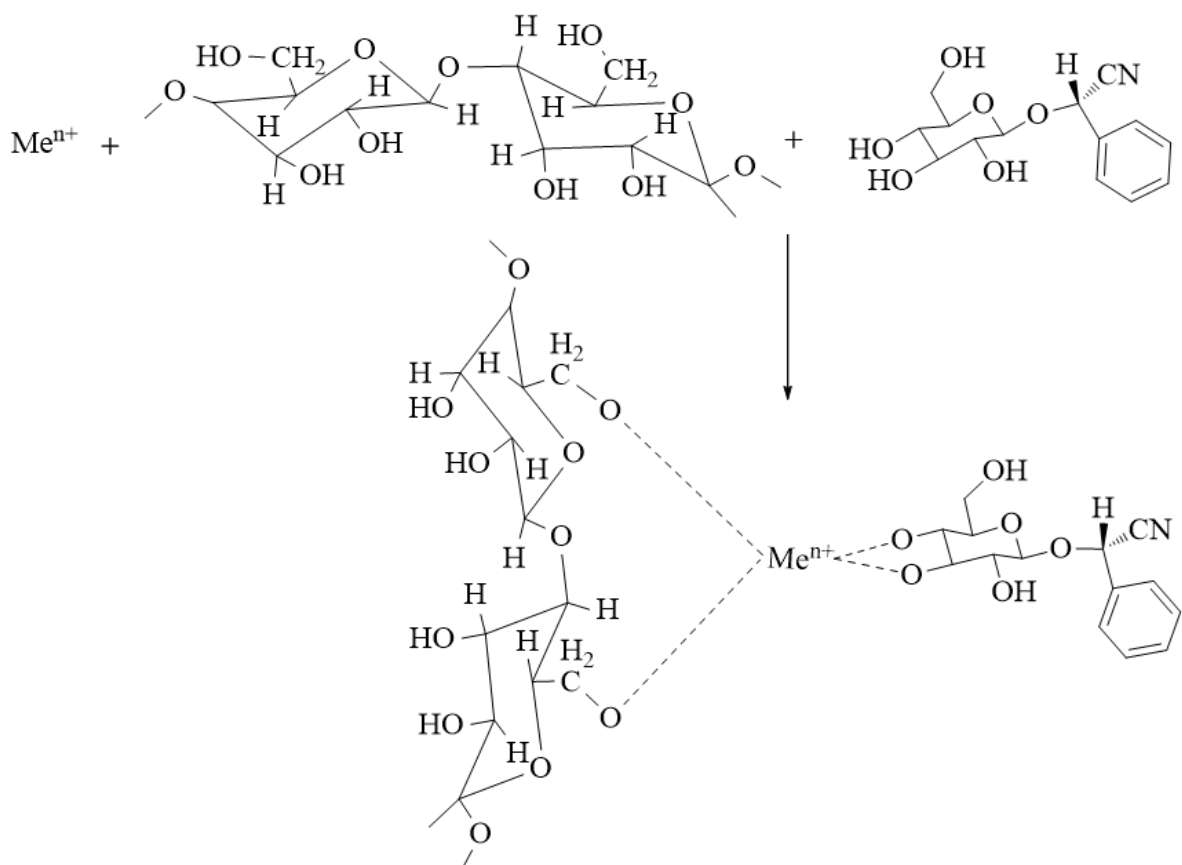


**Figure 3:** Proposed dyeing mechanism of cotton fabric with (S)-sambunigrin ( $M^{n+}$  :  $Cu^{2+}$ ,  $Fe^{2+}$ ,  $Al^{3+}$ ).

### 3.2. Fastness Values and Color Codes

Fastness values and color codes for dyed wool yarns and cotton fabrics were presented in Tables 1 and 2.

**Table 1:** Fastness values and color codes of dyed cotton fabrics.

Method	Mordant	Wash fastness <sup>a</sup>	Rubbing fastness <sup>b</sup> (wet-dry)	Light fastness <sup>c</sup>	Color code (Pantone)
Pre-	FeSO <sub>4</sub>	3–4	5–5	3/4	7535 CS
Meta-	FeSO <sub>4</sub>	4–5	5–5	4	5665 CS
Post-	FeSO <sub>4</sub>	5	5–5	4/5	400CS
Pre-	CuSO <sub>4</sub>	3	5–5	4	427 CS
Meta-	CuSO <sub>4</sub>	4–5	5–5	4/5	406 CS
Post-	CuSO <sub>4</sub>	4–5	5–5	4/5	5527 CS
Pre-	AlK(SO <sub>4</sub> ) <sub>2</sub>	5	5–5	4	5527 CS
Meta-	AlK(SO <sub>4</sub> ) <sub>2</sub>	5	5–5	4/5	5665 CS
Post-	AlK(SO <sub>4</sub> ) <sub>2</sub>	5	5–5	5	7527 CS
	N/A	5	5–5	3–4	5507 CS

<sup>a</sup>Wash and <sup>b</sup>rubbing fastness 1 = poor, 5 = very good, <sup>c</sup>Light fastness 1 = very poor, 8 = outstanding.

When Table 1 is examined, dry and wet rubbing fastnesses in cotton fabric dyeing are very good for all mordants and mordanting methods. Washing fastness is slightly lower for iron sulfate in pre- and meta-mordanting. In dyeings made with copper sulfate mordant, the value obtained in the pre-mordanting is partially lower than in the meta- and post-mordanting. Light fastnesses are lower in pre-

mordanting with iron sulfate, and generally below the medium value (4) for all mordants and mordanting methods. Light gray with alum, beige with iron sulfate, and cream with copper sulfate were obtained. According to the fastness results, the order of mordant activity can be given as alum > copper sulfate > iron sulfate.

**Table 2:** Fastness values and color codes of dyed wool yarn.

Method	Mordant	Wash fastness <sup>a</sup>	Rubbing fastness <sup>b</sup> (wet-dry)	Light fastness <sup>c</sup>	Color code (Pantone)
Pre-	FeSO <sub>4</sub>	5	4.5–5	4	417 CS
Meta-	FeSO <sub>4</sub>	5	5–5	4	404 CS
Post-	FeSO <sub>4</sub>	5	5–5	4–5	402 CS
Pre-	CuSO <sub>4</sub>	5	5–5	4	5625 CS
Meta-	CuSO <sub>4</sub>	5	5–5	3–4	5635 CS
Post-	CuSO <sub>4</sub>	5	5–5	4–5	5655 CS
Pre-	AlK(SO <sub>4</sub> ) <sub>2</sub>	5	5–5	4	401 CS
Meta-	AlK(SO <sub>4</sub> ) <sub>2</sub>	5	5–5	4	414 CS
Post-	AlK(SO <sub>4</sub> ) <sub>2</sub>	5	5–5	4–5	415 CS
	N/A	5	5–5	3–4	5645 CS

<sup>a</sup>Wash and <sup>b</sup>rub fastness 1 = poor, 5 = very good, <sup>c</sup>Light fastness 1 = very poor, 8 = outstanding.

According to Table 2, dry and wet rubbing fastnesses in wool yarns dyeing are very good, that is, 5 for every three mordants and mordanting methods. Washing fastnesses for iron sulfate mordant are 4–5 in pre-mordanting and 5 in others. Light fastnesses are generally medium and below. The light fastnesses detected in the final mordanting were slightly higher than the meta- and pre-mordanting. The effectiveness of mordants in wool dyeing is close to each other. Beige and shades of beige are obtained for alum

mordant, matte green and grey tones for iron sulfate mordant, grass green and beige tones are obtained for copper sulfate.

### 3.3. Determination of Color Performance

Color strength was determined as K/S values of the dyed samples using the Kubelka–Munk equation (Džimbeg-Malčić et al., 2011). K/S and L\*, a\*, b\* values of wool yarns and cotton fabrics are given in Table 3.

**Table 3:** K/S and  $L^*$   $a^*$   $b^*$  values of cotton fabrics and wool yarn.

<b>Fabric</b>	<b>Mordant</b>	<b><math>L^*</math></b>	<b><math>a^*</math></b>	<b><math>b^*</math></b>	<b>K/S</b>
Cotton	FeSO <sub>4</sub>	34.20	3.75	8.46	6.55
	FeSO <sub>4</sub>	29.92	2.99	5.99	4.48
	FeSO <sub>4</sub>	32.60	1.08	6.45	7.01
	CuSO <sub>4</sub>	32.09	0.92	20.56	6.40
	CuSO <sub>4</sub>	33.45	0.78	19.28	5.32
	CuSO <sub>4</sub>	31.90	1.45	21.12	6.00
	AlK(SO <sub>4</sub> ) <sub>2</sub>	40.21	4.23	15.12	4.99
	AlK(SO <sub>4</sub> ) <sub>2</sub>	41.08	4.56	10.02	4.48
	AlK(SO <sub>4</sub> ) <sub>2</sub>	43.20	5.01	9.14	5.01
Wool	FeSO <sub>4</sub>	38.36	4.95	17.90	14.55
	FeSO <sub>4</sub>	37.90	3.26	16.77	14.90
	FeSO <sub>4</sub>	39.76	3.90	15.62	13.80
	CuSO <sub>4</sub>	35.01	-0.99	21.50	9.90
	CuSO <sub>4</sub>	35.05	0.80	21.67	7.27
	CuSO <sub>4</sub>	39.66	-0.77	21.40	6.09
	AlK(SO <sub>4</sub> ) <sub>2</sub>	43.95	5.79	17.66	9.76
	AlK(SO <sub>4</sub> ) <sub>2</sub>	41.24	5.70	16.05	9.20
	AlK(SO <sub>4</sub> ) <sub>2</sub>	42.20	5.99	15.97	8.05
unmordant-cotton	-	36.23	7.76	15.22	3.96
unmordant-wool	-	58.12	8.89	17.44	4.92

As seen in Table 3, it was obtained in different shades of color intensity for cotton fabrics. Grey and beige color tones were obtained for cotton fabrics, in a general manner. The highest K/S value was measured as 6.55 for iron sulfate with pre-mordanting method for dyed cotton fabrics. In

addition, it was obtained in different shades of color intensity for wool yarns. The highest K/S value was detected as 14.90 for iron sulfate mordant. Examples of cotton and wool yarn dyed with *Sambucus ebulus* L. fruit extract are as in Figure 4.

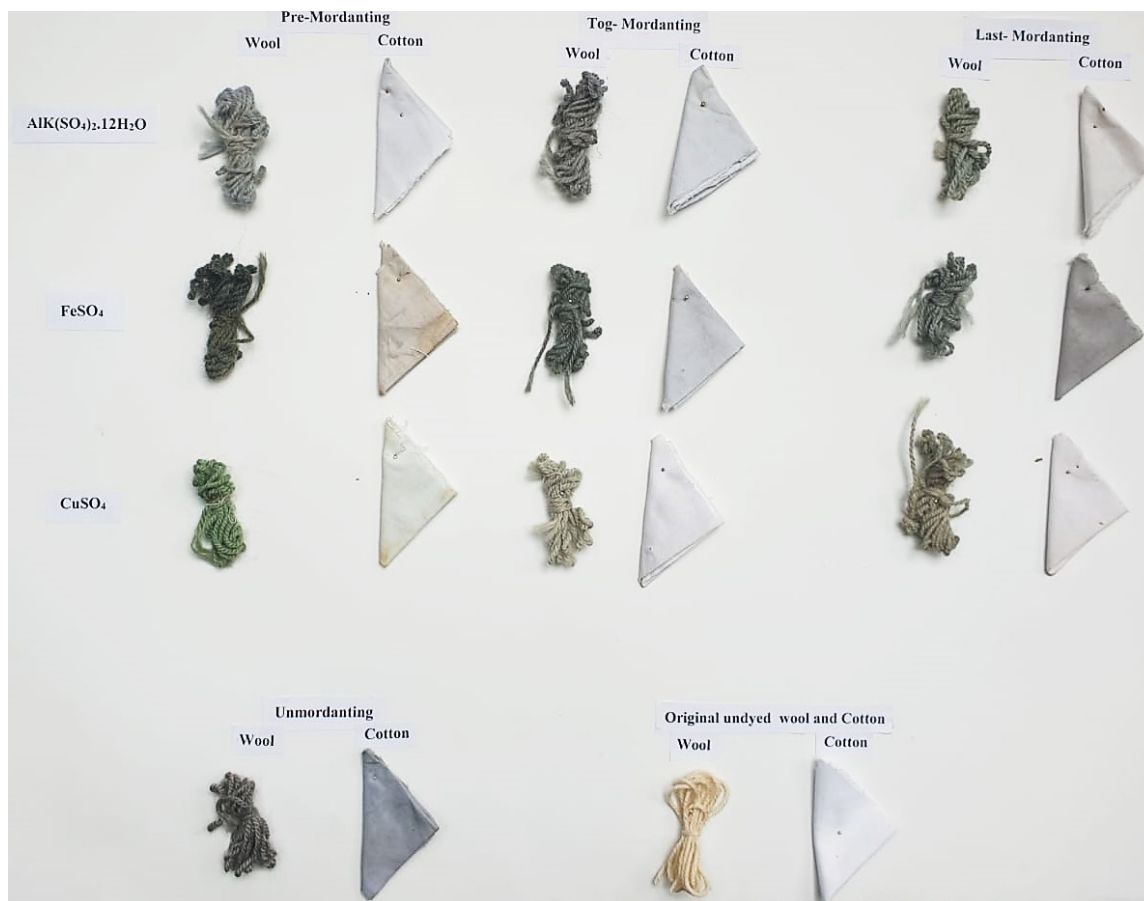


**Figure 4:** Cotton fabric and wool yarn samples dyed with *Sambucus ebulus* L. fruit extract.

#### 4. CONCLUSION

In the present work, the *Sambucus ebulus* L. fruit extract was used for dyeing of cotton fabric and wool yarn. Fabrics and threads were dyed using three different mordants. According to the fastness results, it was determined that the mordanting efficiency was alum > copper sulfate > iron sulfate. Grey, beige, and cream color tones were obtained in dyeing of cotton fabrics. Beige, green, and grey color tones were obtained in the dyeing of wool yarns. Generally, very high fastnesses were obtained in both cotton fabric and wool yarn dyeing. The light fastnesses were at middle and below middle value in wool yarn and cotton fabrics. It is important that dwarf elderberry (*Sambucus ebulus* L.), which is widely used in medicine and pharmacy, is used in dyeing textile materials. In this study, this issue has been proven experimentally. Further investigations are underway.

#### 5. CONFLICT OF INTEREST

There is no conflict of interest between the authors.

#### 6. REFERENCES

- Cumhur, B. (2022). Antioxidant and Anti-Inflammatory Activity Of Different Parts of *Sambucus Ebulus* L. *Journal of Faculty of Pharmacy of Ankara University*, 46(3), 728-741. <https://doi.org/10.33483/jfpau.1115491>
- Džimbeg-Malčić, Z. Barbarić-Mikočević, K. Itrić (2011) Kubelka-munk theory in describing optical properties of paper (I), *Teh. Vjesn.* 18 117–124.
- Jabbari, M., Daneshfard, B., Emtiazy, M., Khiveh, A., & Hashempur, M. H. (2017). Biological effects and clinical applications of dwarf elder (*Sambucus ebulus* L.): A review. *Journal Of Evidence-Based Complementary & Alternative Medicine*, 22(4), 996-1001. <https://doi.org/10.1177/2156587217701322>
- Jiménez, P., Tejero, J., Cordoba-Diaz, D., Quinto, E. J., Garrosa, M., Gayoso, M. J., & Girbés, T. (2015). Ebulin from dwarf elder (*Sambucus ebulus* L.): a mini-review. *Toxins*, 7(3), 648-658. <https://doi.org/10.3390/toxins7030648>
- Kayabaş, N., & Etikan, S. (1998). Mürver *Sambucus nigra* L. Bitkisinden Elde Edilen Renkler ve Bu Renklerin Yün Halı İplikleri Üzerindeki Işık ve Sürtünme Haslıkları. *Journal of Agricultural Sciences*, 4(03), 65-69. [https://doi.org/10.1501/Tarimbil\\_0000000815](https://doi.org/10.1501/Tarimbil_0000000815)
- Önal, A., Özbek, O., Tombul, K. C., & Nached, S. (2021a). Investigation of the dyeing properties of cotton fabrics and wool yarns using *Prunus*

- persica leaf extract. Journal of the Indian Chemical Society, 98(7), 100092. <https://doi.org/10.1016/j.jics.2021.100092>
- Önal, A., Özbek, O., Vanlioglu, F., Teker, A.T., Boyraz, D. (2021b). Investigation of the dyeing properties of the colorant extracted from Juglans regia L. leaves on cellulosic and protein fabrics. Journal of the Turkish Chemical Society Section A: Chemistry, 8(2), 453-460. <https://doi.org/10.18596/jotcsa.856975>
- Önal, A., Özbek, O. & Nached, S. (2020). The production of antiviral-breathing mask against SARS-CoV-2 using some herbal essential oils. Journal of the Turkish Chemical Society Section A: Chemistry, 7(3), 821-826. <https://doi.org/10.18596/jotcsa.788410>
- Önal, A., Durdykulyyeva, S., Özbek, O., & Nached, S. (2022). The use of Hibiscus sabdariffa flower extracts in cotton fabric and wool yarn dyeing. Journal of The Institution of Engineers (India): Series E, 103, 315-321. <https://doi.org/10.1007/s40034-021-00235-z>
- Özdemir, H. (2018) Bodur mürver (*Sambucus ebulus* L.) ile Yün İpliklerin boyanması. Çukurova Üniversitesi Muhendislik Fakültesi Dergisi. 33(1) (2018) 219-228.
- Shokrzadeh, M., & Saravi, S. S. (2010). The chemistry, pharmacology and clinical properties of *Sambucus ebulus*: A review. Journal Of Medicinal Plants Research, 4(2), 095-103
- Salehzadeh, A., Asadpour, L., Naeemi, A. S., & Houshmand, E. (2014). Antimicrobial activity of methanolic extracts of *Sambucus ebulus* and *Urtica dioica* against clinical isolates of methicillin resistant *Staphylococcus aureus*. African Journal of Traditional, Complementary and Alternative Medicines, 11(5), 38-40. <https://doi.org/10.4314/ajtcam.v11i5.6>
- Yesilada, E., Gürbüz, İ., & Toker, G. (2014). Anti-ulcerogenic activity and isolation of the active principles from *Sambucus ebulus* L. leaves. Journal of ethnopharmacology, 153(2), 478-483. <https://doi.org/10.1016/j.jep.2014.03.004>







## RSM Optimization of Direct Orange 26 Adsorption on Low-Cost Silica Fume Adsorbent

Shohre Mortazavi\* , Ebrahim Najafi Kani 

<sup>1</sup>Semnan University, Department of Chemical, Petroleum, and Gas Engineering, Semnan, Iran

**Abstract:** Today, dye pollutants enter resources of water through various industries. Due to the stability and carcinogenicity of dye pollutants, it is necessary to treat colored wastewater before entering the aqueous cycle. One of the important methods for wastewater treatment is adsorption. In this study, the effect of industrial waste of silica fume adsorbent on azo dye Direct Orange 26 (DO26) was investigated. Design of experiment was carried out with CCD method by using Design Expert software version 7 to model and investigate the effects of parameters pH, concentration, amount of adsorbent, and time. The model proposed by the software is a second-order model. According to the findings, important and effective parameters for the quadratic model of experimental design were obtained from ANOVA (analysis of variance). The optimum conditions for the maximum removal of DO26 (95.26%) were obtained to be at pH 2.01, contact time of 55.15 minutes, adsorbent amount of 0.2 g, and initial concentration of 44 ppm. The experimental kinetic data were analyzed through the conventional kinetic models, and the results demonstrate that the sorption kinetics can be accurately described by the pseudo-second order model. Also, based on FESEM image, silica fume has a spherical and porous structure, therefore, silica fume can remove dye pollutants from water as a cheap adsorbent.

**Keywords:** Response surface method, wastewater, adsorption, silica fume.

**Submitted:** January 23, 2023. **Accepted:** July 05, 2023.

**Cite this:** Mortazavi, S., & Najafi Kani, E. (2023). RSM Optimization of Direct Orange 26 Adsorption on Low-Cost Silica Fume Adsorbent. *Journal of the Turkish Chemical Society, Section B: Chemical Engineering*, 6(2), 35-44. **DOI:** <https://doi.org/10.58692/jotcsb.1240859>

\*Corresponding author. E-mail: [mortazavi@semnan.ac.ir](mailto:mortazavi@semnan.ac.ir).

### 1. INTRODUCTION

Today, industrial pollutants enter resources of water and shortage of water is a serious crisis (Yan et al., 2015). Dyes and pigments enter water through industries such as plastic, food, cosmetics, printing, etc. (Genc & Oguz, 2010). Synthetic dyes have a complex aromatic molecular structure, therefore, it is difficult to remove dye pollutants from water (Sohrabi et al., 2016). Also, toxic and carcinogenic nature of dyes threatens health of humans (Kannaujiya et al., 2022). Long-term contact with these dyes causes disorders such as nausea, bleeding, wounds on the skin, and serious damage to vital organs. Therefore, correct and effective treatment of dye pollutants before entering water cycle is necessary (Ghaedi et al., 2015; Zhu, Zhang, & Yan, 2016).

Direct Orange 26 (DO26) is used in coloring cellulosic fibers such as yarn, linen, synthetic silk, as

well as in coloring leather and paper (Safa & Bhatti, 2011). This dye causes harmful effects in case of contact with eyes and skin (Aşçı, 2013). One of the effective methods for removing textile dyes from wastewater is adsorption (Geyikçi et al., 2012). Safa et al. (2011) investigated removal of DO26 dyes from aqueous solutions by rice husk (Safa & Bhatti, 2011). Tomczak et al. (2014) investigated sorption of DO26 onto a cheap plant sorbent (Tomczak & Tosik, 2014).

Silica fume, which is also known as microsilica, is a gray powdery solid with pozzolanic properties containing amorphous silica. In the past, the dust obtained from ferrosilicon arc furnaces was considered as waste of this process (Li et al., 2014). Today, with the advancement of technology and attention to the optimal use of industrial waste, this dust is marketed as a by-product under the brand name of silica fume. Due to the unique properties of silica fume, including high porosity and permeability,

very small particle size, low specific gravity, high specific surface area, low thermal conductivity, good absorption capacity, and chemical inertness, it has received special attention (Zhang et al., 2012). The unique properties of silica fume have led to its use in the cement industry, the production of polymer products, and the absorption of pollutants (Ahmed, Gaber, & Rahim, 2017). Wang et al. (2011) found that the performance of silica fume in adsorption of Rhodamine B from aqueous solutions is better than from coal ash (Wang & Chu, 2011). Kalkan et al. (2014) found silica fume has a high capacity to adsorb nickel (Kalkan, Nadaroglu, & Celebi, 2014). Nadaroglu et al. (2013) and Ahmed et al. (2015) showed that silica fume is a cheap and effective adsorbent for the removal of cadmium (II) and copper and zinc ions from wastewater (Ahmed et al., 2017; Nadaroglu & Kalkan, 2014).

Experiment design causes process evaluation, process efficiency improvement, design selection in such a way that the product or output works well in different conditions, determination of key process parameters that have the greatest impact on process output (Montgomery, 2017). Due to the low cost and high porosity of silica fume, in this study, RSM optimization of DO26 adsorption on low-cost adsorbent silica fume from wastewater has been investigated.

## 2. EXPERIMENTAL SECTION

### 2.1 Materials and Methods

Direct Orange 26 (DO26), with the experimental formula  $C_{33}H_{22}N_6Na_2O_9S_2$  is an azo dye used in the dyeing of cellulose fibers, leather, and paper (Safa & Bhatti, 2011). The molecular weight of DO26 is 756.67, the solubility in water is 50 g/L, and the maximum absorption wavelength is 495 nm.

Silica fume was obtained from Lorestan Ferroalloy Company without any operations. To prepare the adsorbent, silica fume was passed through a 60-mesh sieve. Then the adsorbent was kept in plastic containers to prevent its contact with pollution and moisture. The specific surface area of silica fume is 18.0  $m^2/g$ . Chemical composition and surficial properties of silica fume (determined by X-ray fluorescence) are shown in Table 1. In addition, the maximum wavelength of the used colors was measured by the UV-spectrophotometer (PC 1650-UV, Shimadzu, Japan), and pH meter model AZ8686 with accuracy of  $\pm 0.01$  for pH adjustment used in the adsorption process. Materials were weighed by a digital scale (GK-1203, Sartorius, Germany) and a hot plate magnetic stirrer (TA-105, VELP, France) is used to mix the materials in experiments. Field Emission Scanning Electron Microscopy (FESEM, JSM 6400, JEOL, Japan) is used to identify the microstructure of the adsorbent. Figure (1) shows FESEM image of silica fume.

**Table 1.** Chemical composition and surficial properties of silica fume.

<b>SiO<sub>2</sub></b> <b>(wt. %)</b>	<b>Al<sub>2</sub>O<sub>3</sub></b> <b>(wt. %)</b>	<b>K<sub>2</sub>O</b> <b>(wt. %)</b>	<b>Density</b> <b>(kg/m<sup>3</sup>)</b>	<b>Specific Surface</b> <b>(m<sup>2</sup>/g)</b>	<b>Pore Diameter</b> <b>μm</b>
96.12	0.82	0.4	213	18	13

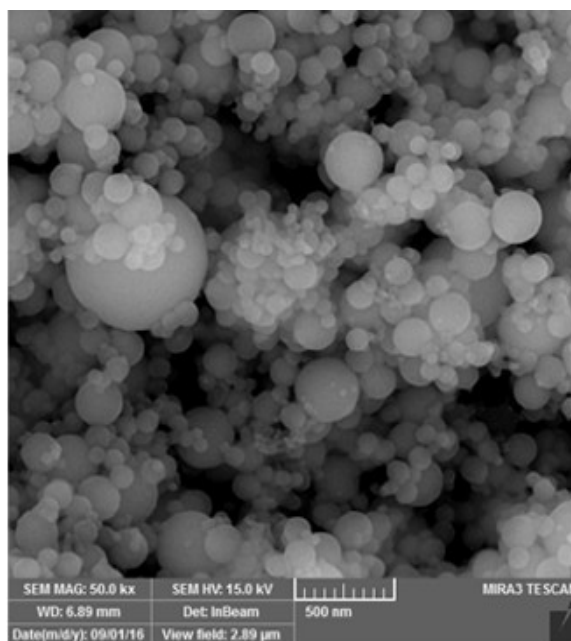


**Figure 1:** FESEM image of silica fume.

## 2.2 Method of Adsorption

Batch adsorption experiments are carried out to evaluate the adsorption performance of the adsorbent. A stock solution of 1000 ppm from dye have been used through the adsorption test. The stock solution was diluted with distilled water to give the appropriate concentration of the working solutions. Batch adsorption experiments were performed by contacting 0.1-0.5 g of silica fume samples with 100 mL of an aqueous solution of DO26 of the desired concentration and pH. The residual DO26 after adsorption was measured with a UV/visible spectrometer (UV2100, Unique, USA) at a  $\lambda_{max}$  corresponding to the maximum absorption for DO26 ( $\lambda_{max}=495$  nm); the percent removal of DO26 as the main goal of the experiments is obtained from the following equation:

$$\%R = \frac{C_0 - C_e}{C_0} \times 100 \quad (\text{Eq. 1})$$

Where R is the percent removal,  $C_0$  is the initial concentration of dye in the aqueous solution (mg/L), and  $C_e$  is the equilibrium concentration (mg/L).

The adsorption capacity of q (mg/g), as the main goal of the experiments, is obtained from the following equation:

$$q = \frac{C_0 - C_f}{M} \times V \quad (\text{Eq. 2})$$

Where q is the adsorption capacity at time t (mg/g),  $C_0$  is the initial concentration of dye in the aqueous solution (mg/L),  $C_f$  is the concentration of dye after the adsorption at time t (mg/L), V is the volume of the aqueous solution (L), and M is the amount of adsorbent (g).

## 2.3 CCD method

Experiments are used to study process and system performance. A process or system is a combination of methods, operations, people, and other resources that transform input into output with one or more response variables by changing parameters. Checking the parameters and their effect on the system is done with one-variable, two-variable, and multi-variable methods. The univariate method, by changing one parameter and considering the other parameters is time-consuming and expensive. To solve these problems, experimental design is performed (Dbik et al., 2022). Experimental design causes process evaluation, process efficiency improvement, design selection in such a way that the product or output works well in different conditions, determination of key process parameters that have the greatest impact on process output (Montgomery, 2017).

There are various methods for experimental design, such as  $2^k$  factorial designs, fractional factorial designs, block designs, response surface method (RSM), etc. (Montgomery, 2017).

RSM method is a set of applied statistical-mathematical methods for analyzing and modeling problems with different parameters to optimize the answer. The following equation shows the linear relationship between response and independent variables (Dargahi et al., 2021):

$$y = b_0 + \sum b_i x_i \quad (\text{Eq. 3})$$

This model is obtained in  $2^k$  factorial design or  $2^{k-p}$  fractional factorial design. It describes the linear relationship between the upper and lower levels and the behavior related to these two levels. If the relationship is not linear, the investigations require at least three levels, and polynomials with a higher power, such as quadratic polynomials, which are defined as follows, should be used (Geyikçi, Kılıç, Çoruh, & Elevli, 2012):

$$y = b_0 + \sum b_i x_i + \sum b_{ii} x_i^2 + \sum b_{ij} x_i x_j \quad (\text{Eq. 4})$$

$b_0$  is the linear constant,  $b_i$  is the coefficient of the linear part,  $b_{ii}$  is the coefficient of the quadratic part, and  $b_{ij}$  is the interaction coefficient.

CCD method includes  $2^k$  full factor or fractional factor, which is coded as  $\pm 1$  in the linear model, with  $2k$  fractional tests and intersection of the axial or star fraction with the axial distance  $\alpha$ , which gives us information about the quadratic model, and  $n_c$  tests in the central points, then the total number of tests in the CCD method is calculated (Geyikçi, Kılıç, Çoruh, & Elevli, 2012):

$$N = 2^k + 2k + n_c \quad (\text{Eq. 5})$$

One of the most important parts of statistical research is choosing the appropriate statistical analysis method, which usually determines the type of statistical tests from the characteristics of the sample and the type of analysis required by the person doing the experiment. Statistical analysis can be done with parameters such as mean and variance. Many statistical tests are parametric, such as T-test and analysis of variance (Aziz et al., 2022).

## 3. RESULTS AND DISCUSSION

### 3.1 Impact of pH on Adsorption

The impact of pH on the adsorption of DO26 for 50 ppm DO26 solution by silica fume was investigated in the pH range of 2-11. The pH levels were adjusted using dilute solutions of HCl and NaOH. The experiment was carried out for 60 minutes with a stirring speed of 300 rpm. After adsorption, the solution was centrifuged, and the adsorption value was measured using a spectrophotometer. Figure 2a presents the effect of pH on the adsorption capacity of DO26 using silica fume. When the initial pH value of the DO26 solution was increased from 2 to 11, the adsorption capacity decreased from 10.48 to 2.891 mg/g. Due to the anionic nature of DO26, an

increase in the electrostatic attraction force between the dye and adsorbent was observed at lower pH values and increased adsorption capacity. The maximum adsorption capacity of 10.48 mg/g was observed at pH 2.

### 3.2 Impact of Contact Time on Adsorption

The relation between adsorption capacity of DO26 and contact time was investigated for 20 to 90

minutes. Figure 2b shows the effect of contact time on the adsorption capacity of DO26 using silica fume at pH 2. According to the results, an increase in contact time led to an increase in the amount adsorbed until equilibrium was reached. In this study, equilibrium was reached after 40 minutes of adsorption.

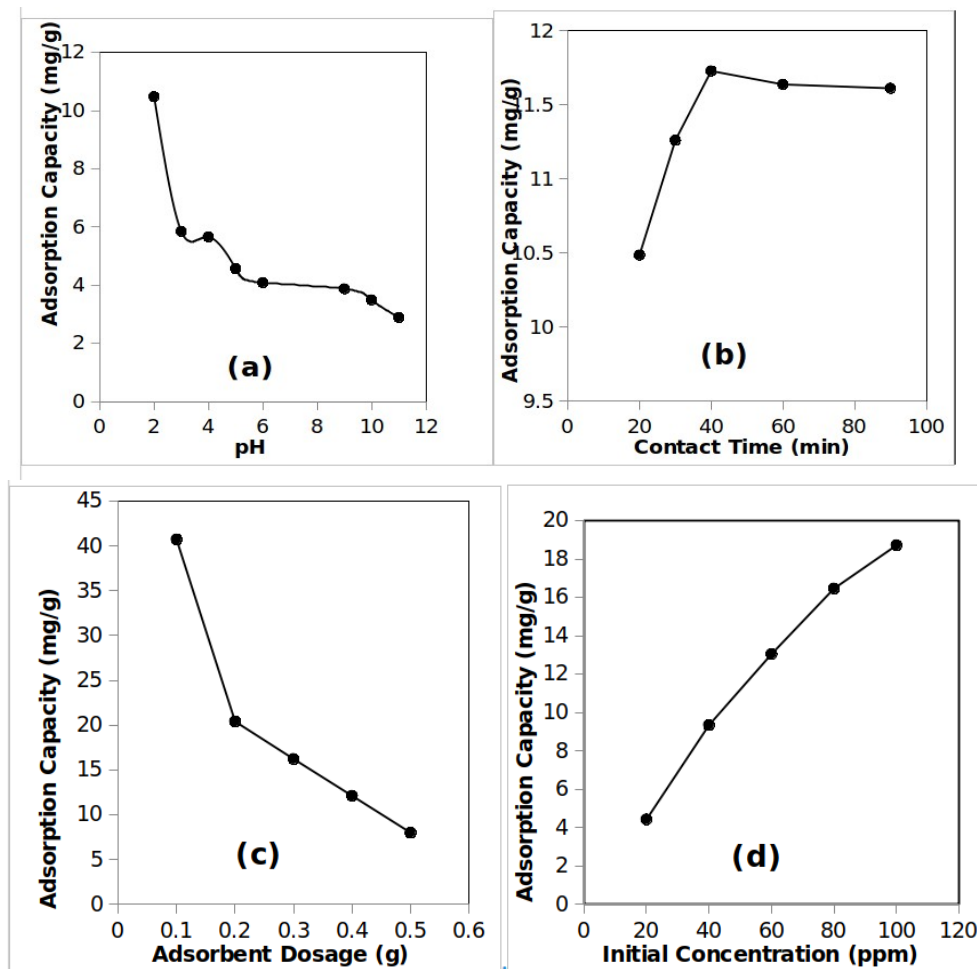


**Figure 2:** Effect of **a)** pH, **b)** contact time, **c)** the amount of adsorbent, and **d)** Initial Concentration on DO26 adsorption using silica fume.

### 3.3 Impact of the amount of adsorbent

Figure 2c shows the impact of the amount of adsorbent on the adsorption capacity of DO26 using silica fume at pH 2. The adsorption capacity of DO26 decreased from 40.7185 to 8.0045 mg/g as the amount of silica fume increased from 0.1- 0.5 g. An increase in the amount of adsorbent reduces the number of active adsorption sites, leading to a decrease in adsorption capacity and affecting the overall process.

### 3.4 Impact of Initial Concentration of the Solution on Adsorption

Figure 2d shows the effect of the initial DO26 concentration on the adsorption capacity using silica fume. These data have been obtained over the initial concentration range of 20 to 100 ppm for DO26 at pH 2. In this study, the adsorption capacity of DO26 increased as the initial DO26 concentration increased from 20- 100 ppm. According to the result, silica fume has an excellent potential for removal of DO26 from wastewater.

### 3.5 Kinetic study

To understand the rate and adsorption mechanism involved in the removal of DO26 by the silica fume, the experimental kinetic data were analyzed through the conventional kinetic models including pseudo-first order, pseudo-second order, and Elovich equations. The linear form of the equation corresponding to each kinetic model and the relative parameters that were calculated are summarized in Table (2).

The results demonstrate that the sorption kinetics can be accurately described by the pseudo-second order model. The high regression correlation coefficients ( $R^2 = 0.9992$ ) and the close agreement between experimental and theoretical adsorption capacity ( $q_e$ ) values confirm that chemisorption is the rate-controlling step throughout the entire adsorption process.

**Table 2:** Summary of the kinetics models for adsorption of DO26 on silica fume.

Model	Equation	Parameters	Values of parameters
First-order	$\ln(q_e - q_t) = \ln q_e - K_1 t$	$K_1$ (L/min) $q_e$ (mg/g) $R^2$	0.0182 0.9977 0.3815
Second-order	$\ln(q_e - q_t) = \ln q_e - K_1 t$	$K_2$ (g/mg min) $q_e$ (mg/g) $R^2$	0.0487 11.9110 0.9992
Elovich	$\ln(q_e - q_t) = \ln q_e - K_1 t$	$\beta$ $\alpha$ $R^2$	1.4643 $2.7090 \times 10^5$ 0.6427

### 3.6 CCD Design and Experimental Response

The effect of absorption parameters pH, adsorbent amount, contact time, initial dye concentration, optimal temperature, and absorption rate were investigated. Then, design of experiment was carried out in the optimal range to investigate the interaction effects of the parameters of the absorption process at three levels. In this study, Design Expert software version of 7 was used. Parameter of pH checked at three levels of 4, 3, and 2, the absorption amount was checked at the levels of 0.4, 0.3, and 0.2, the time levels were 60, 45, and 30, and the concentration checked at the three levels of 60, 40, and 20. CCD design matrix and experimental response values are presented in Table (3).

According to the ANOVA results for the quadratic model, effect of pH, amount of adsorbent, concentration and interaction between pH and amount of adsorbent, pH and concentration, amount of adsorbent and time, amount of adsorbent and

concentration, time and concentration and the double effect of the adsorbent parameters are important and effective for designing model. ANOVA of the regression model is exhibited in Table 4 for DO26. The Model F-value of 135.65 implies the model is significant. There is only a 0.01% chance that an F-value this large could occur due to noise. P-values less than 0.0500 indicate model terms are significant. In this case, A, C, D, AB, AC, AD, BC, CD,  $A^2$ ,  $B^2$ ,  $C^2$ ,  $D^2$  are significant model terms. Values above 0.1000 suggest that the model terms are not significant.

In all experiments, temperature and stirring speed were kept constant. The software examines different models to predict the removal percentage and suggests a model with significant values. In the experimental design for DO26 in the present study, the model proposed by the software is a second-order model. A summary of polynomial models is presented in Table (5).

**Table 3.** CCD design matrix and experimental response values.

Run	Factor 1 A: pH	Factor 2 B: m (g)	Factor 3 C: Time (min)	Factor 4 Concentration (ppm)	Response R1 <sub>experimental</sub>	Response R1 <sub>predicted</sub>
1	4.00	0.40	60.00	60.00	19.9714	19.9315
2	4.00	0.30	45.00	40.00	16.3941	19.9393
3	4.00	0.20	60.00	60.00	23.008	20.3868
4	4.00	0.20	60.00	20.00	36.4599	35.9982
5	2.00	0.40	60.00	20.00	80	77.5424
6	3.00	0.40	45.00	40.00	52.3493	52.3493
7	3.00	0.30	45.00	40.00	33.1254	30.4402
8	3.00	0.30	45.00	40.00	26.5876	30.4402
9	3.00	0.30	60.00	40.00	31.1372	30.6154
10	2.00	0.40	30.00	60.00	79.0333	78.5115
11	2.00	0.40	30.00	20.00	43.6679	47.2111
12	3.00	0.30	45.00	40.00	30.005	30.4402
13	2.00	0.20	30.00	20.00	50.007	49.0634
14	3.00	0.30	45.00	40.00	27.9823	30.4402
15	2.00	0.20	30.00	60.00	75.2386	74.4880
16	3.00	0.30	45.00	40.00	31.7921	30.4402
17	3.00	0.30	45.00	60.00	27.0744	26.2156
18	3.00	0.20	45.00	40.00	48.6275	51.1883
19	3.00	0.30	30.00	40.00	18.9089	19.6766
20	4.00	0.40	30.00	60.00	44.1021	44.0073
21	3.00	0.30	45.00	40.00	33.8864	30.4402
22	4.00	0.40	60.00	20.00	27.9946	29.6672
23	4.00	0.40	30.00	20.00	24	21.9084
24	2.00	0.40	60.00	60.00	74.7034	77.0081
25	4.00	0.20	30.00	60.00	27.3663	28.8405
26	2.00	0.20	60.00	20.00	94	95.0168
27	2.00	0.20	60.00	60.00	87.4986	88.6068
28	2.00	0.30	45.00	40.00	70	66.7007
29	3.00	0.30	45.00	20.00	17.2663	18.3711
30	4.00	0.20	30.00	20.00	14	12.6173

The final quadratic model with  $R^2=0.9922$  was obtained as follows:

$$R1 = +181.68 - 87.49A - 1211.82B + 5/45C + 3.148D + 27.86AB - 0.38AC - 0.12AD - 2.60 + 0.73BD - 0.026CD + 12.88A^2 + 2017.11B^2 - 0.02C^2 - 0.02D^2$$

A: pH

B: adsorbent

C: time

D: concentration

And the binary combination of parameters is obtained by multiplying the symbols.

**Table 4.** ANOVA for response surface quadratic model for DO26 removed by silica fume.

Source	Sum of Squares	df	Mean Square	F-value	p-value	
<b>Model</b>	16005.59	14	1143.26	135.65	< 0.0001	Significant
A-PH	9839.82	1	9839.82	1167.48	< 0.0001	
B-m	5.99	1	5.99	0.7107	0.4124	
C-Time	538.46	1	538.46	63.89	< 0.0001	
D-concentration	276.91	1	276.91	32.86	< 0.0001	
AB	124.17	1	124.17	14.73	0.0016	
AC	509.51	1	509.51	60.45	< 0.0001	
AD	84.67	1	84.67	10.05	0.0063	
BC	244.05	1	244.05	28.96	< 0.0001	
BD	34.52	1	34.52	4.10	0.0612	
CD	1013.44	1	1013.44	120.24	< 0.0001	
A <sup>2</sup>	429.81	1	429.81	51.00	< 0.0001	
B <sup>2</sup>	1054.19	1	1054.19	125.08	< 0.0001	
C <sup>2</sup>	72.62	1	72.62	8.62	0.0102	
D <sup>2</sup>	171.96	1	171.96	20.40	0.0004	
<b>Residual</b>	126.42	15	8.43			
Lack of Fit	84.53	10	8.45	1.01	0.5306	not significant
Pure Error	41.90	5	8.38			
<b>Cor Total</b>	16132.02	29				

**Table 5:** Summary of the models for adsorption of DO26 on silica fume.

Source	Sum of Squares	df	Mean Squares	F Value	p-value Prob > F	
Mean vs Total	53441.60	1	53441.60			
Linear vs Mean	10661.35	4	2665.34	12.18	< 0.0001	
2FI vs Linear	2010.45	6	335.08	1.84	0.1447	
Quadratic vs 2FI	<u>3334.13</u>	<u>4</u>	<u>833.53</u>	<u>98.88</u>	<u>&lt; 0.0001</u>	<u>Suggested</u>
Cubic vs Quadratic	80.70	8	10.09	1.54	0.2903	Aliased
Residual	45.75	7	6.54			
Total	69573.99	30	2319.13			

In Figure 3, the response surface diagrams are presented to investigate the effective parameters for absorption of DO26 on silica fume. The highest

percentage of removal was predicated 95.26% by the software (pH=2.01, adsorbent amount=0.2 g, time=55.15 minutes, and concentration=44 ppm).

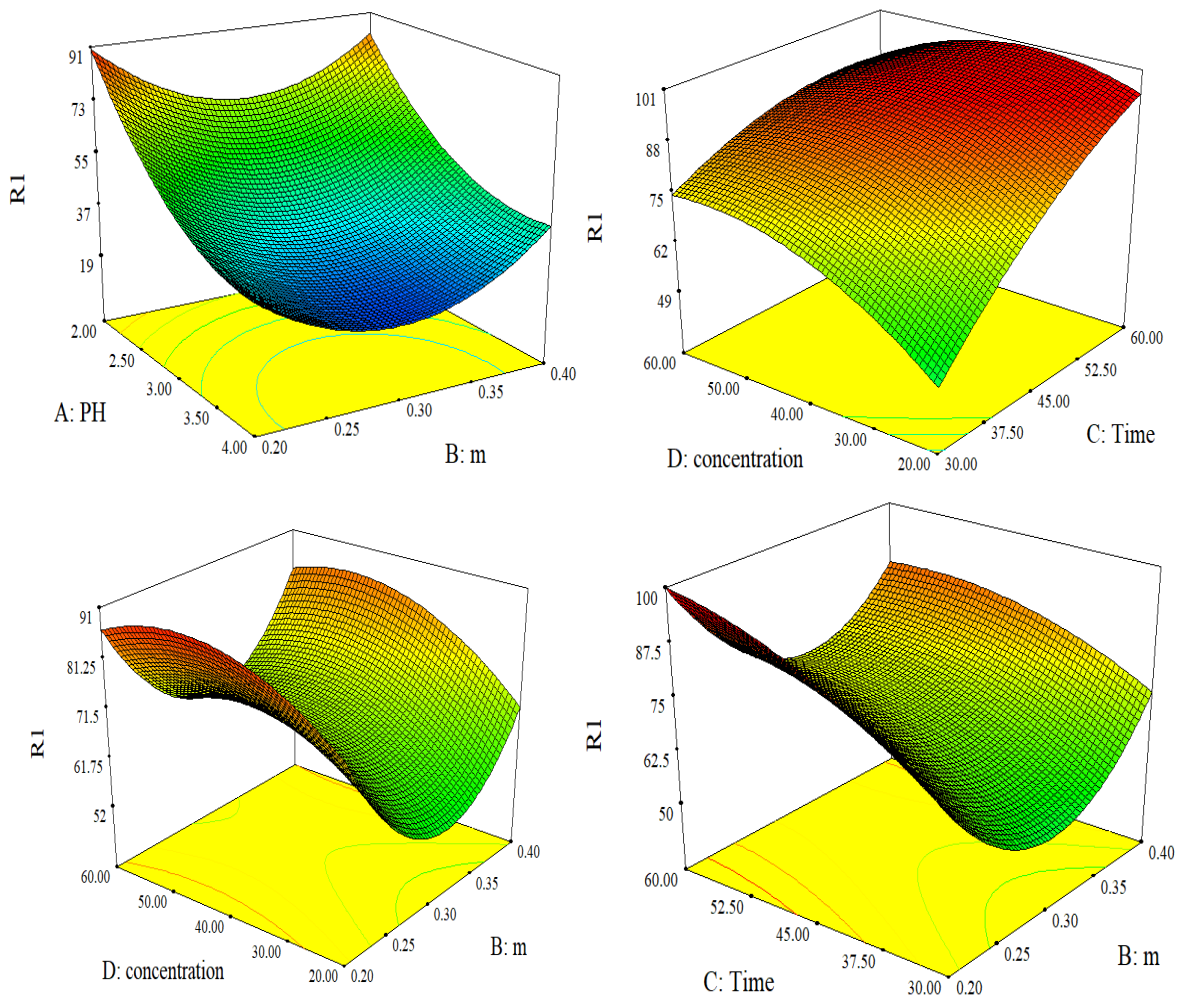


Figure 3: 3D surface plot of DO26 adsorption on silica fume.

Table 6. Summary of kinetics and RSM optimization of the present study and previous studies.

Adsorbent	Dye	Kinetic model	Optimum conditions A=pH B=adsorbent C=time D=concentration	%R <sub>predicated</sub>	Reference
Silica fume	DO26	pseudo-second-order	A=2.01 B=0.2 g c=55.15 min D=44 ppm	95.26%	Present study
Carbon Nano tube doped ZnO/Fe <sub>2</sub> O <sub>3</sub>	DO26	pseudo-second-order	A=5 C=3.8 hours	70.6%	(Tariq et al., 2022)
Cerium- doped mesoporous ZnO	DR81	-	A=3 B=0.02 g C=19.68 min D=40 ppm	94.41%	(Bazgir et al., 2019)
Kola nut shell activated carbon	orange G	-	A=6.0 B=0.30 g C=60 min D=100 mg/l	93.93%	(Chinonye et al., 2018)



#### 4. CONCLUSION

In this study, adsorption of DO26 azo dye on silica fume in a batch system was investigated. Design of the experiment was carried out with CCD method to model and influence the interaction effects of the parameters. According to the ANOVA results for the quadratic model, effect of pH, amount of adsorbent, concentration and interaction between pH and amount of adsorbent, pH and concentration, amount of adsorbent and time, amount of adsorbent and concentration, time and concentration and the double effect of the adsorbent parameters are important and effective. The optimum conditions for maximum removal of DO26 (95.26%) were obtained to be at pH 2.01, contact time 55.15 minutes, adsorbent amount=0.2 g, and initial concentration 44 ppm. The experimental kinetic data were analyzed through the conventional kinetic models, and the results demonstrate that the sorption kinetics can be accurately described by the pseudo-second order model. The literature on the absorption of azo dyes was reviewed, and the findings of this study were compared to previous research in terms of kinetics and RSM outcomes. The summarized results, presented in Table 6, indicate that silica fume outperformed other adsorbents in terms of optimal removal percentage of the dye. Also, according to the FESEM image, silica fume has a spherical and porous structure; Therefore, silica fume as a cheap adsorbent can remove dye pollutants from water.

#### 5. REFERENCES

- Ahmed, S. A., Gaber, A. A. A., & Rahim, A. M. A. (2017). Application of silica fume as a new SP-extractor for trace determination of Zn (II) and Cd (II) in pharmaceutical and environmental samples by square-wave anodic stripping voltammetry. *Applied Water Science*, 7(2), 677-688.
- Aşçı, Y. (2013). Decolorization of Direct Orange 26 by heterogeneous Fenton oxidation. *Desalination and Water Treatment*, 51(40-42), 7612-7620.
- Aziz, K., Aziz, F., Mamouni, R., Aziz, L., Anfar, Z., Azrrar, A., . . . Laknifli, A. (2022). High thiabendazole fungicide uptake using Cellana tramoserica shells modified by copper: Characterization, adsorption mechanism, and optimization using CCD-RSM approach. *Environmental Science and Pollution Research*, 29(57), 86020-86035.
- Bazgir, A., Khorshidi, A., Kamani, H., Ashrafi, S. D., & Naghipour, D. (2019). Modeling of azo dyes adsorption on magnetic NiFe<sub>2</sub>O<sub>4</sub>/RGO nanocomposite using response surface methodology. *Journal of Environmental Health Science and Engineering*, 17, 931-947.
- Chinonye, O.A., Oluchukwu, A.C., & Elijah, O.C. (2018), Statistical analysis for orange G adsorption using kola nut shell activated carbon. *Journal of the Chinese Advanced Materials Society*, 6(4), 605-619.
- Dargahi, A., Samarghandi, M. R., Shabanloo, A., Mahmoudi, M. M., & Nasab, H. Z. (2021). Statistical modeling of phenolic compounds adsorption onto low-cost adsorbent prepared from aloe vera leaves wastes using CCD-RSM optimization: effect of parameters, isotherm, and kinetic studies. *Biomass Conversion and Biorefinery*, 1-15.
- Dbik, A., El Messaoudi, N., Bentahar, S., El Khomri, M., Lacherai, A., & Faska, N. (2022). Optimization of Methylene Blue Adsorption on Agricultural Solid Waste Using Box-Behnken Design (BBD) Combined with Response Surface Methodology (RSM) Modeling. *Biointerface Research in Applied Chemistry*, 12(4), 4567-4583.
- Genc, A., & Oguz, A. (2010). Sorption of acid dyes from aqueous solution by using non-ground ash and slag. *Desalination*, 264(1-2), 78-83.
- Geyikçi, F., Kılıç, E., Çoruh, S., & Elevli, S. (2012). Modelling of lead adsorption from industrial sludge leachate on red mud by using RSM and ANN. *Chemical Engineering Journal*, 183, 53-59.
- Ghaedi, M., Hajati, S., Zaree, M., Shajaripour, Y., Asfaram, A., & Purkait, M. (2015). Removal of methyl orange by multiwall carbon nanotube accelerated by ultrasound devise: Optimized experimental design. *Advanced Powder Technology*, 26(4), 1087-1093.
- Kalkan, E., Nadaroglu, H., & Celebi, N. (2014). Use of Silica Fume as Low-Cost Absorbent Material for Nickel Removal from Aqueous Solutions. *Asian Journal of Chemistry*, 26(18).
- Kannaujiya, M. C., Gupta, G. K., Mandal, T., & Mondal, M. K. (2022). Adsorption of Acid Yellow 2GL dye from simulated water using brinjal waste. *Biomass Conversion and Biorefinery*, 1-14.
- Li, X., Han, C., Zhu, W., Ma, W., Luo, Y., Zhou, Y., . . . Wei, K. (2014). Cr (VI) removal from aqueous by adsorption on amine-functionalized mesoporous silica prepared from silica fume. *Journal of Chemistry*, ID 765856, 1-10.
- Montgomery, D. C. (2017). *Design and analysis of experiments*: John wiley & sons.
- Nadaroglu, H., & Kalkan, E. (2014). Removal of copper from aqueous solution using activated silica fume with/without apocarbonic anhydrase.

- Safa, Y., & Bhatti, H. N. (2011). Kinetic and thermodynamic modeling for the removal of Direct Red-31 and Direct Orange-26 dyes from aqueous solutions by rice husk. *Desalination*, 272(1-3), 313-322.
- Sohrabi, M. R., Moghri, M., Masoumi, H. R. F., Amiri, S., & Moosavi, N. (2016). Optimization of Reactive Blue 21 removal by Nanoscale Zero-Valent Iron using response surface methodology. *Arabian journal of chemistry*, 9(4), 518-525.
- Tariq, W., Arslan, C., Naqvi, S. A., Abdullah, M., Nasir, A., Gillani, S. H., . . . Yamin, M. (2022). Photocatalytic Removal of Azo Dyes Using a CNT Doped ZnO/Fe<sub>2</sub>O<sub>3</sub> Catalyst. *Polish Journal of Environmental Studies*, 31(5), 4279-4289. doi:10.15244/pjoes/131805
- Tomczak, E., & Tosik, P. (2014). Sorption equilibrium of azo dyes Direct Orange 26 and Reactive Blue 81 onto a cheap plant sorbent. *Ecological Chemistry and Engineering*.
- Wang, Y., & Chu, W. (2011). Adsorption and removal of a xanthene dye from aqueous solution using two solid wastes as adsorbents. *Industrial & engineering chemistry research*, 50(14), 8734-8741.
- Yan, L.-g., Qin, L.-l., Yu, H.-q., Li, S., Shan, R.-r., & Du, B. (2015). Adsorption of acid dyes from aqueous solution by CTMAB modified bentonite: kinetic and isotherm modeling. *Journal of Molecular Liquids*, 211, 1074-1081.
- Zhang, D., Ma, Y., Feng, H., Wang, Y., & Hao, Y. (2012). Preparation and characterization of the carbon-Microsilica composite sorbent. *Advanced Powder Technology*, 23(2), 215-219.
- Zhu, X., Zhang, Z., & Yan, G. (2016). Methylene blue adsorption by novel magnetic chitosan nanoadsorbent. *Journal of Water and Environment Technology*, 14(2), 96-105.



## Characterization of Nano-Structured Magnesium-Aluminum Ferrites Synthesized by Citrate-Gel Auto Combustion Method

M. Shahjahan<sup>1\*</sup> , M. A. Bhuyan<sup>1</sup> , M. S. Hossain<sup>2</sup> ,  
M. A. Haque<sup>1</sup> , and D. P. Paul<sup>1</sup> 

<sup>1</sup> Department of Physics, University of Chittagong, Chittagong-4331, Bangladesh.

<sup>2</sup> Industrial Physics Division, BCSIR Laboratories Dhaka, Bangladesh Council of Scientific & Industrial Research (BCSIR), Dhaka -1205, Bangladesh.

**Abstract:** An effort is made to find the solution to the new challenges of modification advancements in ferrite technologies. The hypothetical variation in the structural, magnetic, and electrical properties of cubic spinel magnesium aluminum ferrites introduced by the substitution of doping elements has been rationalized and proven. The outcome of aluminum substitution on the magnesium ferrites has been examined and investigated. Spinel ferrites having compositions of  $MgAl_xFe_{2-x}O_4$  ( $x = 0.1, 0.2, 0.3, 0.4$ ) were prepared by the sol-gel auto-combustion method. The prepared sample's characterization, such as scanning electron microscopy (SEM), DC electrical resistivity, AC electrical resistivity, and dielectric properties measurements, were tested using the respective instruments. The grain size and crystal size of all samples were measured from the micrographs of SEM and XRD Data. It is found that the average grain size is within the range of 300 nm - 550 nm for all different series that are formed, keeping the samples at 1100 °C sintering temperatures. A two-probe method experiment with a temperature range of 30 °C to 500 °C gives data on DC electrical resistivity. The Curie temperature depends on the sintering temperature, and it increases with increasing doping concentration. Also, doping influences grain size, which decreases with increasing concentration. Analyzing the SEM micrographs, it is found that the average grain size must decrease in tendency with increasing Al content. DC electrical resistivity exhibits excellent semiconducting behavior. Frequency dependence, dielectric constant, and dielectric loss factors were measured, keeping the frequency range of 75 Hz to 130 MHz at room temperature. The result shows that the dielectric constant ( $\epsilon$ ) and dielectric loss tangent ( $\tan^{\text{TM}}$ ) decrease with the increase in frequency, while the AC resistivity and Q-factor increase. Comparing the electrical properties of four compositions, it can be suggested that the mixed ferrite, sample-4 ( $x = 0.3$ ), shows the highest Q-factor of all at 1100 °C.

**Keywords:** Mg-Al ferrites, sol-gel, nanocrystalline, magnetic properties, electrical properties, DC resistivity, dielectric, loss tangent.

**Submitted:** April 06, 2023. **Accepted:** July 17, 2023.

**Cite this:** Shahjahan, M., Bhuyan, M. A., Hossain, M. S., Haque, M. A., & Paul, D. P. (2023). Characterization of Nano-Structured Magnesium-Aluminum Ferrites Synthesized by Citrate-Gel Auto Combustion Method. Journal of the Turkish Chemical Society, Section B: Chemical Engineering, 6(2), 45-62. <https://doi.org/10.58692/jotcsb.127857>.

\*Corresponding author. E-mail: [shahjahan@cu.ac.bd](mailto:shahjahan@cu.ac.bd).

### 1. INTRODUCTION

Nanoscience and nanotechnology are more attentive to materials and solid-state systems (Joudeh & Linke, 2022) whose components,

structures, and designs exhibit novel and significantly improved physical, chemical, and biological properties because of their nanoscale size (Saini et al., 2010). Research on nano-size technology and nanoparticles has unlocked so

many scopes and versatile uses due to their novel and excellent properties (Sontakke & Purkait, 2021). It also helps create many new materials and use devices with prospective applications, like medicine, toxicity, electronics, and energy production (Buzea et al., 2007). Also, it has an impact on the environment, consumer products, and global economics (Pathania et al., 2021).

Ferrites have remarkable magnetic properties (Ahmed et al., 2022) due to their versatility, low production cost, exclusive electromagnetic performance, high resistivity, low chemical losses, and excellent chemical stability (Hankare et al., 2011) (Amiri et al., 2019) Within a large frequency range (Dixit et al., 2012). Soft ferrites are mostly used in many electrical components, memory-storing devices, microwave functional devices, and magnetic devices because of their high magnetic permeability and low magnetic losses (Lakshmi Ranganatha et al., 2020) (Giannakopoulou et al., 2002). These materials can also be used for different high-temperature procedures because of their strong thermal stability, low electrical conductivity, electrocatalytic activity, and corrosion resistivity (Olsen & Thonstad, 1999). Among these ferrites' techniques, magnesium aluminum ferrites are considered as they showed permeability, resistivity, saturation magnetization, low losses and relatively large Curie temperature (Gimenes et al., 2012). The general formula of magnesium ferrite,  $M^{+2}Fe^{+3}_2O_4$  ( $AB_2O_4$ ), is a type of crystal compound of spinel structure (where M is from the tetrahedral site and Fe from the octahedral site) (Gorter, 1950).

The spinel ferrites have interesting properties to disperse the cations among the tetrahedral (A) and octahedral (B) sites (Bhatu et al., 2007). Substituting non-magnetic and magnetic ions largely affects the ferrite's properties like lattice-related parameters, magnetic moments, and ion exchange interactions (Zakaria et al., 2003) (Zakaria et al., 2004). Scientists use many chemical techniques for the synthesis of ferrites (Giri et al., 2004)(George et al., 2006) (Wang, 2006) (Hankare, Vader, et al., 2009) (Hankare, Sankpal, et al., 2009) (Zhang et al., 1990). The citrate sol-gel auto-combustion process has several advantages, such as nano-scale yield without the use of expensive equipment (Kamble et al., 2013). Because all the reactants are solutions, molecular mixing occurs, and reactant yield can be controlled accurately (Atassi & Tally, 2006). The purpose of the present research is to present a novel and economical method of preparation of Mg-Al ferrites by the sol-gel auto-combustion method.

Doping  $MgFe_2O_4$  with metals is the finest method, filled with tetrahedral or octahedral sites that can alter the magnetic, electrical, or structural properties of ferrites. Following the procedure, different properties of ferrites can be engineered to fit a particular application (Shokrollahi, 2008). As per our knowledge, information is not available about the nano-sized Mg-Al ferrites produced using the citrate-gel auto combustion method. Some mixed Cu-Mg-Zn ferrites were synthesized through the co-precipitation method by Bhosale et al. (Kuznetsov et al., 1998) where they found the lattice parameter decreases gradually while density increases with the increase in  $Mg^{2+}$  at the substitution level. Qi et al. (Radwan et al., 2003) showed Mn substituted ( $Mg_{0.2}Cu_{0.2}Zn_{0.6}O$ ) ( $Fe_{2-x}Mn_xO_3$ )<sub>0.97</sub> ( $x = 0.00-0.07$ ) ferrites using nanosized precursor powders by a sol-gel method and found Mn showed higher initial permeability and good grain morphology than that of NiCuZn ferrites.

It could be a good material for multi-layer chip inductors with high inductance. Nanoparticles of  $M_{0.5}Mg_{0.5}Fe_2O_4$  ( $M = Ni, Cu, \text{ and } Zn$ ) are prepared by Pradeep et al. (Lakshman et al., 2005) using the sol-gel method and found greater values of lattice constant of mixed CuZn ferrites. Also, particle size was decreased by the substitution of Cu for Zn. Barati (Arulmurugan et al., 2006) found that properties like initial permeability, saturation magnetization, dielectric constant, and dielectric loss were increased, and AC-resistivity was decreased with the increase in doping contents. Prepared materials may be applicable in multilayer chip inductor applications due to their low loss at high frequencies and good magnetic properties.

In this research, we have prepared nano-ferrites having the composition  $MgAl_xFe_{2-x}O_4$  ( $x = 0.1, 0.2, 0.3, 0.4$ ) by the citrate-gel auto combustion method, keeping in mind that the particle size will be small and the magnetic, electrical, and dielectric properties will be improved by the substitution of  $Fe^{+3}$  with  $Al^{+3}$  ions. According to our knowledge, this is the unique observation of Mg-Al nano-ferrites made using the citrate-gel method with small particle sizes. In this article, we show the citrate gel method-based synthesis, XRD, SEM, EDS, and resistance properties of aluminum-doped magnesium ferrites which will be useful for different purposes.

## 2. MATERIALS AND METHOD

Mg-Al nano-ferrites using the chemical formula  $MgAl_xFe_{2-x}O_4$  ( $x = 0.1, 0.2, 0.3, 0.4$ ) were synthesized by the citrate-gel auto combustion technique using magnesium nitrate hexahydrate ( $Mg(NO_3)_2 \cdot 6H_2O$ , 99%), iron(II) nitrate nonahydrate ( $Fe(NO_3)_2 \cdot 9H_2O$ , AR grade), aluminum nitrate

nonahydrate ( $\text{Al}(\text{NO}_3)_3 \cdot 9\text{H}_2\text{O}$ , AR grade), citric acid ( $\text{C}_6\text{H}_8\text{O}_7 \cdot \text{H}_2\text{O}$ ), AR grade, and ammonia ( $\text{NH}_3$ , AR grade). The required amount of nitrate salt and the citric acid solution are formulated using nitrates in a citric acid molar ratio of 1:1. The pH value of the solution is adjusted to 7 with the help of ammonia mixing slowly in the solution. A magnetic hot plate stirrer is used to stir the solution continuously to finish the entire procedure. The solution was poured into a beaker, heated at 100 °C on a hot plate, and stirred continuously till it transformed into a highly viscous gel. All the samples formed as the gel was burned out completely to form a fluffy, loose powder after reaching a proper temperature, starting ignition, and burning in a self-propagating combustion manner. The whole combustion process was done in a short time. Finally, the as-burnt powders were calcinated using the programmable muffle furnace at 500 °C for up to 1 h to get the ferrites of a single phase.

The calcite powders were granulated using a 1% saturated solution of polyvinyl alcohol as a binder and were uniaxially pressed at a fixed pressure up to 0.5 MPa in a stainless-steel die to form pellet specimens of 12 cm diameter. Samples were leveled as sample-1 to sample 4 according to X values. All samples were heated slowly inside the programmable muffle furnace up to 550 °C at a rate of about 2 °C  $\text{min}^{-1}$  to avoid cracking of the samples. Then, the temperature was raised to 1100 °C, and then the samples were kept at this temperature for 6 h in an airtight atmosphere so that they got cooled slowly inside the furnace. The surfaces of all the specimens were polished to remove oxide and any other extra layer formed during the sintering process.

### 2.1. Characterization

The structural structure of the synthesized ferrite samples was tested by X-ray diffractometer (XRD) using Cu  $K_\alpha$  X-ray radiation ( $\lambda=1.5405 \text{ \AA}$ ) at normal temperature in the angle range of 20° to 85°. X-ray data gives us the phase and crystallite size of the prepared samples, which confirm the formation of a single-phase cubic spinel. Also, the surface morphology and surface features of the prepared ferrites were investigated and recorded by SEM. Dielectric properties, electrical properties, and Curie temperature were investigated by the relevant instruments.

## 3. RESULTS AND DISCUSSION

### 3.1. Structural Properties

The X-ray diffraction patterns for the investigated samples have been shown in Figure 1. Powder diffraction by an X-ray powder diffractometer was used to find the crystalline phases using ( $\text{Cu-K}\alpha$ ) = 1.5406 Å at room temperature.

Structural parameters like the lattice parameters and spin phases of all the samples are calculated from the XRD data, and the atomic position of the spinel phases is determined from the literature. All the sharp peaks are in the same position as stated by Giri et al. (2004) which confirmed the sample preparation was accurate and showed a single phase only. The lattice constant is calculated by using the known formula (Iqbal & Siddiquah, 2008)

$$a = d_{hkl} \sqrt{h^2 + k^2 + l^2}$$

Where the Miller indices are  $h, k, l$  and interplanar spacing is  $d_h$

It is observed that the highest intensity peak is at the 35.36° position. Calculation gives the peak to be (311), which tells us the prepared samples are spinel ferrites. The average size of the crystal bulk sample ( $D_p$ ) is calculated using the Scherrer equation (Patterson, 1939)

$$D_p = \frac{0.94 \lambda}{\beta \cos \theta}$$

Where the line broadening in radians is  $\beta$ , Bragg angle is  $\theta$ , and the X-ray wavelength is  $\lambda$ .

Data showed that the crystal size reduces with a decrease in Fe content as it is larger than the Al atoms, as shown in Table 1. From the table data, it is observed that the lattice constant is almost the same for all samples but tends to be larger as the concentration of cations increases in every sample. Also, we have calculated the X-ray density using the formula (Krishna et al., 2012a)

$$\rho_{\text{ferrite}} = \sum \frac{8M}{Na^3}$$

Here,  $M$  is the molecular weight of the sample, Avogadro's number is  $N$ , and the lattice constant is  $a$ .

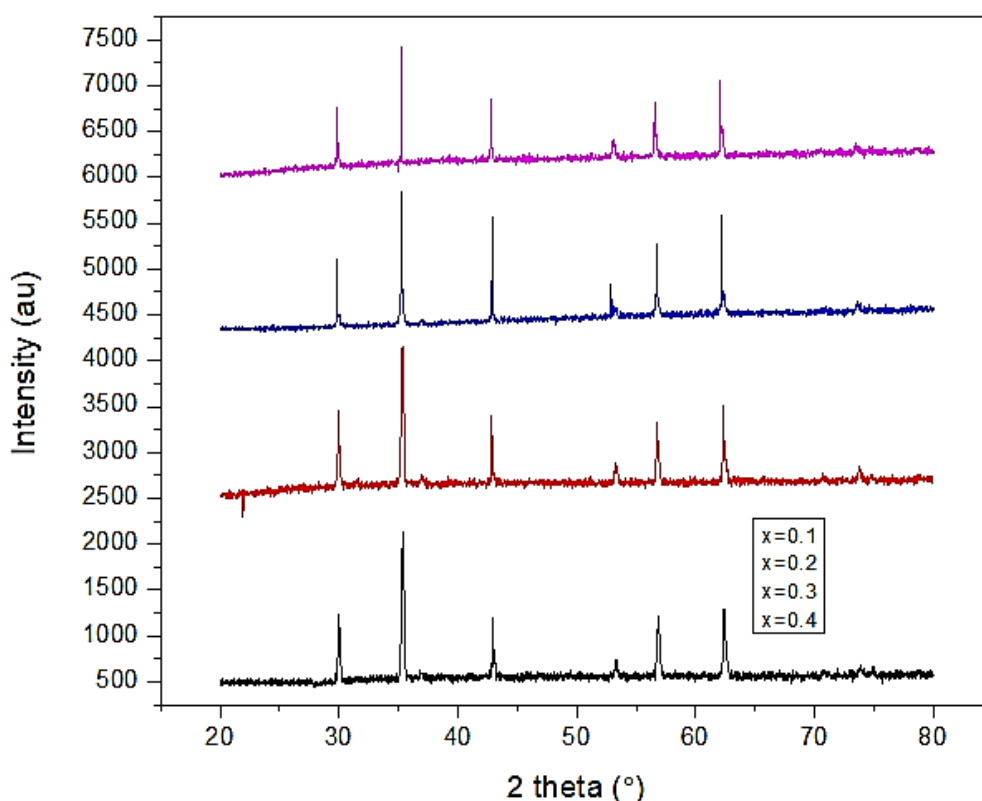


**Figure 1:** XRD patterns for  $\text{MgAl}_x\text{Fe}_{2-x}\text{O}_4$  ferrites.  $x = 0.1$  (purple),  $0.2$  (blue),  $0.3$  (red),  $0.4$  (black).

The actual physical bulk density of the tablet shaped prepared ferrites sample was calculated using the formula (Sujatha et al., 2013)

$$d_{\text{bulk}} = \frac{m}{\pi r^2 t}$$

Here, mass is  $m$ , the pellet radius is  $r$ , and  $t$  is the thickness of the sample. Applying the Archimedeian porosimetry theory, the percentage of porosity (%P) is calculated and shown in Table 1. It was also observed that the porosity from the SEM micrographs manually got a similar result. Observing the lattice constant, a decreasing trend is due to the increase in Al content and the decrease in Fe content. Sample -1 ( $x=0.1$ ) showed the highest bulk density, which means porosity would be lower due to high density and is observed accordingly, as shown in Table 1,

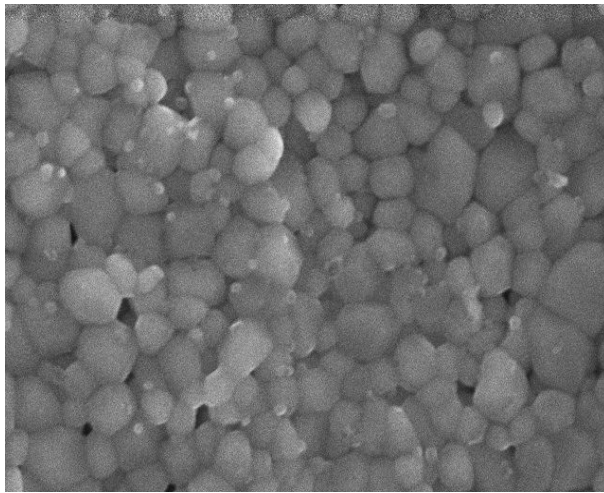
The bulk density of the ferrite samples decreases gradually with the decrease in the  $\text{Fe}^{2+}$

concentration as the large atomic weight of Fe is compared with the Mg atoms shown in Table 1. High porosity is observed in the sample 4 ( $x=0.4$ ) which is lowest density sample. Bulk density is decreased due to a decrease in Fe content, and Al concentration improves the magnification, which decreases the porosity.

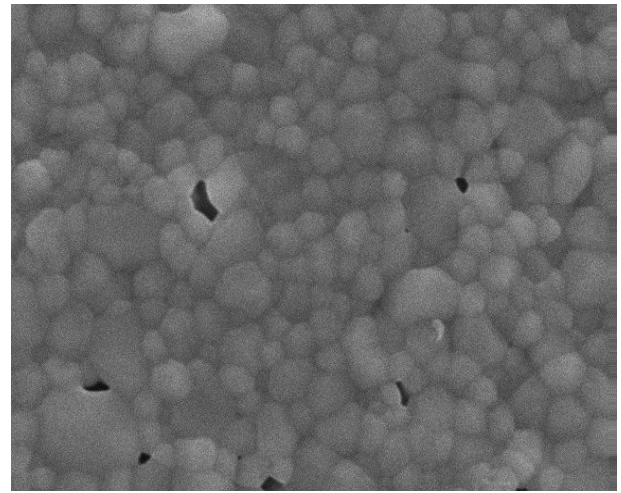
Also, the table showed that the X-ray density calculated has a reducing tendency with the higher Al concentration shown and shows an inverse relation with lattice parameters. Barati et al. got the same result (Giri et al., 2004). It is observed here that, there is a correlation and closed agreement between the theoretical X-ray densities, the observed bulk density, and the porosity of the sintered ferrites. Due to the pore in the sample, X-ray densities are larger than bulk densities. This close relationship with such parameters of ferrites indicated good quality ferrites.

### 3.2. Morphology by SEM

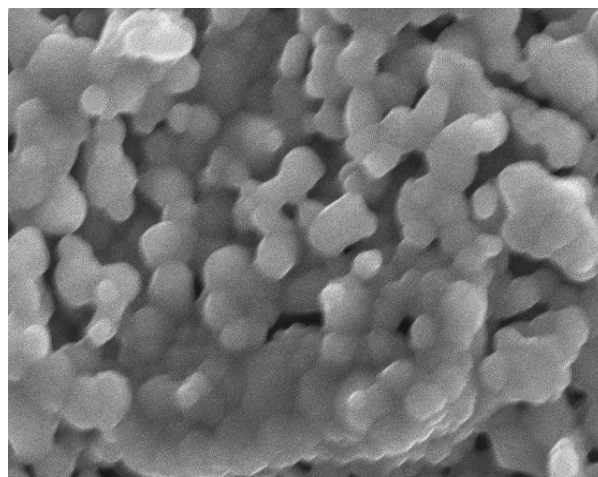
SEM representative micrographs of the samples with different amounts of substitution are shown in Figure 2.



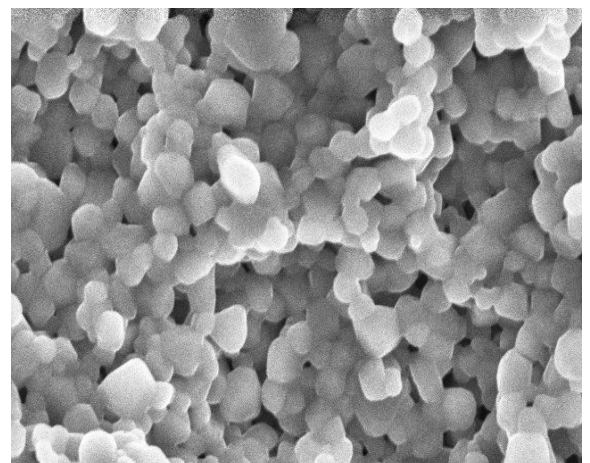
Sample 1



Sample 2



Sample 3



Sample 4

**Figure 2:** SEM micrographs of various compositions.

Images were taken at different magnifications. The images showed large agglomerates of strongly connected cubic aggregates and well-defined particles of the powder sample with an inhomogeneous, broader grain size distribution. Mechanically activated nano-sized particles showed this type of broader size distribution. (Oñoro et al., 2021)

This agglomeration is caused by the interaction of nano-sized magnetic fine particles with a permanent magnetic moment proportional to their volume. Hence, agglomeration results from the contribution of the permanent magnetization

property of each particle (Arulmurugan et al., 2006). The foam-like structure is found in the porous network of sintered bodies. It is assumed that magnesium ions influence ferrite formation; hence, the compound formation showed the least mass. From the SEM micrographs, we also found that the particle size of the sample is in the nanometer range. We found a trend that, with an increase in Al composition, the grain size in the crystal decreased moderately.



### 3.3. Composition Dependent DC Electrical Properties

DC electrical resistivity is used to understand the conductivity of the prepared sample. It is measured using the two probe electrical method. A fixed voltage was applied across the sample holder, keeping the sample in series and the standard resistance lower than the sample resistance. The voltage dropped across the resistance was measured using a voltmeter, and the current was measured using an ampere meter. Using the voltage and current across the sample, resistivity is calculated using the relation

$$R = RA/l \quad \Omega\text{-cm} \quad (\text{Krishna et al., 2012b})$$

Where,  $R_f$ : Fixed Resistance;  $A$ : Surface area of the sample  $= \pi r^2$ ;  $l$ : Thickness of the sample;  $R$  is the resistance of the sample, and it is given by  $R = (V_s/V_f) \times R_f$ . Hence, from the above equations,  $r = AR_f/l (V_s/V_f)$ ,  $V_s$  is the voltage across the sample,  $V_f$  is the voltage across the fixed resistance.

The DC resistivity of the sample was found to increase at a normal temperature from  $0.81 \times 10^6 \Omega\text{-cm}$  to  $1.85 \times 10^6 \Omega\text{-cm}$  and at transition point from  $0.39 \times 10^6 \Omega\text{-cm}$  to  $2.0 \times 10^6 \Omega\text{-cm}$  with increasing  $\text{Al}^{3+}$  from  $x = 0.1$  to  $x = 0.4$ , as mentioned in Table 2.

The DC resistivity ( $\ln\rho$ ) vs. temperature ( $1000/T$ ) curve for all samples at  $1100 \text{ }^\circ\text{C}$  has been plotted as shown in Figure 3. From the figure, we found that the DC resistivity has a common trend for all samples and decreases sharply with increasing temperature up to a transition point. After that temperature, the resistivity decreases with increasing temperature slowly and almost constant after a certain time. The resistivity of all samples shows similar characteristics, but the values of resistivity increase with an increase in the Al concentration, as shown in Table 2. In this case, the Curie temperature,  $T_c$ , is found to be  $115 \text{ }^\circ\text{C}$ ,  $125 \text{ }^\circ\text{C}$ ,  $135 \text{ }^\circ\text{C}$ , and  $140 \text{ }^\circ\text{C}$ , respectively, for all samples.

The increase in resistivity might be due to Al concentration increases, while  $\text{Fe}^{3+}$  concentration decreases for their occupation on octahedral sites, which is produced during sintering (Islam et al.,

2004). The activation energy ( $E_p$ ) increases with the increase in Al content. It increases up to  $x = 0.3$  but again reduces for  $x = 0.4$ . This is due to the Al ions. For many ions, some ions may not participate in the reaction, and the activation energy goes lower. Also, Al concentration has an effect on Curie temperature and shifts it to a higher temperature. Another reason for the increase in  $\rho$  with increasing Al composition is that  $\text{Mg}^{2+}$  ions tend to occupy the tetrahedral sites (A) and Al ions choose to go to the octahedral sites (B). Also, Fe ions partially occupy both A and B sites, which increases temperature and decreases conductivity, and hence resistivity increases which confirms that the prepared ferrite under this research has semiconductor-like properties.

Also, Figure 4 indicates the resistivity variation with the ferrite's composition. It is observed that the resistivity is not linear. At  $x = 0.3$ , resistivity graphs showed slight variation, meaning if Al concentration increases, resistivity decreases slowly and then increases again.

### 3.4. Effect of Al Concentration Variation on AC Resistivity

The electrical measurements are performed for all Mg-Al ferrite samples at room temperature within the frequency ranges from  $75 \text{ kHz}$  to  $2 \text{ MHz}$  using an LCR-Q meter. This is the resistance ( $R_p$  in  $\text{K}\Omega$ ) of the sample that was obtained by changing the input frequencies.

The AC resistivity is easily calculated by using ohm's law,  $R = \rho \frac{l}{A}$  or  $\rho = \frac{RA}{l}$  where  $R$  is the resistance of the sample,  $\rho$  is the resistivity of the sample,  $l$  is the thickness of the specimen or sample, and  $A$  is the area of the sample or specimen. The AC conductivity can therefore be determined as follows:  $\Sigma_{a.c.} = 1/\rho$ . Figure 5 of AC resistivity reveals that the observed samples have low conducting behavior, which increases with frequency. Among the frequency range, conductivity is high in the low-frequency region, and after that, it is moderately frequency-dependent. As the Al content of the sample increases, the conductivity becomes frequency independent, and a line is observed.



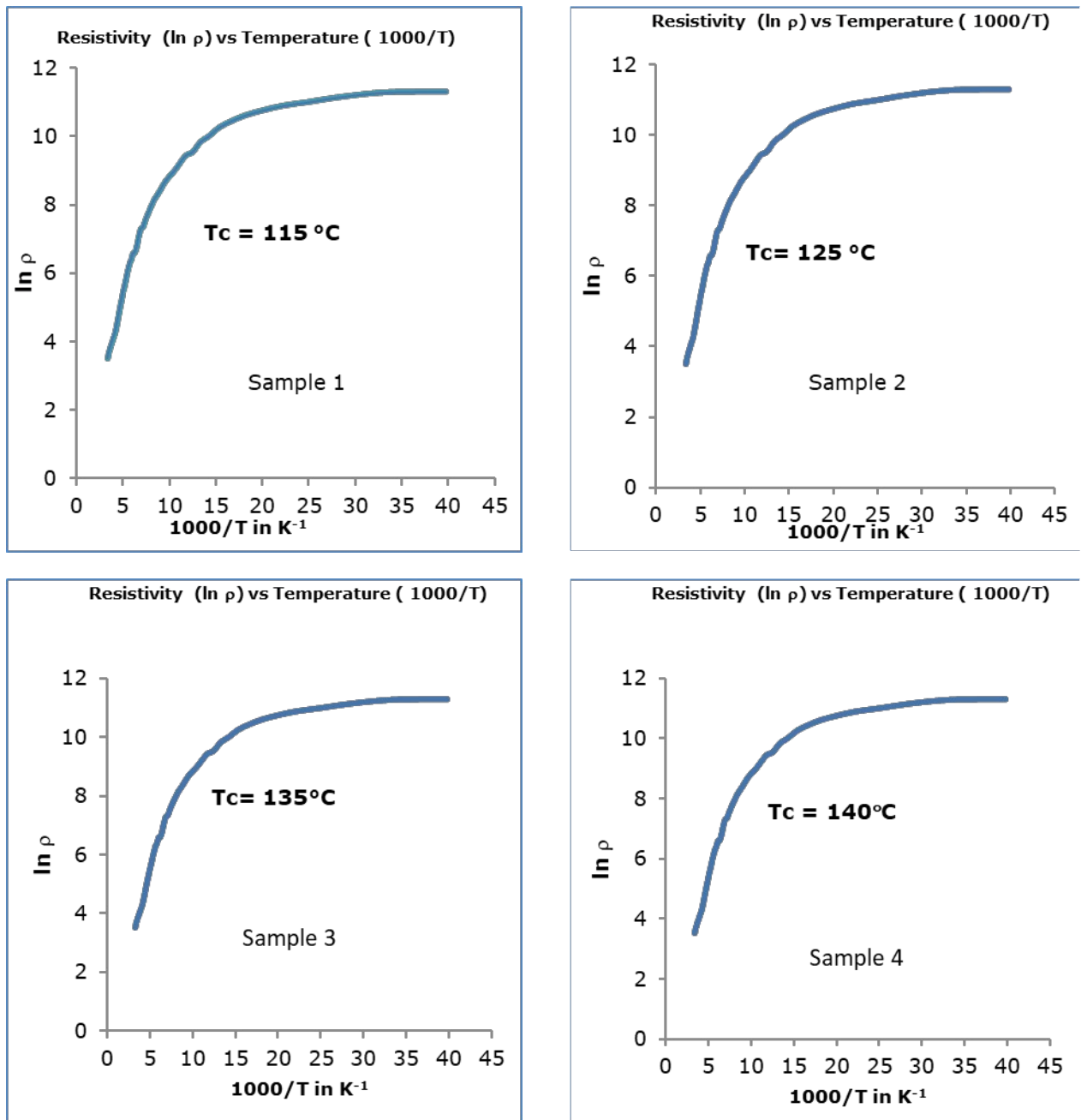


**Figure 3:** DC Resistivity ( $\ln \rho$ ) Vs. Temperature ( $1000/T$ ) curve for all samples.

**Table 1:** The structural parameters measured from the XRD graphs.

Sample Composition	FWHM	Crystallite size (nm)	Crystal Strain	Lattice constant (Å)	X-Ray density ( $r_x$ )(gcm <sup>-3</sup> )	Bulk density ( $r_a$ ) (gcm <sup>-3</sup> )	% (P)
MgAl <sub>0.1</sub> Fe <sub>1.9</sub> O <sub>4</sub>	0.2131	40.31	0.0035	8.4086	4.3826	4.9424	8.62
MgAl <sub>0.2</sub> Fe <sub>1.8</sub> O <sub>4</sub>	0.2458	34.95	0.0040	8.4188	4.3232	4.7713	11.35
MgAl <sub>0.3</sub> Fe <sub>1.7</sub> O <sub>4</sub>	0.2599	33.05	0.0043	8.4174	4.2611	4.5482	10.83
MgAl <sub>0.4</sub> Fe <sub>1.6</sub> O <sub>4</sub>	0.2676	32.1	0.0044	8.4098	4.2082	4.3485	11.16

**Table 2:** Different parameters of Mg-Al ferrites for temperature 1100° C.

Sample Composition	X	Average grain size, L(nm)	Resistivity, r in Ω-m at room temperature	Transition temperature T <sub>c</sub> (°C)	Resistivity r in Ω-m at T <sub>c</sub>	Activation Energy (eV) *10 <sup>-2</sup>
MgAl <sub>0.1</sub> Fe <sub>1.9</sub> O <sub>4</sub>	0.1	436	81181.38	115	3967.97	234
MgAl <sub>0.2</sub> Fe <sub>1.8</sub> O <sub>4</sub>	0.2	300	132336.8	125	7464.56	257
MgAl <sub>0.3</sub> Fe <sub>1.7</sub> O <sub>4</sub>	0.3	365	171720	135	10442.97	255
MgAl <sub>0.4</sub> Fe <sub>1.6</sub> O <sub>4</sub>	0.4	516	185563.1	140	20555.3	248

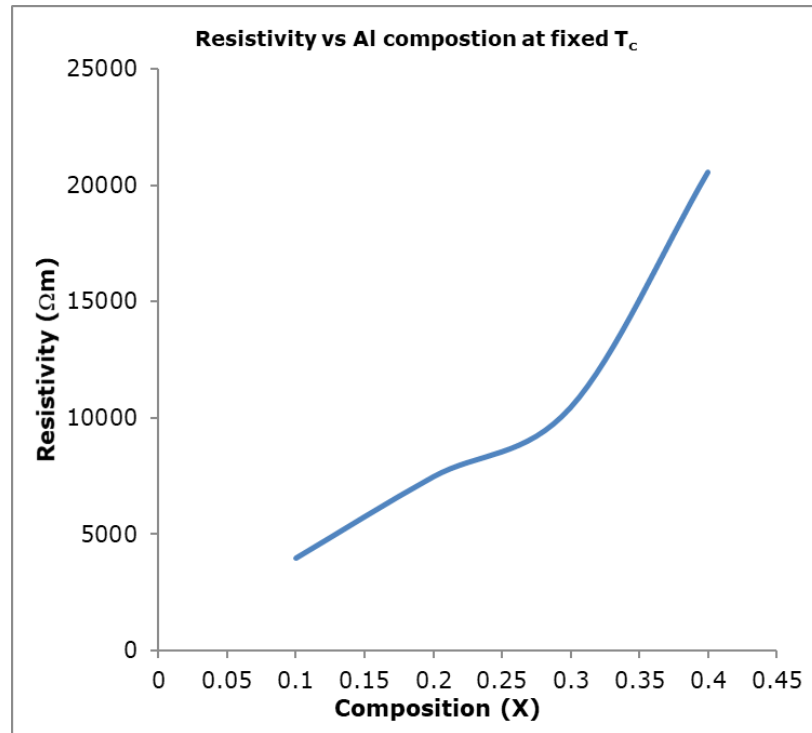


**Figure 4:** Variation of resistivity with all compositions.

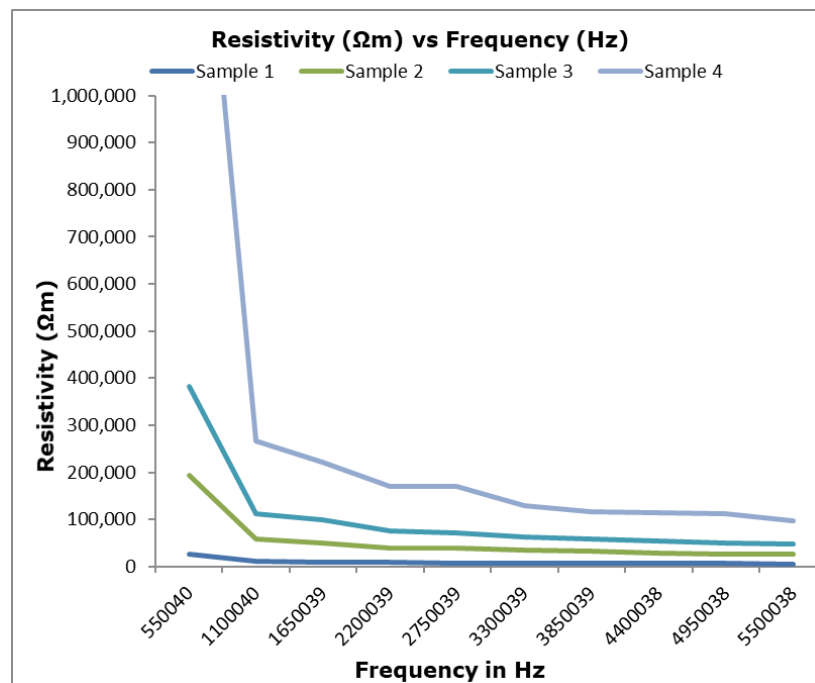


**Figure 5:** Resistivity ( $\Omega m$ ) vs Frequency (Hz) for all samples.

Figures 5 and 6 show how the amount of Al doping affects the resistivity and AC conductivity of different kinds of Mg-Al ferrites at 1100 °C as a function of frequency.

The values of AC resistivity depend on frequency and show a decreasing tendency with frequency

for all samples; hence, AC conductivity has an increasing tendency. Resistivity graphs are identical in shape, but for samples 3, 4, and 5, they decrease more rapidly than 1 and 2 after a certain frequency. But the AC conductivity is going to be maximum for sample 4, and the other 3 samples have a similar pattern.

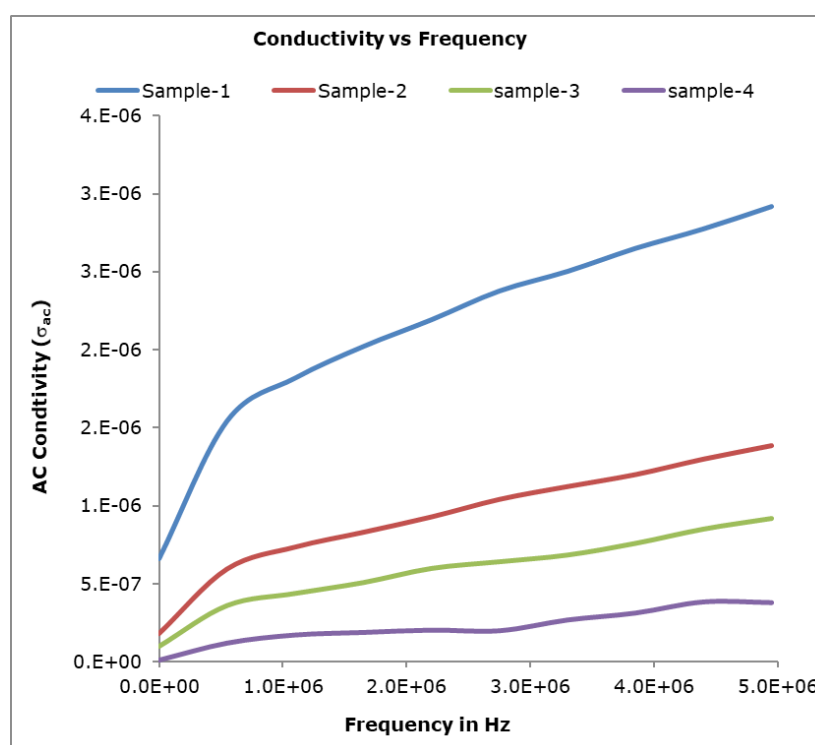


**Figure 6:** AC conductivity ( $\sigma_{AC}$ ) vs Frequency (Hz) for all samples.

### 3.5. Curie temperature ( $T_c$ )

The Curie temperature, or magnetic transition point, gives considerable information about the magnetic states of the substance. It has been determined from the graph of the resistivity as a function of temperature, as shown in Figure 2. It showed a slope at a fixed temperature point, which indicates the transition of the sample from ferrimagnetism to paramagnetism. The Curie temperature is presented for all samples in Table 1, and a graph is presented in Figure 7. It showed that Curie temperature changes with the Al concentration present in the sample and has an increasing tendency from 115 °C to 140 °C with increases in  $Al^{3+}$  composition from  $x = 0.1$  to 0.4.

### 3.6. Activation Energy

Using the electrical data, we have calculated the activation energies of ferrites and paramagnetic regions by following the formula  $\rho = \rho_0 \exp$

$(E_p/K_B T_c)$  used by Bhise et al, Patil et al, Snelling and others (Gu, 2003) and graphs of  $\ln \rho$  versus  $1000/T$  slope are given in Table 1. Here,  $\rho_0$  is the resistivity at  $t = 0$  °C.  $E_p$  is the activation energy.  $K_B$  is the Boltzmann constant. We found that at the 115 °C transition temperature ( $T_c$ ), the activation energy is 0.0234 eV/K. It decreases from 0.0234 eV to 0.0248 eV as the  $Al^{3+}$  composition increases from  $x = 0.1$  to 0.4. Also, it varies with composition, as shown in Figure 8. It has a decreasing trend, which may be due to a lack of oxygen vacancies (Kuznetsov et al., 1998).

Also, resistivity decreases with increasing  $Al^{3+}$  concentration because activation energy acts like DC electrical resistivity (Radwan et al., 2003). Activation energy is getting smaller, representing the electrons hopping among the ions of different valances. The gradual decrease of conductivity calculated at 1 kHz, excluding sample 1, with

increasing Al content shown in Table 1 can cause a decrease in the total number of charge carriers (Willey et al., 1993). Here, we also observed from

the figure that the activation energy is inversely proportional to the conductivity as well as to the ferrite's composition.

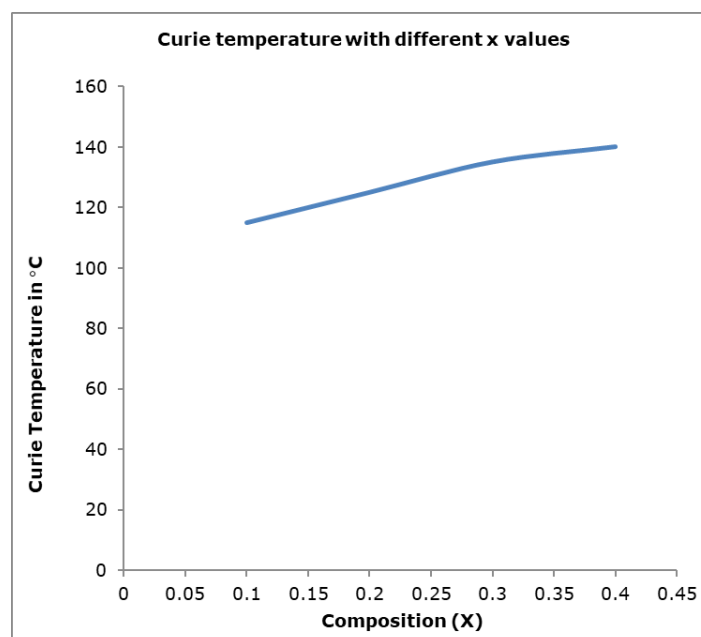


**Figure 7:** Variation of Curie temperature with composition.

**Table 3:** AC electrical properties measurements for four Mg-Al ferrites samples.

Sample No	Dielectric constant ( $\epsilon$ )		Dielectric loss tangent ( $\tan\delta$ )		Q-factor at frequency		Resistivity $\rho$ $\Omega\text{m}$	
	5.5E+5	1.10E+7	5.5E+5	1.10E+7	5.5E+5	1.10E+7	5.5E+5	1.10E+7
at (1100°C)	5	+7	Hz	7	Hz	7	Hz	Hz
	Hz	Hz		Hz		Hz		
X=0.1	5.45	4.85	0.32	0.0097	0.0064	100.23	3.24E+4	3.5E+4
X=0.2	6.81	5.55	0.648	0.048	0.0023	20.7	1.09E+4	6.3E+3
X=0.3	7.37	6.6	0.291	0.0069	0.00571	147.3	2.7E+4	3.52E+4
X=0.4	6.25	5.48	0.3	0.011	0.02	86.8	1.7E+5	3.5E+4

Table 3 showed the numeric values of Dielectric constant ( $\epsilon$ ), Dielectric loss tangent ( $\tan\delta$ ), Q-factor and Resistivity of all samples at different temperatures at frequencies of 5 MHz and 110 MHz

### 3.7. Effect of Al concentration on dielectric constant, loss tangent and Q factor

The electrical measurements were performed on four samples at room temperature for the

frequency ranges from 75 kHz to 2 MHz using an LCR-Q meter. We obtained the values of capacitances ( $C_p$  in  $\mu\text{F}$ ) by changing the frequencies. Using this data, dielectric constants were measured using the following formula:  $\epsilon = C_p / \epsilon_0 A$ . Where  $\epsilon$  is the dielectric constant,  $C_p$  is the capacitance of the sample,  $l$  is the thickness of the specimen or sample,  $A$  is the area of the sample or specimen and  $\epsilon_0$  is the permittivity of the free space. In our present investigation, we have also determined the Q-factor, the dielectric

constant, and the dielectric loss tangent with the help of an LCR-Q meter.

The Dielectric constant has a variation with composition at 100 kHz, as shown in Figure 9. Here, we observed that the dielectric constant increases with increasing Al concentration, which may contribute to the exchange between  $\text{Fe}^{2+3}$  and  $\text{Fe}^{3+}$  ions. This creates the chance to increase the polarization and dielectric constant (Willey et al., 1993). From the figure, it is observed that the dielectric constant decreases with increasing

frequency and ultimately reaches a fixed value. It is because polarization decreasing with frequency is a common trend for dielectric constant.

The observed nanostructural features have a major influence on the dielectric properties of doped Mg-Al ferrites. The value of the dielectric constant depends on the frequency and increases with an increase in Al content. But it showed a significant difference for all samples; this is due to low-temperature synthesis. After a certain frequency, the dielectric constant increases again.

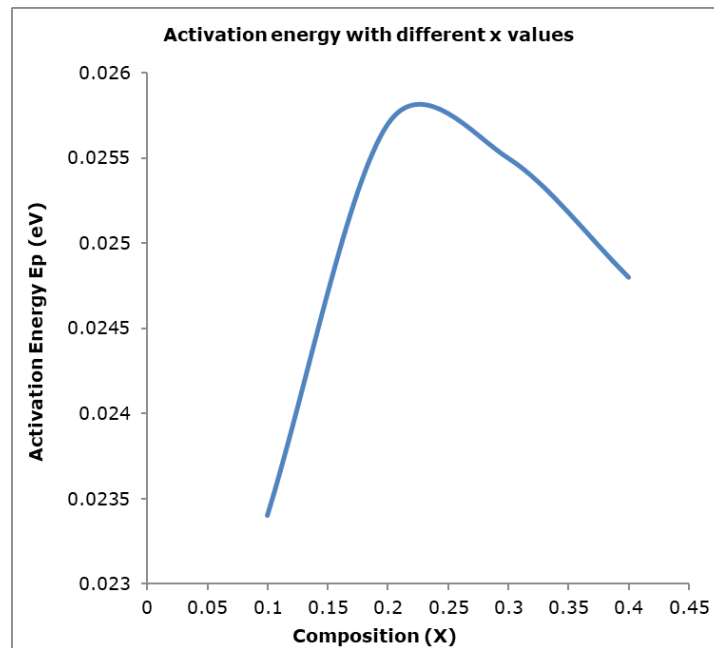


**Figure 8:** Variation of activation energy with composition.

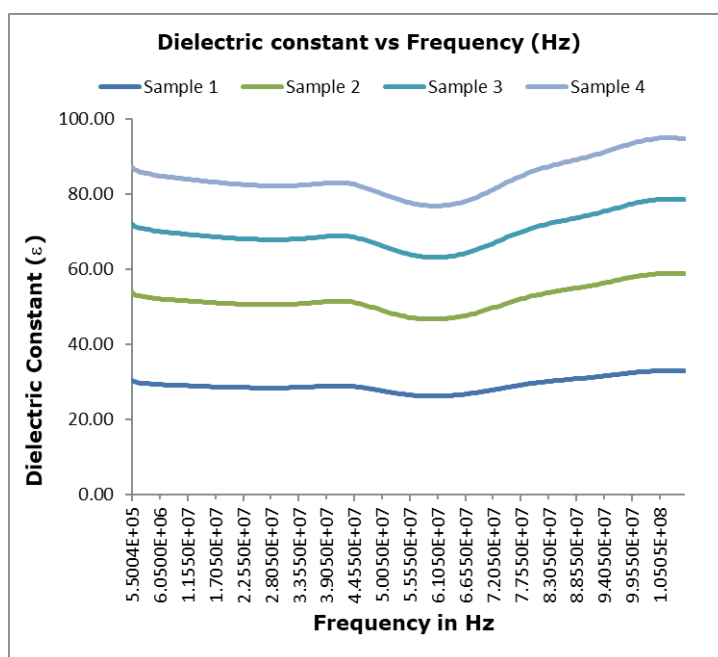


Figure 9: Dielectric constant vs Frequency (Hz) for all samples.

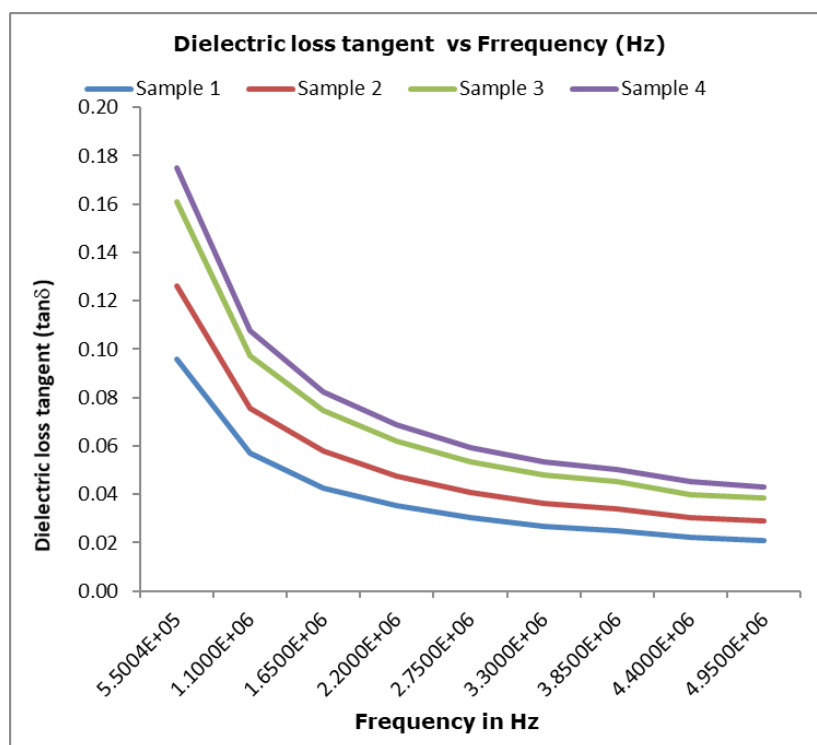


Figure 10: Dielectric loss tangent (tan δ, Y axis) vs (Hz, X axis) for all samples.

The loss factor decreases from 1.8 to 0.02 with the increase in frequency from 0.55 MHz to 4.9 MHz, as shown in Figure 10. The dielectric loss tangent (tanδ) basically depends on stoichiometry, Fe<sup>2+</sup> content, and structural homogeneity, which again depend on

compositional content and sintering temperature. The dielectric loss tangent vs. frequency graph for all samples showed that the dielectric loss tangent decreased with increasing frequency.

According to Iwachi (Oñoro et al., 2021), the conduction mechanism and the dielectric of ferrites have a strong correlation. When the hopping frequency is approximately equal to the externally applied electric field frequency, the loss tangent is highest. It is shown that the dielectric

loss tangent of sample 1 is high. The hopping frequencies are observed with a maximum loss at 0.55 MHz and a minimum loss of 11.36 MHz. The hopping of electrons between  $\text{Fe}^{2+}$  and  $\text{Fe}^{3+}$  plays the role of a conduction mechanism.

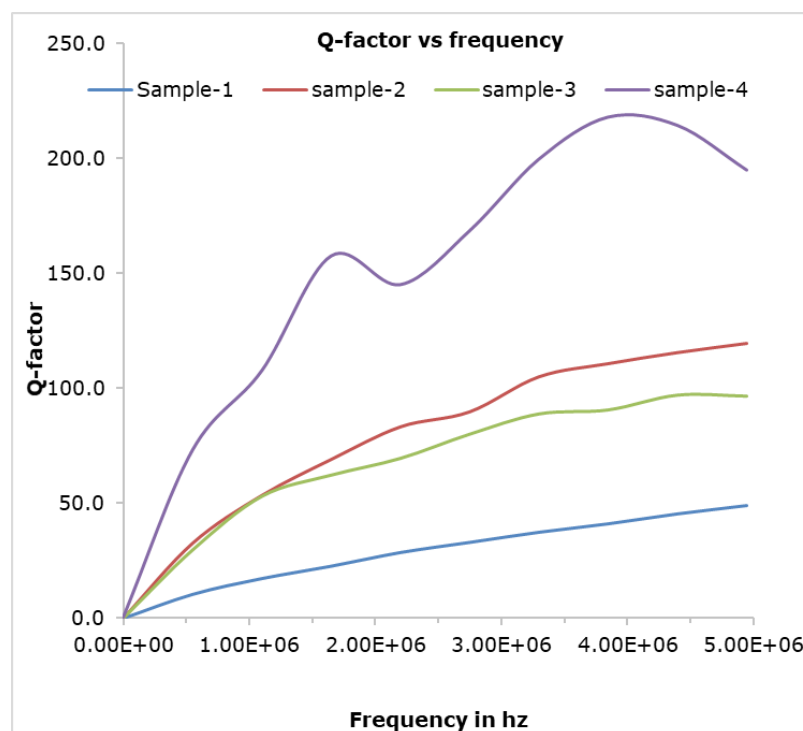


**Figure 11:** Quality factor (Q-factor, Y axis) Vs. Frequency (Hz, X axis) for all samples.

The quality factor (Q-factor) vs. frequency is presented in Figure 11. From the graph, it is observed that the Q-factor has an increasing tendency with the increasing frequency of the applied frequency. Sample 4 showed the highest Q-factor, but the response to the frequency is not linear, as the curve itself is a zigzag path. The other three samples had the same Q-factor response, and sample 2 showed the highest Q-factor.

#### 4. CONCLUSION

Maintaining proper deposition conditions and using the chemical formula  $\text{MgAl}_x\text{Fe}_{2-x}\text{O}_4$  with traces of some additives are reported. The sol-gel autocombustion and formation reaction method has been adopted and applied to prepare the investigated ferrites.

Al substitution for ferrites brought remarkable changes in the structural, electrical, and magnetic properties. XRD spectra supported the formation of spinel ferrites and other crystal

information, including crystal size and shape. From the XRD spectra, the crystal size is calculated at about 30–40 nm. SEM analysis indicates that the ferrites have the expected homogeneity and uniform morphology. It is found that the grain size has an increasing tendency according to the increase in Al ion concentration.

Also, some new nuclei were formed and observed, which is responsible for preventing further grain growth, and it is assumed that the grain size decreased due to this. The DC resistivity increases up to the transition temperature of 115 °C and then decreases. The SEM image gives an idea of substitution's effect on grain size and grain distribution. Comparing the X-ray density and bulk density data demonstrates that all the samples are slightly porous and have a consistent density.

Also, increasing the Al concentration will increase the dielectric constant. The dielectric loss factor decreases largely from 19.82 to 0.481 with the increase in frequency from 80 Hz to 1 M Hz. The



resistivity decreases with frequency, but after  $5.5E+6$  (Hz), it will increase again. The AC resistivity is also frequency-dependent and decreases with frequency. A sample with composition  $x = 0.4$  has a higher value of the Curie temperature. Hence, the materials are suitable for use in the frequency range of 10-1000 kHz.

## 5. ACKNOWLEDGEMENTS

We would like to express our grateful thanks and gratitude to the authorities of the University of Chittagong and BCSIR Laboratories, Dhaka for providing us the opportunity and the necessary permission to carry out this research work. Thanks, are also due to all the employees of the department of Physics, University of Chittagong and Industrial Physics Division at BCSIR Laboratories, Dhaka.

## 6. REFERENCES

- Ahmed, M., Hossain, M. D., Akter, S., Hossain, M. A., Sikder, S. S., Hakim, M. A., & Khan, M. N. I. (2022). Structural and magnetic properties of  $Co_{0.85}Zn_{0.15}YxFe_{2-x}O_4$  ferrites. *Physica B: Condensed Matter*, 645, 414267. <https://doi.org/10.1016/j.physb.2022.414267>
- Amiri, M., Salavati-Niasari, M., & Akbari, A. (2019). Magnetic nanocarriers: Evolution of spinel ferrites for medical applications. *Advances in Colloid and Interface Science*, 265, 29-44. <https://doi.org/10.1016/j.cis.2019.01.003>
- Arulmurugan, R., Vaidyanathan, G., Sendhilnathan, S., & Jeyadevan, B. (2006). Mn-Zn ferrite nanoparticles for ferrofluid preparation: Study on thermal-magnetic properties. *Journal of Magnetism and Magnetic Materials*, 298(2), 83-94. <https://doi.org/10.1016/j.jmmm.2005.03.002>
- Atassi, Y., & Tally, M. (2006). Low sintering temperature of Mg-Cu-Zn ferrite prepared by the citrate precursor method. *Journal of the Iranian Chemical Society*, 3(3), 242-246. <https://doi.org/10.1007/BF03247214>
- Bhatu, S. S., Lakhani, V. K., Tanna, A. R., Vasoya, N. H., Buch, J. U., Sharma, P. U., Trivedi, N., Joshi, H. H., & Modi, K. B. (2007). Effect of nickel substitution on structural, infrared and elastic properties of lithium ferrite. In *Indian Journal of Pure & Applied Physics* (Vol. 45).
- Buzea, C., Pacheco, I. I., & Robbie, K. (2007). Nanomaterials and nanoparticles: Sources and toxicity. *Biointerphases*, 2(4), MR17-MR71. <https://doi.org/10.1116/1.2815690>
- Dixit, G., Singh, J. P., Srivastava, R. C., Agrawal, H. M., & Chaudhary, R. J. (2012). Structural, Magnetic And Optical Studies Of nickel Ferrite Thin Films. *Advanced Materials Letters*, 3(1), 21-28. <https://doi.org/10.5185/amlett.2011.6280>
- George, M., Mary John, A., Nair, S. S., Joy, P. A., & Anantharaman, M. R. (2006). Finite size effects on the structural and magnetic properties of sol-gel synthesized  $NiFe_{2}O_4$  powders. *Journal of Magnetism and Magnetic Materials*, 302(1), 190-195. <https://doi.org/10.1016/j.jmmm.2005.08.029>
- Giannakopoulou, T., Kompotiatis, L., Kontogeorgakos, A., & Kordas, G. (2002). Microwave behavior of ferrites prepared via sol-gel method. *Journal of Magnetism and Magnetic Materials*, 246(3), 360-365. [https://doi.org/10.1016/S0304-8853\(02\)00106-3](https://doi.org/10.1016/S0304-8853(02)00106-3)
- Gimenes, R., Baldissera, M. R., da Silva, M. R. A., da Silveira, C. A., Soares, D. A. W., Perazolli, L. A., da Silva, M. R., & Zaghete, M. A. (2012). Structural and magnetic characterization of  $MnxZn_{1-x}Fe_2O_4$  ( $x=0.2; 0.35; 0.65; 0.8; 1.0$ ) ferrites obtained by the citrate precursor method. *Ceramics International*, 38(1), 741-746. <https://doi.org/10.1016/j.ceramint.2011.07.066>
- Giri, J., Sriharsha, T., & Bahadur, D. (2004). Optimization of parameters for the synthesis of nano-sized  $Co_{1-x}Zn_xFe_2O_4$ , ( $0 \leq x \leq 0.8$ ) by microwave refluxing. *J. Mater. Chem.*, 14(5), 875-880. <https://doi.org/10.1039/B310668C>
- Gorter, E. W. (1950). Magnetization in Ferrites: Saturation Magnetization of Ferrites with Spinel Structure. *Nature*, 165(4203), 798-800. <https://doi.org/10.1038/165798a0>
- Gu, B. X. (2003). Magnetic properties and magneto-optical effect of  $Co_{0.5}Fe_{2.5}O_4$  nanostructured films. *Applied Physics*

- Letters*, 82(21), 3707–3709.  
<https://doi.org/10.1063/1.1573357>
- Hankare, P. P., Patil, R. P., Garadkar, K. M., Sasikala, R., & Chougule, B. K. (2011). Synthesis, dielectric behavior and impedance measurement studies of Cr-substituted Zn-Mn ferrites. *Materials Research Bulletin*, 46(3), 447–452.  
<https://doi.org/10.1016/j.MATERRESBULL.2010.11.026>
- Hankare, P. P., Sankpal, U. B., Patil, R. P., Mulla, I. S., Lokhande, P. D., & Gajbhiye, N. S. (2009). Synthesis and characterization of  $\text{CoCr}_x\text{Fe}_{2-x}\text{O}_4$  nanoparticles. *Journal of Alloys and Compounds*, 485(1-2), 798–801.  
<https://doi.org/10.1016/j.jallcom.2009.06.087>
- Hankare, P. P., Vader, V. T., Patil, N. M., Jadhav, S. D., Sankpal, U. B., Kadam, M. R., Chougule, B. K., & Gajbhiye, N. S. (2009). Synthesis, characterization and studies on magnetic and electrical properties of Mg ferrite with Cr substitution. *Materials Chemistry and Physics*, 113(1), 233–238.  
<https://doi.org/10.1016/j.matchemphys.2008.07.066>
- Iqbal, M. J., & Siddiquah, M. R. (2008). Electrical and magnetic properties of chromium-substituted cobalt ferrite nanomaterials. *Journal of Alloys and Compounds*, 453(1-2), 513–518.  
<https://doi.org/10.1016/j.jallcom.2007.06.105>
- Islam, M. U., Abbas, T., Niazi, S. B., Ahmad, Z., Sabeen, S., & Chaudhry, M. A. (2004). Electrical behaviour of fine particle, co-precipitation prepared Ni-Zn ferrites. *Solid State Communications*, 130(5), 353–356.  
<https://doi.org/10.1016/j.ssc.2004.02.019>
- Joudeh, N., & Linke, D. (2022). Nanoparticle classification, physicochemical properties, characterization, and applications: a comprehensive review for biologists. *Journal of Nanobiotechnology*, 20(1), 262.  
<https://doi.org/10.1186/s12951-022-01477-8>
- Kamble, S. S., Jagtap, V. S., & Pingale, P. C. (2013). Synthesis of  $\text{Mg}_{0.48}\text{Cu}_{0.12}\text{Zn}_{0.40}\text{Fe}_2\text{O}_4$  ferrite and its aptness for multilayer chip component application. *Ceramics International*, 39(4), 3597–3601.  
<https://doi.org/10.1016/j.ceramint.2012.10.187>
- Krishna, K. R., Kumar, K. V., & Ravinder, D. (2012a). Structural and Electrical Conductivity Studies in Nickel-Zinc Ferrite. *Advances in Materials Physics and Chemistry*, 02(03), 185–191.  
<https://doi.org/10.4236/ampc.2012.23028>
- Kuznetsov, M. V., Pankhurst, Q. A., & Parkin, I. P. (1998). Self propagating high-temperature synthesis of chromium substituted magnesium zinc ferrites  $\text{Mg}_{0.5}\text{Zn}_{0.5}\text{Fe}_{2-x}\text{Cr}_x\text{O}_4$  ( $0 \leq x \leq 1.5$ ). *Journal of Materials Chemistry*, 8(12), 2701–2706.  
<https://doi.org/10.1039/a804942d>
- Lakshman, A., Rao, P. S. V. S., Rao, B. P., & Rao, K. H. (2005). Electrical properties of  $\text{In}^{3+}$  and  $\text{Cr}^{3+}$  substituted magnesium-manganese ferrites. *Journal of Physics D: Applied Physics*, 38(5), 673–678.  
<https://doi.org/10.1088/0022-3727/38/5/002>
- Lakshmi Ranganatha, V., Pramila, S., Nagaraju, G., Udayabhanu, Surendra, B. S., & Mallikarjunaswamy, C. (2020). Cost-effective and green approach for the synthesis of zinc ferrite nanoparticles using Aegle Marmelos extract as a fuel: catalytic, electrochemical, and microbial applications. *Journal of Materials Science: Materials in Electronics*, 31(20), 17386–17403. <https://doi.org/10.1007/s10854-020-04295-6>
- Olsen, E., & Thonstad, J. (1999). Nickel ferrite as inert anodes in aluminium electrolysis: Part II Material performance and long-term testing. *Journal of Applied Electrochemistry*, 29(3), 301–311.  
<https://doi.org/10.1023/A:1003464304488>
- Oñoro, M., Macías-Delgado, J., Auger, M. A., Hoffmann, J., de Castro, V., & Leguey, T. (2021). Powder Particle Size Effects on Microstructure and Mechanical Properties of Mechanically Alloyed ODS Ferritic Steels. *Metals*, 12(1), 69.  
<https://doi.org/10.3390/met12010069>
- Pathania, A., Kumar, R., Rojhe, K., Goel, B., Aggarwal, S., & Mahto, D. (2021). Value stream mapping – Panacea for lead time reduction in ferrite core industry. *Materials Today: Proceedings*, 46, 2456–2461.

- <https://doi.org/10.1016/j.matpr.2021.01.362>
- Patterson, A. L. (1939). The Scherrer Formula for X-Ray Particle Size Determination. *Physical Review*, 56(10), 978-982.  
<https://doi.org/10.1103/PhysRev.56.978>
- Radwan, F. A., Ahmed, M. A., & Abdelatif, G. (2003). Screening effect of Ti<sup>4+</sup> ions on the electrical conductivity and thermoelectric power of Mg ferrite. *Journal of Physics and Chemistry of Solids*, 64(12), 2465-2477.  
<https://doi.org/10.1016/j.jpics.2003.08.003>
- Saini, R., Saini, S., & Sharma, S. (2010). Nanotechnology: the future medicine. *Journal of Cutaneous and Aesthetic Surgery*, 3(1), 32-33.  
<https://doi.org/10.4103/0974-2077.63301>
- Shokrollahi, H. (2008). Magnetic properties and densification of Manganese-Zinc soft ferrites (Mn<sub>1-x</sub>Zn<sub>x</sub>Fe<sub>2</sub>O<sub>4</sub>) doped with low melting point oxides. *Journal of Magnetism and Magnetic Materials*, 320(3-4), 463-474.  
<https://doi.org/10.1016/j.jmmm.2007.07.003>
- Sontakke, A. D., & Purkait, M. K. (2021). A brief review on graphene oxide Nanoscrolls: Structure, Synthesis, characterization and scope of applications. *Chemical Engineering Journal*, 420, 129914.  
<https://doi.org/10.1016/j.cej.2021.129914>
- Sujatha, Ch., Venugopal Reddy, K., Sowri Babu, K., RamaChandra Reddy, A., & Rao, K. H. (2013). Effect of sintering temperature on electromagnetic properties of NiCuZn ferrite. *Ceramics International*, 39(3), 3077-3086.  
<https://doi.org/10.1016/j.ceramint.2012.09.087>
- Wang, J. (2006). Prepare highly crystalline NiFe<sub>2</sub>O<sub>4</sub> nanoparticles with improved magnetic properties. *Materials Science and Engineering: B*, 127(1), 81-84.  
<https://doi.org/10.1016/j.mseb.2005.09.003>
- Willey, R. J., Noirclerc, P., & Busca, G. (1993). PREPARATION AND CHARACTERIZATION OF MAGNESIUM CHROMITE AND MAGNESIUM FERRITE AEROGELS. *Chemical Engineering Communications*, 123(1), 1-16.  
<https://doi.org/10.1080/00986449308936161>
- Zakaria, A. K. M., Asgar, M. A., Eriksson, S.-G., Ahmed, F. U., Yunus, S. M., Delaplane, R. G., Stanciu, V., & Svedlindh, P. (2004). Crystallographic and magnetic properties of the spinel type solid solution Zn<sub>0.4</sub>Co<sub>0.6</sub>Al<sub>x</sub>Fe<sub>2-x</sub>O<sub>4</sub> (0 ≤ x ≤ 1). *Materials Research Bulletin*, 39(7-8), 1141-1157.  
<https://doi.org/10.1016/j.materresbull.2004.02.015>
- Zakaria, A. K. M., Asgar, M. A., Eriksson, S.-G., Ahmed, F. U., Yunus, S. M., & Rundlöf, H. (2003). The study of magnetic ordering in the spinel system Zn<sub>x</sub>Ni<sub>1-x</sub>FeCrO<sub>4</sub> by neutron diffraction. *Journal of Magnetism and Magnetic Materials*, 265(3), 311-320.  
[https://doi.org/10.1016/S0304-8853\(03\)00280-4](https://doi.org/10.1016/S0304-8853(03)00280-4)
- Zhang, S.-C., Messing, G. L., & Borden, M. (1990). Synthesis of Solid, Spherical Zirconia Particles by Spray Pyrolysis. *Journal of the American Ceramic Society*, 73(1), 61-67.  
<https://doi.org/10.1111/j.1151-2916.1990.tb05091.x>





## Metal-Free Coal Catalyst for Hydrogen Production: Synthesis and Performance Assessment

Gurbet CANPOLAT , Mustafa KAYA 

Siirt University, Department of Chemistry, 56100 Siirt, Türkiye

**Abstract:** In this study, a coal-based catalyst produced by protonating phosphoric acid was used as a metal-free catalyst for hydrogen production from sodium borohydride ( $\text{NaBH}_4$ ) methanolysis. Experiments were conducted with various acid concentrations, impregnation times, and carbonization temperatures and times in order to produce a metal-free coal catalyst with enhanced catalytic activity. The catalyst impregnated with 3M  $\text{H}_3\text{PO}_4$  for 12 h and subsequently carbonized at  $600^\circ\text{C}$  for 90 min exhibited the highest catalytic activity. The hydrogen production at  $60^\circ\text{C}$  methanolysis with 0.25 g of  $\text{NaBH}_4$  catalyzed by a metal-free coal catalyst was found to be  $11,854 \text{ mL min}^{-1}\text{g}_{\text{cat}}^{-1}$ . Additionally, the activation energy of the catalyst was determined to be  $22.5 \text{ kJ mol}^{-1}$ .

**Keywords:** Coal, Metal-free catalyst, Hydrogen, Phosphoric Acid, Sodium Borohydride, Methanolysis

**Submitted:** May 02, 2023. **Accepted:** July 18, 2023.

**Cite this:** Canpolat, G., Kaya, M. (2023). Metal-Free Coal Catalyst for Hydrogen Production: Synthesis and Performance Assessment. Journal of the Turkish Chemical Society, Section B: Chemical Engineering. 6(2), 63-72. <https://doi.org/10.58692/jotcsb.1291544>.

**\*Corresponding author. E-mail:** [gokalp.gurbet@siirt.edu.tr](mailto:gokalp.gurbet@siirt.edu.tr).

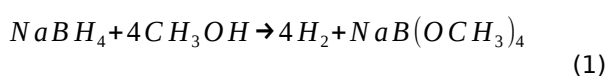
### 1. INTRODUCTION

Population growth, economic expansion, and urbanization are contributing to the demand for energy. Fossil fuels, which are widely accessible and easily extractable, have been the primary source of energy for industries and modern lifestyles since the 1800s. However, this reliance on hydrocarbon energy sources has harmful effects on the environment, such as acid rain, global warming, and climate change, as well as negative impacts on wildlife, plant life, and public health (Akpan & Akpan, 2012). Consequently, a global shift to cleaner and more sustainable renewable energy sources is necessary to mitigate the risks of climate change and its associated health impacts. The term "renewable energy" refers to energy that originates from natural sources and is regenerated over time. It originates from a wide range of self-sustaining natural sources, which include the kinetic energy of water, solar radiation, wind power, geothermal heat, and organic matter such as biomass (Güney, 2019; Panwar et al., 2011).

The intermittent and variable nature of renewable energy sources, along with the goal of reducing

$\text{CO}_2$  emissions, presents a major challenge to their use in transportation. Consequently, energy storage has become an essential aspect of sustainable development (Amrouche et al., 2016; Bull, 2001; Najjar, 2011; Thellufsen et al., 2020). Hydrogen is regarded as a significant energy storage medium for fully utilizing renewable and sustainable energy (Dawood et al., 2020). A range of raw materials, including water, coal, natural gas, biomass, hydrogen sulfide, and boron hydrides, can be utilized for hydrogen production through various processes such as biochemical, thermal, electrolytic, or photolytic methods (Zhang et al., 2016). Hydrogen has the potential to address air pollution and global warming issues (Sürmen & Demirbas, 2002). However, challenges related to hydrogen transportation and storage arise due to its gaseous nature and behavior at normal temperatures and pressures. To address these challenges, a variety of hydrogen storage systems, such as compressed hydrogen, liquid hydrogen, and hydrogen bound to a storage material through chemical bonds like metal hydrides, are currently under development (Demirbas & Arin, 2004). Metallic borohydrides are a promising source of hydrogen due to their high hydrogen content and

ability to be stored and transported under mild conditions (Hamilton et al., 2009; Lang et al., 2020; Yao et al., 2020). Among them, sodium borohydride ( $\text{NaBH}_4$ ) is particularly attractive due to its ability to provide pure hydrogen without producing hydrocarbons or greenhouse gases. Hydrogen can be easily produced from  $\text{NaBH}_4$  by hydrolysis at room temperature using catalysts. (Xu et al., 2012). Recent studies have focused on the advantages of methanolysis of borohydrides, including avoiding freezing issues associated with water, fast hydrogen generation potentially without the need for a catalyst, and reaction products that can be regenerated into sodium borohydride in a single step (Demirci et al., 2020). Equation 1 shows the chemical reaction of  $\text{NaBH}_4$  and methanol, which is commonly referred to as methanolysis.



Despite the various advantages, kinetically zero degradation processes are a drawback of the methanolysis of  $\text{NaBH}_4$ . To overcome this limitation, the focus has shifted towards the catalytic methanolysis of sodium borohydride (Wang et al., 2022). Various noble and non-noble metals, as well as their composites, have been studied in numerous studies as potential catalysts for the methanolysis of  $\text{NaBH}_4$ . Among them, noble metal catalysts are known for their exceptional catalytic activity, but their high cost and limited availability can limit their practical use (Yao et al., 2020). Carbon-based materials have become increasingly popular as catalysts or catalyst supports because of their cost efficiency and environmentally friendly characteristics in recent times. These materials include microalgal species (Duman et al., 2020; Inal et al., 2021; Karakaş et al., 2021), coffee waste (Akdemir et al., 2021; Kaya, 2020a), apricot kernel shells (Fangaj & Ceyhan, 2020), corn stalks (Bolat et al., 2021), cotton fibers (Ali et al., 2019), tea factory waste (Özarslan et al., 2021a; Özarslan et al., 2021b), pomegranate peels (Akdemir et al., 2022; Karakaş, 2021), banana peels (Karakaş et al., 2022), lake sludge (Bekirogullari et al., 2021), metallurgical waste sludge (Fangaj et al., 2020), and orange peels (Karakaş, 2022). Especially, metal-free catalysts provide numerous advantages over catalysts containing metals, stressing their abundance, cost-effectiveness, and sustainability. Additionally, they offer the benefit of reduced side reactions compared to metal catalysts, which are often susceptible to undesired oxidation or reduction reactions.

In this study, a metal-free coal-based catalyst was developed from phosphoric acid protonation for hydrogen production via methanolysis. Various experiments were carried out to enhance the catalytic activity of the catalyst by varying the acid concentrations, impregnation times, and carbonization temperatures and durations.

## 2. EXPERIMENTAL SECTION

### 2.1. Preparation of Metal-Free Coal Catalyst

The raw coal sample (petroleum coke) was supplied from Batman refinery and the coal catalyst was prepared by first grinding the coal to a size of 500 microns and washing it with 3M HCl, followed by rinsing with pure water. Then, the coal was treated with different concentrations of phosphoric acid (ranging from 1M to 7M) at 80 °C for 6-36 hours. After the impregnation process, the mixture was carbonized under  $\text{N}_2$  atmosphere, with temperatures ranging from 500 °C to 800 °C and carbonization times of 30-90 min. Subsequently, kinetic studies were conducted at different solution temperatures (30-60 °C) to analyze the catalyzed methanolysis of  $\text{NaBH}_4$ . The catalyst's ability to be reused was evaluated by conducting five consecutive experiments. Before each experiment, the catalyst was separated, washed, and dried to prepare it for reused.

### 2.2. Procedure for Methanolysis Experiment

Methanol with a purity of  $\geq 99.9\%$  from Sigma Aldrich was used in the experiments. The reactions were conducted in a 50 mL flask equipped with a thermometer for temperature monitoring. The reaction mixture contained 0.25 g of  $\text{NaBH}_4$  (98%, Sigma Aldrich) and 0.10 g of catalyst. To start the methanolysis reaction, 10 mL of methanol was added. The hydrogen gas generated was collected in a gas collection unit, and its volume was measured over a specific time interval.

## 3. RESULTS AND DISCUSSION

### 3.1. Characterization

Elemental analysis was performed using ICP-MS (Inductively Coupled Plasma Mass Spectrometry), which allows us to determine the elemental composition of the raw sample and  $\text{H}_3\text{PO}_4$ -coal, and the results are given in Table 1.

FTIR (Fourier Transform Infrared Spectroscopy) was conducted to characterize the material, providing insights into its molecular structure and chemical composition. These analyses contributed to a comprehensive understanding of the material's characteristics. As shown in Figure 1, the raw coal contains both aromatic and aliphatic hydrocarbons. The vibration bands at 2850 and 800  $\text{cm}^{-1}$  are ascribed to the C-H in aliphatic hydrocarbons and aromatic hydrocarbons, respectively. The broad and intense bands at 1600  $\text{cm}^{-1}$  is assigned to the aromatic like C=C stretching. In addition, after combustion with  $\text{H}_3\text{PO}_4$ , the characteristic peaks of the C-H stretching mode of the raw coal disappear while the peaks at the 1600  $\text{cm}^{-1}$  stretching mode become broader, indicating that the raw carbon materials undergo a structural change.

Additionally, the vibration bands at  $1000\text{ cm}^{-1}$  are attributed to P=O symmetric stretching, which confirm the successful attachment of- $\text{PO}_4$  onto the carbon matrix (Robinson, 1963).

### 3.2. Effect of $\text{H}_3\text{PO}_4$ Concentration on Metal-Free Coal Catalyst Performance

The performance of a metal-free coal catalyst was studied by treating it with four different concentrations of  $\text{H}_3\text{PO}_4$  (1 M, 3 M, 5 M, and 7 M) and subjecting it to carbonization in an inert atmosphere. The catalysts were then incubated at  $80\text{ }^\circ\text{C}$  for 24 hours and carbonized in a  $600\text{ }^\circ\text{C}$  ash furnace for 90 minutes, as presented in Figure 2.

The highest hydrogen production rate of  $1856\text{ mL min}^{-1}\text{g}_{\text{cat}}^{-1}$  was achieved using 3M  $\text{H}_3\text{PO}_4$ , while the 1 M, 5 M, and 7 M  $\text{H}_3\text{PO}_4$  treatments resulted in hydrogen production rates of 1080, 1651, and  $1195\text{ mL min}^{-1}\text{g}_{\text{cat}}^{-1}$ , respectively. Fangaj and Ceyhan (2022) investigated the use of apricot kernels activated with  $\text{H}_3\text{PO}_4$  as a catalyst and found that the highest hydrogen production rate was achieved at a 15% acid concentration. However, the catalytic activity decreased at higher acid concentrations due to structural deformations in the catalyst. These results highlight the significance of optimizing acid concentration for maximizing catalytic activity.

**Table 1.** Chemical analysis of samples.

Element	Raw-coal (ppm)	$\text{H}_3\text{PO}_4$ -coal (ppm)	Element	Raw-coal(ppm)	$\text{H}_3\text{PO}_4$ -coal(ppm)
Li	0.2	8.5	Cu	1.6	46.0
B	10.4	18.8	Zn	17.0	109.7
Na	74.6	1098.7	Ga	7.1	1.4
Mg	145.8	450.0	As	21.4	40.5
Al	224.3	1533.8	Sr	6.5	3.8
P	57.9	21196.4	Ag	0.08	0.4
K	6705.5	11201.4	Cd	0.4	0.01
Ca	1032.9	627.8	Sb	4.3	5.8
Cr	21.0	96.9	Ba	11.7	7.8
Mn	4.0	12.7	Tl	0.2	0.03
Fe	320.6	446.7	Pb	1.1	4.4
Co	1.6	270.8	Bi	0.1	0.01
Ni	291.5	179.0			

### 3.3. Effect of Impregnation Time on Metal-Free Coal Catalyst Performance

The effect of impregnation time on the catalytic activity of methanolysis of  $\text{NaBH}_4$  using metal-free coal catalysts at various times, including 6 h, 12 h, 24 h, and 36 h, was investigated through a series of experiments. According to the findings presented in Figure 3, the most significant efficiency in hydrogen production was obtained when the impregnation time was 12 hours, with a rate of  $6588\text{ mL min}^{-1}\text{g}_{\text{cat}}^{-1}$ . The lowest efficiency was recorded at the 24 h, with a rate of  $1856\text{ mL}$

$\text{min}^{-1}\text{g}_{\text{cat}}^{-1}$  and a reaction completion time of 8 min. Previous studies on hydrogen production from  $\text{NaBH}_4$  methanolysis using different catalysts have shown that the most effective impregnation time is 24 hours. In a study by Saka et al. on hydrogen production from  $\text{NaBH}_4$  methanolysis using  $\text{ZnCl}_2$ -treated *Spirulina microalgala* catalyst, the most effective impregnation time was found to be 24 h (Kaya et al., 2019). Therefore, obtaining the most effective catalyst at a 12 h impregnation time can be considered a cost-efficient option, in accordance with the previous findings.



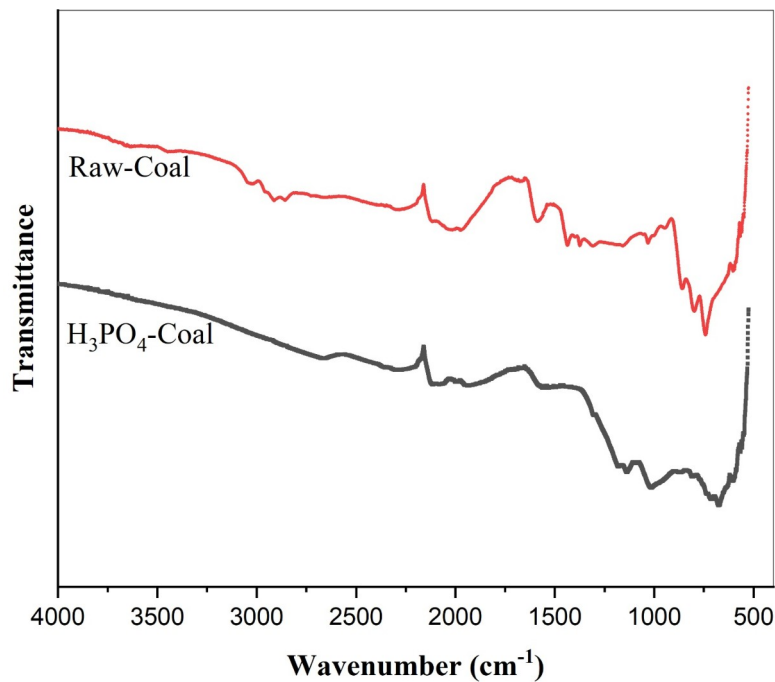


Figure 1: FT-IR spectra of samples.

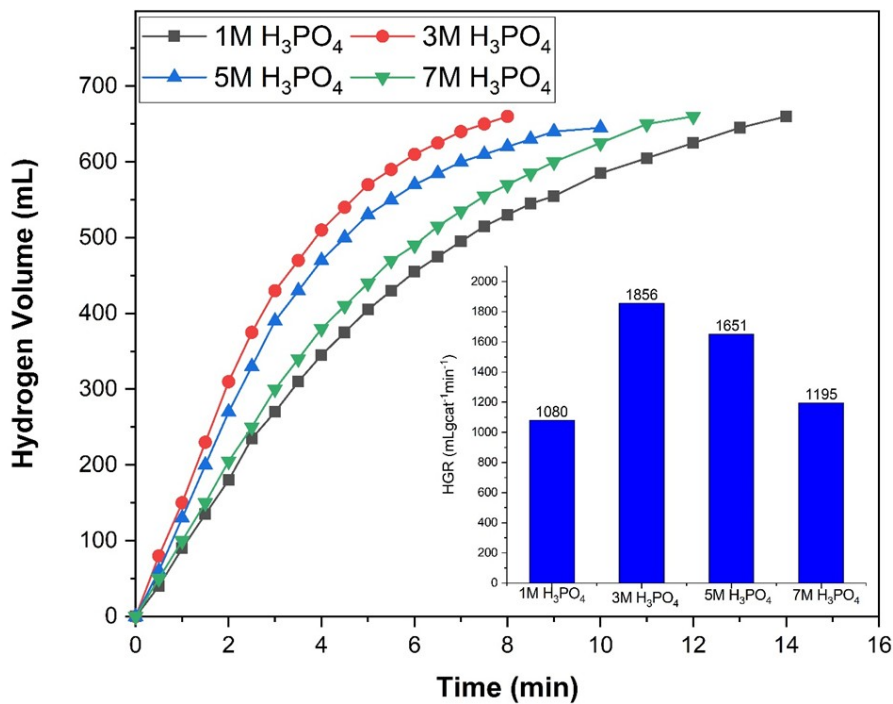
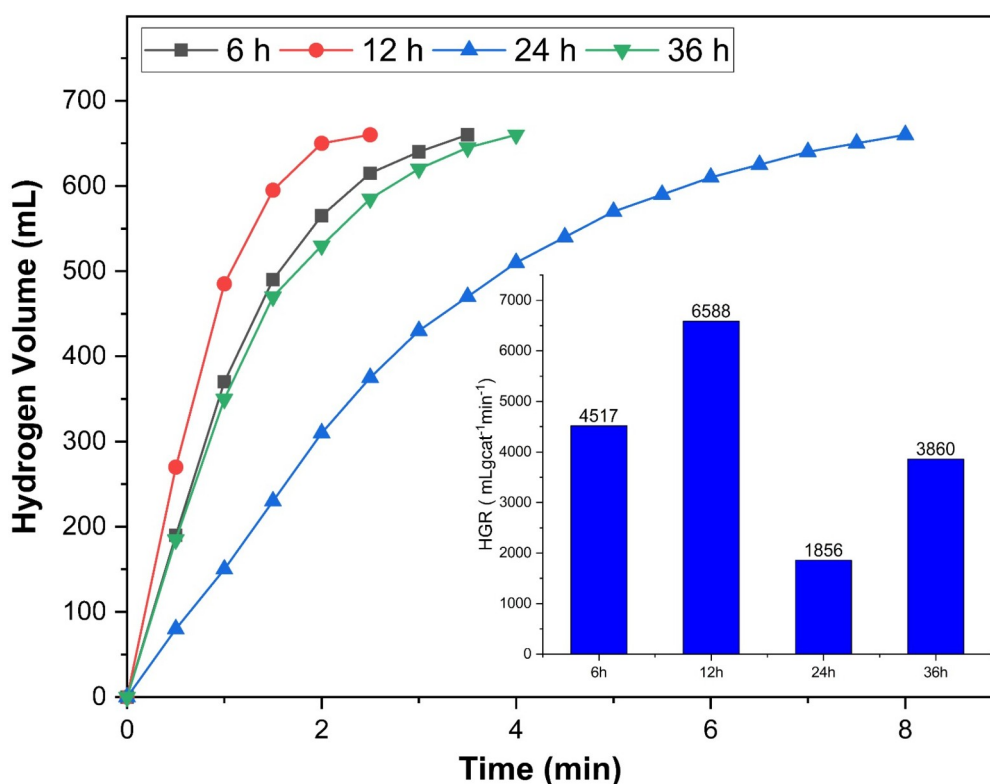


Figure 2: The effect of the concentration of H<sub>3</sub>PO<sub>4</sub> on NaBH<sub>4</sub> methanolysis [Reaction condition: 24 h impregnation time, 600 °C carbonization temperature, 90 min carbonization time, 0.1 g catalyst, 10 mL methanol, 0.25 g NaBH<sub>4</sub>, 30 °C solution temperature.





**Figure 3:** The effect of the impregnation time on NaBH<sub>4</sub> methanolysis [Reaction condition: 3M H<sub>3</sub>PO<sub>4</sub>, 600 °C carbonization temperature, 90 min carbonization time, 0.1 g catalyst, 10 mL methanol, 0.25 g NaBH<sub>4</sub>, 30 °C solution temperature.

### 3.4. Effect of Carbonization Temperature on Metal-Free Coal Catalyst Performance

The effect of different carbonization temperatures on the experimental results was presented in Figure 4. The carbonization process was conducted at four different temperatures, specifically 500 °C, 600 °C, 700 °C, and 800 °C. It was clear that increasing the temperature from 500 °C to 600 °C could significantly improve the activity of metal-free coal catalysts. However, increasing the calcination temperature from 600 °C to 800 °C caused a decrease in the catalytic activity. It has been suggested that the reduction in catalytic activity at higher temperatures may be due to loss of active OH groups via dehydration and dihydroxylation (Fitzgerald et al., 1997). The highest hydrogen production efficiency of 6588 mL min<sup>-1</sup>g<sub>.cat</sub><sup>-1</sup> was recorded for the coal catalyst obtained at 600 °C. Karakaş et al. reached the similar conclusion in their methanolysis experiments using *Spirulina Platensis* waste-supported Pd-Co catalyst and identified the most

efficient carbonization temperature as 600 °C (Karakaş et al., 2021).

### 3.5. Effect of Carbonization Time on Metal-Free Coal Catalyst Performance

The catalytic activity of NaBH<sub>4</sub> methanolysis is highly dependent on the carbonization time. As shown in Figure 4, different carbonization times were studied by experimenting with 30, 60, 90, and 120 minutes. Figure 5 indicates that the production of hydrogen increases gradually with increasing carbonization times up to 90 minutes. However, further increases caused a decrease in the catalytic activity. The highest efficiency for hydrogen production was achieved at 90 minutes, with a recorded rate of mL min<sup>-1</sup>g<sub>.cat</sub><sup>-1</sup>. Using a manganese catalyst supported by *Microcystis aeruginosa*, Duman et al. (2020) investigated the NaBH<sub>4</sub> methanolysis process. They determined that 45 min was the best carbonization time for the reaction, demonstrating the significance of determining an appropriate reaction time for maximizing effectiveness.

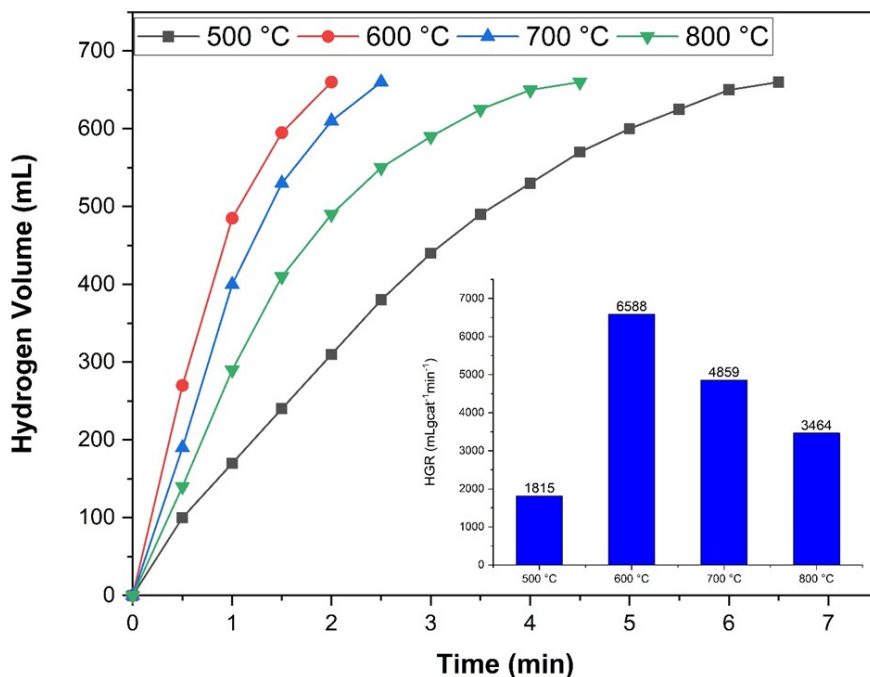


**Figure 4:** The effect of the carbonization temperature on NaBH<sub>4</sub> methanolysis [Reaction condition: 3 M H<sub>3</sub>PO<sub>4</sub>, 12 h impregnation time, 90 min carbonization time, 0.1 g catalyst, 10 mL methanol, 0.25 g NaBH<sub>4</sub>, 30 °C solution temperature.

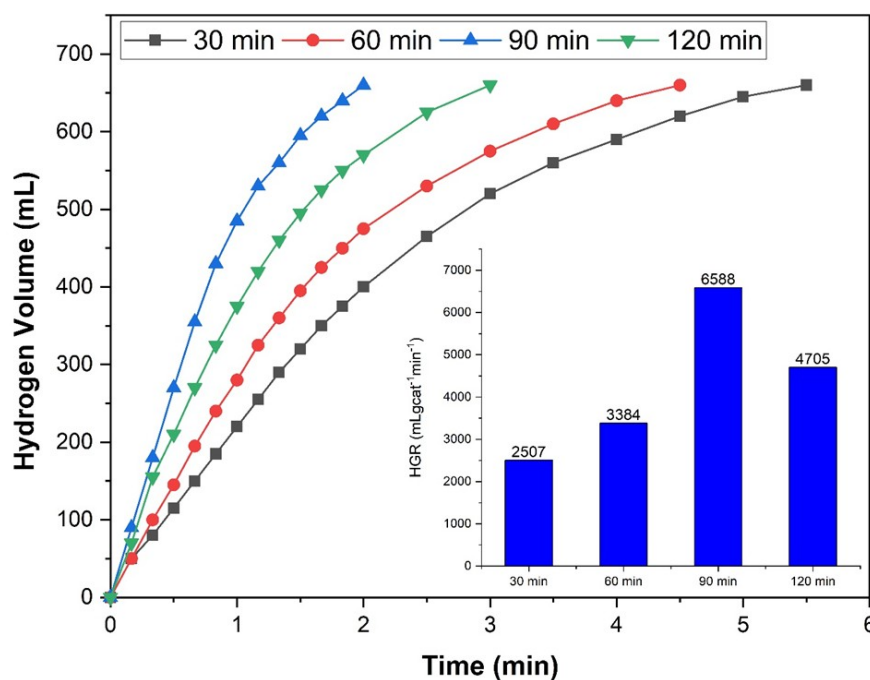


**Figure 5:** The effect of the carbonization time on NaBH<sub>4</sub> methanolysis [Reaction condition: 3M H<sub>3</sub>PO<sub>4</sub>, 12 h impregnation time, 600 °C carbonization temperature, 0.1 g of catalyst, 10 mL of methanol, 0.25 g of NaBH<sub>4</sub>, 30 °C solution temperature.

**3.6. Effect of Solution Temperature on Metal-Free Coal Catalyst Performance**

The study examined the impact of solution temperature on the catalytic performance of metal-

free coal catalyst in the methanolysis of NaBH<sub>4</sub>. The experiment was carried out at four different temperatures: 30, 40, 50, and 60 °C, and the results were presented in Figure 6. The graph

shows the hydrogen volume produced versus reaction time and the hydrogen production rate (HGR) for the methanolysis of  $\text{NaBH}_4$  with 0.25 g of  $\text{NaBH}_4$ , 10 mL of methanol, and 0.1 g of catalyst at varying temperatures. According to the experimental results, the HGR increased gradually with increasing temperature and the highest efficiency ( $11854 \text{ mL min}^{-1}\text{g}_{\text{cat}}^{-1}$ ) was determined at the highest temperature of  $60^\circ\text{C}$ . Previous research has shown that there is a linear relationship between temperature and HGR ratio. One of these was the study in which coffee waste was used as a catalyst for the methanolysis of  $\text{NaBH}_4$ , and a hydrogen production rate of  $13332 \text{ mL min}^{-1}\text{g}_{\text{cat}}^{-1}$  was achieved at  $60^\circ\text{C}$  (Kaya, 2020b). Similarly, the pomegranate peel supported  $\text{NH}_2/\text{PdMnAg}$  catalyst showed hydrogen production yields of 7209.4, 8689.6, 10324 and 11334

$\text{min}^{-1}\text{g}_{\text{cat}}^{-1}$  at  $30^\circ\text{C}$ ,  $40^\circ\text{C}$ ,  $50^\circ\text{C}$  and  $60^\circ\text{C}$ , respectively (Karakas, 2021).

The activation energy in the hydrogen production reaction of the metal-free coal catalyst treated with 3M  $\text{H}_3\text{PO}_4$  in the methanolysis of  $\text{NaBH}_4$  was determined by applying the Arrhenius' equation (2):

$$\ln k = \ln A - \frac{E_a}{RT} \quad (2)$$

Equation (2) consists of the reaction rate constant (k), reaction constant (A), activation energy ( $E_a$ ) measured in  $\text{kJ mol}^{-1}$ , temperature (T) in K, and the ideal gas constant (R). The Arrhenius ( $\ln(k)$  vs  $1/T$ ) plot for the methanolysis of  $\text{NaBH}_4$  catalyzed are given in Figure 7.

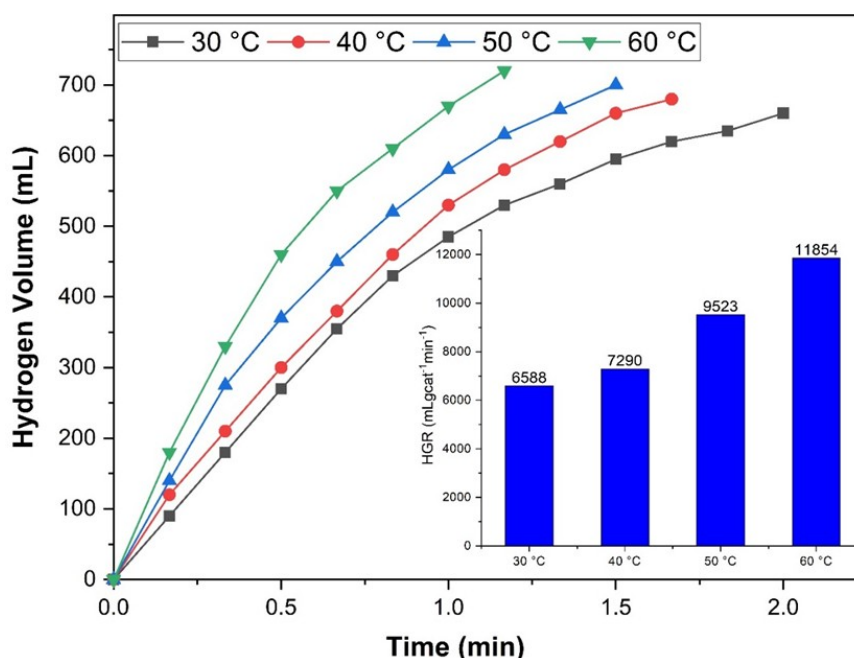


**Figure 6:** The effect of the solution temperature on  $\text{NaBH}_4$  methanolysis [Reaction condition: 3 M  $\text{H}_3\text{PO}_4$ , 12 h impregnation time,  $600^\circ\text{C}$  carbonization temperature, 0.1 g of catalyst, 10 mL of methanol, 0.25 g of  $\text{NaBH}_4$ ].

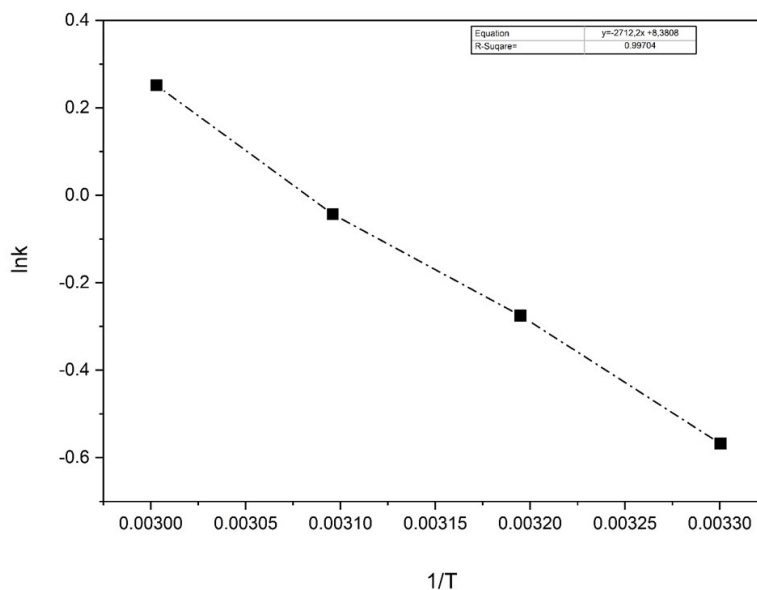


**Figure 7:** Arrhenius' plot for the metal-free coal-based catalyst for methanolysis of NaBH<sub>4</sub>

The activation energy of the metal-free coal catalyst for sodium boron hydride methanolysis hydrogen production was found to be 22.5 kJ mol<sup>-1</sup>, which is very close to the 24 kJ mol<sup>-1</sup> poly (Castor Oil) (p(CO)) organo-particle (Dudu et al., 2022)

stability, in addition to being both cost-effective and eco-friendly. Therefore, the stability performance of metal-free coal catalyst was conducted in five consecutive methanolysis reactions. The stability test produced a histogram of the cycle time and hydrogen generation rate, as illustrated in Figure 8.

### 3.7. Catalytic Stability of Metal-Free Coal for the Methanolysis of NaBH<sub>4</sub>

In addition to having remarkable catalytic activity, a methanolysis catalyst must also have great

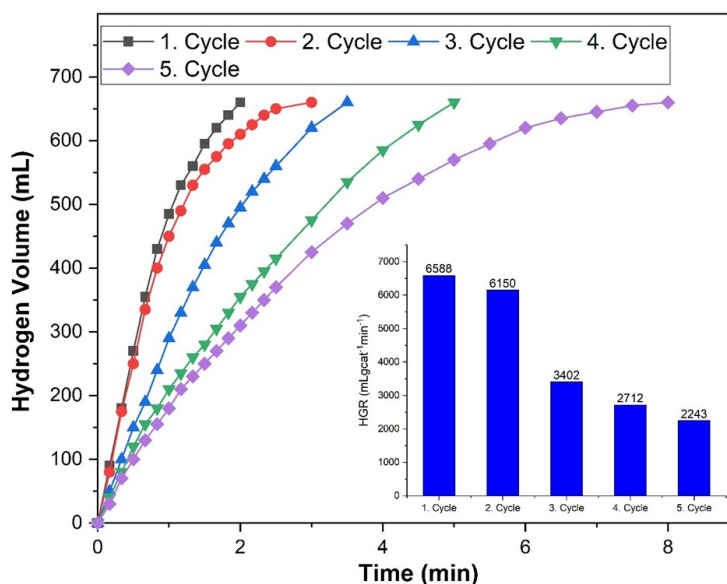


**Figure 8:** Reusability of metal-free coal catalyst in methanolysis of NaBH<sub>4</sub> at solution temperature of 30 °C

According to the findings, the hydrogen generation rate decreased gradually with an increase in the number of cycles. At the 5th cycle, the HGR of the coal catalyst without metal was found to be 2243

mL min<sup>-1</sup>g<sub>cat</sub><sup>-1</sup>. The possible reasons for the decrease in efficiency seen in repeated experiments may be due to mass loss during catalyst preparation or loss of properties during

washing. Xu et al. produced hydrogen from NaBH<sub>4</sub> methanolysis using a Co/Al<sub>2</sub>O<sub>3</sub> catalyst and measured its efficiency through repeated experiments. It was founded that the catalyst surface became smoother after five consecutive experiments, with a loss in the active material content and changes in the surface composition (Xu et al., 2012). Demirci et al. employed porous carbon particles as a catalyst without metal for hydrogen production via NaBH<sub>4</sub> methanolysis. A set of experiments was carried out, where 0.0965 g of NaBH<sub>4</sub> was added to 50 mg of catalyst mixed with 20 mL of methanol, repeated five times. The results indicated that the regeneration process could help slow down the decline in catalytic activity after each use. (Demirci et al., 2020).

#### 4. CONCLUSION

Hydrogen (H<sub>2</sub>) as a renewable energy is considered as a promising energy carrier for future applications due to its eco-friendly fuel with high energy density features. Catalytic methanolysis of NaBH<sub>4</sub> is a significant process for hydrogen H<sub>2</sub> production. An innovative methodology in which carbon-based materials are used as direct catalysts as an alternative to metal-based catalysts has been widely accepted for its cost-effectiveness and environmentally friendly approach. In this study, hydrogen production through NaBH<sub>4</sub> methanolysis using metal-free coal was performed. Different H<sub>3</sub>PO<sub>4</sub> concentrations were used in the catalyst preparation, and the most efficient acid concentration was determined to be 3 M. Then, experiments were conducted on different impregnation times, carbonization temperatures, and durations. The most efficient catalyst conditions were determined as 3 M phosphoric acid, 12 h impregnation time, 600 °C carbonization temperature and 90 min of carbonization time. The catalyst exhibited a hydrogen production efficiency of 11854 mL min<sup>-1</sup>g.cat<sup>-1</sup>, and its activation energy was determined to be 22.5 kJ mol<sup>-1</sup>, according to the findings. The evaluation of prepared metal-free coal as a catalyst is very promising. It is believed that this material can be further modified by different chemical and thermo processes to obtain even more efficient catalysts.

#### 5. CONFLICT OF INTEREST

The authors declare that there is no conflict of interest regarding the study.

#### 6. REFERENCES

- Akdemir, M., Avci Hansu, T., Caglar, A., Kaya, M., & Demir Kivrak, H. (2021). Ruthenium modified defatted spent coffee catalysts for supercapacitor and methanolysis application. *Energy Storage*, 3(4), e243.
- Akdemir, M., Karakaş, D. E., & Kaya, M. (2022). Synthesis of a dual-functionalized carbon-based material as catalyst and supercapacitor for efficient hydrogen production and energy storage: Pd-supported pomegranate peel. *Energy Storage*, 4(1), e284.
- Akpan, U. F., & Akpan, G. E. (2012). The contribution of energy consumption to climate change: a feasible policy direction. *International Journal of Energy Economics and Policy*, 2(1), 21-33.
- Ali, F., Khan, S. B., & Asiri, A. M. (2019). Chitosan coated cellulose cotton fibers as catalyst for the H<sub>2</sub> production from NaBH<sub>4</sub> methanolysis. *international journal of hydrogen energy*, 44(8), 4143-4155.
- Amrouche, S. O., Rekioua, D., Rekioua, T., & Bacha, S. (2016). Overview of energy storage in renewable energy systems. *international journal of hydrogen energy*, 41(45), 20914-20927.
- Bekirogullari, M., Abut, S., Duman, F., & Hansu, T. A. (2021). Lake sediment based catalyst for hydrogen generation via methanolysis of sodium borohydride: an optimization study with artificial neural network modelling. *Reaction Kinetics, Mechanisms and Catalysis*, 134(1), 57-74.
- Bolat, M., Yavuz, C., & Kaya, M. (2021). Investigation of dual-functionalized novel carbon supported Sn material from corn stalk for energy storage and fuel cell systems on distributed generations. *Journal of Materials Science: Materials in Electronics*, 32(13), 18123-18137.
- Bull, S. R. (2001). Renewable energy today and tomorrow. *Proceedings of the IEEE*, 89(8), 1216-1226.
- Dawood, F., Anda, M., & Shafullah, G. (2020). Hydrogen production for energy: An overview. *international journal of hydrogen energy*, 45(7), 3847-3869.
- Demirbas, A., & Arin, G. (2004). Hydrogen from biomass via pyrolysis: relationships between yield of hydrogen and temperature. *Energy Sources*, 26(11), 1061-1069.
- Demirci, S., Sunol, A. K., & Sahiner, N. (2020). Catalytic activity of amine functionalized titanium dioxide nanoparticles in methanolysis of sodium borohydride for hydrogen generation. *Applied Catalysis B: Environmental*, 261, 118242.
- Demirci, S., Yildiz, M., Inger, E., & Sahiner, N. (2020). Porous carbon particles as metal-free superior catalyst for hydrogen release from methanolysis of sodium borohydride. *Renewable Energy*, 147, 69-76.
- Dudu, T. E., Alpaslan, D., & Aktas, N. (2022). Hydrogen production from methanolysis of sodium borohydride by non-metal p (CO) organo-particles synthesized from castor oil. *Journal of Polymers and the Environment*, 30(11), 4562-4570.
- Duman, F., Atelge, M., Kaya, M., Atabani, A., Kumar, G., Sahin, U., & Unalan, S. (2020). A novel Microcystis aeruginosa supported manganese catalyst for hydrogen generation through methanolysis of sodium borohydride. *international journal of hydrogen energy*, 45(23), 12755-12765.
- Fangaj, E., Ali, A. A., Güngör, F., Bektaş, S., & Ceyhan, A. A. (2020). The use of metallurgical waste sludge as a catalyst in hydrogen production from sodium borohydride. *international journal of hydrogen energy*, 45(24), 13322-13329.
- Fangaj, E., & Ceyhan, A. A. (2020). Apricot Kernel shell waste treated with phosphoric acid used as a green, metal-free catalyst for hydrogen generation from hydrolysis of sodium borohydride. *international journal of hydrogen energy*, 45(35), 17104-17117.
- Fitzgerald, J. J., Piedra, G., Dec, S. F., Seger, M., & Maciel, G. E. (1997). Dehydration studies of a high-surface-area alumina (pseudo-boehmite) using

- solid-state  $^1\text{H}$  and  $^{27}\text{Al}$  NMR. *Journal of the American Chemical Society*, 119(33), 7832-7842.
- Güney, T. (2019). Renewable energy, non-renewable energy and sustainable development. *International Journal of Sustainable Development & World Ecology*, 26(5), 389-397.
- Hamilton, C. W., Baker, R. T., Staubitz, A., & Manners, I. (2009). B-N compounds for chemical hydrogen storage. *Chemical Society Reviews*, 38(1), 279-293.
- Inal, I. I. G., Akdemir, M., & Kaya, M. (2021). Microcystis aeruginosa supported-Mn catalyst as a new promising supercapacitor electrode: A dual functional material. *international journal of hydrogen energy*, 46(41), 21534-21541.
- Karakaş, D. E. (2021). Nar kabuğu destekli  $\text{NH}_2/\text{PdMnAg}$  katalizörü varlığında sodyum bor hidrürün metanolizinin araştırılması. *Balıkesir Üniversitesi Fen Bilimleri Enstitüsü Dergisi*, 23(1), 72-83.
- Karakaş, D. E. (2022). A novel cost-effective catalyst from orange peel waste protonated with phosphoric acid for hydrogen generation from methanolysis of  $\text{NaBH}_4$ . *international journal of hydrogen energy*, 47(24), 12231-12239.
- Karakaş, D. E., Akdemir, M., Atabani, A., & Kaya, M. (2021). A dual functional material: Spirulina Platensis waste-supported Pd-Co catalyst as a novel promising supercapacitor electrode. *Fuel*, 304, 121334.
- Karakaş, D. E., Akdemir, M., Kaya, M., Horoz, S., & Yaşar, F. (2022). The dual functionality of  $\text{Zn@BP}$  catalyst: methanolysis and supercapacitor. *Journal of Materials Science: Materials in Electronics*, 33(17), 13484-13492.
- Kaya, M. (2020a). Evaluating organic waste sources (spent coffee ground) as metal-free catalyst for hydrogen generation by the methanolysis of sodium borohydride. *international journal of hydrogen energy*, 45(23), 12743-12754.
- Kaya, M. (2020b). Production of metal-free catalyst from defatted spent coffee ground for hydrogen generation by sodium borohydride methanolysis. *international journal of hydrogen energy*, 45(23), 12731-12742.
- Kaya, M., Bekiroğullari, M., & Saka, C. (2019). Highly efficient CoB catalyst using a support material based on Spirulina microalgal strain treated with  $\text{ZnCl}_2$  for hydrogen generation via sodium borohydride methanolysis. *International journal of energy research*, 43(9), 4243-4252.
- Lang, C., Jia, Y., & Yao, X. (2020). Recent advances in liquid-phase chemical hydrogen storage. *Energy Storage Materials*, 26, 290-312.
- Najjar, Y. S. (2011). Gaseous pollutants formation and their harmful effects on health and environment. *Innovative energy policies*, 1(1).
- Özarslan, S., Atelge, M. R., Kaya, M., & Ünal, S. (2021a). A Novel Tea factory waste metal-free catalyst as promising supercapacitor electrode for hydrogen production and energy storage: A dual functional material. *Fuel*, 305, 121578.
- Özarslan, S., Atelge, M. R., Kaya, M., & Ünal, S. (2021b). Production of dual functional carbon material from biomass treated with  $\text{NaOH}$  for supercapacitor and catalyst. *Energy Storage*, 3(5), e257.
- Panwar, N., Kaushik, S., & Kothari, S. (2011). Role of renewable energy sources in environmental protection: A review. *Renewable and sustainable energy reviews*, 15(3), 1513-1524.
- Robinson, E. A. (1963). Characteristic vibrational frequencies of oxygen compounds of phosphorus and chlorine: correlation of symmetric and asymmetric stretching frequencies of PO and ClO bonds. *Canadian Journal of Chemistry*, 41(1), 173-179.
- Sürmen, Y., & Demrbas, A. (2002). Thermochemical conversion of residual biomass to hydrogen for Turkey. *Energy Sources*, 24(5), 403-411.
- Thellufsen, J. Z., Lund, H., Sorknaes, P., Østergaard, P., Chang, M., Drysdale, D., . . . Sperling, K. (2020). Smart energy cities in a 100% renewable energy context. *Renewable and sustainable energy reviews*, 129, 109922.
- Wang, T., Jiang, T., Zhang, H., & Zhao, Y. (2022). Advances in catalysts for hydrogen production by methanolysis of sodium borohydride. *international journal of hydrogen energy*.
- Xu, D., Zhao, L., Dai, P., & Ji, S. (2012). Hydrogen generation from methanolysis of sodium borohydride over  $\text{Co/Al}_2\text{O}_3$  catalyst. *Journal of natural gas chemistry*, 21(5), 488-494.
- Yao, Q., Ding, Y., & Lu, Z.-H. (2020). Noble-metal-free nanocatalysts for hydrogen generation from boron-and nitrogen-based hydrides. *Inorganic Chemistry Frontiers*, 7(20), 3837-3874.
- Zhang, F., Zhao, P., Niu, M., & Maddy, J. (2016). The survey of key technologies in hydrogen energy storage. *international journal of hydrogen energy*, 41(33), 14535-14552.





## Acid-Catalyzed Atmospheric Organosolv Treatment By Using $\gamma$ -Valerolactone and Ethylene Glycol For The Delignification of Hazelnut Shell and Precipitation of Lignin

Kübra AL<sup>1\*</sup> , Sibel BAŞAKÇILARDAN KABAKCI<sup>2</sup> 

<sup>1</sup>Yalova University, Institute of Graduate Studies, Energy Systems Engineering Department, Yalova, 77100, Türkiye

<sup>2</sup>Yalova University, Engineering Faculty, Energy Systems Engineering Department, Yalova, 77100, Türkiye

**Abstract:** Lignin-based biorefineries are gaining importance day by day to obtain many value-added products from lignin. One of the most important processes that allow the recovery of both cellulose and lignin in those biorefineries is organosolv pretreatment. In this study, organosolv pretreatment was applied to the hazelnut shell at 130 °C for 60 min with ethylene glycol and  $\gamma$ -valerolactone solvents in the presence of a catalyst (either phosphoric acid or acetic acid). The success of solvent-catalyst systems was assessed by delignification efficiency and lignin recovery. Lignins obtained by precipitation were also analyzed by FTIR, TGA, DSC and Py-GC/MS. Highest delignification efficiency (33.9%) was detected for ethylene glycol-phosphoric acid solvent-catalyst pair. It was observed that acetic acid was not an effective catalyst compared to phosphoric acid. The delignification efficiency of  $\gamma$ -valerolactone was low (< 26 %) under atmospheric conditions, and in the presence of acetic acid, lignin was not precipitated from GVL system.

**Keywords:** Organosolv treatment, Delignification, Ethylene glycol,  $\gamma$ -valerolactone, Lignin recovery.

**Submitted:** August 26, 2023. **Accepted:** September 19, 2023.

**Cite this:** Al, K., & BAŞAKÇILARDAN KABAKCI, S. (2023). Acid-Catalyzed Atmospheric Organosolv Treatment By Using  $\gamma$ -Valerolactone and Ethylene Glycol For The Delignification of Hazelnut Shell and Precipitation of Lignin. *Journal of the Turkish Chemical Society, Section B: Chemical Engineering*, 6(2), 73–84. <https://doi.org/10.58692/jotcsb.1350438>.

\*Corresponding author. E-mail: [kubra.al@outlook.com](mailto:kubra.al@outlook.com).

### 1. INTRODUCTION

Among the renewable energy sources, biomass is the main source that allows the production of both power, fuel, and functional materials. Preferring lignocellulosic (including agricultural wastes and residues, food wastes, forestry residues, etc.) among biomass resources can also be a solution to critical problems such as resource scarcity, sustainable energy, waste management, and energy security. Lignocellulosic biomass is also the most accessible feedstock to produce biofuels, bio-based chemicals, and value-added materials (Velvizhi et al., 2022). According to recent research, around 181.5 billion tons of lignocellulosic biomass is annually produced worldwide (Ashokkumar et al., 2022). Lignocellulosic biomass mainly consists of three polymeric structures, cellulose (40-60%), hemicellulose (20-40%), and lignin (10-25%) (Deng et al., 2023). Cellulose, the major component of

plant cell wall, consists of a linear polysaccharide in which repeating glucose units are linked by  $\beta$ -1,4-glycosidic bonds (Bhatia et al., 2020).  $\beta$ -1,4-glycosidic bonds are known for being resistant to enzymatic hydrolysis. Hemicellulose is a branched heteropolymer that consist of pentoses (mainly arabinose and xylose) and hexoses (glucose, mannose, and galactose) (Sun et al., 2022a). Lignin is an amorphous polyphenolic macromolecule found in the cell wall of plants, consisting of three main phenylpropane units: coniferyl alcohol, sinapyl alcohol, and p-coumaryl alcohol (Ferreira et al., 2020; Ponnusamy et al., 2018). Common linkages between phenylpropane units includes  $\beta$ -O-4,  $\alpha$ -O-4,  $\beta$ -1,  $\beta$ -5,  $\beta$ - $\beta$ , 5-5, 4-O-5 and  $\alpha$ -O- $\gamma$ , where the ether  $\beta$ -O-4 linkage is the most abundant and the carbon-carbon bond  $\beta$ - $\beta$  is the second (Liu, 2013; Jędrzejczak et al., 2021). Due to the irregular structure and high degree of polymerization of lignin, it is highly resistant to chemical and

biological degradation (Cao et al., 2019; Lim et al., 2021).

Pretreatment processes, which are required for breaking down the complex structure of lignocellulose, enable the valorization of each cellulose, hemicellulose, and lignin fractions. There are several pretreatment options including physical pretreatment processes (milling, crushing, shredding, microwave pretreatment, ultrasound treatment), chemical pretreatment processes (acidic hydrolysis, alkaline hydrolysis, treatment with ionic liquids and deep eutectic solvents, organosolv treatment), physico-chemical pretreatment processes (steam explosion, hydrothermal treatment, ammonia fiber explosion, supercritical fluid treatment) and biological pretreatment (Dharmaraja et al., 2022; Zhang et al., 2023; Zhou and Tian, 2022). The selection of the pretreatment process depends on the type of biomass, the end-products desired and cost (Haldar and Purkait, 2021).

Since a wide range of products can be obtained from lignin, processes in which lignin can be recovered have been preferred in recent years (Cao et al., 2019; Yao et al., 2022). Among the pretreatment methods, the organosolv treatment enables to recover high quality lignin from lignocellulosic biomass. At the same time, very little degradation of the cellulose occurs as a result of the process and very low amount of ash is produced (Zhang et al., 2021; Pin et al., 2020). The organosolv method is carried out in pressurized systems or atmospheric conditions at temperatures of 100-250 °C with different types of solvents in the presence or absence of catalysts (Vaidya et al., 2022; Rabelo et al., 2022). The yield of delignification and lignin recovery depends on parameters such as solvent type and concentration, solvent/biomass ratio, catalyst type, concentration, temperature, retention time and lignin precipitation conditions (Sidiras et al., 2022; Ferreira et al., 2020). A wide range of solvents are used in organosolv treatment including ethanol (Alio et al., 2021; Tchuidiang et al., 2021; Schmatz et al., 2022), methanol (Weerasari et al., 2021; Pan et al., 2022a), butanol (Teramura et al., 2018), acetone (Salapa et al., 2018)  $\gamma$ -valerolactone (Giannoni et al., 2021; Raj et al., 2021; Momayez et al., 2022), ethylene glycol (Wei et al., 2021; Ling et al., 2022; Chin et al., 2021), glycerol (Wei Kit Chin et al., 2020; Chotirotsukon et al., 2019; Pascal et al., 2019), tetrahydrofuran (THF) (Liang et al., 2022; Zhao et al., 2022; Kalogiannis et al., 2020). Catalysts are used for promoting the cleavage of the lignin bonds and the selectivity of the solvent (Jiang et al., 2018). The most preferred catalysts are H<sub>2</sub>SO<sub>4</sub>, NaOH, HCl, oxalic acid, AlCl<sub>3</sub>, ammonia (Jiang et al., 2018; Ferreira and Taherzadeh, 2020; Rabelo et al., 2023).

Most of the studies focused on delignification of lignocellulosic biomass in pressurized systems. The cost of high-pressure systems and the risk of high pressure limit the use of low boiling point solvents.

High-boiling point solvents (such as glycerol, ethylene glycol,  $\gamma$ -valerolactone, etc.) can be used in milder conditions, without requiring pressurized reactors. However, precipitation and recovery of lignin from high boiling solvents have been rarely studied.

This study aims to delignify hazelnut shell and recover lignin by using ethylene glycol (EG) and  $\gamma$ -valerolactone (GVL) as solvents, and phosphoric acid (PA) and acetic acid (AA) as catalysts. While the catalysts FA and AA, which were selected in this study, have not been used with the selected solvents up to now, EG and GVL were preferred as the solvents for the reasons listed below (Sui et al., 2021; Raj et al., 2021; Sun et al., 2022; Meng et al., 2023):

- Organosolv studies with EG and GVL are very few.
- Both EG and GVL are suitable for working under atmospheric conditions since they have high boiling points of 198 °C and GVL 205 °C, respectively.
- Both EG and GVL have high lignin solubility.
- Both EG and GVL are green solvents.

Since the solvent-catalyst pairs (EG-FA, EG-AA, GVL-FA, GVL-AA) used in this study have not been tested before, the results will make an important contribution to organosolv studies and biorefining methods.

## 2. EXPERIMENTAL SECTION

### 2.1. Materials

In the present study, the hazelnut shell was preferred as lignocellulosic biomass because of the reason that 70% of worldwide hazelnut production is supplied by Türkiye, resulting a considerable amount of agricultural waste (FAO, 2023). Hazelnut shell (HS) samples were supplied from Of district, Trabzon. All samples were dried (105 °C for 24 h) before analyses. After grinding, samples were sieved by using RESTCH AS 200 vibrating sieve to have a uniform particle size (250  $\mu$ m). Chemicals including GVL (BioRenewable,  $\geq$ 99.9%, Sigma-Aldrich ReagentPlus®), EG (Extra pure, TK.010101.05001, Tekkim), PA (Merck), AA (100%, Merck) and H<sub>2</sub>SO<sub>4</sub> (95-97%, 07208, Sigma-Aldrich) were of analytical grade and used without further purification.

### 2.2. Organosolv Pretreatment

10 g of dry HS, 160 mL of solvent (either EG or GVL), 40 mL of deionized water, 10 mL catalyst (either AA or FA) were mixed (EG-AA, EG-FA, GVL-AA, GVL-FA) in a two-necked glass reactor equipped with a reflux condenser and a thermocouple. The mixture was continuously stirred under reflux at 130 °C for 60 min. At the end of the treatment, cellulose-rich pulp was separated from the liquor, and washed with hot water (water at 55 °C) and then dried in an oven at 100 °C for 24 h. To precipitate the lignin, filtrate was diluted with deionized water to 1 L (at 55 °C) and the pH was decreased to 2-2.5 by using 0.1 M H<sub>2</sub>SO<sub>4</sub>. After precipitation, lignin was separated, washed with deionized water, and then dried. All



organosolv treatments were repeated in triplicate. The lignins and cellulose rich pulps were named as: EGAAL (solvent: ethylene glycol, catalyst: acetic acid, product: lignin), EGAAP (solvent: ethylene glycol, catalyst: acetic acid, product: cellulose rich pulp), EGFAL (solvent: ethylene glycol, catalyst: phosphoric acid, product: lignin), EGFAP (solvent: ethylene glycol, catalyst: acetic acid, product: cellulose rich pulp), GVLAAL (solvent:  $\gamma$ -valerolactone, catalyst: acetic acid, product: lignin), GVLAAP (solvent:  $\gamma$ -valerolactone, catalyst: acetic acid, product: cellulose rich pulp), GVLFAAL (solvent:  $\gamma$ -valerolactone, catalyst: phosphoric acid, product: cellulose lignin), GVLFAAP (solvent:  $\gamma$ -valerolactone, catalyst: phosphoric acid, product: cellulose rich pulp).

The efficiency of each organosolv solvent-catalyst system was assessed in terms of delignification efficiency and lignin recovery:

Delignification efficiency (%) = ((lignin in the sample (g lignin) - lignin in the pulp (g lignin)) / lignin in the sample (g lignin)) x100

Lignin recovery (%) = (lignin precipitate (g lignin) / lignin in the sample (g lignin)) x100

### 2.3. Analyses

The thermal behavior of each pulp and lignin sample was done in Ege University Applications and Research Center for Testing and Analysis (EGE-MATAL) by using a simultaneous thermogravimetric analyzer (TGA) and differential scanning calorimetry (DSC) (TA Instruments SDT Q600). The analyses were conducted in the temperature range of 25 °C-800 °C at a heating rate of 15 °C/min, under N<sub>2</sub> atmosphere (100 mL/min).

The C, H, and N analyses were carried out in an elemental analyzer (LECO CHN628). Acid-insoluble lignin content of each sample was determined by using gravimetric method as described in NREL/TP-510-42618 (Sluiter et al., 2012). Extractive content was identified according to ASTM E1690-08 Standard Test Method for Determination of Ethanol Extractives in Biomass (American Society for Testing and Materials, 2016).

Fourier Transform Infrared (FTIR) spectra of EGAAL, EGFAL and GVLFAAL were obtained using a spectrometer (Perkin Elmer Spectrum 100) coupled with a universal attenuated total reflectance (ATR) sampling device with a diamond crystal. The spectra were recorded with a resolution of 4 cm<sup>-1</sup>, in the range between 650 and 4000 cm<sup>-1</sup>.

Py-GC/MS analyses were done in Bilecik Şeyh Edebali University Central Research Laboratory (BARUM). Fast pyrolysis analyses were performed in a pyrolyzer (Frontier/PY2020is), which was connected to a GC/MS (Shimadzu/QP 2010 Ultra). Each fast pyrolysis was performed at 600 °C (heating rate: 10 °C/ms) with a dwell time of 15 s. Pyrolysis products were purged with He (1 mL/min)

into a GC capillary column (Teknokroma, 30 m\*0.25 mm\*0.25  $\mu$ m). The oven temperature of GC was held at 40 °C for 2 min and then programmed to 200 °C with a heating rate of 5 °C/min and held there for 2 min, then further heated to 280 °C with a heating rate of 10 °C/min and held there for 2 min. The MS was operated by electron impact ionization at 70 eV with the mass scan range of m/z 30–600 amu. The ion source temperature and interphase temperature were 230 °C and 280 °C, respectively. Peaks were identified by NIST mass spectral library, which was configured in GC/MS.

### 3. RESULTS AND DISCUSSION

The elemental composition and proximate analysis of HS is given Table 1. HS is a lignin-rich agricultural residue, which contains considerable amount of carbon.

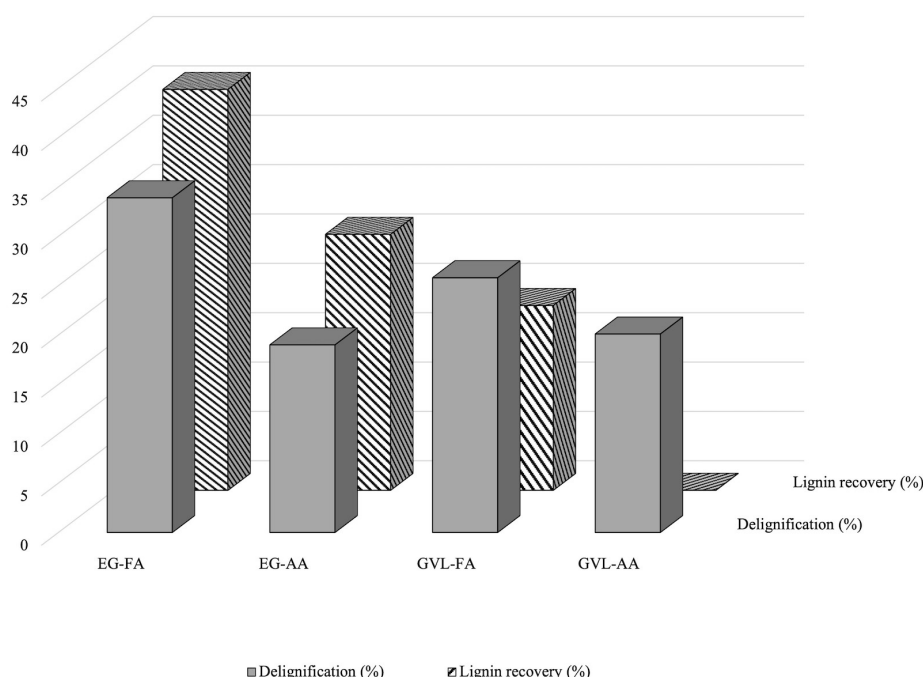
The delignification efficiencies and lignin recovery rates of EG-FA, EG-AA, GVL-FA and GVL-AA solvent-catalyst pairs are shown in Figure 1. In order to compare the efficacy of solvent-catalyst pairs, all organosolv treatments were carried out at the same temperature and mixing period. The lignin precipitation procedures were also the same for all solvent-catalyst pairs. Accordingly, EG-FA was the solvent-catalyst pair with the highest delignification with 33.9% efficiency. This system was followed by the GVL-FA solvent-catalyst pair with a delignification efficiency of 25.8%. The delignification efficiencies of GVL-AA and EG-AA solvent-catalyst pairs were close to each other (20% and 19%, respectively) and the efficiency was lower compared to other solvent-catalyst pairs (Dong et al., 2022; Pan et al., 2022b; Gaudino et al., 2018; Xu et al., 2023; Li et al., 2019). Millan et al. (2022) delignified *Pinus Radiata* using GVL and EG, where lignin extraction efficiency of EG-%1 H<sub>2</sub>SO<sub>4</sub> solvent-catalyst pair and GVL-%1 H<sub>2</sub>SO<sub>4</sub> solvent-catalyst pair were 33% and 48 %, respectively.

Based on Figure 1, AA is not an effective catalyst for EG and GVL solvents when it comes to delignification. In the recovery of lignin by precipitation, the highest recovery rate was found in the EG-FA solvent-catalyst pair (40.6%). The lignin recovery rate from the EG-AA solvent-catalyst couple was higher (26%) compared to the GVL solvent systems. In the GVL-FAA system, lignin recovery was less than 20%, while lignin was never recovered from the GVL-AA solvent-catalyst pair. Millan et al. (2022) also showed that the amount of water which was added to precipitate lignin affected the purity and amount of lignin. Yu et al. (2019), who also observed the dependency of lignin recovery to the water amount, found the maximum lignin recovery was 27% (biomass: softwood mixture; solvent: EG; catalyst: 1 wt% H<sub>2</sub>SO<sub>4</sub>; temperature: 180 °C). Low lignin recovery (< 15%) from GVL containing solvent-catalyst systems was also observed by Wu et al. (2016).

**Table 1:** Elemental and proximate analysis of HS.

<b>Hazelnut Shell</b>	
Ethanol extractives (% db*)	14.16
Klason lignin (% db*)	41.4
Volatile matter content (% db*)	75.3
Fixed carbon content (% db*)	21.4
Ash (% db)	3.3
C (% db*)	48.98
H (% db*)	6.31
N (% db*)	0.64
S (% db*)	0
O (%)	40.77

\* db: dried basis

**Figure 1:** Delignification efficiency and lignin recovery in EG-FA, EG-AA, GVL-FA, GVL-AA solvent-catalyst pairs.

The FT-IR spectra of EGFAL, EGAAL and GVLFAL samples in the wavelength range of 650-4000  $\text{cm}^{-1}$  are shown in Figure 2. Published studies on lignin were used for defining the FTIR bands (Ibrahim and Kruse, 2020; Lin et al., 2015; Khongchamnan et al., 2021; Zhuang et al., 2020). FTIR spectra of EGFAL, EGAAL and GVLFAL presented almost the same peaks with different intensities, which were all comply with the FTIR spectra of lignin. The O-H stretching vibration of hydroxyl groups in aromatic and aliphatic structures was appearing at 3250-3333  $\text{cm}^{-1}$ . C-H stretching vibration of alkyls and C-H asymmetric vibration of methylene group were observed at 2923  $\text{cm}^{-1}$  and 2853  $\text{cm}^{-1}$ , respectively.

The intensity of the C-H peaks in EGAAL and GVLFAL samples was considerably higher than that of EGFAL. The peak at 1710  $\text{cm}^{-1}$  was due to C=O non-conjugate stretching vibration of carbonyl groups (such as ketone, carboxylic acid, and ester). Lignin specific peaks appearing at 1607  $\text{cm}^{-1}$ , 1510  $\text{cm}^{-1}$ , 1448  $\text{cm}^{-1}$ , 1266  $\text{cm}^{-1}$ , 862  $\text{cm}^{-1}$  and 818  $\text{cm}^{-1}$  indicated C=O stretching vibration conjugated to aromatic skeletal vibration of lignin, aromatic ring vibration in lignin, C-H deformation in lignin, C-O stretch of the guaiacyl ring of lignin, aromatic C-H out of plane bending in lignin and C-H bending of syringyl unit, respectively.

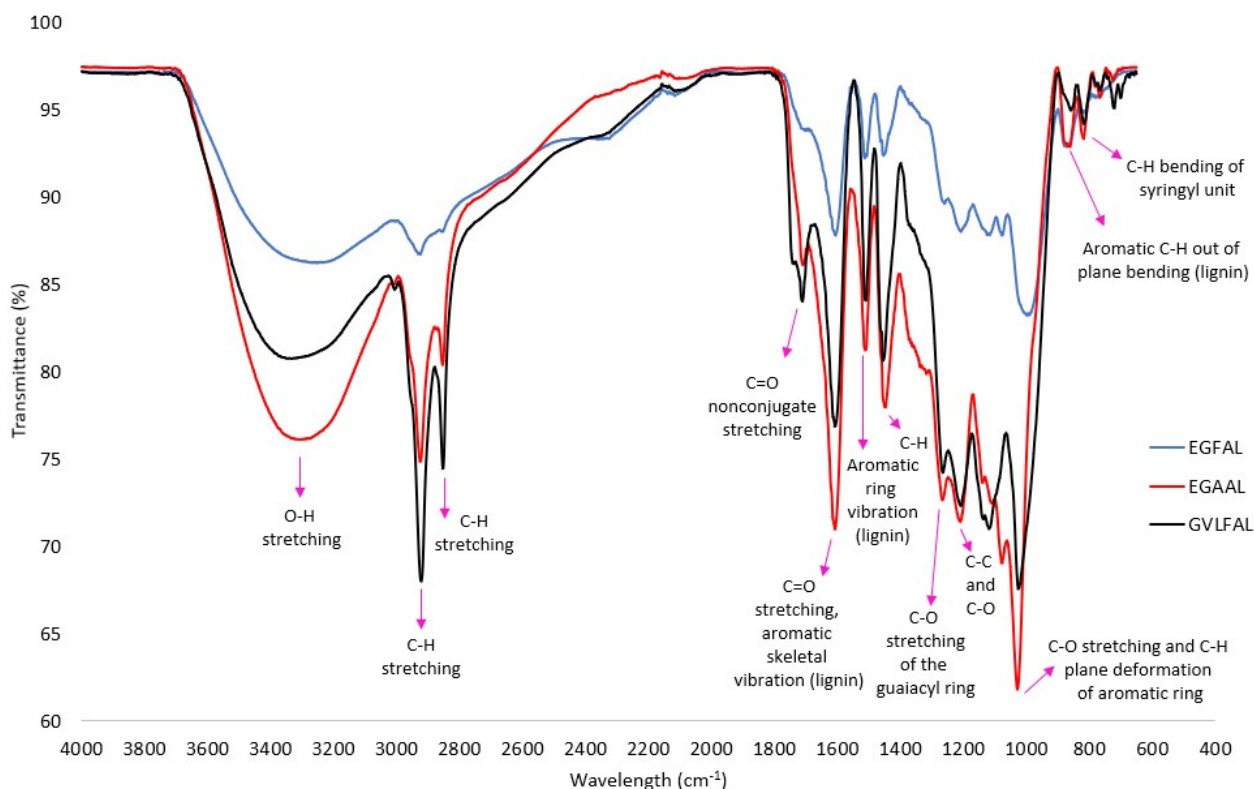


**Figure 2:** FT-IR spectra of EGFAL, EGAAL and GVLFAL.

Figure 3 (a) shows the thermogravimetric analysis curves of EGAAP, EGFAP, GVLAAP and GVLFAP. Thermal decomposition of EGFAP, EGAAP, GVLAAP and GVLFAP started with removal of moisture and light gases (such as CO, CO<sub>2</sub>) below 100 °C. The mass loss in this first step ranged between 2.86% (GVLAAP) and 5.22% (EGAAP). Second stage, which occurred in a wider temperature change (150-600 °C), was due to mass loss during thermal decomposition of hemicellulose, cellulose, and residual lignin. Main mass loss was observed in this stage. In GVLAAP, GVLFAP and EGAAP, a small peak observed (attached to the main peak) around 250 °C due to hemicellulose decomposition. In the thermogravimetric curve of EGFAP, the decomposition of hemicellulose (almost 4.6% mass loss) was observed as a single degradation at temperatures between 150-200 °C. The cleavage of 1,4 glycosidic bond in glucose during cellulose decomposition was observed around 310-350 °C (Bessa et al., 2023). T<sub>max</sub> (the temperature of the maximum mass loss rate) of EGFAP, EGAAP, GVLAAP, and GVLFAP were 330.6 °C, 362 °C, 369.3 °C, and 348.2 °C, respectively. The thermal decomposition of char was observed in the third stage (600-800 °C) with a less mass loss. The overall mass loss percentage due to thermal decomposition of EGFAP, EGAAP, GVLFAP and GVLAAP was 76%, 78%, 76.5% and 73.3%, respectively.

Like the thermogravimetric curves of cellulose-rich pulps, the thermal decomposition of EGAAL, EGFAL

and GVLFAL are given in Figure 3(b). Since the lignin was not precipitated from GVL-AA solvent-catalyst pair, GVLAAL is not seen in Figure 3(b). Compared to cellulose-rich pulps, EGAAL, EGFAL and GVLFAL decomposed in a wider temperature range (up to 700 °C). First stage, which was due to removal of moisture and light gases, occurred before 100 °C. In the second stage (150-700 °C), thermal decomposition each EGAAL, EGFAL and GVLFAL showed two or more peaks showing that precipitated lignin had no uniform structure. While EGFAL showed three peaks at 217 °C, 305 °C (T<sub>max</sub>) and 415.8 °C, EGAAL showed two peaks at 313 °C (T<sub>max</sub>) and 403.7 °C. A shift of the peak temperature to a lower value indicates the decomposition of lower molecular weight compounds in lignin fraction (Ramezani and Sain, 2018). T<sub>max</sub> values of both EGFAL and EGAAL are lower than that of soda and Kraft lignins (Domiguez-Robles et al., 2017). In the decomposition of GVLFAL, thermogravimetric curve showed two peaks at 372.7 °C (T<sub>max</sub>) and 419 °C. GVLFAL obviously included high molecular weight compounds in the lignin fraction. Similar observation was done by Jampa et al. (2019), where lignin precipitated from GVL-H<sub>2</sub>SO<sub>4</sub> solvent-catalyst pair showed a T<sub>max</sub> around 400 °C. Thus, GVLFAL is the most thermally stable lignin in this study. Total mass loss due to thermal decomposition was 52%, 62% and 63% for EGFAL, EGAAL and GVLFAL, respectively.

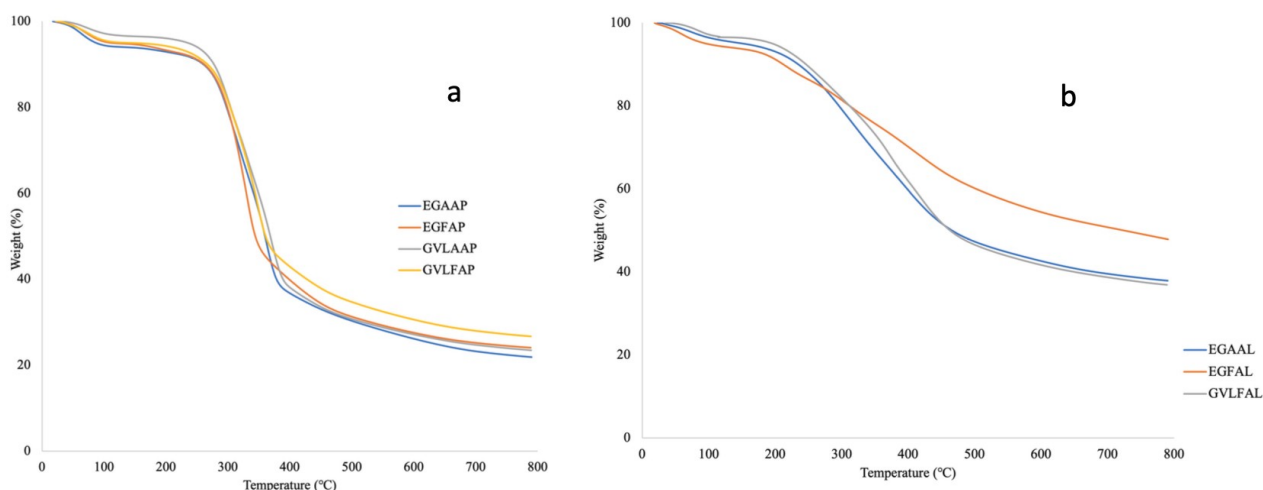


**Figure 3:** Thermogravimetric curves of pulps (a) and lignins (b).

The DSC curves of EGAAP, EGFAP, GVLAAP and GVLFAP are shown in Figure 4 (a). All the pulp samples showed endothermic and exothermic changes during heating from room temperature to 800 °C. The endothermic change due to moisture evaporation was observed at a temperature interval of 80-150 °C (peak at 100 °C). EGAAP, GVLAAP, and GVLFAP exhibited highly exothermic reactions due to cellulose decomposition (Kurian et al., 2015) at a temperature interval of 300-450 °C, where EGFAP

showed less energy release due to decomposition at temperatures around 350-450 °C.

The DSC curves of EGAAL, EGFAL and GVLFAL are illustrated in Figure 4(b). Similar to pulps, lignins also showed an endothermic change due to moisture removal at around 100 °C. Exothermic decomposition of lignin occurred in a wider temperature range (250-550 °C).

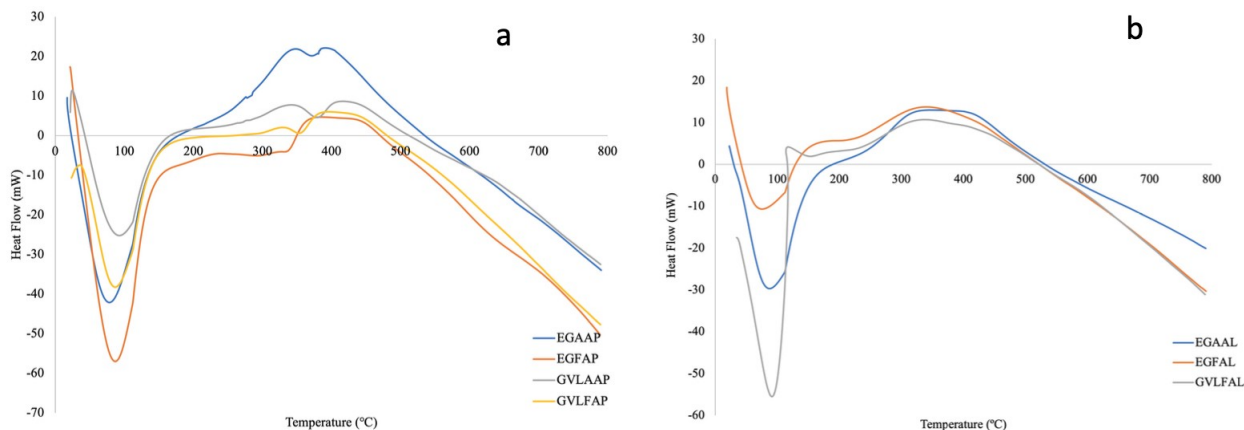


**Figure 4:** DSC curves of pulps (a) and lignins (b).

The major fast pyrolysis products of EGFAL, EGAAL and GVLFAL were identified using Py-GC/MS. The chromatograms of EGFAL, EGAAL and GVLFAL identified 64 peaks, 88 peaks, and 71 peaks, respectively. Figure 5-7 show the common compounds identified by Py-GC/MS. Commonly, lignin pyrolysis yields phenolic compounds, carbonyl

compounds (like aldehydes, acids, esters), and other hydrocarbons (Lin et al., 2015; Liu et al., 2016). However, the method of isolation of lignin and the lignin structure of the biomass has a great influence on the pyrolysis volatiles of lignin (Wang et al., 2015; Margellou et al., 2021).

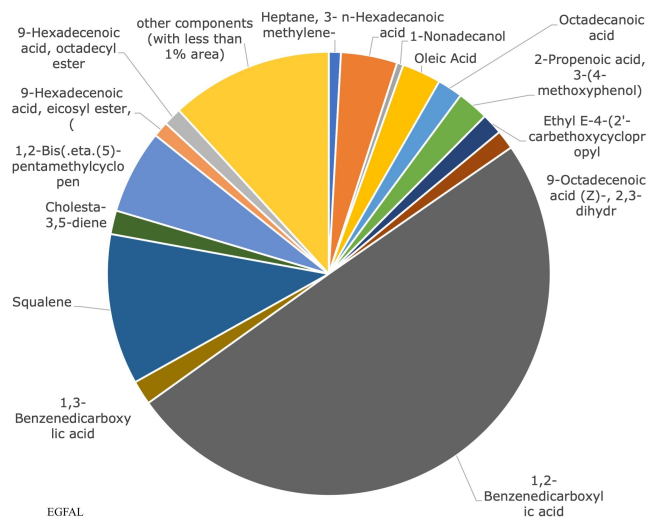


**Figure 5:** Relative composition of pyrolysis volatiles of EGFAL (which are represented as the percentage of the total chromatographic peak area).

All three of the pyrolysis products of EGFAL, EGAAL and GVLFAL had components in common: 3-methylene heptane, n-hexadecanoic acid, 1-nonadecanol, oleic acid, octadecanoic acid, 3-(4-methoxyphenyl)2-propenoic acid, 1,3-benzenedicarboxylic acid, squalene, cholesta-3,5-diene. The chromatograms were quite different from that of other lignins (Brebü et al., 2013; Qian et al., 2023). This is mainly due to biomass type, lignin

structure in the biomass, organosolv severity and precipitation conditions. Lignin is used in various areas such as constructions (Jędrzejczak et al., 2021) and buildings (Agustin et al., 2021), energy storage systems (Wang et al., 2023), wastewater (Sun et al., 2021), biomedical applications (Liu et al., 2020), adhesives (Gao et al., 2020) etc. Therefore, once the lignin is precipitated and separated, it has a vast range of end-use.

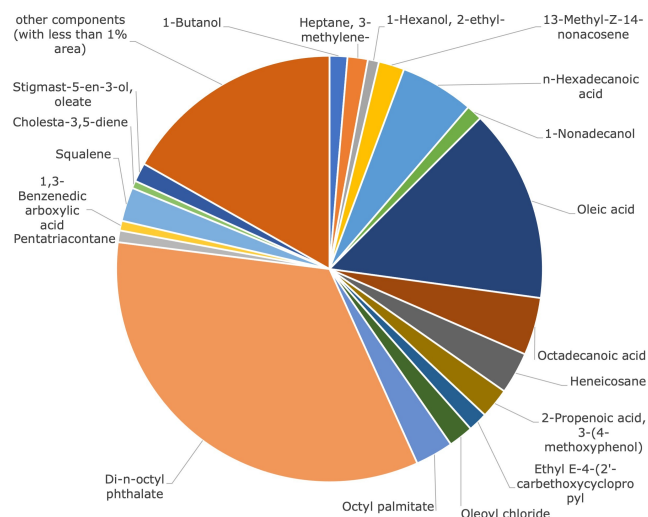


**Figure 6:** Relative composition of pyrolysis volatiles of EGAAL (which are represented as the percentage of the total chromatographic peak area).

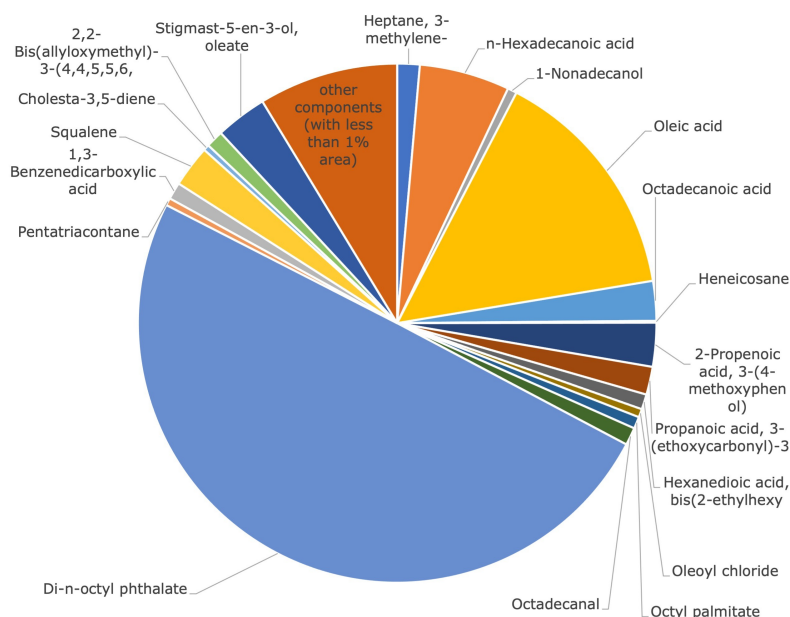


**Figure 7:** Relative composition of pyrolysis volatiles of GVLAL (which are represented as the percentage of the total chromatographic peak area).

#### 4. CONCLUSION

In the present study, hazelnut shell was subjected to organosolv treatment with different solvent (ethylene glycol and  $\gamma$ -valerolactone) and catalysts (phosphoric acid and acetic acid) under atmospheric conditions. Cellulose-rich pulp was separated from the solution and lignin fraction was precipitated and characterized. Based on results, the delignification yield and lignin recovery depended on the chosen solvent-catalyst system. The best performance in terms of delignification yield and lignin recovery was observed in EG-FA solvent-catalyst system. In terms of thermal stability, GVLAAP and GVLAL fractions were the most stable cellulose-rich pulp and lignin. According to Py-GC/MS results, lignins obtained by EG and GVL can be used as additives in plastics, packaging films, adhesives, surfactants, detergents, lubricants, coatings, cosmetics, and personal care products.

#### 5. CONFLICT OF INTEREST

No conflict of interest was declared by the authors.

#### 6. ACKNOWLEDGMENTS

This research was financially supported by Yalova University Scientific Research Unit (Project No: 2022/YL/0019).

#### 7. REFERENCES

- Agustin, M. B., de Carvalho, D. M., Lahtinen, M. H., Hilden, K., Lundell, T., & Mikkonen, K. S. (2021). Laccase as a tool in building advanced lignin-based materials. *ChemSusChem*, 14(21), 4615-4635. <https://doi.org/10.1002/cssc.202101169>
- Alio, M. A., Marcati, A., Pons, A., & Vial, C. (2021). Modeling and simulation of a sawdust mixture-based integrated biorefinery plant producing bioethanol. *Bioresource technology*, 325, 124650. <https://doi.org/10.1016/j.biortech.2020.124650>
- Ashokkumar, V., Venkatkarthick, R., Jayashree, S., Chuetor, S., Dharmaraj, S., Kumar, G., ... & Ngamcharussrivichai, C. (2022). Recent advances in lignocellulosic biomass for biofuels and value-added bioproducts-A critical review. *Bioresource technology*, 344-359, <https://doi.org/10.1016/j.biortech.2021.126195>.
- Bessa, W., Trache, D., Tarchoun, A. F., Abdelaziz, A., Hussin, M. H., & Brosse, N. (2023). Unraveling the Effect of Kraft and Organosolv Processes on the Physicochemical Properties and Thermal Stability of Cellulose and Its Microcrystals Produced from Eucalyptus Globulus. *Sustainability*, 15(4), 3384. <https://doi.org/10.3390/su15043384>
- Bhatia, S. K., Jagtap, S. S., Bedekar, A. A., Bhatia, R. K., Patel, A. K., Pant, D., ... & Yang, Y. H. (2020). Recent developments in pretreatment technologies on lignocellulosic biomass: effect of key parameters, technological improvements, and challenges. *Bioresource technology*, 300, 122724, <https://doi.org/10.1016/j.biortech.2019.122724>
- Brebu, M., Tamminen, T., & Spiridon, I. (2013). Thermal degradation of various lignins by TG-MS/FTIR and Py-GC-MS. *Journal of analytical and applied pyrolysis*, 104, 531-539. <https://doi.org/10.1016/j.jaap.2013.05.016>
- Cao, Y., Chen, S. S., Zhang, S., Ok, Y. S., Matsagar, B. M., Wu, K. C. W., & Tsang, D. C. (2019). Advances in



lignin valorization towards bio-based chemicals and fuels: Lignin biorefinery. *Bioresource technology*, 291, 121878. <https://doi.org/10.1016/j.biortech.2019.121878>

- Cheng, F., Zhao, X., & Hu, Y. (2018). Lignocellulosic biomass delignification using aqueous alcohol solutions with the catalysis of acidic ionic liquids: A comparison study of solvents. *Bioresource technology*, 249, 969-975. <https://doi.org/10.1016/j.biortech.2017.10.089>
- Chin, D. W. K., Lim, S., Pang, Y. L., Lim, C. H., Shuit, S. H., Lee, K. M., & Chong, C. T. (2021). Effects of organic solvents on the organosolv pretreatment of degraded empty fruit bunch for fractionation and lignin removal. *Sustainability*, 13(12), 6757. <https://doi.org/10.3390/su13126757>
- Chotirotasukon, C., Raita, M., Champreda, V., & Laosiripojana, N. (2019). Fractionation of sugarcane trash by oxalic-acid catalyzed glycerol-based organosolv followed by mild solvent delignification. *Industrial Crops and Products*, 141, 111753. <https://doi.org/10.1016/j.indcrop.2019.111753>
- Deng, W., Feng, Y., Fu, J., Guo, H., Guo, Y., Han, B., ... & Zhou, H. (2023). Catalytic conversion of lignocellulosic biomass into chemicals and fuels. *Green Energy & Environment*, 8(1), 10-114. <https://doi.org/10.1016/j.gee.2022.07.003>
- Dharmaraja, J., Shobana, S., Arvindnarayan, S., Francis, R. R., Jeyakumar, R. B., Saratale, R., ... & Kumar, G. (2022). Lignocellulosic biomass conversion via greener pretreatment methods towards biorefinery applications. *Bioresource technology*, 128328. <https://doi.org/10.1016/j.biortech.2022.128328>
- Dong, C., Meng, X., Leu, S. Y., Xu, L., Wu, Z., Cravotto, G., & Fang, Z. (2022). Enhancing  $\alpha$ -etherification of lignin in Eucalyptus diol pretreatment to improve lignin monomer production. *Industrial Crops and Products*, 185, 115130. <https://doi.org/10.1016/j.indcrop.2022.115130>
- Ferreira, J. A., & Taherzadeh, M. J. (2020). Improving the economy of lignocellulose-based biorefineries with organosolv pretreatment. *Bioresource technology*, 299, 122695. <https://doi.org/10.1016/j.biortech.2019.122695>
- Food and Agriculture Organization of the United Nations (FAO), Hazelnut Production, Access date: 08.08.2023 Access: <https://www.fao.org/3/x4484e/x4484e03.htm>
- Gao, S., Cheng, Z., Zhou, X., Liu, Y., Wang, J., Wang, C., ... & Zhang, D. (2020). Fabrication of lignin based renewable dynamic networks and its applications as self-healing, antifungal and conductive adhesives. *Chemical Engineering Journal*, 394, 124896. <https://doi.org/10.1016/j.cej.2020.124896>
- Gaudino, E. C., Tabasso, S., Grillo, G., Cravotto, G., Dreyer, T., Schories, G., ... & Telysheva, G. (2018). Wheat straw lignin extraction with bio-based solvents using enabling technologies. *Comptes Rendus Chimie*, 21(6), 563-571. <https://doi.org/10.1016/j.crci.2018.01.010>
- Giannoni, T., Gelosia, M., Bertini, A., Fabbrizi, G., Nicolini, A., Coccia, V., ... & Cavalaglio, G. (2021). Fractionation of *Cynara cardunculus* L. by Acidified Organosolv Treatment for the Extraction of Highly Digestible Cellulose and Technical Lignin. *Sustainability*, 13(16), 8714. <https://doi.org/10.3390/su13168714>
- Haldar, D., & Purkait, M. K. (2021). A review on the environment-friendly emerging techniques for pretreatment of lignocellulosic biomass: Mechanistic insight and advancements. *Chemosphere*, 264, 128523. <https://doi.org/10.1016/j.chemosphere.2020.128523>
- Ibrahim, Q., & Kruse, A. (2020). Prehydrolysis and organosolv delignification process for the recovery of hemicellulose and lignin from beech wood. *Bioresource Technology Reports*, 11, 100506. <https://doi.org/10.1016/j.biteb.2020.100506>
- Jędrzejczak, P., Collins, M. N., Jesionowski, T., & Kłapiszewski, Ł. (2021). The role of lignin and lignin-based materials in sustainable construction—a comprehensive review. *International Journal of Biological Macromolecules*, 187, 624-650. <https://doi.org/10.1016/j.ijbiomac.2021.07.125>
- Jiang, Z., Zhao, P., & Hu, C. (2018). Controlling the cleavage of the inter-and intra-molecular linkages in lignocellulosic biomass for further biorefining: a review. *Bioresource Technology*, 256, 466-477. <https://doi.org/10.1016/j.biortech.2018.02.061>
- Kalogiannis, K. G., Karnaouri, A., Michailof, C., Tzika, A. M., Asimakopoulou, G., Topakas, E., & Lappas, A. A. (2020). OxiOrganosolv: A novel acid free oxidative organosolv fractionation for lignocellulose fine sugar streams. *Bioresource Technology*, 313, 123599. <https://doi.org/10.1016/j.biortech.2020.123599>
- Khongchamnan, P., Wanmolee, W., Laosiripojana, N., Champreda, V., Suriyachai, N., Kreetachat, T., ... & Imman, S. (2021). Solvothermal-based lignin fractionation from corn stover: Process optimization and product characteristics. *Frontiers in Chemistry*, 9, 697237. <https://doi.org/10.3389/fchem.2021.697237>
- Kurian, J. K., Garipey, Y., Orsat, V., & Raghavan, G. S. (2015). Comparison of steam-assisted versus microwave-assisted treatments for the fractionation of sweet sorghum bagasse. *Bioresources and*

- Bioprocessing*, 2(1), 1-16.  
<https://doi.org/10.1186/s40643-015-0059-3>
- Li, Y. J., Li, H. Y., Sun, S. N., & Sun, R. C. (2019). Evaluating the efficiency of  $\gamma$ -valerolactone/water/acid system on Eucalyptus pretreatment by confocal Raman microscopy and enzymatic hydrolysis for bioethanol production. *Renewable Energy*, 134, 228-234.  
<https://doi.org/10.1016/j.renene.2018.11.038>
- Liang, L., Wang, Y. Y., Bhagia, S., Sethuraman, V., Yang, Z., Meng, X., ... & Ragauskas, A. J. (2022). Chemical and Morphological Structure of Transgenic Switchgrass Organosolv Lignin Extracted by Ethanol, Tetrahydrofuran, and  $\gamma$ -Valerolactone Pretreatments. *ACS Sustainable Chemistry & Engineering*, 10(28), 9041-9052.  
<https://doi.org/10.1021/acssuschemeng.2c00948>
- Lim, H. Y., Yusup, S., Loy, A. C. M., Samsuri, S., Ho, S. S. K., Manaf, A. S. A., ... & Rianawati, E. (2021). Review on conversion of lignin waste into value-added resources in tropical countries. *Waste and Biomass Valorization*, 12(10), 5285-5302.  
<https://doi.org/10.1007/s12649-020-01307-8>
- Lin, X.; Sui, S.; Tan, S.; Pittman, C.U., Jr.; Sun, J.; Zhang, Z. Fast Pyrolysis of Four Lignins from Different Isolation Processes Using Py-GC/MS. *Energies* 2015, 8, 5107-5121.  
<https://doi.org/10.3390/en8065107>
- Ling, R., Wei, W., & Jin, Y. (2022). Pretreatment of sugarcane bagasse with acid catalyzed ethylene glycol-water to improve the cellulose enzymatic conversion. *Bioresource Technology*, 361, 127723,  
<https://doi.org/10.1016/j.biortech.2022.127723>
- Liu, C., Hu, J., Zhang, H., & Xiao, R. (2016). Thermal conversion of lignin to phenols: Relevance between chemical structure and pyrolysis behaviors. *Fuel*, 182, 864-870.  
<https://doi.org/10.1016/j.fuel.2016.05.104>
- Liu, R., Dai, L., Xu, C., Wang, K., Zheng, C., & Si, C. (2020). Lignin-based micro-and nanomaterials and their composites in biomedical applications. *ChemSusChem*, 13(17), 4266-4283.  
<https://doi.org/10.1002/cssc.202000783>
- Liu, S. (2013). *An Overview of Biological Basics. Bioprocess Engineering*, 21–84. doi:10.1016/b978-0-444-59525-6.00002-0
- Manzhao Yao, Xiaoyun Bi, Zuhao Wang, Peng Yu, Alain Dufresne, Can Jiang, Recent advances in lignin-based carbon materials and their applications: A review, *International Journal of Biological Macromolecules*, Volume 223, Part A, 2022, Pages 980-1014, ISSN 0141-8130,  
<https://doi.org/10.1016/j.ijbiomac.2022.11.070>.
- Margellou, A. G., Lazaridis, P. A., Charisteidis, I. D., Nitsos, C. K., Pappa, C. P., Fotopoulos, A. P., ... & Triantafyllidis, K. S. (2021). Catalytic fast pyrolysis of beech wood lignin isolated by different biomass (pre) treatment processes: Organosolv, hydrothermal and enzymatic hydrolysis. *Applied Catalysis A: General*, 623, 118298.  
<https://doi.org/10.1016/j.apcata.2021.118298>
- Meng, X., Wang, Y., Conte, A. J., Zhang, S., Ryu, J., Wie, J. J., ... & Ragauskas, A. J. (2022). Applications of biomass-derived solvents in biomass pretreatment-strategies, challenges, and prospects. *Bioresource technology*, 128280.  
<https://doi.org/10.1016/j.biortech.2022.128280>
- Millán, D., González-Turen, F., Perez-Recabarren, J., Gonzalez-Ponce, C., Rezende, M. C., & Lopes, A. M. D. C. (2022). Solvent effects on the wood delignification with sustainable solvents. *International Journal of Biological Macromolecules*, 211, 490-498.  
<https://doi.org/10.1016/j.ijbiomac.2022.05.030>
- Momayez, F., Hedenström, M., Stagge, S., Jönsson, L. J., & Martin, C. (2022). Valorization of hydrolysis lignin from a spruce-based biorefinery by applying  $\gamma$ -valerolactone treatment. *Bioresource Technology*, 359, 127466.  
<https://doi.org/10.1016/j.biortech.2022.127466>
- Pan, Z., Li, Y., Wang, B., Sun, F., Xu, F., & Zhang, X. (2022a). Mild fractionation of poplar into reactive lignin via lignin-first strategy and its enhancement on cellulose saccharification. *Bioresource Technology*, 343, 126122.  
<https://doi.org/10.1016/j.biortech.2021.126122>
- Pan, Z., Li, Y., Zhang, Z., Xu, F., Ramaswamy, S., Abdulkhani, A., & Zhang, X. (2022b). Fractionation of light-colored lignin via lignin-first strategy and enhancement of cellulose saccharification towards biomass valorization. *Industrial Crops and Products*, 186, 115173.  
<https://doi.org/10.1016/j.indcrop.2022.115173>
- Pascal, K., Ren, H., Sun, F. F., Guo, S., Hu, J., & He, J. (2019). Mild acid-catalyzed atmospheric glycerol organosolv pretreatment effectively improves enzymatic hydrolyzability of lignocellulosic biomass. *ACS omega*, 4(22), 20015-20023.  
<https://doi.org/10.1021/acsomega.9b02993>
- Pin, T. C., Nascimento, V. M., Costa, A. C., Pu, Y., Ragauskas, A. J., & Rabelo, S. C. (2020). Structural characterization of sugarcane lignins extracted from different protic ionic liquid pretreatments. *Renewable Energy*, 161, 579-592.  
<https://doi.org/10.1016/j.renene.2020.07.078>
- Ponnusamy, V. K., Nguyen, D. D., Dharmaraja, J., Shobana, S., Banu, J. R., Saratale, R. G., ... & Kumar, G. (2019). A review on lignin structure, pretreatments, fermentation reactions and biorefinery potential. *Bioresource technology*, 271, 462-472.  
<https://doi.org/10.1016/j.biortech.2018.09.070>



- Rabelo, S. C., Nakasu, P. Y. S., Scopel, E., Araújo, M. F., Cardoso, L. H., & da Costa, A. C. (2022). Organosolv pretreatment for biorefineries: Current status, perspectives, and challenges. *Bioresource Technology*, 128331. <https://doi.org/10.1016/j.biortech.2022.128331>.
- Raj, T., Chandrasekhar, K., Banu, R., Yoon, J. J., Kumar, G., & Kim, S. H. (2021). Synthesis of  $\gamma$ -valerolactone (GVL) and their applications for lignocellulosic deconstruction for sustainable green biorefineries. *Fuel*, 303, 121333. <https://doi.org/10.1016/j.fuel.2021.121333>
- Ramezani, N., & Sain, M. (2018). Thermal and physiochemical characterization of lignin extracted from wheat straw by organosolv process. *Journal of Polymers and the Environment*, 26, 3109-3116.
- Salapa, I., Topakas, E., & Sidiras, D. (2018). Simulation and optimization of barley straw organosolv pretreatment. *Industrial crops and products*, 113, 80-88. <https://doi.org/10.1016/j.indcrop.2018.01.018>
- Schmatz, A. A., Masarin, F., & Brienza, M. (2022). Lignin removal and cellulose digestibility improved by adding antioxidants and surfactants to organosolv pretreatment of sugarcane bagasse. *BioEnergy Research*, 15(2), 1107-1115. <https://doi.org/10.1007/s12155-021-10367-0>
- Sidiras, D., Politi, D., Giakoumakis, G., & Salapa, I. (2022). Simulation and optimization of organosolv based lignocellulosic biomass refinery: A review. *Bioresource Technology*, 343, 126158. <https://doi.org/10.1016/j.biortech.2021.126158>
- Sluiter, A., Hames, B., Ruiz, R., Scarlata, C., Sluiter, J., Templeton, D., & Crocker, D. L. A. P. (2012). Determination of structural carbohydrates and lignin in biomass: laboratory analytical procedure (LAP). *National Renewable Energy Laboratory*, 1617(1), 1-16. <https://www.nrel.gov/docs/gen/fy13/42618.pdf>
- Sui, W., Liu, X., Sun, H., Li, C., Parvez, A. M., & Wang, G. (2021). Improved high-solid loading enzymatic hydrolysis of steam exploded corn stalk using rapid room temperature  $\gamma$ -valerolactone delignification. *Industrial Crops and Products*, 165, 113389. <https://doi.org/10.1016/j.indcrop.2021.113389>
- Sun, C., Ren, H., Sun, F., Hu, Y., Liu, Q., Song, G., ... & Show, P. L. (2022a). Glycerol organosolv pretreatment can unlock lignocellulosic biomass for production of fermentable sugars: Present situation and challenges. *Bioresource technology*, 344, 126264 <https://doi.org/10.1016/j.biortech.2021.126264>
- Sun, C., Song, G., Pan, Z., Tu, M., Kharaziha, M., Zhang, X., ... & Sun, F. (2022b). Advances in organosolv modified components occurring during the organosolv pretreatment of lignocellulosic biomass. *Bioresource Technology*, 128356. <https://doi.org/10.1016/j.biortech.2022.128356>
- Sun, Y., Wang, T., Sun, X., Bai, L., Han, C., & Zhang, P. (2021). The potential of biochar and lignin-based adsorbents for wastewater treatment: Comparison, mechanism, and application—A review. *Industrial Crops and Products*, 166, 113473. <https://doi.org/10.1016/j.indcrop.2021.113473>
- Tchuidjang, T. T., Noubissié, E., & Ali, A. (2021). Optimization of the pre-treatment of white sawdust (Triplochiton scleroxylon) by the organosolv process for the production of bioethanol. *Oil & Gas Science and Technology—Revue d'IFP Energies nouvelles*, 76, 23. <https://doi.org/10.2516/ogst/2021004>
- Teramura, H., Sasaki, K., Oshima, T., Kawaguchi, H., Ogino, C., Sazuka, T., & Kondo, A. (2018). Effective usage of sorghum bagasse: Optimization of organosolv pretreatment using 25% 1-butanol and subsequent nanofiltration membrane separation. *Bioresource technology*, 252, 157-164. <https://doi.org/10.1016/j.biortech.2017.12.100>
- Vaidya, A. A., Murton, K. D., Smith, D. A., & Dedual, G. (2022). A review on organosolv pretreatment of softwood with a focus on enzymatic hydrolysis of cellulose. *Biomass conversion and biorefinery*, 12(11), 5427-5442, <https://doi.org/10.1007/s13399-022-02373-9>
- Velvizhi, G., Balakumar, K., Shetti, N. P., Ahmad, E., Pant, K. K., & Aminabhavi, T. M. (2022). Integrated biorefinery processes for conversion of lignocellulosic biomass to value added materials: Paving a path towards circular economy. *Bioresource technology*, 343, 126151, <https://doi.org/10.1016/j.biortech.2019.122695>
- Wang, H., Fu, F., Huang, M., Feng, Y., Han, D., Xi, Y., ... & Niu, L. (2023). Lignin-based materials for electrochemical energy storage devices. *Nano Materials Science*, 5(2), 141-160. <https://doi.org/10.1016/j.nanoms.2022.01.002>
- Wang, S., Ru, B., Lin, H., Sun, W., & Luo, Z. (2015). Pyrolysis behaviors of four lignin polymers isolated from the same pine wood. *Bioresource technology*, 182, 120-127. <https://doi.org/10.1016/j.biortech.2015.01.127>
- Weerasai, K., Laosiripojana, N., Imman, S., Kreetachat, T. & Suriyachai, N., (2021). Reusable alkaline catalyzed organosolv pretreatment and delignification of bagasse for sugar platform biorefinery. *Biomass Conversion Biorefinery* 1–11. <https://doi.org/10.1007/s13399-020-01269-w>

- Wei Kit Chin, D., Lim, S., Pang, Y. L., & Lam, M. K. (2020). Fundamental review of organosolv pretreatment and its challenges in emerging consolidated bioprocessing. *Biofuels, bioproducts and biorefining*, 14(4), 808-829. <https://doi.org/10.1002/bbb.2096>
- Wei, W., Wang, B., Wang, X., Ling, R., & Jin, Y. (2021). Comparison of acid and alkali catalyzed ethylene glycol organosolv pretreatment for sugar production from bagasse. *Bioresource Technology*, 320, 124293. <https://doi.org/10.1016/j.biortech.2020.124293>
- Wu, M., Yan, Z. Y., Zhang, X. M., Xu, F., & Sun, R. C. (2016). Integration of mild acid hydrolysis in  $\gamma$ -valerolactone/water system for enhancement of enzymatic saccharification from cotton stalk. *Bioresource technology*, 200, 23-28. <https://doi.org/10.1016/j.biortech.2015.09.111>.
- Xu, X., Wang, K., Zhou, Y., Lai, C., Zhang, D., Xia, C., & Pugazhendhi, A. (2023). Comparison of organosolv pretreatment of masson pine with different solvents in promoting delignification and enzymatic hydrolysis efficiency. *Fuel*, 338, 127361. <https://doi.org/10.1016/j.fuel.2022.127361>
- Yu, O., Yoo, C. G., Kim, C. S., & Kim, K. H. (2019). Understanding the effects of ethylene glycol-assisted biomass fractionation parameters on lignin characteristics using a full factorial design and computational modeling. *ACS omega*, 4(14), 16103-16110. <https://doi.org/10.1021/acsomega.9b02298>
- Zhang, K., Pei, Z., & Wang, D. (2016). Organic solvent pretreatment of lignocellulosic biomass for biofuels and biochemicals: A review. *Bioresource Technology*, 199, 21-33. <https://doi.org/10.1016/j.biortech.2015.08.102>
- Zhang, Y., Ding, Z., Hossain, M. S., Maurya, R., Yang, Y., Singh, V., ... & Awasthi, M. K. (2022). Recent advances in lignocellulosic and algal biomass pretreatment and its biorefinery approaches for biochemicals and bioenergy conversion. *Bioresource Technology*, 128281. <https://doi.org/10.1016/j.biortech.2022.128281>
- Zhao, J., Yao, F., & Hu, C. (2022). Enhancing enzymatic hydrolysis efficiency of crop straws via tetrahydrofuran/water co-solvent pretreatment. *Bioresource Technology*, 358, 127428. <https://doi.org/10.1016/j.biortech.2022.127428>
- Zhou, M., & Tian, X. (2022). Development of different pretreatments and related technologies for efficient biomass conversion of lignocellulose. *International Journal of Biological Macromolecules*, 202, 256-268. <https://doi.org/10.1016/j.ijbiomac.2022.01.036>
- Zhuang, J.; Li, M.; Pu, Y.; Ragauskas, A.J.; Yoo, C.G. Observation of Potential Contaminants in Processed Biomass Using Fourier Transform Infrared Spectroscopy. *Applied Science*, 2020, 10, 4345. <https://doi.org/10.3390/app10124345>



## Preparation of Waste Fabric Based Activated Carbon and Determination of Adsorption Performance Using Methylene Blue

Yavuz Gokce 

<sup>1</sup>Ankara University, Department of Chemical Engineering, Ankara, 06100, Turkey

**Abstract:** The acceleration of industrialisation and population growth throughout the world have caused the rapid depletion of water resources in the last century. Industrial wastes are one of the major factors causing water pollution. One of the most effective and well-known methods to prevent water pollution is adsorption process. In this study, highly porous activated carbons were produced using waste fabric samples and their adsorption performances were determined in the presence an adsorbate to prevent water pollution. Methylene blue (MB) as the adsorbate was used for the adsorption tests. The waste fabric samples were carbonised at 400 °C, 500 °C and 600 °C to determine the effect of pre-carbonisation temperature on the adsorption performance. The activated carbon surface properties varied depending on the pre-carbonisation temperature. The surface areas of the samples were 1385 m<sup>2</sup>/g, 1583 m<sup>2</sup>/g and 1276 m<sup>2</sup>/g, and the total pore volumes were 0.7688 cm<sup>3</sup>/g, 0.9545 cm<sup>3</sup>/g and 0.7394 cm<sup>3</sup>/g, respectively. The results showed that the pre-carbonisation temperature affected the adsorption performance. The adsorption capacities of the activated carbons calculated according to the Langmuir adsorption model were 531.46 mg/g, 630.26 mg/g and 655.40 mg/g, respectively.

**Keywords:** Activated carbon, carbonisation, activation, heat treatment, adsorption

**Submitted:** September 05, 2023. **Accepted:** September 27, 2023.

**Cite this:** Gokce, Y. (2023). Preparation of Waste Fabric Based Activated Carbon and Determination of Adsorption Performance Using Methylene Blue. Journal of the Turkish Chemical Society, Section B: Chemical Engineering, 6(2), 85-94. <https://doi.org/10.58692/jotcsb.1355600>.

\*Corresponding author. E-mail: [ygokce@eng.ankara.edu.tr](mailto:ygokce@eng.ankara.edu.tr).

### 1. INTRODUCTION

Water is a crucial substance necessary for all living things in the world to survive. The continuity and diversity of life depend on the existence of water (Shiklomanov, 2000). Developments in the fields of science, technology, and health after the Industrial Revolution have caused radical changes throughout the world. The most important of these is the rapid increase in the world population. The world population, which was 1 billion at the beginning of the 19th century, reached 7.8 billion in 2021 and exceeded 8 billion today, because of the developments in the health sector and the rapid decrease in child mortality rates (Unnerstall, 2022). Due to the increase in population, the amount of water per capita is also decreasing. On the other hand, production amounts are increasing in every sector due to industrialisation. The increase in production naturally leads to an increase in the amount of industrial waste generated. Industrial wastes are one of the important factors that have negative effects on water pollution (Shukla et al., 2002). Therefore,

protecting all water resources, especially drinking and utility water, keeping them clean and cleaning contaminated water resources are vital for the sustainability of life. Methods for cleaning contaminated water are generally grouped under six main processes: adsorption, biotechnology, catalytic, membrane, ionising radiation, and magnetically assisted processes (Ambashta & Sillanpää, 2010). These methods have various advantages and disadvantages compared to each other. The process of cleaning contaminated water by adsorption is the most preferred among them (Chai et al., 2021). Thousands of studies on this topic are published in literature every year.

In the process of water purification, contaminants in water are retained on the surface of a solid (adsorbent) by adsorption. There are many factors that affect the amount of contaminant that can be adsorbed on the solid surface. Many studies are frequently conducted on many parameters such as the amount of solid, the surface chemistry of the solid, the physical properties of the solid such as particle size and surface area, the molecular size of

the adsorbate, temperature, mixing, ambient pH value (Bushra et al., 2021; Rápó & Tonk, 2021). The characteristics (physical and chemical) of the adsorbent are the most important factors that affect the adsorption performance. It is possible to find studies using many different adsorbents such as clay (Bentchikou et al., 2017), biomass (Darama et al., 2022), activated carbon (Gokce et al., 2021), metal oxide (Ayrancı et al., 2023), metal organic lattice structures (Wang et al., 2021), carbon nanotube (Avcı et al., 2020), graphene (Yang & Cao, 2022). The low price and easy accessibility of the raw material from which the adsorbent is obtained is the reason for economic preference as it will reduce the cost of the adsorption process. Materials such as clay and biomass are very economical materials since they are found spontaneously in nature, but the adsorption capacity of such adsorbents is not at the expected level. Activated carbons are materials with very good adsorption performance thanks to their high surface area. They are not found in nature by themselves. However, they can be easily produced from carbon-containing materials such as fossil-based coal (Yaglıkci et al., 2021), biomass (Gürten İnâl et al., 2020), polymers (Wróbel-lwaniec et al., 2015). Carbon-containing materials, especially in waste form, reduce the production cost as they are very cheap. For this reason, activated carbons are one of the most preferred materials in the adsorption process. Water treatment systems in which activated carbons are used in industrial or domestic scale are very common in daily life. The adsorption properties of activated carbons come to the fore in sectors such as treatment systems, mining, health, defense industry, energy storage (Gayathiri et al., 2022). Activated carbon has been prepared using various waste biomasses such as coconut shell (Daud & Ali, 2004), bamboo (Liu et al., 2010), hazelnut shell (Ozpınar et al., 2022), tea waste (Gokce & Aktas, 2014), olive kernel (Eder et al., 2021), cumin stalk (Gürten İnâl et al., 2018) etc. and their adsorption performances against various pollutants have been tested. Such raw materials make activated carbon production sustainable as they are formed by themselves in tons every year. Another raw material that will enable sustainable activated carbon production even if it does not occur spontaneously in nature is waste textile products. Textile products are produced from carbon-based natural and synthetic fibres. The most commonly used natural fibre source is cotton and synthetic fibre source is polyester. Cotton is composed of cellulose, and cellulose is the most abundant natural polymer in nature.

The amount of production of textile products is increasing in a yearly basis. Especially in the last 200 years, when the population has increased very rapidly, the total amount of textile fibres required for clothing production has also increased rapidly. Annual fibre production is expected to increase further as they are being used in the fields of medicine, construction, automotive, agriculture, packaging, electronics, etc. due to their technical properties. The amount of fibre production, which

was around 57 million tons in the 2000s, reached 110 million tons a few years ago (Ütebay et al., 2020). The gradual increase in textile production brings up an important problem such as textile waste. The recycling percentage of textile waste is very low at 25% (Juanga-Labayen et al., 2022). The low recycling percentage significantly affects the sustainability of the textile industry. Although the number of scientific or applied studies on the recycling of textile solid wastes is limited, interest in these wastes has been increasing in recent years (Cao et al., 2022; Pais et al., 2022; Reike et al., 2023; Ütebay et al., 2020). Some applications where new products are used through recycling of textile wastes are as follows; disposable diapers, sanitary napkins, sterile wraps, workwear, wiping cloths, biogas production, dress lining, carpet and upholstery fabrics, wall coverings, car interior and headliner, seat belts, filtration systems, sound insulation materials, reinforced cement, ground reinforcement for roads, building insulation, etc. (Barbero-Barrera et al., 2016; Jeihanipour et al., 2013). In recent years, the production of new garments using recycled fibres has also become increasingly common among brands. Another recycling application of textile wastes is activated carbon production. Some studies on the adsorption performance of activated carbons produced from textile wastes were found in periodicals. However, none of these studies included the impacts of the change in activated carbon surface properties on adsorption performance.

Within the scope of this study, it was intended to produce suitable adsorbent using a waste shirt with 100% cotton fabric content and to investigate the methylene blue adsorption capability of the adsorbent from water. Since it is known that activated carbon surface properties directly affect adsorption performance, different pre-carbonisation temperatures were tried during production. Thus, it was also investigated how the physical and chemical properties of the produced activated carbon samples affect the adsorption performance.

## 2. EXPERIMENTAL SECTION

### 2.1. Materials

A 100% cotton shirt that cannot be worn and repaired was used as the waste fabric raw material. Since the selected fabric cannot be used for the purpose of production (wearing), it is considered as waste. Potassium hydroxide (KOH, Merck) was used as activating material in activated carbon production. Methylene blue (MB, Merck) was preferred in adsorption experiments as the adsorbate. No further purification process was performed for the chemicals used.

### 2.2. Activated Carbon Production

A piece of at least 1 g was cut from the waste shirt, which is cut into smaller pieces and dried in the oven at 105 °C for 12 h. The dried fabric pieces were weighed, and the amount of starting material was determined. Activated carbon production consists of two steps: carbonisation (pre-

carbonisation) in the presence of N<sub>2</sub> (first step) and carbonisation/activation in an inert N<sub>2</sub> atmosphere at a higher temperature (second step). The pre-carbonisation temperature was changed to determine the effects of activated carbons surface properties on adsorption performance. In the pre-carbonisation process, the dried waste fabric samples were transferred to a porcelain crucible and placed in a heat treatment furnace with the lid closed. The furnace was set to the desired pre-carbonisation temperature in N<sub>2</sub> atmosphere for 1 h. The heating rate was 10 °C/min. The furnace was then allowed to cool down to room temperature on its own. The pre-carbonisation temperatures examined in the study were 400 °C, 500 °C and 600 °C. For activated carbon production, the pre-carbonised samples are mixed with KOH so that the ratio of carbonised sample:KOH by weight is 1:3. The appropriate amount of KOH was dissolved in 30 mL of distilled water, carbonised fabric samples were added and mixed for at least 3 h. The mixture was dried at 105 °C for overnight to remove water. After drying, the furnace was set to 800 °C with a heating rate of 10 °C/min and the final carbonisation and activation processes were carried out for 1 h. The final carbonisation and activation temperature was kept constant for all samples. The samples obtained at the end of the process were washed in distilled water and the activation chemical was completely removed. The prepared activated carbon samples were labelled as AC-400, AC-500 and AC-600 according to the pre-carbonisation temperature applied.

### 2.3. Adsorption Tests

The adsorption performances of the produced samples were determined using MB dye which is frequently used in textiles. Before the adsorption process, a stock MB solution was prepared at a concentration of 500 ppm. Using the stock dye solution, dye solutions of 25 ppm, 50 ppm, 100 ppm, 150 ppm, 200 ppm, 250 ppm, 300 ppm and 350 ppm were prepared in 50 mL volumes. 0.01 g of activated carbon was added to each solution and stirred for 16 h at 30 °C with the help of an orbital shaker (Gerhardt) operating at 150 rpm. After mixing, 10 mL samples of each solution were separated using disposable PTFE filters (0.45 µm).

### 2.4. Characterisation Studies

Brunauer-Emmett-Teller (BET) surface areas and pore size distributions of activated carbon samples were determined by Quantachrome NOVA 2200 series volumetric gas adsorption system. Non-local density functional theory (NLDFT) was used for pore size distributions. Fourier-Transform Infrared Spectroscopy (FTIR, Shimadzu FTIR-8040) was used for the determination of the surface functional groups present in the structures of the samples. FTIR analysis was performed in the wavenumber range of 4000-400 cm<sup>-1</sup>. Before the analysis, the AC-400, AC-500 and AC-600 samples were mixed with potassium bromide at a ratio of 1:1200 (activated carbon: potassium bromide) to prepare pellets. Pellet preparation was carried out under vacuum to remove carbon dioxide and moisture

that may be trapped in the interparticle spaces and on the particle surface. The wettability properties of the samples were determined by Attension Theta Lite Optical Contact Angle device according to the sessile drop contact angle method. The adsorption capacities of the AC-400, AC-500 and AC-600 samples were determined with the help of a UV-Vis spectrophotometer (Scinco S-3100) at a wavelength of 664 nm where MB has a maximum absorbance.

## 3. RESULTS AND DISCUSSION

### 3.1. Specific Surface Area and Pore Size Distribution

The effects of pre-carbonisation temperature on the structural surface properties of the produced activated carbon samples was determined by BET surface area and pore size distribution analysis. N<sub>2</sub> adsorption-desorption isotherms of the samples are given in Figure 1. As can be seen from the figure, the adsorbed N<sub>2</sub> volumes differed for all samples. This result showed that activated carbons had different surface areas. The BET surface area values were calculated using 0.05-0.3 relative pressure (P/P<sub>0</sub>) data. The BET surface areas of AC-400, AC-500 and AC-600 samples were 1385 m<sup>2</sup>/g, 1583 m<sup>2</sup>/g and 1276 m<sup>2</sup>/g, respectively. The isotherms were like Type IV isotherms according to the pore classification of the International Union of Pure and Applied Chemistry (IUPAC). The rapid increase of adsorption isotherms at low relative pressure values indicated the presence of micropores in the structure. Also, it was clearly seen from the isotherms that adsorption and desorption curves do not follow the same path and hysteresis occurs. This indicated the presence of mesopores in the structure in addition to micropores.

The pore size distributions are shown in Figure 2. Supporting the results obtained by adsorption-desorption isotherms, all samples had micropore and mesoporous structure simultaneously. AC-500 had the highest surface area and the highest cumulative pore volume. The total pore volume values of AC-400, AC-500 and AC-600 samples were calculated with the help of adsorption isotherms data at 0.99 relative pressure. The total pore volume values were 0.7688 cm<sup>3</sup>/g, 0.9545 cm<sup>3</sup>/g and 0.7394 cm<sup>3</sup>/g, respectively. Structural surface properties of the samples such as the BET surface area, total pore volume, micropore and mesopore volumes, micropore and mesopore fractions were given in Table 1. According to IUPAC, pores smaller than 2 nm were classified as micropores. Micropore volumes were determined using the data obtained by NLDFT method. Mesopore volumes were calculated from the difference between total pore volumes and micropore volumes. As can be deduced from the results, micropore volumes of the samples were higher than mesopore volumes. However, different BET surface areas, pore volumes and pore fractions were formed due to the change in pre-carbonisation temperature.

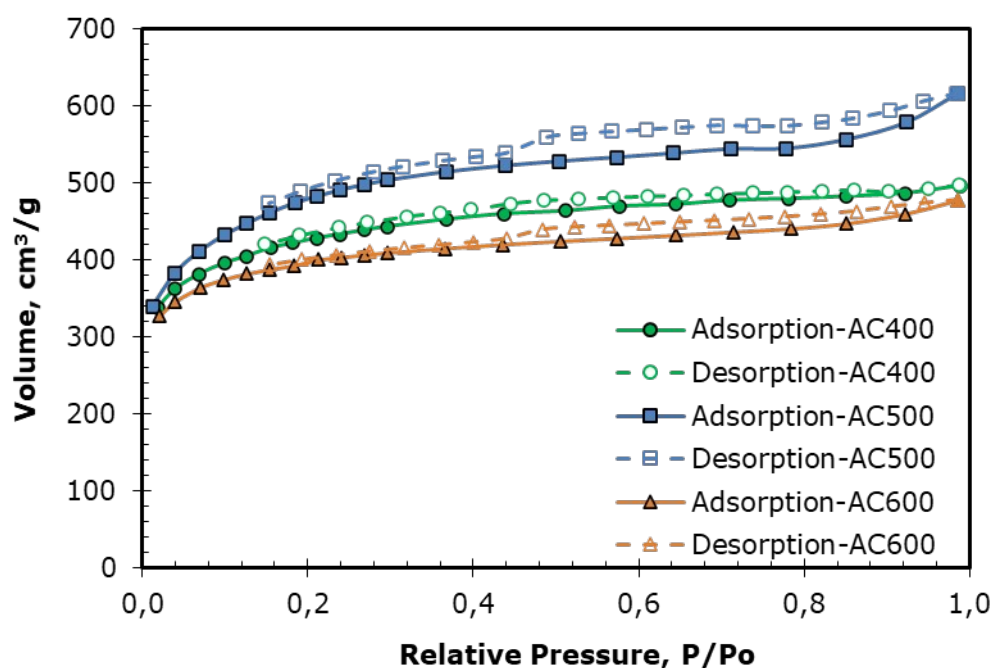


**Figure 1:** N<sub>2</sub> adsorption-desorption isotherms of AC-400, AC500 and AC-600.

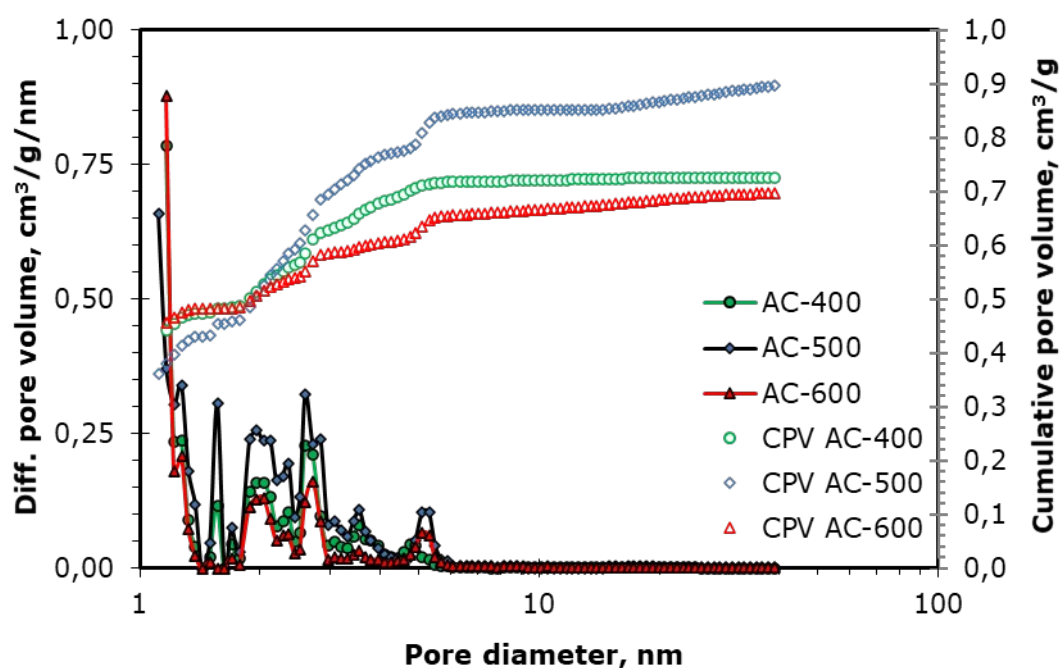


**Figure 2:** Pore size distributions (NLDFT) and cumulative pore volumes of AC-400, AC500 and AC-600 (CPV: Cumulative pore volume).

**Table 1:** Surface area and pore volume values of AC-400, AC-500, and AC-600.

Sample	BET surface area, m <sup>2</sup> /g	Total pore volume <sup>a</sup> , cm <sup>3</sup> /g	V <sub>micro</sub> <sup>b</sup> , cm <sup>3</sup> /g	V <sub>meso</sub> <sup>c</sup> , cm <sup>3</sup> /g	V <sub>micro</sub> , %	V <sub>meso</sub> , %
AC-400	1385	0.7688	0.5206	0.2482	67.72	32.28
AC-500	1583	0.9545	0.5152	0.4393	53.98	46.02
AC-600	1276	0.7394	0.5115	0.2279	69.18	30.82

<sup>a</sup> calculated at P/P<sub>0</sub> = 0.99

<sup>b</sup> according to NLDFT



$$V_{\text{meso}} = \text{Total pore volume} - V_{\text{micro}}$$

The micropore volumes of the samples were very close to each other and it can be argued that they were not affected much by the pre-carbonisation temperature. However, there was a significant difference in mesopore volume values. While the AC-400 and AC-600 samples had close micropore and mesopore fractions, AC-500 contained the highest mesopore fraction. It was clear that microporosity was dominant for AC-400 (67.72%) and AC-600 (69.18%). On the other hand, AC-500 had a balanced pore distribution (53.98% micropores, 46.02% mesopores). The mesopore volume was almost twice as much as that of the other samples. The differences observed in the structural surface properties of the activated carbon samples due to the change in pre-carbonisation temperature were related to the surface chemistry. With the increase in pre-carbonisation temperature, the surface functional groups on the fabric surface started to break away from the structure. Therefore, it was thought that the surface properties of carbonised samples obtained by applying different pre-carbonisation temperatures showed chemical differences. The most sensitive groups to heat treatment are oxygen-containing groups and they will naturally remove from the structure in different amounts with increasing temperature. When the carbonised samples with different surface chemistry are activated with KOH, the activated carbons

produced (AC-400, AC-500, and AC-600) are expected to show physically and chemically different surface behaviours. The results given in Table 1 clearly show the physical changes in the structure.

### 3.2. FTIR Analysis

FTIR analyses were applied to investigate the effects of pre-carbonisation process on the surface chemical properties of the AC-400, AC-500 and AC-600 samples. The type of surface functional groups can be determined by FTIR analysis. Figure 3 shows the FTIR spectra of the samples. It is seen that all samples have similar absorption peaks, but the peak intensities are different. The surface functional groups corresponding to the bands obtained were as follows. The broad peak observed in the wavenumber range 3700-3200  $\text{cm}^{-1}$  corresponds to phenolic hydroxyl, alcohol groups or moisture-induced O – H stress vibrations absorbed into the structure. The absorption bands observed around 3000-2850  $\text{cm}^{-1}$  indicates aliphatic C – H stretching. C = O stretching vibrations in conjugated carbonyl groups were observed as small absorption bands in the 1750-1700  $\text{cm}^{-1}$  region (Gokce & Aktas, 2014). The absorption band at 1628  $\text{cm}^{-1}$  is attributed to C = C stretching vibrations originating from quinone groups and/or aromatic ring.

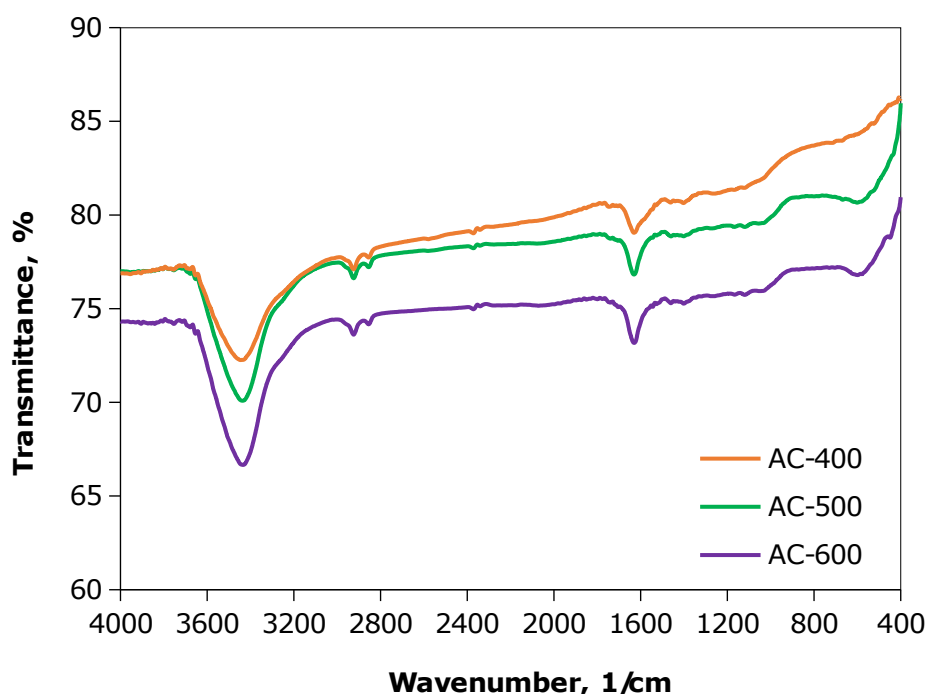


**Figure 3:** FTIR spectra of AC-400, AC-500 and AC-600.

The small peaks observed at 1442  $\text{cm}^{-1}$  and 1396  $\text{cm}^{-1}$  represents C – H deformation vibrations. In the fingerprint region (1200-700  $\text{cm}^{-1}$ ), C – O – C vibrations, aromatic CH in-plane deformation, C – O and C – C stretching vibrations or C – OH bending vibrations that may be due to hydroxyl, ether and

ester structures are observed. Although the FTIR spectra did not give information about the amounts of functional groups present in the structure depending on the pre-carbonisation temperature applied, the peak intensities proved that these

groups are present in the structure in different ratios.

### 3.3. Contact Angle Measurements

Wettability properties of AC-400, AC-500 and AC-600 samples were determined by contact angle analysis (Figure 4). In general, samples with a contact angle below 90° have a water-loving (hydrophilic) surface. As the contact angle increases above 90°, the surface becomes water-repellent (hydrophobic). Activated carbons are amphoteric materials that contain both hydrophilic

and hydrophobic surface functional groups. Polar and non-polar groups in the structures of the samples were determined by FTIR analyses. The amount of these groups directly affects the hydrophilicity or hydrophobicity of the surface. The contact angle values of AC-400, AC-500 and AC-600 samples were measured as 43.28°, 53.85° and 65.74°, respectively. The results supported the FTIR analysis. As the pre-carbonisation temperature increased from 400 °C to 600 °C, the amount of oxygen-containing functional groups removed from the structure increased.

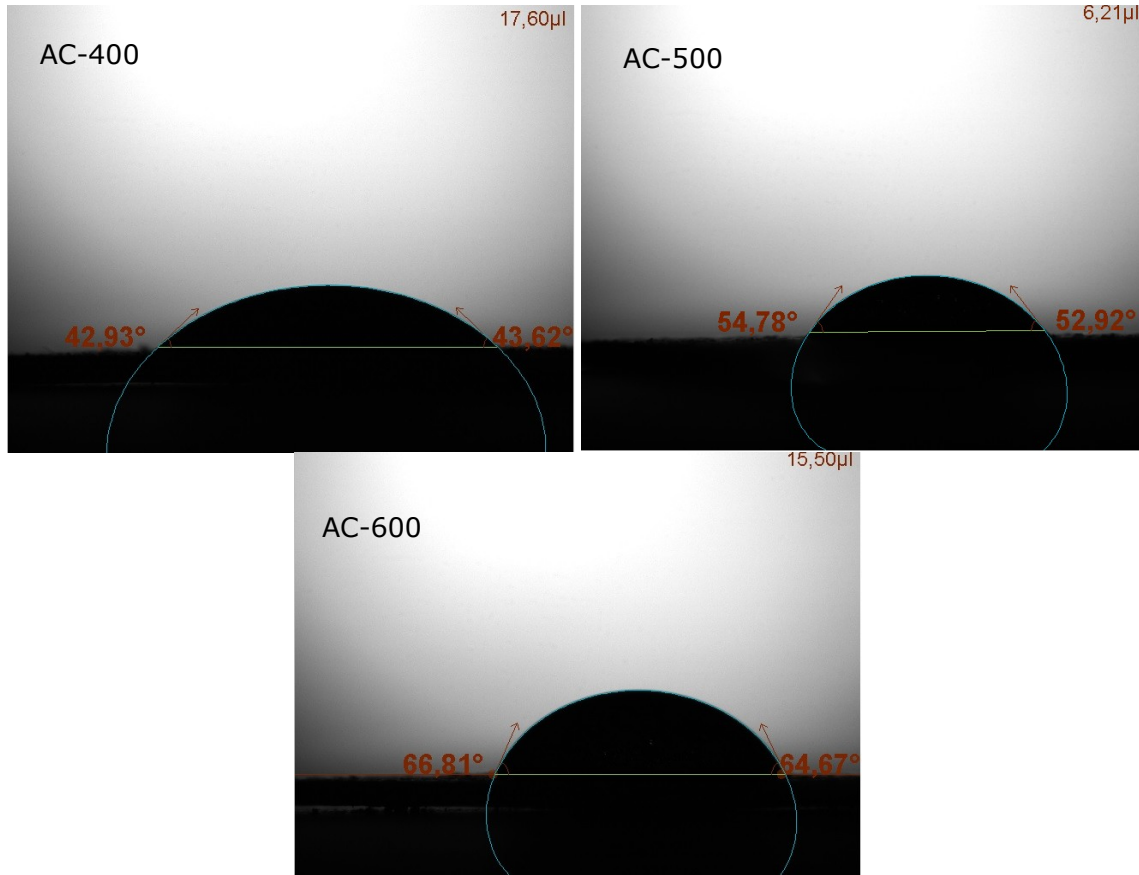


**Figure 4:** Contact angle measurements of AC-400, AC-500 and AC-600.

In other words, a more hydrophobic surface was formed with increasing temperature. This allowed the functional group with less oxygen content to react during activation and to form a more hydrophobic product. Contact angle measurement results also supported this phenomenon. The AC-400 had the most hydrophilic surface among the samples, while, as expected, the AC-600 was the most hydrophobic.

### 3.4. Adsorption Studies

The data obtained from MB adsorption experiments of the samples prepared with different pre-carbonisation processes are given in Figure 5 and Figure 6. The suitability of the adsorption data to Langmuir and Freundlich adsorption models was examined within the scope of the study. Langmuir and Freundlich adsorption models are given in Equations 1 and 2, respectively (Freundlich, 1906;

Langmuir, 1918). To determine the appropriate model, appropriate curves were fitted to Equation 1 and Equation 2 with the help of SigmaPlot 12 program.

$$q_e = \frac{q_m k_L C_e}{1 + k_L C_e} \quad (\text{Eq. 1})$$

$$q_e = k_F C_e^{\frac{1}{n}} \quad (\text{Eq. 2})$$

Figure 5 shows the experimental adsorption data and the curves fitted according to the Langmuir model and Figure 6 shows the experimental adsorption data and the curves fitted according to the Freundlich model. The terms  $q_e$ ,  $q_m$ ,  $k_L$  and  $C_e$  in Equation 1 refer to equilibrium adsorption capacity, maximum monolayer adsorption capacity,



Langmuir constant and equilibrium concentration, respectively. The terms  $k_F$  and  $n$  in Equation 2 refer

to the Freundlich constant and the exponent of the equation, respectively.

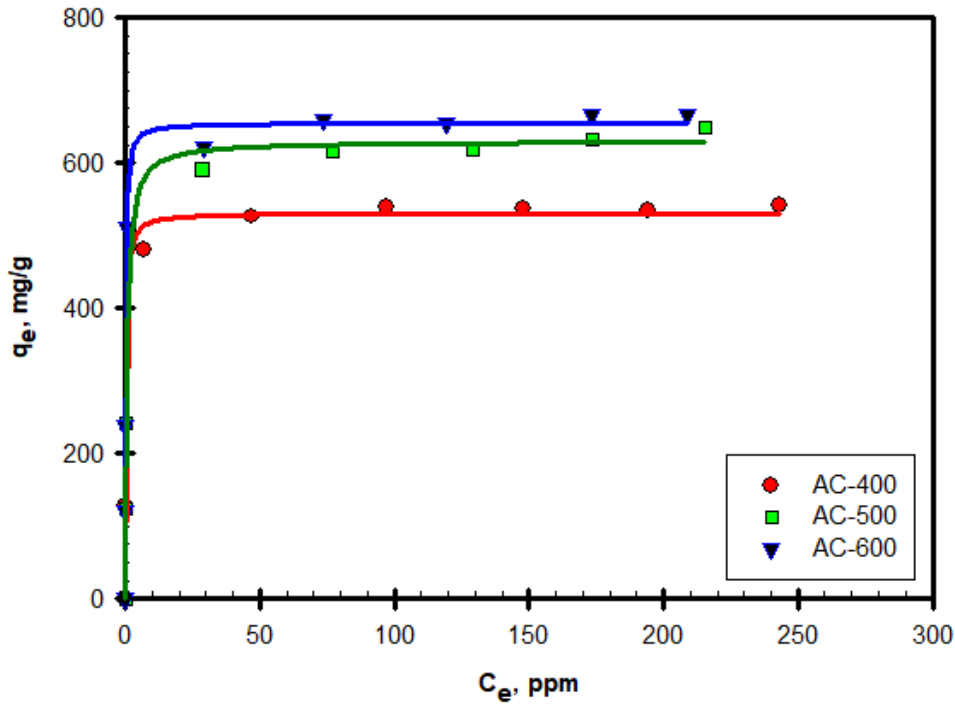


Figure 5: MB adsorption isotherms of activated carbon samples (Langmuir Adsorption Model).

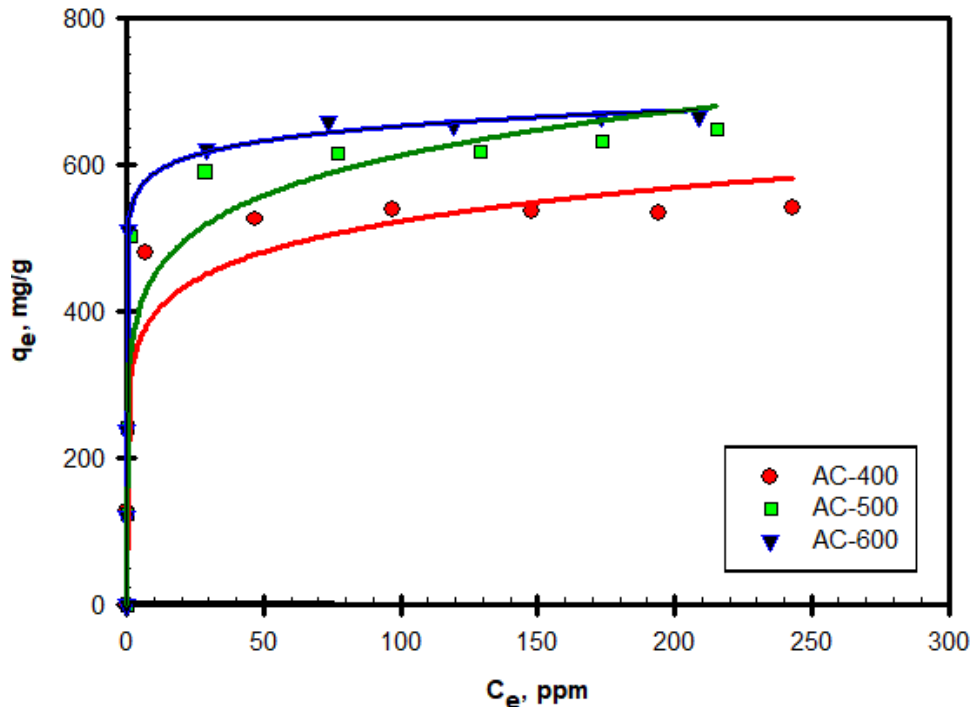


Figure 6: MB adsorption isotherms of activated carbon samples (Freundlich Adsorption Model).

The Langmuir and Freundlich model parameters calculated using the equations and adsorption data were presented in Table 2. When the  $R^2$  values given in the table are compared, it is seen that the data fit well the Langmuir adsorption model more. Therefore, it can be said that MB is adsorbed to the

surface by monolayer adsorption. The maximum monolayer adsorption capacities calculated from Langmuir adsorption model are 531.46 mg/g, 630.26 mg/g and 655.40 mg/g, respectively. It is clearly demonstrated with the help of adsorption isotherms that the change in pre-carbonisation

temperature has significant effects on adsorption performance. The highest adsorption capacity was obtained for the AC-600. Although the AC-500 had 24% higher BET surface area and 29% higher pore volume than AC-600, it exhibited lower adsorption performance. This revealed that besides physical surface properties, chemical surface properties were also important for adsorption. High surface area and mesopore structure are important parameters for dye adsorption on activated carbons. High surface area is a desirable property in activated carbons as it increases the number of potential active positions. The activated carbons should have a suitable pore opening for the dye molecules to enter the pores easily. Although the AC-500 sample had these desired properties, its lower performance against MB than AC-600 was attributed to the adsorbent-adsorbate interaction. When MB molecules diffuse into activated carbon pores, they adsorbed to certain positions on the surface. The adsorption can be through the central aromatic ring or side chain groups. It has been reported that the MB molecule may undergo molecular orientation on the activated carbon surface according to the hydrophilic/hydrophobic structure of the surface (Chalil Oglou et al., 2023).

In other words, the adsorption of the molecule on the surface occurred at a certain angle depending on the number of adsorbed molecules per unit area. As the interest of the molecule to be adsorbed to the surface increases, a more regular stacking may occur.

The MB adsorption performances of the activated carbons produced within the scope of the study were compared with the performances of activated carbons similarly produced from the waste fabric and reported in Table 3. There are not many studies on the MB adsorption of activated carbons produced from the waste fabrics in available literature. When the studies in Table 3 are compared, it is seen that the highest adsorption performance was achieved with this study. All the samples performed better than the results obtained in previously published studies. It is known that the type of activation chemical used affects the activated carbon surface properties. It is thought that activated carbon produced from cotton waste fabric with KOH activation forms a more suitable surface chemistry for MB adsorption and higher adsorption performance is obtained.

**Table 2:** MB adsorption parameters of AC-400, AC-500 and AC-600.

Sample	Langmuir model			Freundlich model		
	$q_m$ , mg/g	$k_L$ , L/mg	$R^2$	$n$	$k_F$ , $\text{mg}^{1-1/n}\text{L}^{1/n}/\text{g}$	$R^2$
AC-400	531.46	4.108	0.992	8.27	300	0.927
AC-500	630.26	1.593	0.951	7.39	328.9	0.878
AC-600	655.40	6.245	0.870	22.06	530.1	0.874

**Table 3:** Comparison of MB adsorption performance of activated carbons produced from textile wastes.

Raw material	Activation agent	Surface area, $\text{m}^2/\text{g}$	Adsorption capacity, mg/g	Reference
PET fabric	-	846	163.9	(Li et al., 2020)
Acrylic fabric	Vapour	2400	300	(You et al., 2000)
Polyester fabric	$\text{FeCl}_3$ , $\text{FeCl}_2$ , $\text{FeSO}_4$	1415 - 1393 - 382	445.51 - 450.23 - 149.12	(Xu et al., 2019)
Polyester fabric	$\text{ZnCl}_2$	1101.5	504	(Yu et al., 2018)
Cotton fabric	KOH	1385 - 1583 - 1276	531.46 - 630.26 - 655.40	This study

#### 4. CONCLUSION

It was aimed to produce activated carbon samples to be tested in MB adsorption using waste shirt with 100% cotton content. To examine how the change in activated carbon surface properties will affect methylene blue adsorption, the pre-carbonisation temperature was changed during the production process. Activated carbons with three different surfaces were successfully produced by applying three different pre-carbonisation temperatures, and the differences in surface properties were revealed by characterisation studies. The produced activated carbon samples have suitable surface area and pore volume values for MB adsorption. The highest surface area and pore volume values were found in the AC-500 sample. However, the adsorption experiments showed that there was a strong relationship

between the activated carbon surface chemical properties and MB adsorption. As the pre-carbonisation temperature increased, a more hydrophobic surface was obtained, and MB was adsorbed more on the activated carbon sample (AC-600). Although AC-600 has 24% lower surface area, it has the most suitable surface property for the MB adsorption. The high performance of this sample was associated with the adsorption of more dye molecules per unit surface area. When the findings obtained were compared with the studies in periodicals, it was revealed that the highest methylene blue adsorption performance was achieved in this study.

#### 5. REFERENCES

Ambashta, R. D., & Sillanpää, M. (2010). Water purification using magnetic assistance: A review.

- Journal of Hazardous Materials*, 180(1-3), 38-49. <https://doi.org/10.1016/j.jhazmat.2010.04.105>
- Avcı, A., İnci, İ., & Baylan, N. (2020). Adsorption of ciprofloxacin hydrochloride on multiwall carbon nanotube. *Journal of Molecular Structure*, 1206, 127711. <https://doi.org/10.1016/j.molstruc.2020.127711>
- Ayranpınar, İ., Duyar, A., Göçer, S., Kozak, M., Köroğlu, E. O., & Cırık, K. (2023). Demir (II, III) Oksit (Fe<sub>3</sub>O<sub>4</sub>) Nanopartiküller Kullanılarak Tekstil Atıklarının Arıtılması. *Kahramanmaraş Sütçü İmam Üniversitesi Mühendislik Bilimleri Dergisi*, 26(1), 1-7. <https://doi.org/10.17780/ksujes.1142242>
- Barbero-Barrera, M. del M., Pombo, O., & Navacerrada, M. de los Á. (2016). Textile fibre waste bindered with natural hydraulic lime. *Composites Part B: Engineering*, 94, 26-33. <https://doi.org/10.1016/j.compositesb.2016.03.013>
- Bentchikou, L., Mechelouf, F. Z., Neggaz, F., & Mellah, A. (2017). REMOVAL OF HEXAVALENT CHROMIUM FROM WATER BY USING NATURAL BROWN CLAY. *Journal of the Turkish Chemical Society Section B: Chemical Engineering*, 2, 43-52.
- Bushra, R., Mohamad, S., Alias, Y., Jin, Y., & Ahmad, M. (2021). Current approaches and methodologies to explore the perceptive adsorption mechanism of dyes on low-cost agricultural waste: A review. *Microporous and Mesoporous Materials*, 319, 111040. <https://doi.org/10.1016/j.micromeso.2021.111040>
- Cao, H., Cobb, K., Yatvitskiy, M., Wolfe, M., & Shen, H. (2022). Textile and Product Development from End-of-Use Cotton Apparel: A Study to Reclaim Value from Waste. *Sustainability*, 14(14), 8553. <https://doi.org/10.3390/su14148553>
- Chai, W. S., Cheun, J. Y., Kumar, P. S., Mubashir, M., Majeed, Z., Banat, F., Ho, S.-H., & Show, P. L. (2021). A review on conventional and novel materials towards heavy metal adsorption in wastewater treatment application. *Journal of Cleaner Production*, 296, 126589. <https://doi.org/10.1016/j.jclepro.2021.126589>
- Chalil Oglou, R., Gokce, Y., Yagmur, E., & Aktas, Z. (2023). Production of demineralised high quality hierarchical activated carbon from lignite and determination of adsorption performance using methylene blue and p-nitrophenol: The role of surface functionality, accessible pore size and surface area. *Journal of Environmental Management*, 345, 118812. <https://doi.org/10.1016/j.jenvman.2023.118812>
- Darama, S. E., Mesci Oktay, B., & Çoruh, S. (2022). Investigation of the use of walnut shells as a natural biosorbent for zinc removal. *Kahramanmaraş Sütçü İmam Üniversitesi Mühendislik Bilimleri Dergisi*, 25(4), 556-564. <https://doi.org/10.17780/ksujes.1126719>
- Daud, W. M. A. W., & Ali, W. S. W. (2004). Comparison on pore development of activated carbon produced from palm shell and coconut shell. *Bioresource Technology*, 93(1), 63-69. <https://doi.org/10.1016/j.biortech.2003.09.015>
- Eder, S., Müller, K., Azzari, P., Arcifa, A., Peydayesh, M., & Nyström, L. (2021). Mass Transfer Mechanism and Equilibrium Modelling of Hydroxytyrosol Adsorption on Olive Pit-Derived Activated Carbon. *Chemical Engineering Journal*, 404, 126519. <https://doi.org/10.1016/j.cej.2020.126519>
- Freundlich, H. (1906). Adsorption in solution. *Phys Chem Soc*, 40, 1361-1368.
- Gayathiri, M., Pulingam, T., Lee, K. T., & Sudesh, K. (2022). Activated carbon from biomass waste precursors: Factors affecting production and adsorption mechanism. *Chemosphere*, 294, 133764. <https://doi.org/10.1016/j.chemosphere.2022.133764>
- Gokce, Y., & Aktas, Z. (2014). Nitric acid modification of activated carbon produced from waste tea and adsorption of methylene blue and phenol. *Applied Surface Science*, 313, 352-359. <https://doi.org/10.1016/j.apsusc.2014.05.214>
- Gokce, Y., Yaglikci, S., Yagmur, E., Banford, A., & Aktas, Z. (2021). Adsorption behaviour of high performance activated carbon from demineralised low rank coal (Rawdon) for methylene blue and phenol. *Journal of Environmental Chemical Engineering*, 9(2), 104819. <https://doi.org/10.1016/j.jece.2020.104819>
- Gürten İnal, İ. İ., Gökçe, Y., Yağmur, E., & Aktaş, Z. (2020). Nitrik asit ile modifiye edilmiş biyokütle temelli aktif karbonun süperkapasitör performansının incelenmesi. *Gazi Üniversitesi Mühendislik Mimarlık Fakültesi Dergisi*, 35(3), 1243-1256. <https://doi.org/10.17341/gazimmfd.425990>
- Gurten Inal, İ. İ., Holmes, S. M., Yagmur, E., Ermumcu, N., Banford, A., & Aktas, Z. (2018). The supercapacitor performance of hierarchical porous activated carbon electrodes synthesised from demineralised (waste) cumin plant by microwave pretreatment. *Journal of Industrial and Engineering Chemistry*, 61, 124-132. <https://doi.org/10.1016/j.jiec.2017.12.009>
- Jeihanipour, A., Aslanzadeh, S., Rajendran, K., Balasubramanian, G., & Taherzadeh, M. J. (2013). High-rate biogas production from waste textiles using a two-stage process. *Renewable Energy*, 52, 128-135. <https://doi.org/10.1016/j.renene.2012.10.042>
- Juanga-Labayen, J. P., Labayen, I. V., & Yuan, Q. (2022). A Review on Textile Recycling Practices and Challenges. *Textiles*, 2(1), 174-188. <https://doi.org/10.3390/textiles2010010>
- Langmuir, I. (1918). The adsorption of gases on plane surfaces of glass, mica and platinum. *Journal of the American Chemical Society*, 40(9), 1361-1403.
- Li, M., Lu, J., Li, X., Ge, M., & Li, Y. (2020). Removal of disperse dye from alcoholysis products of waste PET fabrics by nitric acid-modified activated carbon as an adsorbent: Kinetic and thermodynamic studies. *Textile Research Journal*, 90(17-18), 2058-2069. <https://doi.org/10.1177/0040517520909510>
- Liu, Q.-S., Zheng, T., Li, N., Wang, P., & Abulikemu, G. (2010). Modification of bamboo-based activated carbon using microwave radiation and its effects on the adsorption of methylene blue. *Applied Surface Science*, 256(10), 3309-3315. <https://doi.org/10.1016/j.apsusc.2009.12.025>
- Ozpinar, P., Dogan, C., Demiral, H., Morali, U., Erol, S., Samdan, C., Yildiz, D., & Demiral, I. (2022). Activated carbons prepared from hazelnut shell waste by phosphoric acid activation for supercapacitor electrode applications and comprehensive electrochemical analysis. *Renewable Energy*, 189, 535-548. <https://doi.org/10.1016/j.renene.2022.02.126>
- Pais, J. C., Santos, C. R. G., & Lo Presti, D. (2022). Application of textile fibres from tire recycling in asphalt mixtures. *Road Materials and Pavement Design*, 23(10), 2353-2374. <https://doi.org/10.1080/14680629.2021.1972034>
- Rápó, E., & Tonk, S. (2021). Factors Affecting Synthetic Dye Adsorption; Desorption Studies: A Review of Results from the Last Five Years (2017-2021). *Molecules*, 26(17), 5419. <https://doi.org/10.3390/molecules26175419>
- Reike, D., Hekkert, M. P., & Negro, S. O. (2023). Understanding circular economy transitions: The

- case of circular textiles. *Business Strategy and the Environment*, 32(3), 1032–1058.  
<https://doi.org/10.1002/bse.3114>
- Shiklomanov, I. A. (2000). Appraisal and Assessment of World Water Resources. *Water International*, 25(1), 11–32.  
<https://doi.org/10.1080/02508060008686794>
- Shukla, A., Zhang, Y.-H., Dubey, P., Margrave, J. L., & Shukla, S. S. (2002). The role of sawdust in the removal of unwanted materials from water. *Journal of Hazardous Materials*, 95(1–2), 137–152.  
[https://doi.org/10.1016/S0304-3894\(02\)00089-4](https://doi.org/10.1016/S0304-3894(02)00089-4)
- Unnerstall, T. (2022). *Factfulness Sustainability*. Springer Berlin Heidelberg. <https://doi.org/10.1007/978-3-662-65558-0>
- Ütebay, B., Çelik, P., & Çay, A. (2020). *Waste in Textile and Leather Sectors* (A. Körlü, Ed.). IntechOpen. <https://doi.org/10.5772/intechopen.90014>
- Wang, C., Xiong, C., He, Y., Yang, C., Li, X., Zheng, J., & Wang, S. (2021). Facile preparation of magnetic Zr-MOF for adsorption of Pb(II) and Cr(VI) from water: Adsorption characteristics and mechanisms. *Chemical Engineering Journal*, 415, 128923. <https://doi.org/10.1016/j.cej.2021.128923>
- Wróbel-Iwaniec, I., Díez, N., & Gryglewicz, G. (2015). Chitosan-based highly activated carbons for hydrogen storage. *International Journal of Hydrogen Energy*, 40(17), 5788–5796.  
<https://doi.org/10.1016/j.ijhydene.2015.03.034>
- Xu, Z., Tian, D., Sun, Z., Zhang, D., Zhou, Y., Chen, W., & Deng, H. (2019). Highly porous activated carbon synthesized by pyrolysis of polyester fabric wastes with different iron salts: Pore development and adsorption behavior. *Colloids and Surfaces A: Physicochemical and Engineering Aspects*, 565, 180–187.  
<https://doi.org/10.1016/j.colsurfa.2019.01.007>
- Yaglikci, S., Gokce, Y., Yagmur, E., Banford, A., & Aktas, Z. (2021). Does high sulphur coal have the potential to produce high performance - low cost supercapacitors? *Surfaces and Interfaces*, 22, 100899.  
<https://doi.org/10.1016/j.surfin.2020.100899>
- Yang, W., & Cao, M. (2022). Study on the difference in adsorption performance of graphene oxide and carboxylated graphene oxide for Cu(II), Pb(II) respectively and mechanism analysis. *Diamond and Related Materials*, 129, 109332.  
<https://doi.org/10.1016/j.diamond.2022.109332>
- You, S. Y., Park, Y. H., & Park, C. R. (2000). Preparation and properties of activated carbon fabric from acrylic fabric waste. *Carbon*, 38(10), 1453–1460.  
[https://doi.org/10.1016/S0008-6223\(99\)00278-X](https://doi.org/10.1016/S0008-6223(99)00278-X)
- Yu, X., Wang, S., & Zhang, J. (2018). Preparation of high adsorption performance activated carbon by pyrolysis of waste polyester fabric. *Journal of Materials Science*, 53(7), 5458–5466.  
<https://doi.org/10.1007/s10853-017-1928-2>



## Synthesis and Investigation of Thermal and Dynamic Mechanical Properties of Urethane-Containing Epoxy Resins

Orçun YÜKSEL , Eren YILDIRIM , Oğuz YÜCEL , Serkan EMİK\* 

Istanbul University-Cerrahpaşa Chemical Engineering Department, Istanbul, 34320, TURKEY

**Abstract:** This study aims to improve the thermal and mechanical properties of epoxy-based materials. For this purpose, the structure of epoxy resins was changed by chemical modification and epoxy resin containing urethane was synthesized. The synthesized resin was blended with commercial epoxy resin at the ratios of 25%, 50%, 75% by weight and hardened by curing. The thermal and mechanical properties of urethane-containing epoxy materials prepared in different proportions were compared with those produced from commercial epoxy resin. The structural characterization of the prepared materials was investigated by Fourier Transform Infrared Spectroscopy (FTIR) analysis, their thermal behavior was investigated by Thermogravimetric Analysis (TGA), and their mechanical properties were investigated by Dynamic Mechanical Analysis (DMA). TGA and DMA analyses of the materials showed that the presence of urethane in the structure of epoxy resins significantly changed the mechanical and thermal properties. It was observed that the storage and loss modulus values of urethane-containing resins increased approximately 2.5 times compared to commercial epoxy resins, and a decrease of approximately 10% in thermal degradation temperatures was observed.

**Keywords:** Epoxy, Urethane, FTIR, TGA, DMA.

**Submitted:** June 04, 2023. **Accepted:** September 26, 2023.

**Cite this:** Yüksel, O., Yıldırım, E., Yücel, O., & Emik, S. (2023). Synthesis and Investigation of Thermal and Dynamic Mechanical Properties of Urethane-Containing Epoxy Resins. *Journal of the Turkish Chemical Society, Section B: Chemical Engineering*, 6(2), 95-106. <https://doi.org/10.58692/jotcsb.1309480>.

\*Corresponding author. E-mail: [serkan.emik@iuc.edu.tr](mailto:serkan.emik@iuc.edu.tr)

### 1. INTRODUCTION

Epoxy resins, an essential and widely used class of thermosetting polymers, are used in various fields such as electrical and structural applications, surface protective coating applications because they have desirable properties such as chemical resistance, mechanical and thermal properties, low shrinkage after curing, and insulation properties (DAG, 2023; Paul Swaraj, 1995). They contain one or more 1,2 oxirane groups in their structure and can be converted into thermoset form or three-dimensional network structure (Ellis, 1993; Stefani et al., 2001). Although the commercial production of epoxy resins began in the late 1930s, and there are different types of epoxy resins today, these materials still suffer from some disadvantages, such as considerable internal stress, brittleness, flammability, low degradability, little impact resistance, and high moisture absorption (Akovali, 2001; Ellis, 1993). In order to improve the toughness of epoxy resins, several techniques are employed, i.e., improvement of the flexibility of the

cured epoxy resins (Jin et al., 2015; Jin & Park, 2008; May, 2018).

The importance of using epoxy resins in various fields is due to the easy conversion of this resin to high molecular weight materials by curing reactions. The prepolymers containing two epoxide end groups are cured with suitable curing agents to give cross-linked networks (Kricheldorf, Hans R.; Nuyken, Oskar; Swift, 2004). Increasing the toughness of epoxy resins by improving their flexibility may be done by two general procedures: I) Introduction of a toughening agent into the epoxy network or II) chemical modification of the epoxy structure. In the case of using toughening agents, liquid elastomers (Kunz & Beaumont, 1981; Levita et al., 1985), thermoplastics (Huang et al., 1997; Yang & Gu, 2009), interpenetrating polymer networks (Anand Prabu & Alagar, 2004; K. H. Hsieh et al., 2001; Prabu & Alagar, 2004), rigid phase (T. H. Hsieh et al., 2010), and inorganic particles, which may cause deterioration of the final properties, are commonly used (Demčenko et al., 2014; Jiang et al., 2012; Jin & Park, 2008). Thus, a

chemical modification of the epoxy can improve the overall physical properties. Besides several chemical modifications of epoxy prepolymers with epoxy-terminated liquid polybutadiene (Barcia et al., 2003), polytriazolesulfone (Lee et al., 2019), carboxyl-terminated butadiene acrylonitrile copolymer and hydroxyl-terminated polybutadiene (Ramos et al., 2005), incorporation of a urethane group into the main chain, e.g. urethane coupling containing modified propylene carbonate (Wazarkar et al., 2016), isocyanate-capped polydimethylsiloxane (HTPDMS) prepolymer (Rath et al., 2009), polymethylene polyphenylene isocyanate (Chen et al., 2018), blocked isocyanate prepolymers (Kirillov, 2014) hyperbranched polyester-toluene diisocyanate (Dhevi et al., 2014) is easy and popular route to achieve enhanced physical properties (i.e. high flexibility, toughness).

In this study, a urethane-containing epoxy resin was successfully synthesized and blended with a commercial epoxy resin at 25, 50, and 75% ratios by weight and cured. The chemical, mechanical, and thermal properties of urethane-containing epoxy materials were investigated by Fourier Transform Infrared Spectroscopy (FTIR), dynamic mechanical analysis (DMA), thermogravimetric analysis (TGA), and differential scanning calorimetry (DSC) analyses.

## 2. EXPERIMENTAL SECTION

### 2.1. Materials

Bisphenol A (BPA), toluene 2,4 diisocyanate (TDI), epichlorohydrin (ECH), Triethylenetetra amine (TETA), and diazobicyclooctane (DABCO) were purchased from Sigma Aldrich Sigma Aldrich Co., (USA). Commercial Epoxy Resin (CER) (epoxy equivalent weight 185–190 g/mol) was supplied from Dow Chemical Company (USA). The rest of the materials were of analytical grade and purchased from Merck, Germany.

### 2.2. Synthesis of Urethane Containing Epoxy Resin

BPA-based epoxy resin containing urethane bonds was synthesized in two steps. In the first step, an intermediate product was obtained by the reaction of BFA and TDI. The second stage was completed with the intermediate and ECH condensation reaction.

In the first step, 0.375 moles (85.5 g) of BFA and 75 mL of acetone were placed in a three-neck reactor. The BFA was mixed in a mechanical heater stirrer at 50 °C until dissolved. After the complete dissolution of the BFA, 0.093 mol (13.49 mL) of TDI was added to the reactor in the presence of 1.01 g

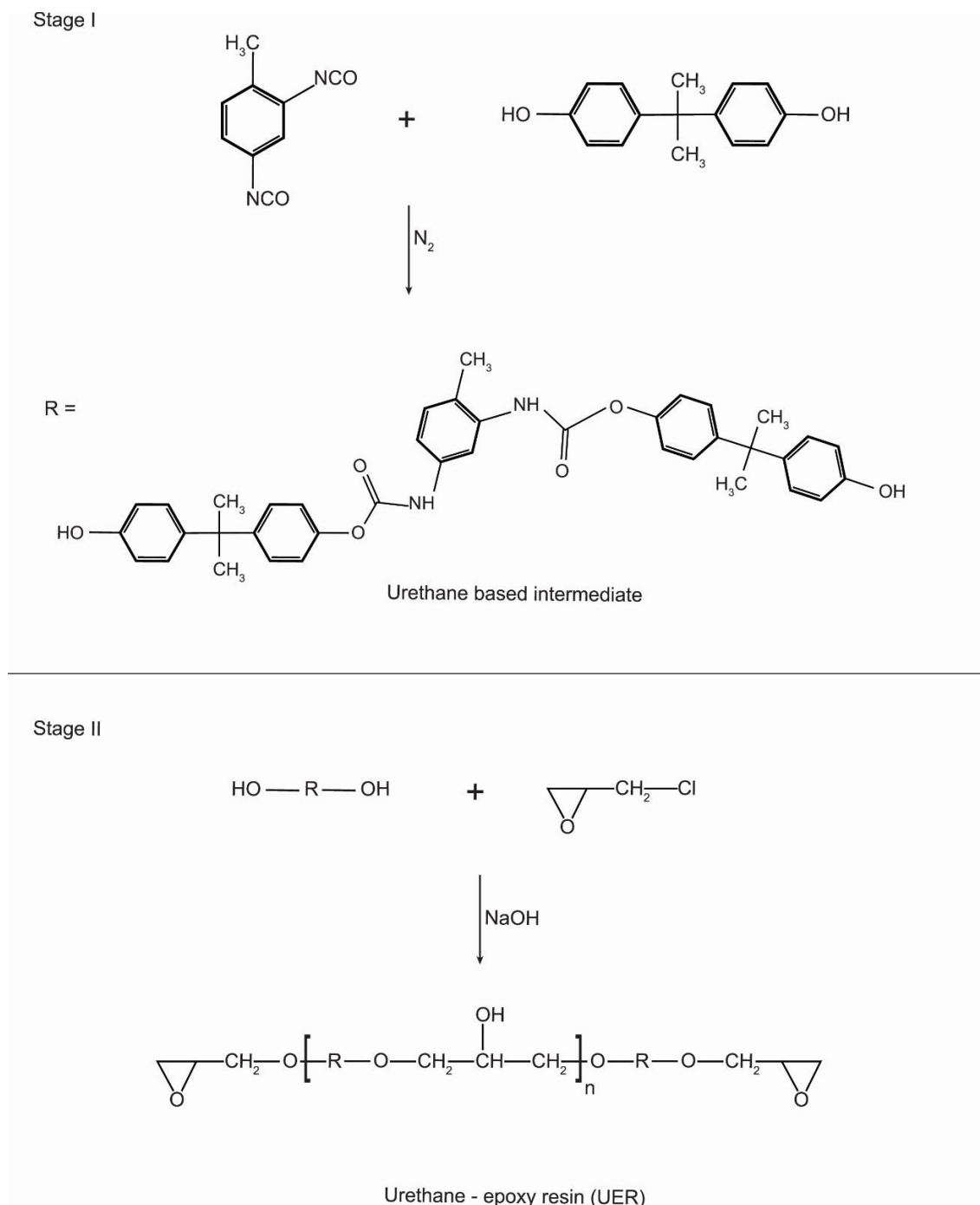
of catalyst (DABCO). The reaction was carried out at 80 °C under reflux. FTIR samples were taken every 15 minutes of the reaction, and the presence of isocyanate in the medium was monitored. At the end of 1 hour, the reaction was terminated, and the acetone in the reaction medium was removed under vacuum with a rotary evaporator device. The obtained product was yellow and viscous liquid.

In the second stage, the intermediate product and ECH (5 eq) were loaded into the reactor, and 40% NaOH solution was added dropwise with the help of a dropping funnel while the temperature was increasing to 100 °C. The reaction was continued for 3 hours at this temperature. Afterwards, the product was cooled to room temperature, dissolved in xylene as 1:1 (v:v) and taken into a separator funnel. After 2-3 minutes, the water phase formed in the lower part was separated and discarded. Another 50 mL portion of distilled water was added to the xylene organic phase, and phases were separated again. This process was repeated for 3-4 times. Finally, the organic solvent phase was removed with a rotary evaporator and light yellow viscous "urethane-containing epoxy resin" (UER) was obtained. The schematic representation of the whole reaction is given in Figure 1.

### 2.3. Sample preparation and Characterization

#### 2.3.1. Preparation of urethane-containing epoxy-based materials

The preparation of urethane-containing epoxy-based materials was carried out in two stages. In the first stage, the synthesized UER resin and CER were blended in specific proportions with weight (25%; 25UER), 50%; 50UER, and 75%; 75UER). Then, according to epoxy equivalent weight (EEW), which was determined using the dioxane-hydrochloric acid method described elsewhere (Basnet et al., 2015), they were mixed with stoichiometric amounts of curing agent (TETA). In the second stage, the mixtures were poured into rectangular Teflon moulds of 10×10×0.5 mm and allowed to be cured at room temperature for 24 hours. Cured materials were post-cured to increase the cross-link density and complete the curing reactions. Post curing process was carried out by keeping the materials in an oven at 150 °C for 3 hours. In order to make a comparative interpretation, samples containing pure UER and CER were prepared by the same procedure. Their sample codes were given as UER and CER, respectively. In addition, "-RC" and "-C" abbreviations were added to the end of the room temperature cured and post-cured sample codes, respectively. Sample codes, their UER, CER contents, EEW values, and amounts of TETA added for curing are given in Table 1.

**Figure 1:** Schematic representation of the synthesis of UER.**Table 1:** Sample contents and codes.

Resin Code	CER (g)	UER (g)	EEW	TETA(g)	Room temperature cured sample	Post-cured sample code
UER	--	3	442	0.58	UER-RC	UER-C
75UER	1.2	3.6	338	0.19	75UER-RC	75UER-C
50UER	2	2	272	0.40	50UER-RC	50UER-C
25UER	3	1	228	0.41	25UER-RC	25UER-C
CER	4	--	195	0.49	CER-RC	CER-C

### 2.3.2. Characterizations

The chemical structures of the synthesized products were elucidated with Agilent Technologies brand Cary 630 model Fourier Transform Infrared Spectrophotometer (FT-IR).

**Thermal Gravimetric Analysis (TGA)** Thermal analyses of the obtained products were carried out with Linsesis brand STA P 750 TGA model Thermal Gravimetric Analyzer. TGA studies were performed with approximately 20 mg samples under an air atmosphere by heating from room temperature to 800 °C with a heating rate of 10 °C/min. The temperatures at which the products first begin to decompose (IDT) and at which 5%, 10%, 25%, and 50% weight losses occur were determined.

**Dynamic Mechanical Analysis (DMA)** studies were performed with the Seiko brand Extar 6000 model instrument. For the tests, post-cured rectangular cross-section samples of 10x10x0.5 mm were used. DMA tests are performed under a nitrogen atmosphere at 1 Hz oscillation frequency, in the

20-150 °C temperature range with 3°C/min heating rate. The storage module and loss module of the prepared products were determined.

## 3. RESULTS AND DISCUSSION

### 3.1. FT-IR Analyses

The progress of the first step reaction in the synthesis of urethane-containing epoxy resins was followed by FTIR analyses. The presence of isocyanate groups was monitored by taking samples from the reaction medium every 15 minutes, and the obtained FT-IR spectra were given in Figure 2. As seen, the intensity of the characteristic peak of the isocyanate groups at 2270  $\text{cm}^{-1}$  decreases over time. It disappears after 60 minutes, while a new peak is observed in the 1700  $\text{cm}^{-1}$  region depending on the formation of the urethane bond (Socrates, 2001). These findings indicate that the intermediate, whose chemical structure is given in Figure 1, was successfully synthesized.

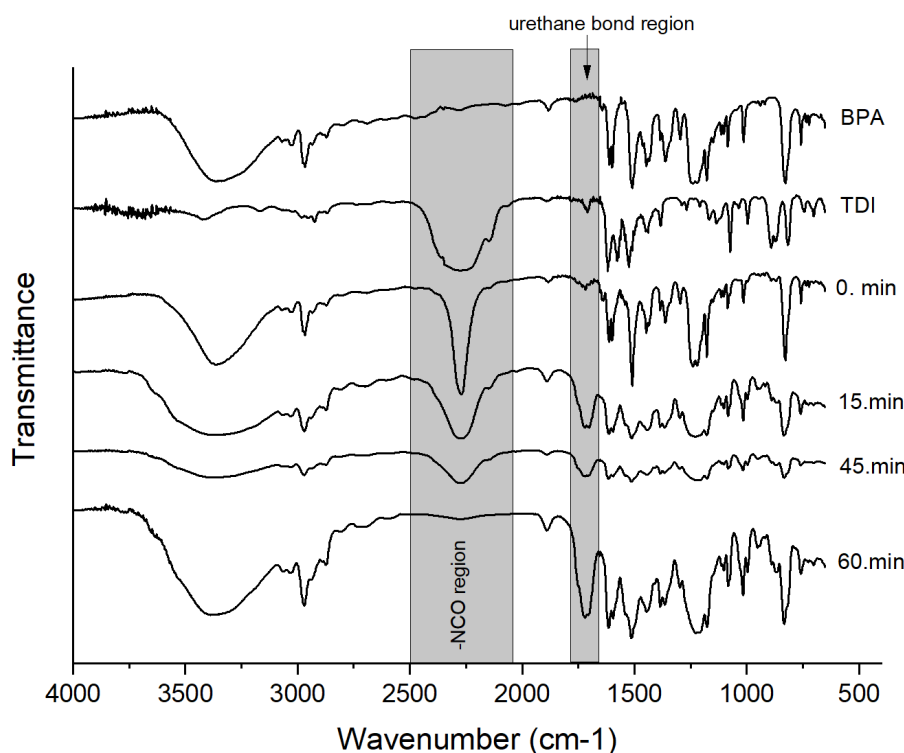


**Figure 2:** The variation of the isocyanate IR peak during the reaction and the FT-IR spectrum of the intermediate.

FTIR spectra of CER and synthesized UER are given in Figure 3. The peak at 912  $\text{cm}^{-1}$  confirms the presence of the epoxide functionality in both resins. In addition, the peak at 1700  $\text{cm}^{-1}$  region shows the urethane bond functionality in UER. Furthermore, in the spectrum of UER, the intensity of the widespread peak due to -OH bonds in the 3300  $\text{cm}^{-1}$  region also increases. This interesting finding indicates that the molecular weight increases during the synthesis of urethane-epoxy

resin. As a matter of fact, when the EEW values given in Table 1 are examined, it is seen that the EEW value of UER is 442, which indicates that the molecular weight of the resin is higher than that of CER. As the molecular weight of epoxy-based resins increases, the number of -OH groups in the structure increases due to the repeating unit. Thus, it is an expected result that the intensity of the -OH characteristic band increases in the FTIR spectrum. These findings indicate that the UER, whose



chemical structure is given in Fig. 1, was successfully synthesized.

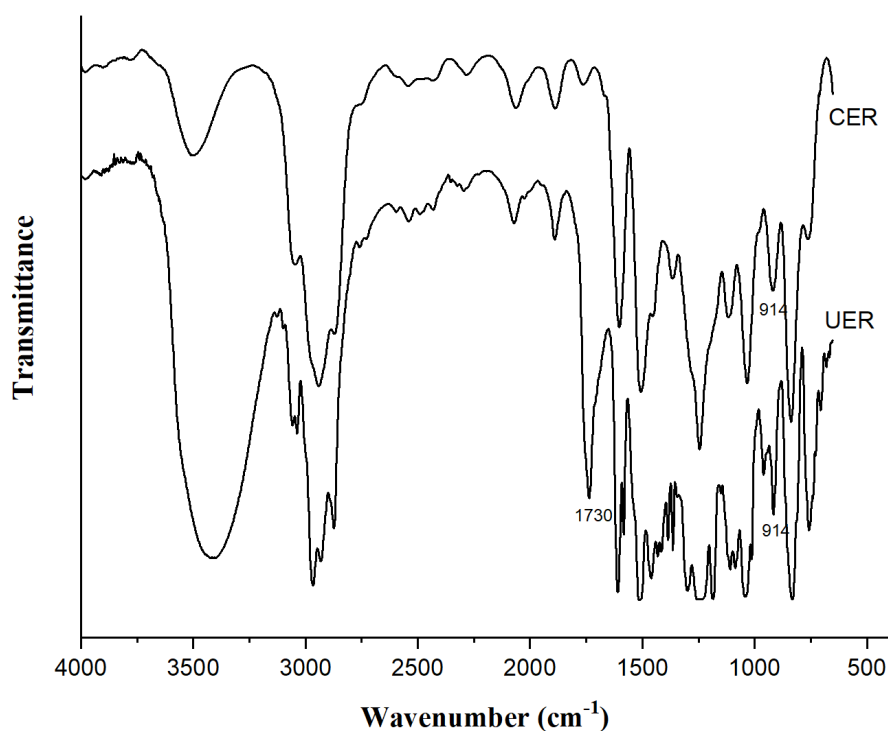


**Figure 3:** The FT-IR spectrum of commercial epoxy resin (CER) and urethane-epoxy resin (UER).

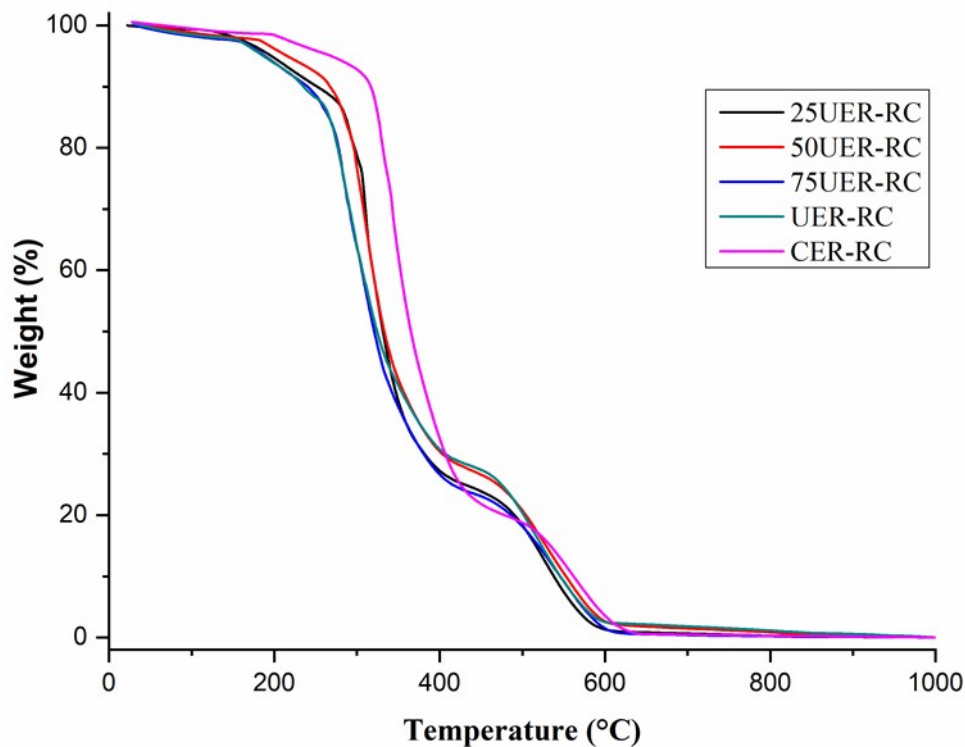
### 3.2. Thermal Analysis

In order to examine the thermal-oxidative degradation properties of the room-temperature cured and post-cured urethane-epoxy materials, TGA studies were performed, and the results were illustrated in Figure 4 and 5. In addition, the

temperatures at which the products begin to decompose (initial decomposition temperature; IDT) and the temperatures at which 5%, 10%, 25%, and 50% weight losses occur were listed in Table 2 and 3.

**Table 2:** Thermal-oxidative degradation behavior of room temperature cured compositions.

Sample	IDT (°C)	T <sub>(5)</sub> (°C)	T <sub>(10)</sub> (°C)	T <sub>(25)</sub> (°C)	T <sub>(50)</sub> (°C)
UER	165	211	252	286	326
75UER	163	215	255	286	323
50UER	184	245	276	304	334
25UER	126	205	261	307	332
CER	196	289	319	339	366

**Figure 4:** TGA curves of room temperature cured materials with different compositions.

According to the TGA results of the room temperature cured materials prepared in different compositions given in Figure 3 and Table 2, it is seen that the first weight losses of room temperature cured urethane-containing epoxy materials (UER-RC group) started at approximately 250 °C. The thermal behavior of CER-RC differs

from other UER-RC groups. For example, while the first degradation temperature of CER-RC occurs at 196 °C, this value is determined as 126 °C in 25UER-RC. In addition, while 5% weight loss of CER-RC occurs at 289 °C, approximately 25% weight loss is observed in the UER-RC group at this temperature.

**Table 3:** Thermal-oxidative degradation behavior of post-cured compositions.

Sample	IDT (°C)	T <sub>(5)</sub> (°C)	T <sub>(10)</sub> (°C)	T <sub>(25)</sub> (°C)	T <sub>(50)</sub> (°C)
UER-RC	267	275	281	300	342
75UER-RC	235	258	274	293	332
50UER-RC	254	274	286	308	341
25UER-RC	257	281	291	312	337
CER-RC	310	323	330	347	381

TGA results of post-cured materials with different compositions are given in Figure 5 and Table 3. As it is seen, after the post-curing process, the IDT for CER-C is determined as 310 °C and a significant increase in thermal oxidative resistance is observed for all materials. In the case of post-cured urethane-containing epoxy materials (UER-C group), the IDT values increase and are around 250 °C for the whole UER-C group. These IDT values are

70-130 °C higher than their room temperature-cured counterparts. In conclusion, due to the increased amount of cross-linking by the post-curing process, significant increases are observed in the thermal stability of all materials. The temperature values at which 10% weight loss occurs, an essential value for commercial applications, are determined as 330 °C for CER-C and between 280-290 °C for the UER-C group.

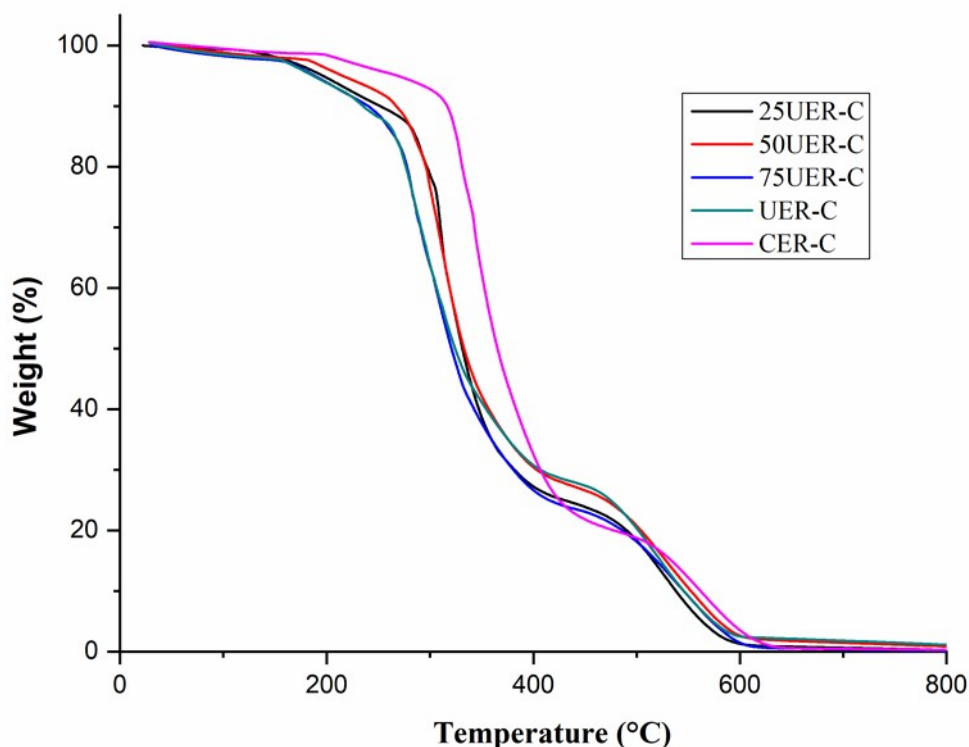


**Figure 5:** TGA curves of post-cured materials with different compositions.

### 3.3. Dynamic Mechanic Analysis

The dynamic mechanical analysis (DMA) test results of the epoxy-based materials, elastic modulus - temperature, storage modulus - temperature, and  $\tan \delta$  - temperature curves are shown in Figures 6-8, and the obtained data are listed in Table 4. In DMA curves, the response of a viscoelastic material to an applied force, energy, is divided into two terms: elastic response and viscose (dissipation) response. While the pure elastic response is considered a reversible deformation, the viscose is considered energy dissipation due to movement (segmental in solid-state), friction between molecules and the heat generated by such mechanisms. The calculated  $\tan \delta$  value is a very useful indicator for a material's glass transition temperature ( $T_g$ ). In addition, its height indicates the material is viscose (large  $\tan \delta$ ) or elastic (small  $\tan \delta$ ) under the given condition.

As it is seen from Figures 6-8 and Table 4, the storage modulus value of CER-C is low, and a significant increase is observed when it is blended with urethane-containing epoxy resin. In the case of the UER-C group, it is determined that the storage modulus value of UER-C is approximately 2.5 times that of CER-C, and there is a significant increase in the values of other resins containing urethane in different ratios, 25, 50 and 75 UER-C.

When the lost modulus values are compared, a significant increase is observed in the modulus values of the UER-C group compared to the CER-C. This case is probably observed due to the presence of urethane in the structure of epoxy resins, increasing the viscoelastic properties of these materials.

When the  $\tan \delta$  temperature values of the prepared materials are compared, as the amount of resin containing urethane increases, it is seen that the  $\tan \delta$  temperature values shift to the

higher region compared to the CER-C. This situation is interpreted as an increase in the  $\alpha$  transition temperatures of the prepared materials, in other words,  $T_g$ , depending on the increase in the cross-link densities of the materials with the post-curing process. This change, which occurs due

to the restriction of molecular mobility due to the increase in cross-link density, is an expected situation, and the observed temperature values are also consistent with previous similar studies (Garcia et al., 2007).

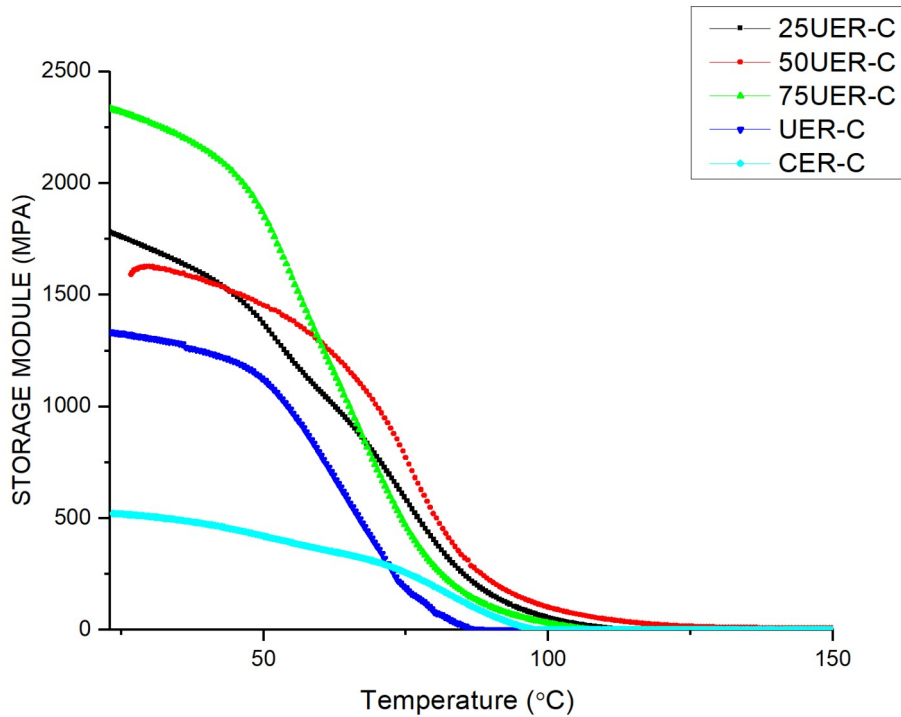


**Figure 6:** Store modulus-temperature curves of the post-cured materials with different compositions.

**Table 4:** Storage modulus, loss modulus, and  $\tan \delta$  values of post-cured materials.

Sample Code	Storage modulus (MPa)	Loss modulus (MPa)	Tan $\delta$ temp. (°C)
UER-C	1329	1412	90.5
75UER-C	2337	2188	110
50UER-C	1652	1483	113
25UER-C	1810	1474	117
CER-C	520	398	99

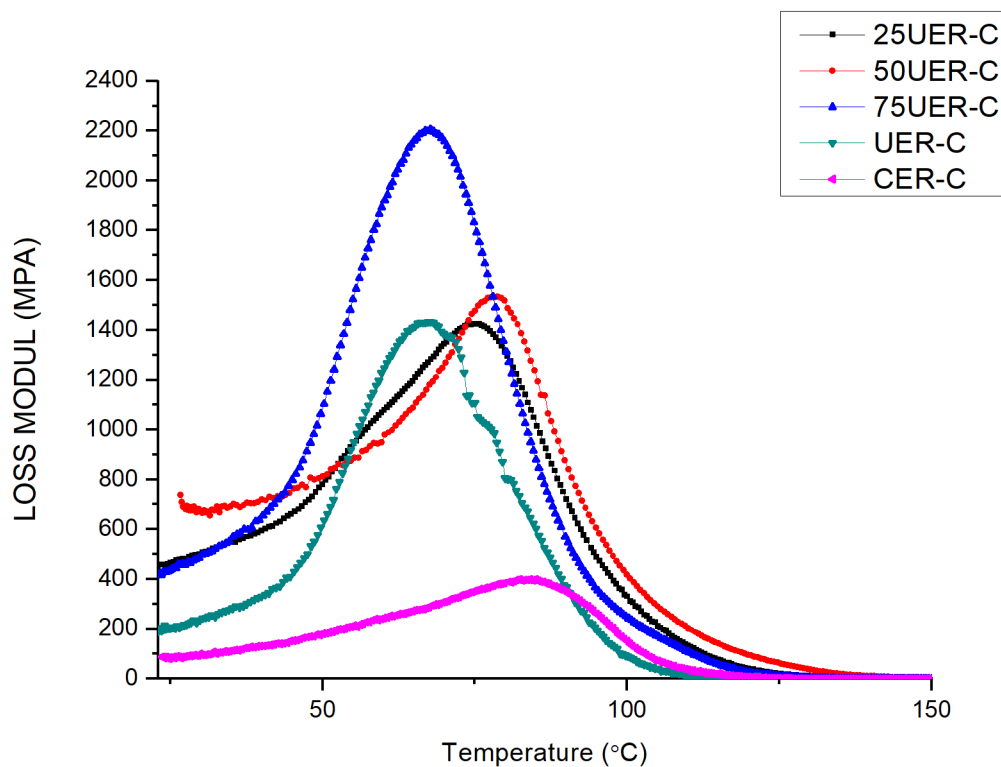


**Figure 7:** Loss modulus-temperature curves of the post-cured materials with different compositions.

Another interesting result determined in DMA studies is the intensity of the  $\tan \delta$  curve: All UER-C groups except for 25UER-C show a more intense peak than the CER-C without following any sequence. Since the peak intensity in the  $\tan \delta$  curves is a measure of the total amount of energy that a material can absorb, the large area (and/or

the intense peak) under the  $\tan \delta$  curve indicates a significant degree of molecular mobility that translates to better-damping properties (Zhou et al., 2018). That means that the material can better absorb and dissipate energy. For this reason, it is concluded that the UER-C group have better damping properties than that of CER-C.

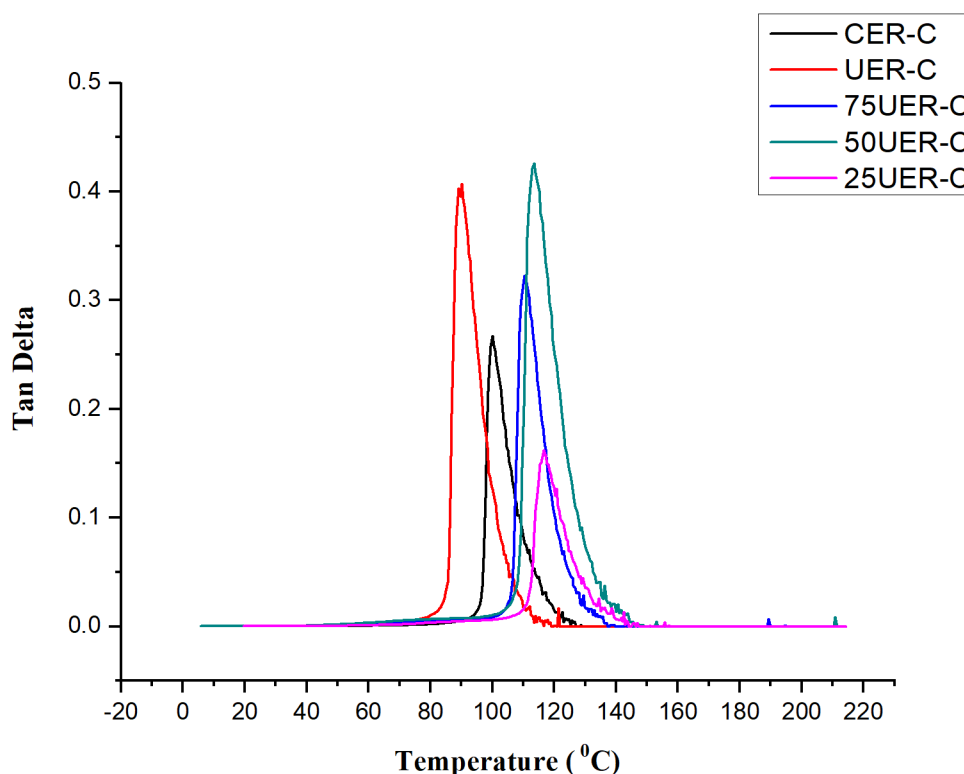


**Figure 8:** Tan delta-temperature curves of the post-cured materials with different compositions.

#### 4. CONCLUSION

Modified epoxy resins with reduced brittleness and high thermal stability benefit many commercial applications today. According to the results of TGA studies, the modified epoxy resins obtained with the modifications carried out in this study exhibited higher thermal stability than the modified commercial resins. In addition, the DMA analysis determined that the storage modulus of UER-C was approximately 2.5 times that of CER-C, and similarly, 25, 50 and 75 UER-C have significantly higher storage modulus than CER-C. The same applies to loss modulus properties. In the case of  $\tan \delta$  data, it is determined that all UER-C compositions have significantly high  $\tan \delta$  values, which indicate that these materials can better absorb and dissipate energy, so the UER-C group have better-damping properties than that of CER-C. However, in the study, it was determined that the curing process performed with TETA at room temperature was insufficient; thus, a post-curing process procedure was optimized with DSC analyses (results not given) at 150 °C for two hours.

In conclusion, it has been determined that significant improvements can be achieved, especially in terms of damping properties, of the products obtained by incorporating urethane bonds into the epoxy main structure. In future studies, helpful studies can be carried out to produce products with improved damping properties, an essential area for materials science, by working on the ideal curing process of these compositions and similar ones.

#### 5. CONFLICT OF INTEREST

The authors declare no conflict of interest.

#### 6. ACKNOWLEDGMENTS

The authors would like to thank Prof. Dr. Ali Durmuş and Assoc. Prof. Dr. Alper Kaşgöz for their assistance in DMA analysis.

This study was funded by Scientific Research Projects Coordination Unit of Istanbul University-Cerrahpasa. Project number:56922.

#### 7. REFERENCES

- Akovali, G. (2001). Handbook of Composite Fabrication. Smithers Rapra Publishing. <https://books.google.com.tr/books?id=klcCAAACAAJ>
- Anand Prabu, A., & Alagar, M. (2004). Mechanical and electrical studies of silicone modified polyurethane-epoxy intercrosslinked networks. *Polymer Journal*, 36(10), 848-855. <https://doi.org/10.1295/polymj.36.848>
- Barcia, F. L., Amaral, T. P., & Soares, B. G. (2003). Synthesis and properties of epoxy resin modified with epoxy-terminated liquid polybutadiene. *Polymer*, 44(19), 5811-5819. [https://doi.org/10.1016/S0032-3861\(03\)00537-8](https://doi.org/10.1016/S0032-3861(03)00537-8)
- Basnet, S., Otsuka, M., Sasaki, C., Asada, C., & Nakamura, Y. (2015). Functionalization of the active ingredients of Japanese green tea (*Camellia sinensis*) for the synthesis of bio-based epoxy resin. *Industrial Crops and Products*, 73, 63-72. <https://doi.org/10.1016/j.indcrop.2015.03.091>

- Chen, K., Tian, C., Liang, S., Zhao, X., & Wang, X. (2018). Effect of stoichiometry on the thermal stability and flame retardation of polyisocyanurate foams modified with epoxy resin. *Polymer Degradation and Stability*, 150, 105-113. <https://doi.org/10.1016/j.polymdegradstab.2018.02.015>
- Dağ, M. (2023). Obtaining Diatomite Reinforced Epoxy Composite and Determination of Its Thermophysical Properties. *Journal of the Turkish Chemical Society Section B: Chemical Engineering*, 6(1), 9-16. <https://doi.org/10.58692/jotcsb.1174746>
- Demčenko, A., Koissin, V., & Korneev, V. A. (2014). Noncollinear wave mixing for measurement of dynamic processes in polymers: Physical ageing in thermoplastics and epoxy cure. *Ultrasonics*, 54(2), 684-693. <https://doi.org/10.1016/j.ultras.2013.09.011>
- Dhevi, D. M., Prabu, A. A., Kim, H., Pathak, M. (2014). Studies on the toughening of epoxy resin modified with varying hyperbranched polyester-toluene diisocyanate content. *Journal of Polymer Research*, 21, Art.no. 503, <https://doi.org/10.1007/s10965-014-0503-7>.
- Ellis, B. (Ed.). (1993). *Chemistry and Technology of Epoxy Resins*. Springer Netherlands. <https://doi.org/10.1007/978-94-011-2932-9>
- Garcia, F. G., Soares, B. G., Pita, V. J. R. R., Sánchez, R., & Rieumont, J. (2007). Mechanical properties of epoxy networks based on DGEBA and aliphatic amines. *Journal of Applied Polymer Science*, 106(3), 2047-2055. <https://doi.org/10.1002/app.24895>
- Hsieh, K. H., Han, J. L., Yu, C. T., & Fu, S. C. (2001). Graft interpenetrating polymer networks of urethane-modified bismaleimide and epoxy (I): Mechanical behavior and morphology. *Polymer*, 42(6), 2491-2500. [https://doi.org/10.1016/S0032-3861\(00\)00641-8](https://doi.org/10.1016/S0032-3861(00)00641-8)
- Hsieh, T. H., Kinloch, A. J., Masania, K., Sohn Lee, J., Taylor, A. C., & Sprenger, S. (2010). The toughness of epoxy polymers and fibre composites modified with rubber microparticles and silica nanoparticles. *Journal of Materials Science*, 45(5), 1193-1210. <https://doi.org/10.1007/s10853-009-4064-9>
- Huang, P., Zheng, S., Huang, J., Guo, Q., & Zhu, W. (1997). Miscibility and mechanical properties of epoxy resin/polysulfone blends. *Polymer*, 38(22), 5565-5571. [https://doi.org/10.1016/S0032-3861\(97\)00104-3](https://doi.org/10.1016/S0032-3861(97)00104-3)
- Jiang, W., Jin, F.-L., & Park, S.-J. (2012). Thermo-mechanical behaviors of epoxy resins reinforced with nano-Al<sub>2</sub>O<sub>3</sub> particles. *Journal of Industrial and Engineering Chemistry*, 18(2), 594-596. <https://doi.org/10.1016/j.jiec.2011.11.140>
- Jin, F.-L., Liu, H.-C., Yang, B., & Park, S.-J. (2015). Synthesis and thermal properties of urethane-containing epoxy resin. *Journal of Industrial and Engineering Chemistry*, 24, 20-23. <https://doi.org/10.1016/j.jiec.2014.10.006>
- Jin, F.-L., & Park, S.-J. (2008). Interfacial toughness properties of trifunctional epoxy resins/calcium carbonate nanocomposites. *Materials Science and Engineering: A*, 475(1-2), 190-193. <https://doi.org/10.1016/j.msea.2007.04.046>
- Kirillov, A. N. (2014). Epoxy-urethane binders based on the blocked isocyanate Desmocap 11. *Polymer Science Series D*, 7(1), 14-18. <https://doi.org/10.1134/S1995421214010079>
- Kricheldorf, H. R.; Nuyken, O.; Swift, G. (Ed.). (2004). *Handbook of Polymer Synthesis*. CRC Press.
- Kunz, S. C., & Beaumont, P. W. R. (1981). Low-temperature behaviour of epoxy-rubber particulate composites. *Journal of Materials Science*, 16(11), 3141-3152. <https://doi.org/10.1007/BF00540323>
- Lee, M., Kwon, W., Kwon, D., Lee, E., & Jeong, E. (2019). Fracture toughness of the novel in-situ polytriazolesulfone modified epoxy resin for carbon fiber/epoxy composites. *Journal of Industrial and Engineering Chemistry*, 77, 461-469. <https://doi.org/10.1016/j.jiec.2019.05.012>
- Levita, G., Marchetti, A., & Butta, E. (1985). Influence of the temperature of cure on the mechanical properties of ATBN/epoxy blends. *Polymer*, 26(7), 1110-1116. [https://doi.org/https://doi.org/10.1016/0032-3861\(85\)90238-1](https://doi.org/https://doi.org/10.1016/0032-3861(85)90238-1)
- May, C. (2018). *Epoxy resins: chemistry and technology*. Routledge.
- Paul Swaraj. (1995). *Surface Coatings Science Technology* (2nd ed.). Wiley.
- Prabu, A. A., & Alagar, M. (2004). Mechanical and thermal studies of intercross-linked networks based on siliconized polyurethane-epoxy/unsaturated polyester coatings. *Progress in Organic Coatings*, 49(3), 236-243. <https://doi.org/10.1016/j.porgcoat.2003.09.018>
- Ramos, V. D., da Costa, H. M., Soares, V. L. P., & Nascimento, R. S. V. (2005). Modification of epoxy resin: a comparison of different types of elastomer. *Polymer Testing*, 24(3), 387-394. <https://doi.org/10.1016/j.polymertesting.2004.09.010>
- Rath, S. K., Chavan, J. G., Sasane, S., Srivastava, A., Patri, M., Samui, A. B., Chakraborty, B. C., & Sawant, S. N. (2009). Coatings of PDMS-modified epoxy via urethane linkage: Segmental correlation length, phase morphology, thermomechanical and surface behavior. *Progress in Organic Coatings*, 65(3), 366-374. <https://doi.org/10.1016/j.porgcoat.2009.02.007>
- Socrates, G. (2001). Infrared and Raman characteristic group frequencies. Tables and charts.
- Stefani, P. M., Moschiar, S. M., & Aranguren, M. I. (2001). Epoxy-urethane copolymers: Relation between morphology and properties. *Journal of Applied Polymer Science*, 82(10), 2544-2552. <https://doi.org/10.1002/app.2105>
- Wazarkar, K., Kathalewar, M., & Sabnis, A. (2016). Development of epoxy-urethane hybrid coatings via non-isocyanate route. *European Polymer Journal*, 84, 812-827. <https://doi.org/10.1016/j.eurpolymj.2016.10.021>
- Yang, K., & Gu, M. (2009). Fabrication, morphology and cure behavior of triethylenetetramine-grafted multiwalled carbon nanotube/epoxy nanocomposites. *Polymer Journal*, 41(9), 752-763. <https://doi.org/10.1295/polymj.PJ2009064>
- Zhou, S., Yang, C., Hu, J., He, X., & Zhang, R. (2018). Damping analysis of some inorganic particles on poly(butyl-methacrylate). *Materials*, 11(6), 1-12. <https://doi.org/10.3390/ma11060992>







## Chromium Coating of Wollastonite Filled Polyamide 6 and Evaluation of Thermal Cycle Strength

Ramiz Gültekin Akay<sup>1\*</sup> , Hakan Yazıcı<sup>1</sup> 

<sup>1</sup>Kocaeli University, Department of Chemical Engineering, Kocaeli, 41380, Türkiye

**Abstract:** The chromium coating of plastic/polymer materials through electrolysis method has attracted attention for improving material properties. The most common material used to be coated is the Acrylonitrile Butadiene Styrene (ABS), but has disadvantages compared to polyamides (PA), such as low thermal resistance. PA's high water retention disadvantage can be substituted by using fillers such as clay, etc; so in this study, 40% Wollastonite filled PA has been used for chromium plating to increase the thermal resistance of the PA. The plates used were produced by injection molding method. The research is focused on the effect of time and concentration on coating performance in etching, activation (by palladium) and accelerator processes. SEM and EDX were used to characterize samples for surface morphologies and the microstructures of etching, activation and accelerator in the PA sub-plates. Additionally, cross-cut adhesion test has been applied to analyze the adhesion power of the interfaces. It was found that the thermal resistance of the metal plate on the polymer surface decreased as the time increased, in relation with the increasing wearing time of the metal plate mentioned above. The thermal resistance decreased as the polymer deformed in relation with the increase in etching solution's concentration. It is also seen that the thermal resistance improved as the activation time increased. The adhesion and the thermal resistance did not improve as the time in accelerator process increased. Furthermore, the cross - cut adhesion tests on the same samples concluded that the results are in agreement with the other thermal resistance results.

**Keywords:** Adhesion, electrolysis, chrome plating, plating on plastics, thermal cycle resistance.

**Submitted:** August 18, 2023. **Accepted:** September 29, 2023.

**Cite this:** Akay, R. G., & Yazıcı, H. (2023). Chromium Coating of Wollastonite Filled Polyamide 6 and Evaluation of Thermal Cycle Strength. Journal of the Turkish Chemical Society, Section B: Chemical Engineering, 6(2), 107-122. <https://doi.org/10.58692/jotcsb.1345824>.

\*Corresponding author. E-mail: [gultekin.akay@kocaeli.edu.tr](mailto:gultekin.akay@kocaeli.edu.tr).

### 1. INTRODUCTION

The use of plastics has increased greatly due to their important advantages such as lightness, durability, flexibility, lower unit cost compared to metal alternatives, easy reproducibility, resistance to abrasion, etc. They are the increasing industrial demands that have led to the replacement of metals with plastics as building materials in a wide range of applications. To respond to the increasing demands for metal replacement with plastics in fields such as automotive, aircraft, textiles, plumbing and household appliances, the use of metal coatings on plastics has a high potential. Such composite materials can outperform plastic or metal materials alone. In the industry, this process is known as POP-Plating On Plastics. In the literature, it is seen that the number of plastic coating studies carried out to increase the impact strength and thermal cycle resistance of plastics is very few. Probably, this is

due to difficulties in coating the plastic. It should be remembered that not all plastics can be coated. Among the plastics with coating properties, there are a group of plastics such as Acrylonitrile Butadiene Styrene (ABS), Polyetherimide, Teflon, Poly-arylether, Polycarbonate, Polyphenylene oxide, Polypropylene, Polysulfone, Polyethersulfone, Polyacetal, mineral reinforced nylon, and platable phenolics. Although these plastics can be coated, the market has always been dominated by ABS. Currently, it is estimated that over 90%, ABS is used as the material in electroplating-related applications. Another material that has the potential to replace ABS is Nylon 6 (N6). However, the major challenge with N6 is that it readily absorbs water, which results in swelling and changes in physical and mechanical properties in wet conditions. This disadvantage of N6 makes the electrolysis process difficult, but if this problem can be overcome; N6 is a suitable and cheap material with good physical

and mechanical properties. It can be partially coated in conventional industrial chrome plating lines. Although it can be coated, its thermal cycle resistance is very low. Plastics can be reinforced/filled with other materials to improve their properties such as tensile strength, impact strength, thermal strength, dimensional stability etc. Reinforcement materials can be in the form of fiber (fiber) and filler (elephant). Although there is no sharp difference between these two material groups, the fiber reinforcement system is generally preferred to improve the properties (Eksi O., 2007).

Wollastonite used as a filling material in this study is a naturally occurring calcium metasilicate ( $\text{Ca-SiO}_3$ ). It is a non-metallic, acicular (needle-tipped) crystal structure, alkaline (pH 9.8), and a white mineral. The main reason for the commercial use of wollastonite is its crystal structure and special chemistry (Ciullo P.A., 1996; Kogel, 2006). Many unique properties of wollastonite have led to its use in many applications that are increasing day-by-day basis. Thanks to these properties, it is used as a filling material for ceramics, plastics and paints, in thermal and electrical insulators, as a melting and wetting agent for glazes, and as a metal melter (Springer, 1994)

Electroplating is an application in which electric current is used to form a metal coating on an electrode to improve the surface properties of objects such as providing lubricity, electrical conductivity or decorative appearance, as well as providing resistance to wear and corrosion in both industrial applications and decorative arts. The electrolyte used in the electroplating process acts as a conductive medium for the passage of electricity between the anode and the cathode. The sample to be coated is the cathode connected to the negative pole. The anode (positive) is the metal that dissolves and deposits on the cathode. When electric current starts to flow through the circuit, negatively charged ions begin to move towards the anode and positively charged ions move towards the cathode. The electric current flow in the circuit is completed by the transmission of ions from one electrode to the other through the electrolyte. The positively charged metallic ions in the electrolyte are attracted by the cathode and the surface at the cathode begins to be coated. Figure 1 below shows the various steps of electroplating of plastics.

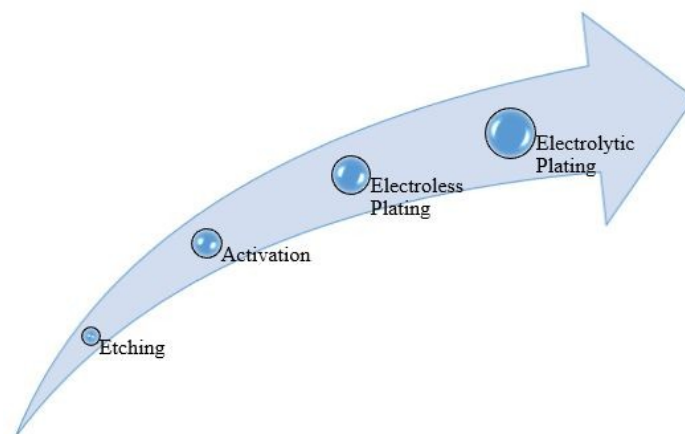


**Figure 1:** Steps related with the electroplating of plastics .

Among these steps, the most important steps are the etching and the activation for a successful plating. For the etching process, the mineral filler can be removed from the resin surface by contacting it with a suitable organic or mineral acid that will dissolve and be removed from the filler surface. Acids normally having a normality of less than 4.0 and preferably between about 1.0-3.0 are generally preferred. Preferably, the parts to be etched are immersed in a suitable acid bath at an operating temperature of about 15-45 °C. Many different acids (acetic, chromic, formic, hydrochloric, sulfuric, etc.) can be used in the etching process, their concentrations vary greatly, dipping times are generally between 3-10 minutes (Stevenson, M. R., 1985).

In the patent study of Shigemitsu, H. (1986), inorganic filler, wollastonite, talc, glass fiber, carbon fiber, etc., which can be used alone or as a mixture, were used. In carrying out the invention, a desired

molded article obtained by molding any of the above-mentioned polyamide resins by a conventional molding method was first subjected to initial etching with an aqueous solution of stannic chloride. After this initial etching, the molded product was washed with water. It was then subjected to a second etching with an aqueous acid solution. The concentration of the aqueous stannic chloride solution was 5 to 50% by weight, preferably 5 to 40% by weight. The acid used for the second etching was preferably inorganic acids such as hydrochloric acid, phosphonic acid, boric acid, and the like, and organic acids such as acetic acid, formic acid, oxalic acid, and the like, and especially hydrochloric acid and acetic acid. The concentration of the aqueous solution of the acid is 50 wt% or less, preferably 3-40 wt%. Although the temperatures of etching processes are determined by considering the concentration of etching solutions, they are usually 20 - 70 °C. It was preferred in terms of controlling the process to adjust the temperatures of

etching processes and their concentrations. The contact times of the etching solutions were between 5 and 30 minutes (Shigemitsu H., 1986).

In the activation process, the sensitizing-activating method may involve adsorbing a relatively strong reducing agent, such as stannic chloride, hypophosphoric acid, hydrazine chloride, or the like, on the surface of the molded article, and then immersing the molded article in a catalyst solution. Gold, silver, palladium, or similar noble metal ions are deposited on the surface of the molded product as a catalyst. This catalyst-accelerator method involves immersing the molded material in a tin-palladium mixed catalyst solution and then activating the catalyst solution mentioned of with an acid such as hydrochloric acid, sulfuric acid, or the like to deposit palladium on the surface as a catalyst. Electroless coating process, electroless nickel plating, and electroless copper process are applicable. Electrolytic coating process, current copper plating process, double layer nickel (bright nickel, bright nickel) plating process, and chromium(VI) plating process are valid.

Electroless coating process are generally has a very similar electroless nickel plating and electroless copper processes described anywhere for ABS plastic coating. In the electrolytic coating process, the current copper plating process, double-layer nickel (bright nickel, bright nickel) plating process and chromium(VI) plating process described for ABS plastic plating are valid.

Metal atoms are deposited on a nonconductive surface via an electrochemical reaction in which a polymeric workpiece is immersed in a reducing agent to form a continuous metallic layer of nearly 1- $\mu\text{m}$  thickness in electroless plating, (Melentiev et al., 2022). After electroless plating additional electroplating of a thicker metallic coating can be performed since the material surface is electrically conductive now. Kuzmik, J. J. (1974) proposed 14 foundational electroplating steps in the classic electroless plating process of nonconductive materials such as ABS, polyethylene, and polypropylene. The process proceeds in a series of stages: (i) pretreatment stage that involves cleaning or degreasing (Step 1) and chromic acid etching, followed by polymer surface modification via acid etching, neutralization, and water rinsing (Steps 2-5); (ii) catalytic stage that involves surface sensitization and activation by immersion in different chemical baths (Steps 6-10); (iii) electroless plating stage that involves chemical plating without an external current source (Steps 11-13); and (iv) final electroplating stage that involves the deposition of a thin metal layer on the electroless-plated substrate (Step 14). Kuzmik then combined two or more of the steps involving degreasing, chromic acid etching, sensitization, and activation to prepare a plastic substrate for the electroless plating of metals. More recently, Charbonnier (Charbonnier & Romand, 2003) confirmed a different route for the conventional method of Kuzmik with combined sensitization,

activation, and acceleration steps. The first process involves sensitization (dipping in a  $\text{SnCl}_2$  solution) and activation (dipping in a  $\text{PdCl}_2/\text{HCl}$  solution) steps. The second process, which is more practical today, involves activation (dipping in a  $\text{PdCl}_2/\text{SnCl}_2/\text{HCl}$  colloidal solution) and consequent acceleration (dipping in a  $\text{HCl}$  or  $\text{NaOH}$  solution) steps. In summary, polymer electroplating is a multistep procedure wherein a workpiece is placed in more than one dozen chemical baths to form conductive and then coated metallic layers. Only some of these electro-chemical plating routes have been discovered to date (Melentiev et al., 2022).

To understand the critical steps and mechanisms for the coating formation and adhesion strength the current understanding of the reactions in the electroless steps and their effects on the integrity of polymer surfaces should be described. These were summarized in the review of Melentiev (Melentiev et al., 2022) according to the recent studies and our electroplating experience: Cleaning or degreasing is performed to remove greasy substances from the polymer surface, during the cleaning step, the polymer plate is immersed in a bath containing an alkaline surfactant ( $\text{NaOH}$ ). This step can increase the wettability of the surface by reducing the surface tension. Appropriate degreasing functions as a pre-etching process that preliminarily modifies the initial surface morphology and chemical properties (Mittal, 1990). The etching step is conducted to promote the formation of useful functional or chemical groups (chemical modification) and roughen the surface (morphological modification). Both modifications improve the chemical adhesion and mechanical interlocking at the polymer-metal interface. Etching is typically performed by immersing the polymeric substrate in a bath containing a mixed solution of chromium trioxide ( $\text{CrO}_3$ ) and sulfuric acid ( $\text{H}_2\text{SO}_4$ ) (called sulfochromic acid) at 65-75 °C. Taking ABS as an example since more than 90% of the polymers coated are ABS today, the hexavalent chromium ion in the sulfochromic etching solution removes or dissolves butadiene rubber particles via a redox reaction involving  $-\text{CH}$  double-bond opening to create a  $-\text{COOH}$  functional base and other polar groups, such as  $-\text{SO}_3\text{H}$  or  $-\text{CONH}$ . The oxidation process consumes large amounts of acid and  $\text{Cr(VI)}$  and produces large quantities of  $\text{Cr}^{3+}$  and  $\text{H}_2\text{O}$ .

In the review of Melentiev (2022), it was also stated that excessive exposure of the polymer surface to acid—called overetching—can reduce the interlocking potential of the polymer topography and weaken the overall ABS. Over time, this causes the discoloration and severe degradation of the ABS surface. Overetching occurs when a high concentration of etching mixture is applied over a long duration. After performing experiments using various grades of ABS polymers, the optimal etching duration was found to vary between 3 and 10 min (Figure 4). At this etching duration, the level of interlocking guarantees the cohesive failure of the coated film during peeling. Exposure durations exceeding this range do not increase the peeling

forces. We will soon present these findings in a separate report (Melentiev et al., 2022).

Kato et al. (Kato, 1968) investigated the effect of the sulfochromic etching duration on the morphology of two commercial grades of ABS along the thickness direction. According to his analysis, long etching durations severely damaged the polymeric material. The effects of different etching stages (underetching, optimum etching, and overetching) on an ABS surface were schematically presented by Bucknall (1977). The synergy between the etching effects on the surface porosity and functional groups transforms the nature of the polymer surface from hydrophobic to hydrophilic. Hydrophilicity ensures the pore penetration of the liquid solutions in the subsequent sensitization and activation steps and the deposition of a palladium seed layer for consequent chemical plating. After etching, the micropores and their interconnected cavities provide numerous sites for the mechanical interlocking (or anchoring) of the ABS surface.

## 2. MATERIALS AND METHODS

### 2.1. Materials

DuPont company's Minlon® material was used as the plastic raw material to be coated. This reinforced nylon material shows better dimensional stability and friction resistance than unreinforced nylons. The raw materials are originally in pellet form with a nominal granule size of 3 mm and a natural color. EKSAŞ AŞ for Cu and Ni electroplating. Two 5l polypropylene (PP) tanks produced by the company were used. In order to increase chemical resistance and acid resistance, the inside of the tank is covered with PVC. The tank is shown in Figure 2 below.



**Figure 2:** Polypropylene tank.

Electroplating bags: The anode bag (Figure 3) is basically a filter that prevents solid anode particles from entering the electroplating solution. It prevents these particles in the galvanic solution from causing roughness on the coating parts. Electroplating anode bags used in the research consist of PP material supplied by Coventya company.



**Figure 3:** Electroplating anode bag used in Cu and Ni coating.

The sides of the bags are double-stitched to prevent the bag from tearing by the rough movement created by the aerial agitation in the coating bath. PP material has excellent resistance to alkalis, mineral acids, organic acids, organic solvents, and oxidizing agents. Copper and Nickel anodes: Ni and Cu anodes were supplied from Ortam Metal and Luvata companies. Cu anodes are of two types, Electrolytic Copper (EC) and Phosphorus De - Oxidized (PDO). EC is a pure form of copper and is used in cyanide copper plating baths. PDO anodes have a low trace of phosphorus, on average 0.05% phosphorus. PDOs are important in acid Cu coating solutions using organic additives. Since organic additives are used in electroplating, the second type of anode (Ni anodes) were used in the study. These are the purest type of Ni anodes and generally cost less. It is usually available in strips or in small pieces ('F' - circles, 'R' - bullets). Flat type Ni anode was used in the study.

The chemicals used in the preparation of electrolytic baths are shown in Figure 4 and respectively; Hydrochloric acid (a), Sulfuric acid (b) were supplied from Ortam Metal Kimya. Cubrac 440 Base (c), Cubrac 440 Brightener (d), Cubrac 440 Leveller (e), Crystal Surfact 47G (f), Criterion Sb100 Brightener (g), Criterion Sb 100 Additive (h), Criterion Sb100 Base (i) Coventya Supplied from. Copper sulfate salt (m), Nickel sulfate salt (l), Nickel chloride salt (k), Boric acid (j) were supplied from Ortam Metal Kimya.



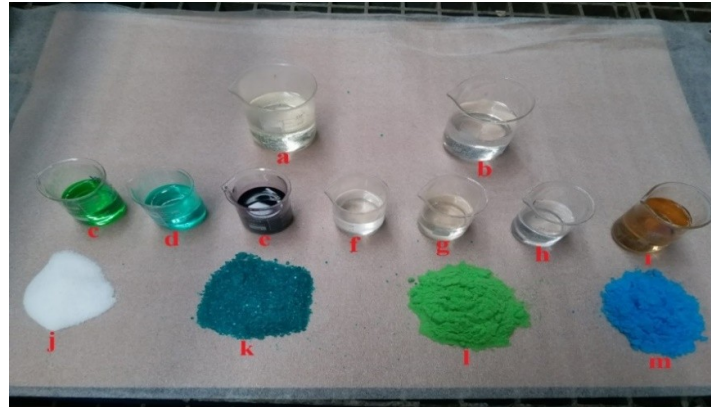


Figure 4: Chemicals used in electroplating.

2.2. Methods

PA6 M40 (40% mineral filled) polymer pellets are produced by injection molding to form standard test specimens by drying at 80 oC for 4 hours. The molded PA samples are then subjected to electroplating. In this study, the effects of time and concentration values in the etching, activation, and accelerator processes on the morphology of the material and thermal cycle resistance were investigated for PA samples. For this purpose, SEM images, EDX analysis characterization studies and thermal cycle resistance tests of the coated PA samples were carried out. The research flow chart of the study is given in Figure 5.

Preparation of PA samples by injection molding method: A HAITIAN 1200KN branded injection machine was used in the preparation of PA samples. The injection molding process is carried out by feeding the pellet thermoplastic (PA6) into the chamber of the injection machine. The injection molding machine consists of a hollow steel sleeve in which heaters are provided for the liquefaction of pellets; The barrel also includes a rotating screw to advance the molten plastic through the entire sleeve and into the die. Barrel temperature varies between 220-280 °C. The temperatures of the four zones of the injection molding machine are; the feeding zone is 220 °C, the compression zone is 240 °C, the measuring area is 260 °C and the nozzle tip is 280 °C. Once enough plastic has been collected in the barrel, a hydraulic pusher is used to push the screw forward to push the plastic through a casting hole into the mold cavity. Care is also taken to see that the mold heats up before the mold is injected into the plastic. This process allows rapid injection into the mold before it hardens. The molding then takes the shape of the mold cavity. The samples are stored in an oven at 80 °C for 24 hours before being taken to the coating process. Figure 6 (A,B,C) shows the sample produced and the width, length, depth and wall thickness measurements of the sample.

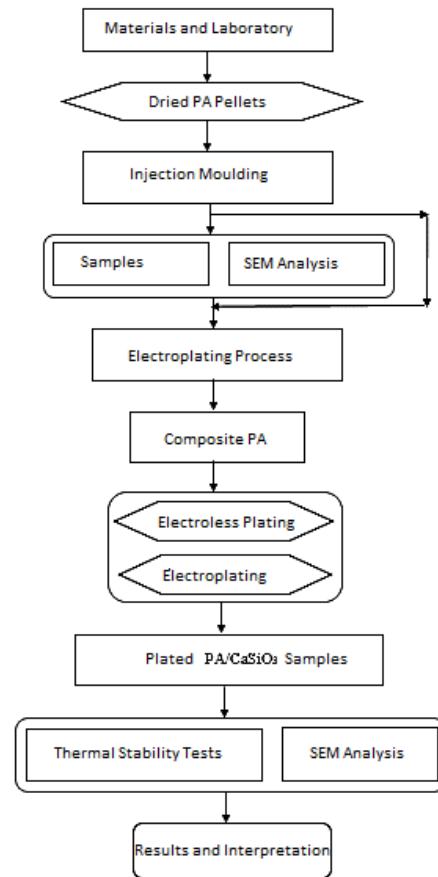


Figure 5: Research flow-chart.

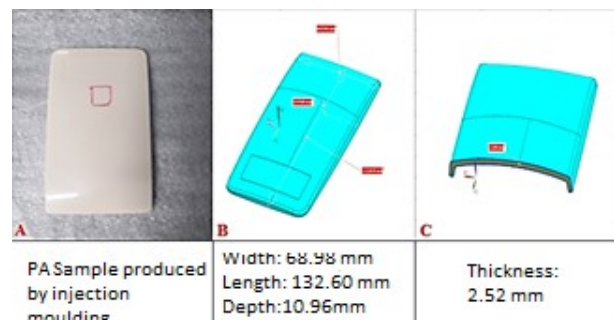


Figure 6: Produced sample and its width, length, depth, and wall thickness measurements.

Metallization of PA samples: Detailed information on the various steps followed during the electroplating of ABS plastics is covered in the following sections.

Etching Process: In this process, samples are immersed in a tank containing ethylene glycol and hydrochloric acid. The etching solution creates tiny microscopic holes on the surface of the samples. These holes act as places to hold the metallic

particles. The prepared etching bath chemicals and their compositions are as shown in Table 1. Ethylene glycol up to 75% of the bath is added to the bath. Then, the required amount of Silken Etch PA 310 is added and the bath temperature is kept constant at 45 °C and mixed until a homogeneous mixture is obtained. The samples to be etched are dipped into the etching solution. After the etching process is finished, it is rinsed with 33% HCl acid solution and then rinsed in demineralized water.

**Table 1:** Etching bath chemicals and their compositions.

Samples	Chemicals and Concentrations	
	Silken Etch PA 310 (HCL)	Ethylene Glycol
1,2,3,7,8,9,10	245 mL/L	75%
4	300 mL/L	75%
5	350 mL/L	75%
6	400 mL/L	75%

Activation Process: The activation process, also called the catalysis process, is a process in which a catalytic film on the surface is deposited to prepare

the substrate for electrolytic metal plating. Activation bath chemicals and their compositions are given in Table 2.

**Table 2:** Activation bath chemicals and their compositions.

Sample	Chemical	Concentration
1,2,3,4,5,6,7,8,9,10	Silken Catalyst PA 510	500 ppm
	Silken Etch PA 310	138mL/L

Micro and macroporous samples from the previous step are immersed in the bath for the times given in Table 3 and then removed.

**Table 3:** The immersion times of the samples in the activation bath.

Sample	Duration (min)
1,2,3,4,5,6,9,10	5
7	10
8	15

Samples subjected to the activation process at different durations are as in Figure 7. They are then rinsed in de-mineralized water.

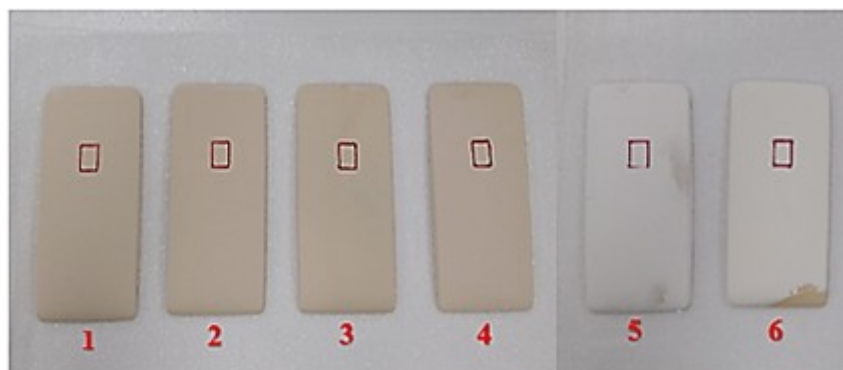


**Figure 7:** Etched PA specimens.

The samples were immersed in the accelerator bath for rapid reduction of the catalysts. In Table 4, accelerator bath chemicals and their compositions;

In Table 5, the immersion times in the accelerator bath were given.



**Table 4:** Accelerator bath chemicals and their compositions.

Sample	Chemical	Concentration
1,2,3,4,5,6,7,8,9,10	Silken Accelerator 610F	28 mL/L
	Demineralized water	97%

**Table 5:** The immersion times of the samples in the accelerator bath.

Sample	Duration (min)
1,2,3,4,5,6,7,8	3.5
9	7.5
10	11.5

Electroless Coating Process: The solution is prepared by mixing nickel sulfate, sodium hypophosphite, and demineralized water in the desired proportions, then adjusting the pH with ammonium hydroxide. After completion of the activation process, all PA samples

are immersed in an alkaline bath partially complexed with ammonium hydroxide at a pH of about 9.0 for 12 minutes at 30 °C. It is then rinsed with demineralized water. The chemicals used and their compositions are listed in Table 6.

**Table 6:** Electroless Ni bath chemicals and their compositions.

Sample	Chemical	Concentration
1,2,3,4,5,6,7,8,9,10	Nickel sulfate hexahydrate, NiSO <sub>4</sub> ·6H <sub>2</sub> O	2,5 g/L
	sodium hypophosphite hydrate, NaPH <sub>2</sub> O <sub>2</sub> ·H <sub>2</sub> O	15 g/L
	Ammonium hydroxide, NH <sub>4</sub> OH (30%)	pH:9

Acid copper plating process: Acid copper plating is called "Copper electroplating". Acid copper plating solution is prepared by mixing copper sulfate, sulfuric acid, and hydrochloric acid with demineralized water. The chemicals used and their compositions are listed in Table 7. The prepared solution is mixed with high-intensity air for 1 hour to achieve homogeneity. Cubrac 440 Base, Cubrac 440 Brightener, and Cubrac 440 Leveller are added to the prepared solution in organics and then

transferred to the electroplating bath. The copper anode is placed in a titanium basket and placed in the bath. The current density is 2.5 A/dm<sup>2</sup> and the operating temperature is kept around 25 °C. The current efficiency is between 95-99%. PA samples are then immersed in the prepared solution for 45 minutes. Electroplated samples are then rinsed with 50% H<sub>2</sub>SO<sub>4</sub> to clean and dull the copper shiny copper layer surface. The samples are then rinsed in demineralized water to remove surface acid.

**Table 7:** Acid copper bath chemicals and their compositions.

Sample	Chemical	Concentration
1,2,3,4,5,6,7,8,9,10	Copper sulfate, CuSO <sub>4</sub> ·5H <sub>2</sub> O	190 g/L
	Sulfuric acid, H <sub>2</sub> SO <sub>4</sub>	65 g/L
	Hydrochloric acid, HCl	90 mg/L
	*Cubrac 440 Base	8 mL/L
	*Cubrac 440 Brightener	---
	*Cubrac 440 Leveller	0.5 mL/L
<b>* Organic compounds</b>		

Nickel (Half bright Ni and bright Ni) plating process: Semi-bright nickel plating solution is prepared by mixing copper sulfate, sulfuric acid, and boric acid with demineralized water. The chemicals used and their compositions are listed in Table 8. The organics of Criterion Sb 100 Base, Criterion Sb 100 Brightener, Criterion Sb 100 Additive, Crystal Surfact 47 G are added to the prepared solution and transferred to the electroplating bath.

The working temperature of the solution is kept constant at 55 °C, the nickel anode is placed in a titanium basket and placed in the bath containing the solution. Current density 2.2 A/dm<sup>2</sup> is applied. The current efficiency is about 95%. The copper plating samples are then immersed in the nickel plating bath solution for approximately 12-16 minutes. The coated samples are then rinsed with demineralized water. The same conditions, chemicals and concentrations are established in the

bright nickel plating solution as in the semi-bright nickel solution.

**Table 8:** Nickel bath chemicals and their compositions.

Sample	Chemical	Concentration
1,2,3,4,5,6,7,8,9,10	Nickel sulfate, NiSO <sub>4</sub> ·6H <sub>2</sub> O	290 g/L
	Nickel chloride, NiCl <sub>2</sub> ·6H <sub>2</sub> O	50 g/L
	Boric acid, H <sub>3</sub> BO <sub>3</sub>	50 g/L
	*Criterion SB 100 Base	15 mL/L
	*Criterion SB 100 Brightener	0.6 mL/L
	*Criterion SB 100 Additive	0.3 mL/L
	*Crystal Surfact 47 G	10 mL/L

Chromium (hexavalent) plating process: Chromium plating solution is prepared by mixing chromic acid and sulfuric acid with demineralized water. The chemicals used and their compositions are listed in Table 9. Chrome plating provides excellent hardness, gloss, and a bright appearance resistant to corrosive environments and can be easily applied

at low cost. The working temperature of the solution is 40 °C. Wear resistant lead anodes are used as anodes. The current density is 5 A/dm<sup>2</sup>. PA samples coming out of the bright nickel bath are immersed in the +6 valence chrome bath solution for 4 minutes. The coated samples are then rinsed with demineralized water.

**Table 9:** Chromium bath chemicals and their compositions.

Sample	Chemical	Concentration
1,2,3,4,5,6,7,8,9,10	Chromic acid, CrO <sub>3</sub>	280 g/L
	Chromic acid/sulfate	280:1

### 2.3. Characterization Methods

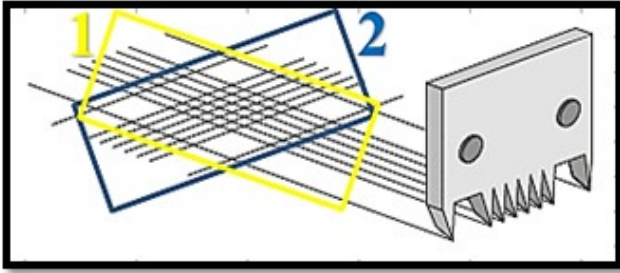
**Thermal cycle endurance test:** Coated samples are subjected to thermal cycle endurance test by using BINDER ED 720 heating oven and Uğur UED 380 deep freezer. This test method is usually done to measure the adhesion of the coating on the plastic surface. The most important point to be considered in this test is to ensure that the temperature is not higher than the melting temperature of the plastic. The samples are first left in the heating furnace at 104 °C for 60 minutes. Then it is kept in the environment at 250 °C for 15 minutes. It is then left in the cooling cabinet at -30 °C for 60 minutes. This process is repeated 3 times, continuing with the same samples.

**Cross - Section:** Coated samples are prepared for cold mounting by precision cutting with the Metkon MICRACUT 152 device. Cold mounting specimens are prepared for SEM with Metkon FORCIPOL 2V sanding and polishing device. The coated samples are first sanded with Metkon DEMPAX Ø200 Sandpaper, 800 Grit for 7 minutes, and Metkon DEMPAX Ø200 Sandpaper, 2500 Grit for 13 minutes. Then FEDO-3 Ø200mm is polished with 3 µm diamond suspension for 8 minutes, Metkon FEDO-1S Ø200mm with 1 µm diamond suspension for 2.5 minutes.

**Scanning electron microscopy (SEM) and energy dispersive x-ray (EDX) analysis:** Plastic and metallized samples were coated for SEM with QUORUM Q150R ES model coater at 80%Au+20%Pd ratios. Microstructures and surface morphologies of the samples whose surfaces were coated with gold and palladium were visualized with the ZEISS SUPRA

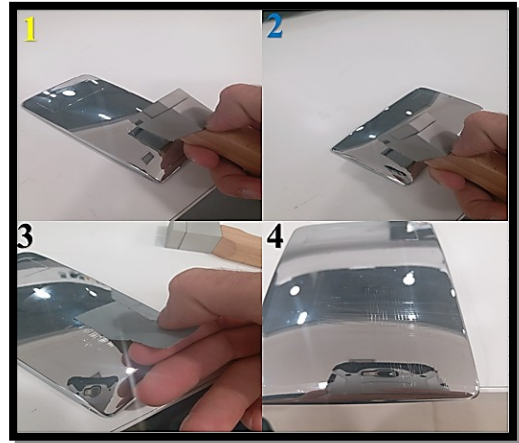
40VP model scanning electron microscope and energy dispersive x-ray analyses were performed (Bilecik Şeyh Edebalı University Central Research Laboratory).

**Adhesion tape testing:** The durability of coatings is fundamental in many applications, and one of the main factors governing this durability is adhesion. Adhesion refers to the bond (chemical or physical) between two adjacent materials and relates to the force required to achieve their complete separation (Davies & Whittaker, 1967). The adhesion of a coating to the surface is critical to its function. Mechanical, chemical and metallurgical factors may contribute to these adhesions. For a coating to maintain and function, its adhesion to the substrate must tolerate mechanical stresses and elastoplastic degradation, thermal stress, and environmental or process fluid displacement. The good adhesion performance of a coating depends on various properties of the interface region, including its atomic adhesion structure, elastic modulus and stress state, thickness, purity, and fracture toughness (Baglin, 1988). In the adhesion tape test, samples are drawn with a cross cutting tool on the coating in the directions indicated in Figure 8.



**Figure 8:** Drawing on the part with the cross cutter.

A special adhesive tape (Tesa 4657) is used in this procedure. The tape is pressed against the grid and then quickly pulled away in a smooth motion. The grid area is then examined using an illuminated magnifying glass (Figure 9).

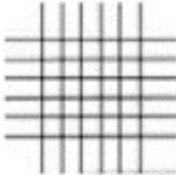
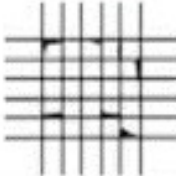
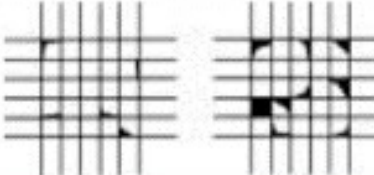
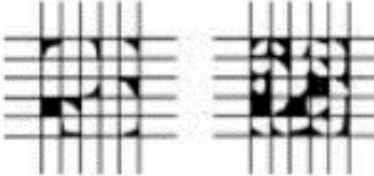
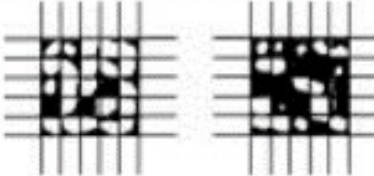
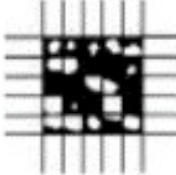


**Figure 9:** Adhesion tape test application.

Adhesion tests were carried out on the coated samples with the BYK - Gardner cross cut test device in accordance with DIN EN ISO 2409, ASTM D 3002, ASTM D 3359 International standards. The results obtained in this way are then classified by comparison with the standards given in Figure 10 (ASTM Adhesion Standards)).

### 3. RESULTS AND DISCUSSION

All process parameters of 10 samples prepared according to different etching time, etching concentration, and different accelerator times selected are summarized in Table 10. SEM images of these samples were taken and SEM/EDX analyzes, thermal cycle resistance tests and cross-cut adhesion tests of the coated samples were performed. Parameters indicated with yellow fill in Table 10 show the modified parameters.

<p><b>ISO Class: 0/ASTM Class: 5B</b> The edges of the cuts are completely smooth; none of the squares of the lattice is detached.</p>	
<p><b>ISO Class: 1/ASTM Class: 4B</b> Detachment of small flakes of the coating at the intersections of the cuts. A cross-cut area not significantly greater than 5% is affected.</p>	
<p><b>ISO Class: 2/ASTM Class: 3B</b> The coating has flaked along the edges and/or at the intersections of the cuts. A cross-cut area significantly greater than 5%, but not significantly greater than 15%, is affected.</p>	
<p><b>ISO Class: 3/ASTM Class: 2B</b> The coating has flaked along the edges of the cuts partly or wholly in large ribbons, and/or it has flaked partly or wholly on different parts of the squares. A cross-cut area significantly greater than 15%, but not significantly greater than 35%, is affected.</p>	
<p><b>ISO Class: 4/ASTM Class: 1B</b> The coating has flaked along the edges of the cuts in large ribbons, and/or some squares have detached partly or wholly. A cross-cut area significantly greater than 35%, but not significantly greater than 65%, is affected.</p>	
<p><b>ISO Class: 5/ASTM Class: 0B</b> Any degree of flaking that cannot even be classified by classification 4.</p>	

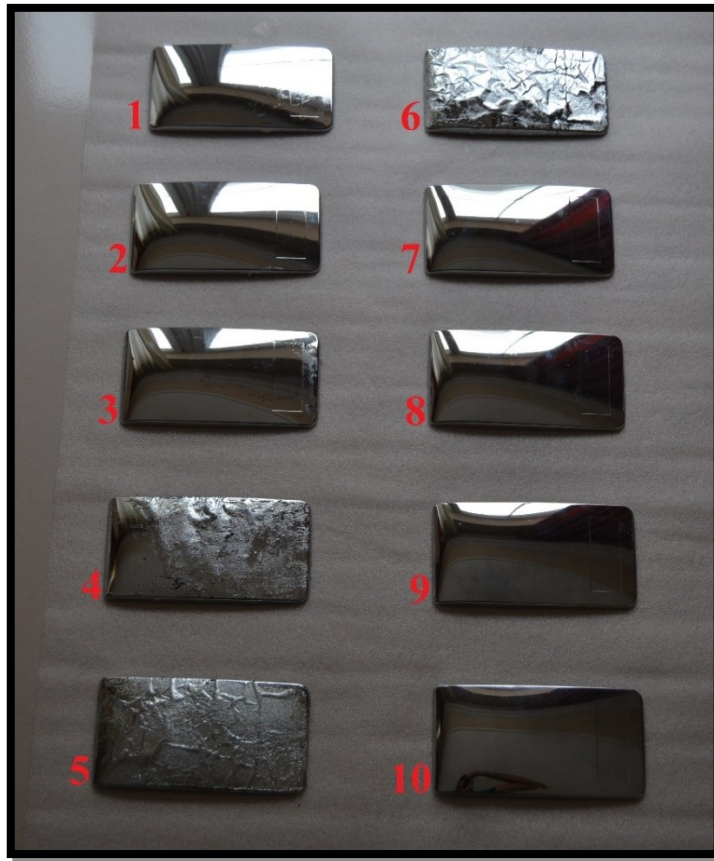
**Figure 10:** Adhesion tape test method classification standards (ASTM).

Table 10: Process parameters used for all samples.

Samp.	Observations	ETCHING		ACTIVATION			ACCELERATOR			CHEMICAL-NICKEL				COPPER	Half bright Nickel	Bright Nickel	Chrome +6	
		Temp. C	time min	Kons. PA 310 ml	Temp C	Zaman dk	Kons. PA 310 ml	Kons. PA 610F ml	PH	Temp C	time min	Kons. Hipofosfit ml	Kons. Nikel ml					Ph
1	Good Adhesion	45	15	245	30	5	138	500 ppm	3,60	28	11,5	30	12	15	2,5	9	2,2 amp-14 dk	5 amp-4 dk
2	Cracks and bulging	45	20	245	30	5	138	500 ppm	3,60	28	11,5	30	12	15	2,5	9	2,2 amp-14 dk	5 amp-4 dk
3	Cracks and bulging	45	30	245	30	5	138	500 ppm	3,60	28	11,5	30	12	15	2,5	9	2,2 amp-14 dk	5 amp-4 dk
4	Cracks and bulging	45	15	300	30	5	138	500 ppm	3,60	28	11,5	30	12	15	2,5	9	2,2 amp-14 dk	5 amp-4 dk
5	Cracks and bulging	45	15	350	30	5	138	500 ppm	3,60	28	11,5	30	12	15	2,5	9	2,2 amp-14 dk	5 amp-4 dk
6	Cracks and bulging	45	15	400	30	5	138	500 ppm	3,60	28	11,5	30	12	15	2,5	9	2,2 amp-14 dk	5 amp-4 dk
7	Good Adhesion	45	15	245	30	10	138	500 ppm	3,60	28	11,5	30	12	15	2,5	9	2,2 amp-14 dk	5 amp-4 dk
8	Good Adhesion	45	15	245	30	15	138	500 ppm	3,60	28	11,5	30	12	15	2,5	9	2,2 amp-14 dk	5 amp-4 dk
9	Good Adhesion	45	15	245	30	5	138	500 ppm	7,60	28	11,5	30	12	15	2,5	9	2,2 amp-14 dk	5 amp-4 dk
10	Cracks	45	15	245	30	5	138	500 ppm	11,60	28	11,5	30	12	15	2,5	9	2,2 amp-14 dk	5 amp-4 dk

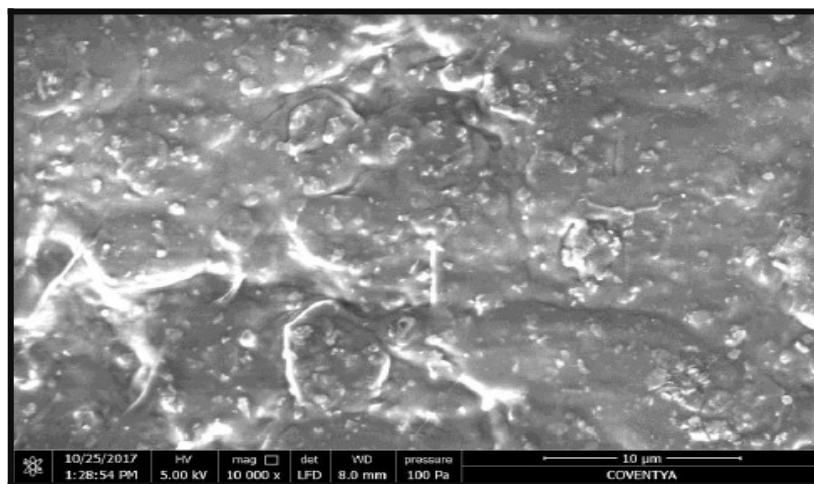


The images of the samples after the thermal cycle resistance test are given in Figure 11.



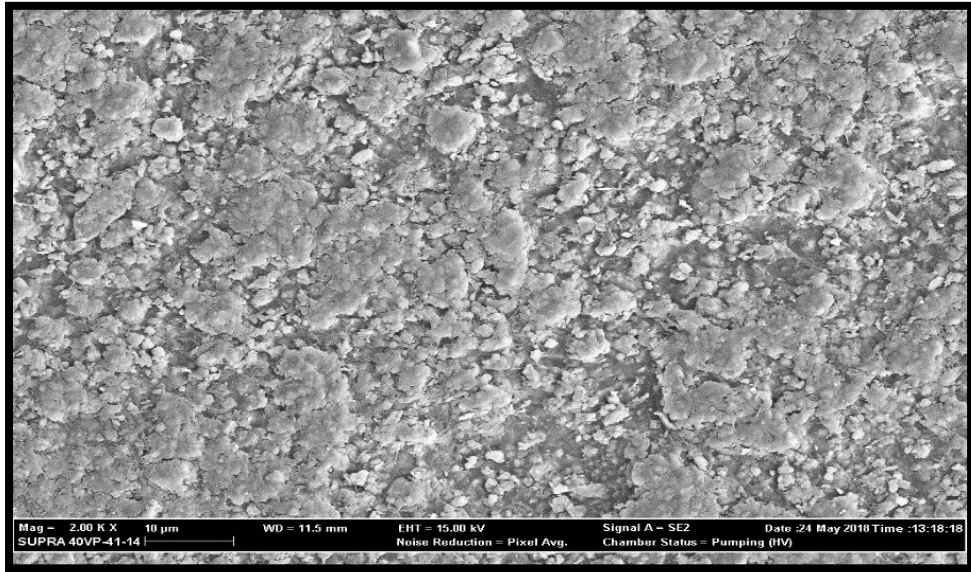
**Figure 11:** Samples after thermal cycle endurance test.

Figure 12 shows the SEM micrograph of the non-abraded PA material.



**Figure 12:** SEM micrograph of the PA specimen (no etching).

Figure 13 shows 10-micron SEM micrograph showing the etched PA surface. The micro- and macro-pores formed on the surface of the plastic represent the binding sites for the deposited metal.



**Figure 13:** 15-min etching SEM micrograph of plastic PA sample 1.

Copper layer thickness and nickel layer thickness were measured in the SEM micrograph of PA sample 1 from the cross-section as 29.64  $\mu\text{m}$  13.27  $\mu\text{m}$  respectively (Figure 14). After the thermal

resistance test of Sample 1, it was observed that the plastic layer and the metal film layer adhered well to each other.

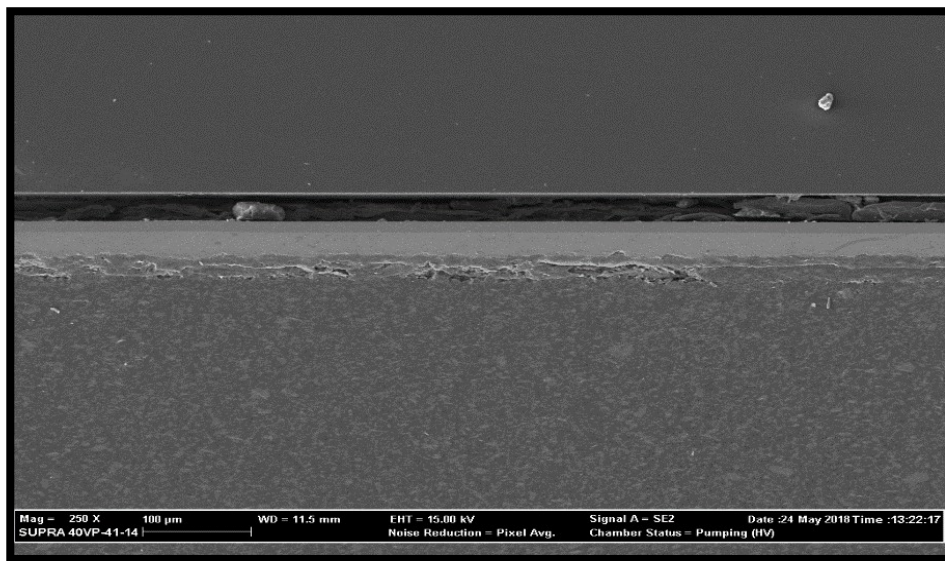


**Figure 14:** Cross-section SEM micrograph of metallized PA sample 1.

No impurities were observed in the elemental composition analysis between the plastic and copper layer of PA sample 1 in Figure 15. The copper element percentage is seen as 83.12.



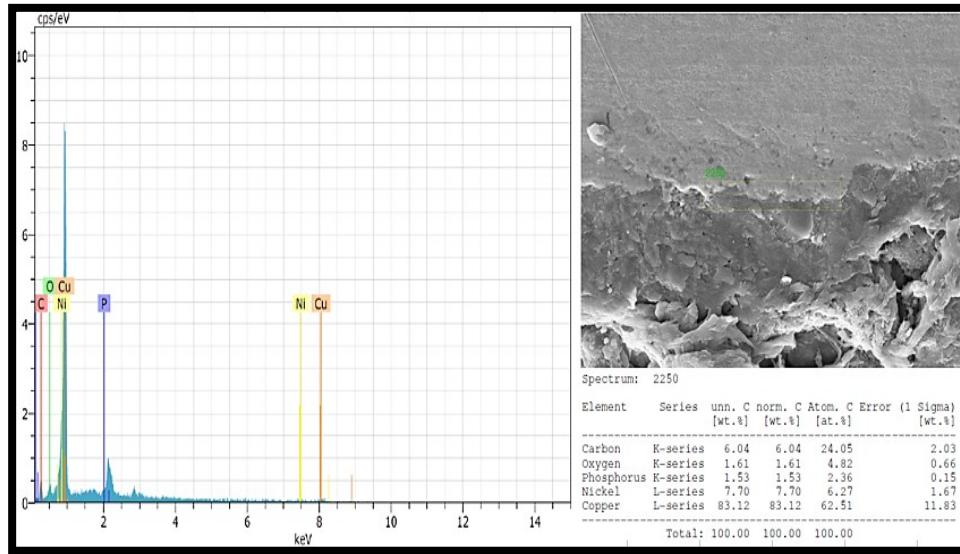


Figure 15: EDX analysis of PA Sample 1.

The thermal cycle endurance observation results are summarized in Table 11.

Table 11: Thermal cycle endurance test results.

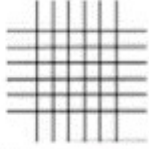
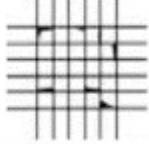
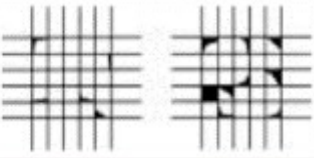
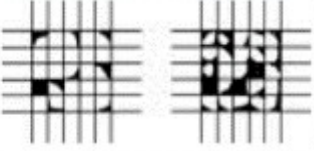
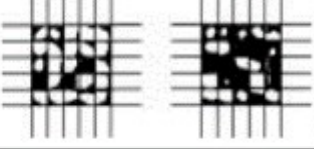
Sample	Observation	Result
1	Crack, no bulging	Good adhesion
2	Crack, bulging	Bad adhesion
3	Crack, bulging	Bad adhesion
4	Crack, bulging	Bad adhesion
5	Crack, bulging	Bad adhesion
6	Crack, bulging	Bad adhesion
7	Crack, bulging	Good adhesion
8	Crack, bulging	Good adhesion
9	Crack, bulging	Good adhesion
10	Crack	Bad adhesion

Cross-Cut Adhesion Test Results of PA samples are given in Table 12.

For samples 1, 2, and 3: All parameters were kept constant and the metal plating process was carried out by keeping them in the etching bath for 15 minutes, 20 minutes, and 30 minutes, respectively. Considering the thermal cycle resistance test and cross-cut test results of Sample 1 (etching bath time 15 min), it was observed that the plastic and metal layers adhered to each other very well. It was observed that the plastic and metal layers did not stick to each other and were separated from each other in sample 2 (etching bath time 20 min) and sample 3 (etching bath time 30 min). The increase in the etching time adversely affects the adhesion of plastic and metal layers to one of them. In addition, in the SEM/EDX analyzes performed for the samples, it was observed that the metal layer could not adhere to the surface as a result of deformation as a result of deterioration in the polymer structures of

sample 2 and sample 3. For sample 4 (etching bath concentration 300 mL/L), sample 5 (etching bath concentration 350 mL/L) and sample 6 (etching bath concentration 400 mL/L), the etching bath concentrations based on the parameters of sample 1 are 300 mL/L, respectively. Metal coating process was carried out by making 350 mL/L, 400 mL/L. Thermal cycle endurance test and adhesion tape test results are negative for all three samples. It was observed that the adhesion between the plastic and metal layers was very bad. The increase in the abrasive concentration adversely affected the adhesion between the plastic and metal layer. In the SEM/EDX analyzes performed for the samples, it was observed that the metal layer could not adhere to the surface as a result of deformation in the polymer structures of all three samples.

**Table 12:** Cross-cut adhesion test results of PA samples.

Samples	Standard and Explanation	
1, 7 and 8	<b>ISO Class: 0/ASTM Class: 5B</b> The edges of the cuts are completely smooth; none of the squares of the lattice is detached.	
9	<b>ISO Class: 1/ASTM Class: 4B</b> Detachment of small flakes of the coating at the intersections of the cuts. A cross-cut area not significantly greater than 5% is affected.	
-	<b>ISO Class: 2/ASTM Class: 3B</b> The coating has flaked along the edges and/or at the intersections of the cuts. A cross-cut area significantly greater than 5%, but not significantly greater than 15%, is affected.	
2	<b>ISO Class: 3/ASTM Class: 2B</b> The coating has flaked along the edges of the cuts partly or wholly in large ribbons, and/or it has flaked partly or wholly on different parts of the squares. A cross-cut area significantly greater than 15%, but not significantly greater than 35%, is affected.	
3	<b>ISO Class: 4/ASTM Class: 1B</b> The coating has flaked along the edges of the cuts in large ribbons, and/or some squares have detached partly or wholly. A cross-cut area significantly greater than 35%, but not significantly greater than 65%, is affected.	
4, 5, and 6	<b>ISO Class: 5/ASTM Class: 0B</b> Any degree of flaking that cannot even be classified by classification 4.	

For sample 7 (activation process time 10 min) and sample 8 (activation bath time 15 min), metal plating process was carried out by keeping the times in the activation bath for 10 min and 15 min, respectively, based on sample 1 parameters. Thermal cycle resistance test and adhesion tape test results were positive for both samples. In SEM / EDX analyses, it was observed that the increase in the activation bath time increased the amount of Pd catalyst on the polymer surface and positively affected the adhesion between the polymer and the metal layer.

For sample 9 (accelerator bath time 7.5 min) and sample 10 (accelerator bath time 11.5 min), metal plating was carried out by keeping the accelerator bath for 7.5 min and 11.5 min, respectively, based on sample 1 parameters. It was observed that the thermal cycle strength test and adhesion tape test result of sample 9 were positive, but the results for sample 10 were negative. It was observed that as the waiting time in the accelerator bath increased, it negatively affected the adhesion between the polymer and the metal layer. In SEM / EDX analyses, the presence of Pd catalyst decreased with the

increase in bath time, which negatively affected the good adhesion of the metal layer.

As a result of the study, it can be used together with Vollastonite ( $\text{CaSiO}_3$ ), which helps form a conductive surface on PAs, to improve coatings on PAs. Increases in the etching time, etching concentration and acceleration process time in the coating process adversely affected the thermal cycling resistance of PAs. Since the coatingability of PAs is difficult, it is recommended that the etching process time be kept at 15 minutes and the etching process concentration should not exceed 245 mL/L, activation process time up to 15 minutes and acceleration process time not exceeding 7.5 minutes. In order to obtain better results, different chemicals, different etching concentrations and times, different activation and accelerator bath times can be tried. In addition, in order to reduce the cost in the industry, different filling materials are added to PAs, for example clay, talc, or silica can be added and their ability to be coated can be examined.

#### 4. CONCLUSION

In this study, the trade name Minlon 73M40 NC010 40% Wollastonite Filled PA (Dupont) polymer was used to increase the thermal cycling resistance of PA. The plates used in the experiments were produced by injection molding method. The effects of time and concentration parameters on the coating performance were investigated in etching, activation (with palladium), and accelerator processes of the PA coating.

As a result of the study, it can be used together with Wollastonite ( $\text{CaSiO}_3$ ), which helps to form a conductive surface on PAs, to improve coatings on PAs. Increases in the etching time, etching concentration and acceleration process time in the coating process adversely affected the thermal cycling resistance of PAs. Since the coating ability of PAs is difficult, it is recommended that the etching process time be kept at 15 minutes and the etching process concentration should not exceed 245 mL/L, activation process time up to 15 minutes and acceleration process time not exceeding 7.5 minutes. In order to obtain better results, different chemicals, different etching concentrations and times, different activation and accelerator bath times can be tried. In addition, in order to reduce the cost in the industry, different filling materials are added to PAs, for example; Clay, talc, silica can be added and their ability to be coated can be examined.

#### 5. REFERENCES

- Baglin, J. E. E. (1988). Thin film adhesion: New possibilities for interface engineering. *Materials Science and Engineering: B*, 1(1), 1-7. [https://doi.org/10.1016/0921-5107\(88\)90024-4](https://doi.org/10.1016/0921-5107(88)90024-4)
- Bucknall, C. (1977). *Toughened Plastics*. .
- Charbonnier, M., & Romand, M. (2003). Polymer pretreatments for enhanced adhesion of metals deposited by the electroless process. *International Journal of Adhesion and Adhesives*, 23(4), 277-285. [https://doi.org/10.1016/S0143-7496\(03\)00045-9](https://doi.org/10.1016/S0143-7496(03)00045-9)
- Ciullo P.A. (1996). *Industrial Minerals and Their Uses: A handbook & Formulary*. Noyes Publication.
- Davies, D., & Whittaker, J. A. (1967). Methods of testing the adhesion of metal coatings to metals. *International Materials Reviews*, 12(1), 15-26. <https://doi.org/10.1179/imr.1967.12.1.15>
- Eksi O. (2007). *Plastik Esaslı Malzemelerin Isıl Sekil Verme Özelliklerinin İncelenmesi*. <https://tez.yok.gov.tr/UlusalTezMerkezi>
- Kato, K. (1968). Electron Microscope Studies on the Etching of ABS Moldings for Electroplating. *Journal of Electron Microscopy*. <https://doi.org/10.1093/oxfordjournals.jmicro.a049589>
- Kogel, J. E. , T. N. C. , B. J. M. , K. S. T. (2006). *Industrial Minerals & Rocks : Vol. 7th Edition*. Society for Mining, Metallurgy, and Exploration, Inc.
- Kuzmik JJ. (1974). *Preparation of plastic substrates for electroless plating and solutions therefor*. (Patent 3,790,400). United States Patent. .
- Melentiev, R., Yudhanto, A., Tao, R., Vuchkov, T., & Lubineau, G. (2022). Metallization of polymers and composites: State-of-the-art approaches. *Materials & Design*, 221, 110958. <https://doi.org/10.1016/j.matdes.2022.110958>
- Mittal, K. L. (1990). *Metallized plastics 2, Fundamental and Applied Aspects*. .
- Murdan, S., Kerai, L., & Hossin, B. (2015). To what extent do in vitro tests correctly predict the in vivo residence of nail lacquers on the nail plate? *Journal of Drug Delivery Science and Technology*, 25, 23-28. <https://doi.org/10.1016/j.jddst.2014.11.002>
- Shigemitsu H. (1986). *Method For Plating Polyamide Resin Molded Article* (Patent U.S. Patent No:4,563,242.). Patent Ohtake. Japan.
- Springer, J. S. (1994). *Ontario Wollastonite: Uses, Markets and Ontario's Potential as a Future Producer*. Ministry of Northern Development, Mines, Natural Resources and Forestry.
- Stevenson M. R. (1985). *Metal Plating Of Polyamide Thermoplastics* (Patent U.S. Patent No:4,552,626.). United States Patent Grosse Pointe woods. Mich. .



## Simulation And Optimization Of Hydrogen Production By Steam Reforming Of Natural Gas

Akbar Khoshnoudi<sup>1</sup> , Ramiz Gultekin Akay<sup>1\*</sup> 

<sup>1</sup>Kocaeli University, Department of Chemical Engineering, Kocaeli, 41380, Türkiye

**Abstract:** Hydrogen (H<sub>2</sub>) production through natural gas steam reforming is widely adopted due to its cost-effectiveness and energy efficiency. A simulation and optimization study was performed on an industrial natural gas steam reforming system using Aspen Hysys V12 software to optimize this process. The study focused on optimizing various parameters, including the Reformer Reactor, Water Gas Shift Reactor, and purification units such as the Separator and Pressure Swing Adsorption (PSA). The Reformer and Water Gas Shift reactors were set at 900 °C and 300 °C, respectively, to maximize hydrogen production. Under specific conditions of 5 atm pressure and a steam-to-carbon ratio (S/C) of 2.5, the process achieved a hydrogen production rate of 402.2 kg/h. The treatment zone effectively eliminated ~ 100% of undesirable CO<sub>2</sub> and CO gases, with only trace amounts of CH<sub>4</sub> and H<sub>2</sub> remaining in the waste gases. Additionally, the PSA unit efficiently removed ~ 100% of the water from the separator, ensuring water-free dry gases were sent to the PSA unit. The integration of heating and cooling heat exchange units reduced energy consumption by approximately 51.6%. After the removal of undesired gases in our PSA unit, the production yield for the final product (H<sub>2</sub>, based on dry gas inlet to PSA) is 77.83%, resulting in 100% pure dry H<sub>2</sub>. In the waste gas outlet (tail gas) of PSA a composition (22.17%), includes CO, CO, H<sub>2</sub>O, and CH<sub>4</sub>. Resulting high-quality hydrogen is well-suited for a wide range of applications, including fuel cells, petroleum refining, natural gas refineries, and petrochemical processes.

**Keywords:** Natural Gas Steam Reforming, Hydrogen Production Process Simulation, Process Optimization, Reformer, Water Gas Shift (WGS)

**Submitted:** August 18, 2023. **Accepted:** September 29, 2023.

**Cite this:** Khoshnoudi, A., & Akay, R. G. (2023). Simulation And Optimization Of Hydrogen Production By Steam Reforming Of Natural Gas. Journal of Turkish Chemical Society, Section B: Chemical Engineering, 6(2), 123-136. <https://doi.org/10.58692/jotcsb.1346122>.

**\*Corresponding author. E-mail:** [gultekin.akay@kocaeli.edu.tr](mailto:gultekin.akay@kocaeli.edu.tr).

### 1. INTRODUCTION

An increase in the global population of 7.98 billion in 2022 and in heavy industrialization of 3.217% in 2018, has been enormously rising energy demand. Thus, world energy consumption is expected to grow by nearly 50% by 2050, predisposing the world's economic and political stability into a precarious position. In this context, and as awareness increases, a growing coalition between governments and oil and gas giants, is seeking an advanced prospect of the hydrocarbon reserve that would be capable of powering complex industrial processes and growing population demands (El-Shafie et al., 2019). Therefore, according to the "The Future of Hydrogen" report, released by the international energy agency IEA in 2019, hydrogen got the world's attention due to its potent role. Its demand within various industrial sectors is now at the

highest level in history. For instance, according to the U.S. Department of Energy, global hydrogen demand surpassed the threshold of 70 MMT in 2018. Hydrogen acts as an energy vector that can be transported, stored, and easily blended. Moreover, most of today's demand of 70 million tons of produced H<sub>2</sub> worldwide annually, is for chemical applications and the petrochemical industry. Therefore, these industries represent 63% of the total industrial hydrogen demand according to certify where, ammonia is by far the largest consumer in the chemical sector, ranging between 27 and 53% of the total demand. The methanol industry, accounting for 12% of the market share, is the second largest hydrogen consumer in the petrochemical sector. Moreover, the project hydrogen demand for ammonia and methanol is expected to reach 14 MT (H<sub>2</sub>/Year) by 2030 (a 31% increase under existing policies for ammonia and

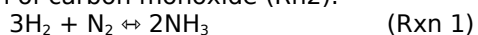
methanol due to economic and population growth) (Alves et al., 2013). Accordingly, refineries represent the second largest consumer of hydrogen after the petrochemical industry segment, with a market share of 30%. And, hydrogen is used for the hydro-processing of crude oil and petroleum products involving sulfur, nitrogen, metal impurities removal, as well as for the production of lighter and more valuable products (Sarkarzadeh M, et al., 2019). A wide variety of technologies is currently used for hydrogen production, such as gasification, solar (or wind) water electrolysis, high-temperature electrolysis (HTE) water splitting, and natural gas steam reforming including steam methane reforming (SMR) (Goswami et al., 2003). On a commercial scale, SMR is considered the invaluable and the most practical technology to produce H<sub>2</sub>, thus it is capable to produce high hydrogen yield efficiency of approximately 75% with an estimated cost of around 1.8 - 2.3 \$/kg versus an average between 3 and 5.80 \$/kg for the (HTE) and versus the incomparable highest production cost for wind and solar electrolysis (production cost >7 \$/kg H<sub>2</sub>). SMR is relatively environmentally friendly in comparison with coal gasification technology. SMR will be a practical and brilliant idea to boost the petrochemical and refinery industries in the world (Lemus & Martínez Duart, 2010). This work covers a detailed analysis of a steady state simulation and optimization of an industrial natural gas steam reforming process capable of meeting the hydrogen demand of petrochemical-refining industries and fuel cell technology. In SMR high methane purity in natural gas is needed in order to save on the capital and operating cost of the system, by decreasing the load of the purification stage. An optimization of the operating conditions in the main units of the process was performed. The effect of, i) steam to carbon ratio (S/C), ii) pressure, and iii) temperature was conducted by Aspen HYSYS v12. Presently, the hydrogen demand around the globe is majorly met the steam methane reforming with the natural gas feedstock. Hydrogen (H<sub>2</sub>) production through natural gas steam reforming is widely adopted due to its cost-effectiveness and energy efficiency. A simulation and optimization study was performed on an industrial natural gas steam reforming system using Aspen Hysys V12 software to optimize this process. The study focused on optimizing various parameters, including the Reformer Reactor, Water Gas Shift Reactor, and purification units such as the Separator and Pressure Swing Adsorption (PSA). The Reformer and Water Gas Shift reactors were set at 900 °C and 300 °C, respectively, to maximize hydrogen production.

## 2. MATERIALS AND METHODS

The adopted methodology in this study is summarized by the following three steps: i) calculation of a certain market need in hydrogen (MT/year); ii) simulation of a natural gas steam reforming process aiming to produce the required Hydrogen needs; iii) optimization of the adopted process in order to maximize hydrogen yield, to

reduce energy consumption and to minimize the production of polluting gases. Simulation software was adopted to perform a steady-state study involving all the thermodynamic parameters and the simulator was the commonly used Aspen HYSYS. Finally, results were obtained from software and the calculation of hydrogen production. Hydrogen produced is mostly used by ammonia, petroleum refineries, and fertilizer-producing companies. A total of 99% of hydrogen comes from fossil fuel reforming, as it is the most conventional and cost-effective method, but it is not beneficial for the environment due to CO<sub>2</sub> emission. Hydrogen production goes through an unprecedented revolution under the net-zero emissions scenario. When the global output reaches 200 MT H<sub>2</sub> in 2030, low-carbon technologies will account for 70% of that production (electrolysis) (Ramachandran & Menon, 1998). By 2050, the amount of hydrogen produced will have increased to about 500 MT H<sub>2</sub>, almost entirely due to low-carbon technologies. Different technologies will be needed to alter the energy system to achieve net-zero emissions by 2050. Energy efficiency, behavioral modification, electrification, renewable energy, hydrogen, and hydrogen-based fuels, and carbon capture utilization storage (CCUS) are likely to be the major pillars for decarbonizing the world's energy system. In the net zero emissions scenario, strong hydrogen demand growth and the adoption of cleaner technologies for its production will allow hydrogen and hydrogen-based fuels to prevent up to 60 gigatonnes (GT) of CO<sub>2</sub> emissions in 2021–2050 or 6.5% of all cumulative emissions reductions. Utilizing hydrogen fuel is especially important for cutting emissions in hard-to-decarbonize industries including heavy industries (especially steel and chemical) heavy-duty road transport, shipping, and aviation where direct electrification is challenging. Hydrogen Generation Market by Technology (SMR, POX, Coal Gasification, Electrolysis), Application (Refinery, Ammonia Production, Methanol Production, Transportation, Power Generation), Source (Blue, Green, Gray). The global hydrogen generation market is projected to reach USD 263.5 billion by 2027, at a compound annual growth rate (CAGR) of 10.5% between 2022 to 2027 ("Global Hydrogen Review"., 2021). The growing demand for hydrogen for fuel cell electric vehicles (FCEV) and rockets in the aerospace industry is driving market growth. Utilization of hydrogen fuel cells in lightweight vehicles such as bicycles, cars, buses, trains, material handling equipment, boats, ships, commercial aircraft, auxiliary power units (APUs) of aircraft, marine vessels, and specialty vehicles such as forklifts are fostering the market growth in the transportation sector. In this regard, ammonia could be synthesized from a mixture of hydrogen and nitrogen gas via the process (Rn1), and methanol could be prepared from a syngas mixture which is the product of methane steam reforming process (CO & H<sub>2</sub> mixture or CO<sub>2</sub> & H<sub>2</sub> mixture). However, a one-pass methanol yield of nearly 55% can be obtained for pure CO, while pure CO<sub>2</sub> would only yield 18% of CH<sub>3</sub>OH. This illustrates the possibility of

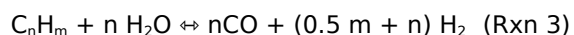
a more effective methanol production via the hydrogenation of carbon monoxide (Rn2).



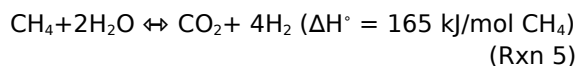
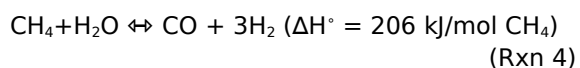
In this respect, the mentioned quantities were calculated via stoichiometry co-efficient of (Rxn1&Rxn2) taking into account the imported amounts of methanol and ammonia fertilizers of the year 2019 (Leonzio G., 2018).

### 2.1. Natural gas feedstock requirement

Industrial steam reforming is a well-established process that reacts natural gas and steam in order to produce high-purity hydrogen, according to the following chemical reaction (Rxn3).



The heavier is the natural gas the lower is the H<sub>2</sub>/CO ratio (Speight JG., 2011). In this sense, high ratios are favored by reacting almost pure methane pre-extracted via a cryogenic separation process natural gas with high methane content where CH<sub>4</sub> undergoes following steam reforming reaction (Rn4, Rn5) (Cherbanski R, & Molga E., 2018). where (Rn4) is the major steam reforming reaction instead of (R5).



Where  $\Delta H^0$  represents the standard enthalpy of the reaction. Because natural gas is expected to have a similar composition to raw gas with a high methane fraction of 99% as seen in Table 1, a natural gas stream could be directly fed into the process plant to undergo the principal reforming reactions (Rxn4), (Rxn6-Rxn12) and the water gas shift reaction (Rxn13). The purpose of this measure was to avoid the pre-purification step of the main stream hence, to save on the capital & operation costs. Moreover, the steam reforming reactions of all the natural gas components (Rxn6-Rxn12), were taken into consideration in the stoichiometric approach in order to maximize the calculation accuracy (Olateju et al., 2017). The average natural gas components in the hydrogen production unit plant layout are provided in Table 1.

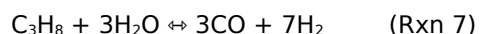
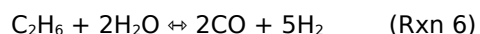
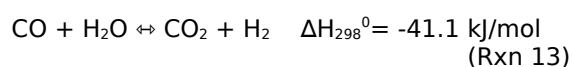
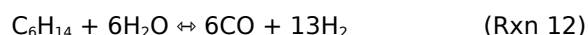
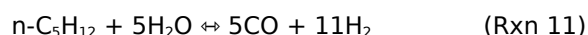


**Table 1:** Natural gas composition.

Component	Mole fraction (Xi)
Methane	0.989
Ethane	0.003365
Propane	0.001631
i-butane	0.000421
n-butane	0.000421
i-pentane	0.000245
n-pentane	0.000096
C6+	0.001471
N <sub>2</sub>	0.002146
CO <sub>2</sub>	0.001192



In this perspective, the stoichiometric natural gas quantity required to produce 3,524,275 MT/year and found to be 402.2 Kg/h. Based on pre-determined input stream parameters and the reformer and shift reactor operating conditions, the HYSYS simulator calculated the outlet compositions of the production zone and the purification zone units. In order to check the HYSYS accuracy in the production zone. Almost similar hydrogen molar flow rate was calculated by utilizing the Aspen HYSYS software 402.2 Kg/h respectively.

### 2.2. Optimization Of Steam Methane Reforming Process Aspen Hysys Simulation

The simulation and optimization study of hydrogen production through steam methane reforming, using Aspen HYSYS V12 software, has been conducted. Steam methane reforming is considered a cost-effective method for producing the majority of the world's hydrogen (H<sub>2</sub>), considering product yield and energy consumption. In this study, the simulation and optimization of an industrial steam methane reforming process, using Aspen HYSYS V12 software, was performed. All parameters, including units in the hydrogen production area (reformer, water gas shift reactor), and purification area (separator and pressure swing adsorption), were simulated and optimized to execute a comprehensive process. Moreover, the study incorporated a detailed analysis of the economic viability of this method in comparison to other hydrogen production methods. The software's flexibility allowed for the simulation of multiple scenarios with varying parameters, therefore providing a more comprehensive understanding of the impact of different operational conditions on the process. Additionally, the study considered the environmental impact of the process, analyzing the carbon footprint and identifying possible opportunities for reducing emissions. All in all, this study provides a thorough evaluation of the steam methane reforming process for hydrogen production using Aspen HYSYS V12 software, with a focus on optimizing yield, energy consumption, and



environmental impact. Typical industrial natural steam reforming processes are well known for involving a reaction zone to produce hydrogen gas (steam reformer with successive shift reactors) followed by a purification zone to get rid of carbon oxides  $\text{CO}_2$  and  $\text{CO}$ . In this study, the simulation and optimization of an industrial steam methane reforming process, using Aspen HYSYS V12 software, was performed. All parameters, including units in the hydrogen production area (reformer, water gas shift reactor), and purification area (separator and pressure swing adsorption), were simulated and optimized to execute a comprehensive process. Moreover, the study incorporated a detailed analysis of the economic viability of this method in comparison to other hydrogen production methods. The software's flexibility allowed for the simulation of multiple scenarios with varying parameters, therefore providing a more comprehensive understanding of the impact of different operational conditions on the process. Additionally, the study considered the environmental impact of the process, analyzing the carbon footprint and identifying possible opportunities for reducing emissions. All in all, this study provides a thorough evaluation of the steam methane reforming process for hydrogen production using Aspen HYSYS V12 software, with a focus on optimizing yield, energy consumption, and environmental impact. Typical industrial natural steam reforming processes are well known for

involving a reaction zone to produce hydrogen gas (steam reformer with successive shift reactors) followed by a purification zone to get rid of  $\text{CO}_2$  and  $\text{CO}$ . Hence, a conceptual process was performed on Aspen HYSYS V12 as shown in Figure 1, simulating a steady-state model where the hydrogen production, the  $\text{CO}_2$ , and  $\text{CO}$  removal were optimized in function of each unit operating parameters. Natural gas and steam were mixed and heated before being fed to a Gibbs reforming reactor. Conventional steam reforming reactors use Ni-based catalysts between 10 and 20 wt% on  $\alpha\text{-Al}_2\text{O}_3$ , calcium, or magnesium aluminate with a typical lifetime of 3-5 years due to the low cost of nickel, its wide availability, and sufficient catalytic activity (Olateju, et al., 2017). Then, the head headstreams reformer is cooled down in cooler E-101 and fed to a water gas shift (WGS) Gibbs reactor generally operating with a copper-based catalyst (Vozniuk et al., 2019). The simulation process was performed after determining the operating conditions. Figure 1, illustrates the process model for hydrogen production. The simulation was conducted using the specified feed conditions, aiming to obtain highly efficient hydrogen production. The average natural gas components in the hydrogen production unit plant layout are provided in Table 1. Detailed reference supporting information is given for the description of the factory layout scheme. Natural gas feed is assumed to be approximately 100% methane.

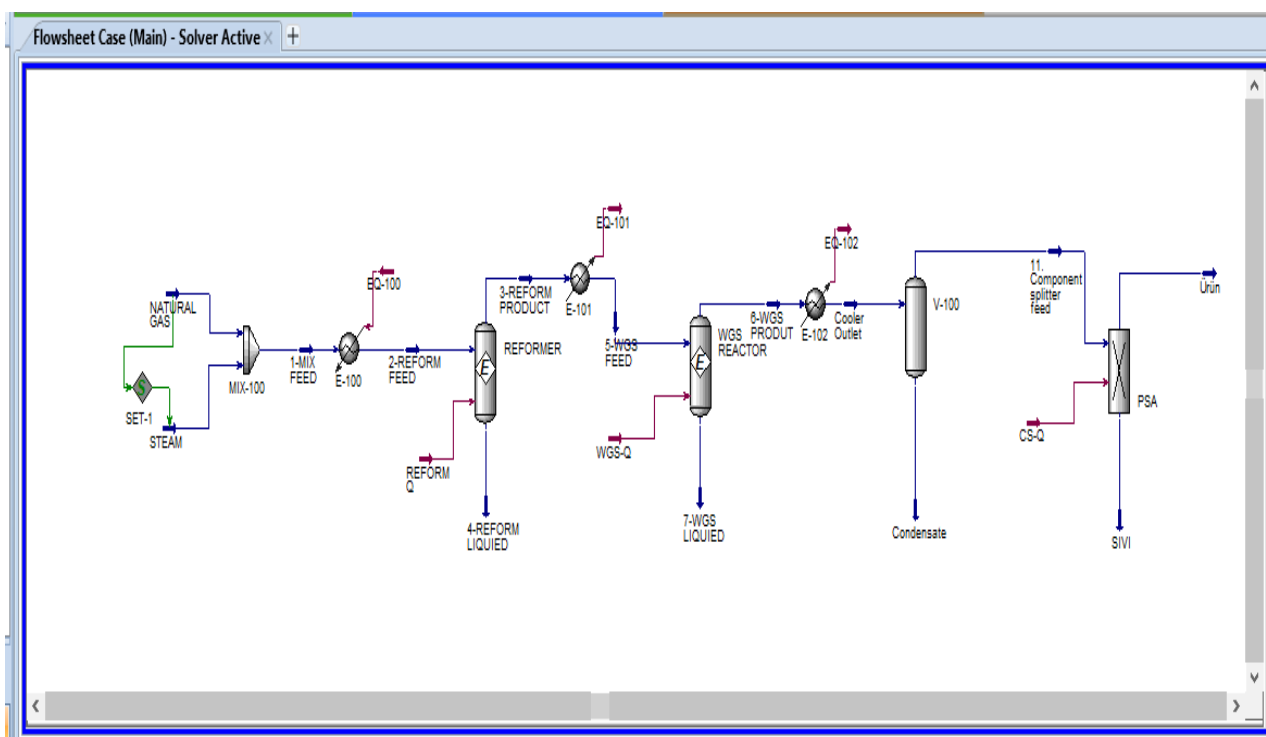


**Figure 1:** Steam methane reforming process Aspen HYSYS V12 simulation.

### 2.3. Choice of fluid packages and reactors

In order to optimize the process simulation in the reformer and water gas shift reactors, a Peng Robinson fluid package was selected (gas law

shown in supporting information). This package could accurately predict the thermodynamic data (pressure & temperature) of light gases ( $\text{CH}_4$ ,  $\text{C}_2\text{H}_6$ ,  $\text{C}_3\text{H}_8$ ,  $\text{C}_n\text{H}_m$ ,  $\text{CO}_2$ ,  $\text{CO}$ ,  $\text{H}_2$ ). In addition, the



product yield and the consumption of the reactants were simulated by having Aspen HYSYS calculate the reaction equilibrium constant (Eq. 1) from the change in the Gibbs free energy at a specified temperature by taking into consideration the non-ideal behavior of the relatively light gases predicted by the thermo-package of Peng Robinson.

$$\ln K_{eq} = \frac{-\Delta G_{reaction}}{RT} \quad (\text{Eq. 1})$$

Where  $K_{eq}$   $\Delta G$  reaction,  $R$ , and  $T$  are the reaction equilibrium constant, variation in Gibbs free energy, the universal gas constant, and the temperature respectively. In this context, a Gibbs reactor was chosen to model the following production units: Reformer and WGS.

#### 2.4. Thermodynamic parameters optimization

After choosing the fluid packages and the convenient reactors for the steady state model, pressures (P), temperatures (T), and steam-to-carbon ratio (S/C) were optimized in the production zone (Reformer, WGS) in order to maximize the  $H_2$  production. Moreover, the pressure, temperature, and purification zone in order to reach the highest  $CO_2$  removal and CO conversion. In addition, the heat duty required to operate at optimum conditions was computed by the Aspen HYSYS simulator. The results are thus discussed in the following section. The optimization of reformer and water-gas shift (WGS) reactor temperatures is a crucial step for maximizing hydrogen production and optimizing energy consumption. In general, achieving high conversion and hydrogen yield is attainable at temperatures exceeding 700 °C. and literature suggests that reformer reactor temperatures should ideally range between 700 °C and 1000 °C. Furthermore, it is worth mentioning that temperatures exceeding 950 °C can result in coke formation on the catalyst. Therefore, the selection of 900 °C as the operating temperature is a deliberate choice to prevent coke formation and ensure a high hydrogen yield. It is important to note that the water gas shift reaction is slightly exothermic, while steam-reforming reactions are significantly

endothermic, making it challenging to favor both reactions in a single reactor. Elevated reformer temperatures enhance hydrocarbon conversion rates, thus increasing hydrogen yield; however, excessively high temperatures can lead to catalyst deactivation and heightened energy costs. In contrast to the reformer, the WGS reactor operates at lower temperatures, which are conducive to carbon monoxide conversion into hydrogen. These distinct temperature conditions collectively impact overall hydrogen production, striking a balance between yield and energy efficiency within the process. Given that wgs reactors are exothermic, they are typically operated at lower temperatures, typically falling between 200 °c and 400 °c to optimize the conversion process (Dejong et al., 2009).

### 3. RESULTS AND DISCUSSION

#### 3.1. Reformer

After defining the adequate fluid package and the reactor type, a balance between the effect of the operating parameters of each reactor, such as P, T, and S/C was tuned. This step is critical to overcoming the imposed thermodynamic limitation on the natural gas (NG) conversion due to the steam reforming and WGS reaction's reversibility. For this purpose, reformer temperature and pressure were first adjusted at a stoichiometric S/C = 2.5. The reason behind adjusting the reformer pressure first relies on its designated purpose to favor the main steam reforming reactions (Rxn 4, Rxn6-Rxn12) that are strongly affected by the pressure variation, at the expense of the WGS reaction (Rxn13) that is pressure independent according to Peng-Robinson principle. Because, the water gas shift reaction is slightly exothermic, while the steam-reforming reactions are heavily endothermic, both reactions could not be favored in the same reactor. Hence, the  $H_2$  molar flow rate was plotted at the reformer outlet in the function of the industrial scale pressure and temperature range of 1-20 atm and 700-1000 °C respectively, while S/C was fixed at its stoichiometric level of 2.5. As a result, it can be seen in Figure 2, that the thermodynamic response of the system of existing reactions turned out to be in conformity with the Peng-Robinson of the system of existing reactions turned out to be in conformity with the Peng-Robinson principle.

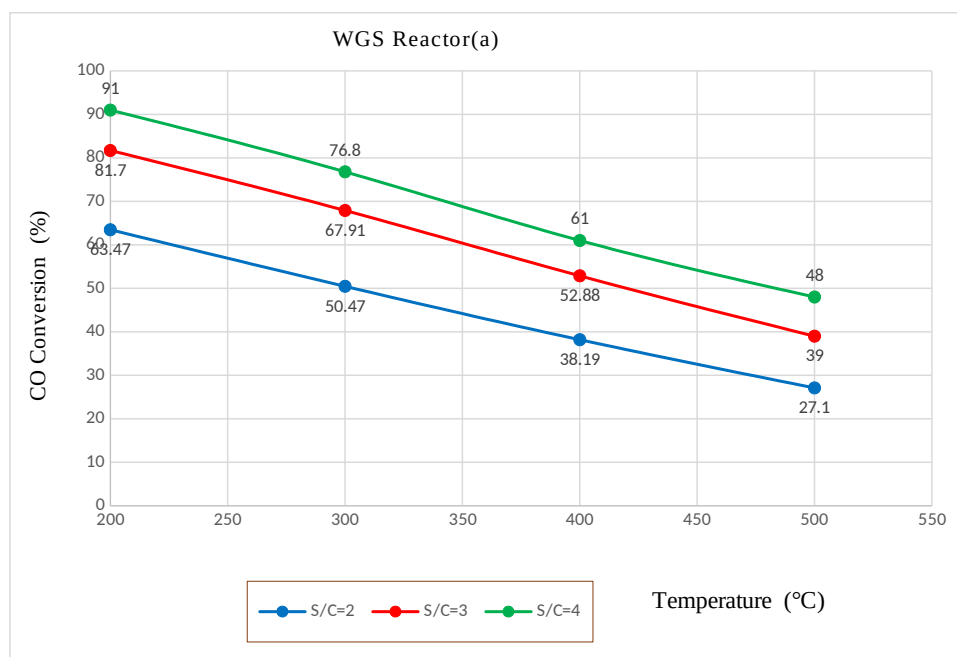


**Figure 2:** Hydrogen molar flow rate versus temperature and pressure variation at the stoichiometric S/C=2.5

A decrease in the operating pressure down to 1 atm was found sufficient enough to push the steam reforming reactions to a maximum H<sub>2</sub> molar flow rate of ~3807 kmol/h while still operating at a relatively moderate T= 900 °C. However, by increasing the pressure to 20 atm, a maximum molar flow rate of ~2700 kmol/h was only reached by raising the temperature to 900 °C. Such a notable difference in operating temperatures could be found in the thermodynamic behavior of the endothermic steam reforming reactions. Thus, very low pressure was sufficient to drastically move the reaction (Rxn 4, Rxn6-12) equilibrium to the right, translated into a high H<sub>2</sub> molar flow rate, yet, any increase in pressure from that level (shifting the equilibrium to the left) required higher operating temperature to restore back the equilibrium to a previous state. As a result, a low operating pressure of 1 atm and a relatively high temperature of 900 °C, would provide a maximum natural gas conversion and would save on the heater's and the compressor's duties (Vozniuk et al., 2019). Moreover, it is preferable to avoid harsh temperatures >950 °C because they could increase coke deposition on the Ni-based catalyst according to the side reaction (Rn14).

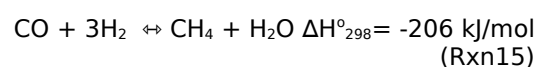


However, in industrial natural gas steam reforming plants, such low pressure creates some limitations on the adsorption of the natural gas (NG) on the catalyst's surface, thus preventing the catalytic mechanism, lowering its efficiency, and creating low conversion kinetics (Mokheimer E, et al., 2015). For this specific reason, a pressure trade-off between high H<sub>2</sub> yield and enabling adsorption on the catalyst

surface was made and a pressure of 5.2 atm was chosen for this case study. In addition, a temperature trade-off between high hydrogen yield and coke build-up was made and an operating temperature of 900 °C was also chosen. Another important parameter to be adjusted was the reformer inlet temperature. Hence, the non-uniform temperature distribution could result in carbon deposition at this reactor inlet where methane concentration is at the highest level. This carbon deposition contributes to the catalyst fouling and deactivation. However, experience has shown that a normal inlet temperature from 500 to 650 °C keeps coke formation at its lower level. For this reason, an inlet temperature of 550 °C was chosen. Consequently, the initial natural gas stream could be fed to the heater at any pressure >5 atm (in this case, P = 5.2 atm was chosen) to assure its natural circulation in the process and then mixed with the steam (also fed with P > 5 atm). This measure aimed to deliver a new stream of a temperature of 550 °C to the reformer inlet.

### 3.2. Water Gas Shift Reactors

Once the reformer pressure and temperature were adjusted, the WGS reactors' temperatures were tuned to favor the best conditions for the WGS reaction (Rxn 13) to take place. The operating pressure was preserved at 5 atm to limit the methanation reaction (Rxn15) (here hydrogen consumption) at this process stage.



As for the operating temperature, high CO conversion is favored at low temperatures (according to Peng Robinson's Principle), while

higher temperatures kinetically increase the reaction rate. Therefore, in industrial plants, water gas shifting is performed in a reactor at temperature regimes, (between 200 and 330 °C). In this scope, a minimum temperature of 300 °C was chosen for the WGS reactor in order to reach a maximum CO conversion especially since lower temperatures than 300 °C would favor the undesired reaction (Rxn15). For the operating temperature, the approach was to accelerate the reaction and to reach a high CO conversion (remaining CO on a dry basis) within the industrial range of 3-5%. For this reason, the CO conversion was plotted in Figure 3 as a function of the operating temperature at different S/C ratios. According to Peng Robinson's Principle, it was observed that increasing the S/C from 2 to 4 consistently reduced the CO conversion as seen in Fig. 3a while rising the temperature from 200 to 500 °C had an opposite effect on it. In order to operate within the industrial range at a relatively convenient temperature condition, an S/C=4, and a temperature of 500 °C were chosen. Consequently, optimizing the WGS temperatures resulted in an overall CO conversion of ~99.86% measured at the end of the WGS zone as seen in Figure 3b. Thus the measured CO content on a dry basis at the WGS

outlet was reduced to a relatively lower percentage (of ~0.14%) than the minimum required (0.3- 1%), resulting in an enhanced conversion of CO into H<sub>2</sub>. In a hydrogen production process, the number of WGS (Water-Gas Shift) reactors required depends on the desired hydrogen-to-carbon monoxide (H<sub>2</sub>/CO) ratio and the level of conversion needed. In this study, a single reactor was found to achieve the required conversion and ratio effectively, as indicated by Figure 4, where the co-conversion is 96.52%, CH<sub>4</sub>-conversion is 96.52%, and H<sub>2</sub> yield is 70.2%. The highest conversion, particularly in the temperature range of 200 °C to 300 °C, is evident from Figures 3a and 3b. Consequently, a second WGS reactor was not deemed necessary in our simulation. The primary function of the WGS reactor is to adjust the ratio of hydrogen to carbon monoxide in the reformat gas by reacting carbon monoxide with water vapor. This adjustment is critical because downstream processes or applications often require a specific H<sub>2</sub>/CO ratio. Following the WGS reaction, the gas mixture typically undergoes separation processes in a separation column to eliminate unwanted water through pressure swing adsorption (PSA). Subsequently, the gas is directed to PSA units to remove undesired CO and CO<sub>2</sub>.

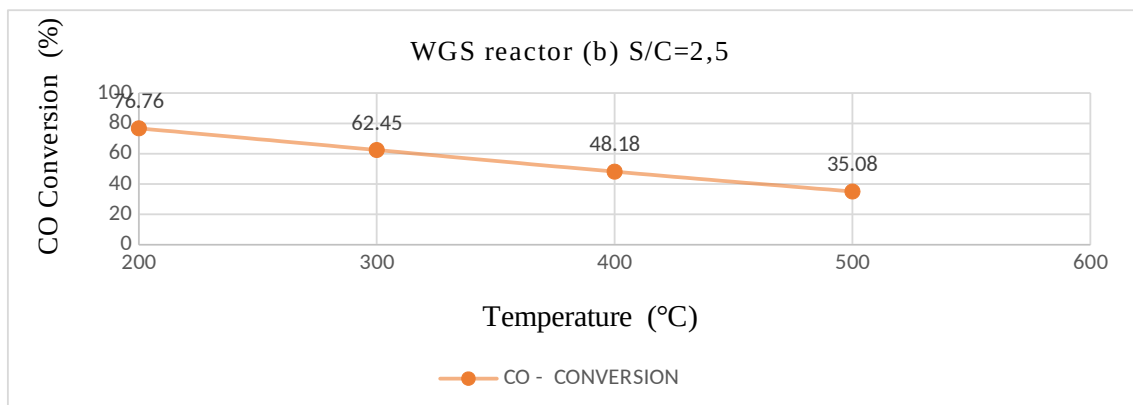


Figure 3: (a) CO conversion variation in the WGS reactor versus its operating temperature and S/C ratio

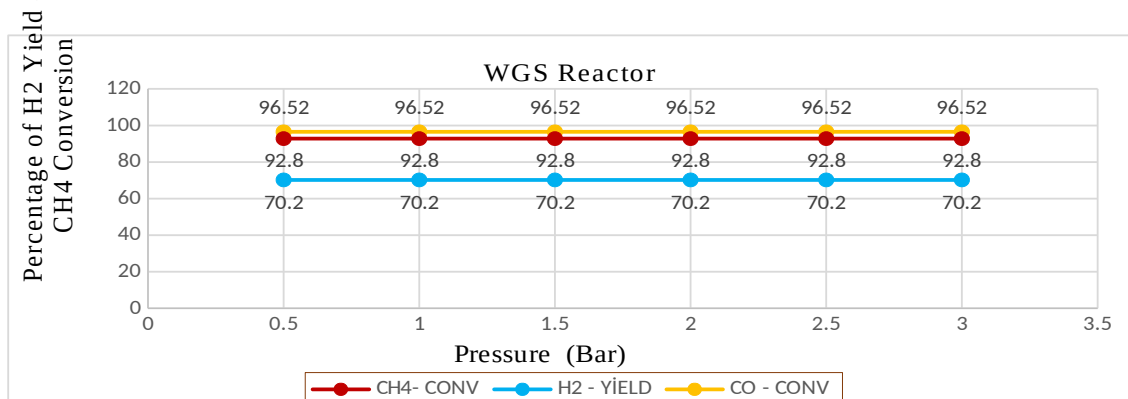
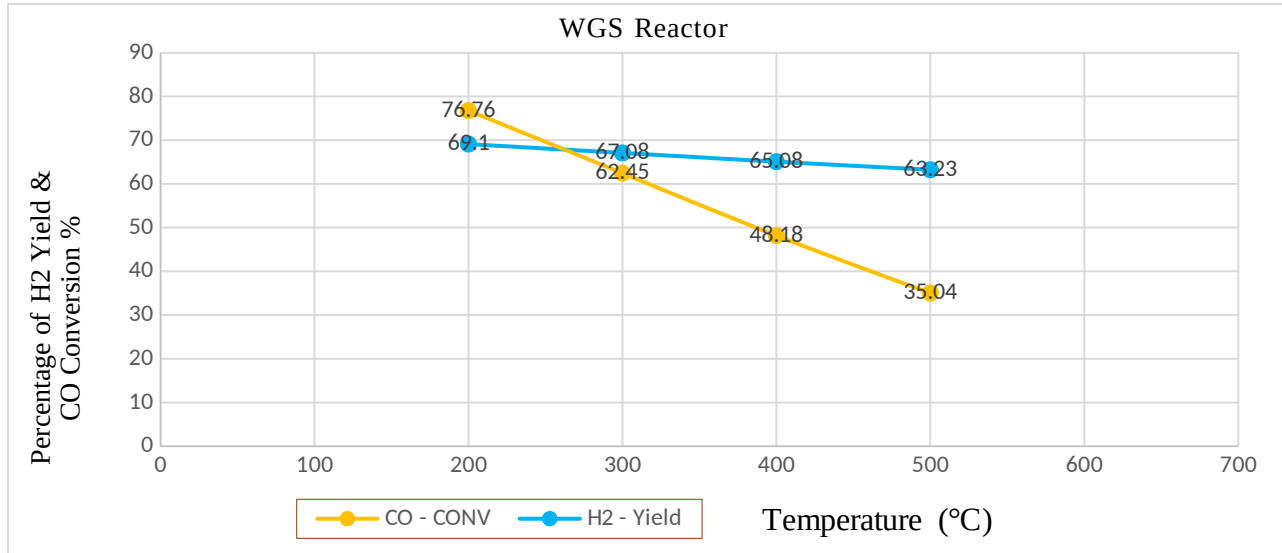


Figure 3 (b) Variation of the CO conversion at the WGS outlet in the function of the WGS temperature at S/C=2.5.

**3.3. Effect Of Pressure on WGS Reaction Conversion and H<sub>2</sub> Yield**

Pressure has a zero effect on the conversion in the WGS equilibrium reactor. This means that an increase or decrease in the pressure on the reactor has no effect on the conversion and ultimately on

the yield of H<sub>2</sub> in the product stream. From the equation of (Rxn2), the number of moles on both sides of the equation is balanced. As a result, there is no net shift in the equilibrium of the system due to an increase or decrease in pressure shown in Figure 4.



**Figure 4:** Effect of pressure on WGS reaction conversion and H<sub>2</sub> yield.

**3.4. Effect Of Temperature on WGS Reaction Conversion and H<sub>2</sub> Yield**

The water gas shift (WGS) reaction in the converter reactor is exothermic, and therefore, lower temperatures are preferred. As shown in Figure 5, at a temperature of 500 °C, the H<sub>2</sub> efficiency is 63.23%, at 400 °C it is 65.05%, and at 300 °C it is 67.08% for obtaining H<sub>2</sub> product. This indicates that the highest H<sub>2</sub> efficiency can be achieved at temperatures of 300 °C and below in the water gas shift reactor. In this simulation modeling, an H<sub>2</sub> efficiency of 67.08% was observed at a temperature of 300 °C in the

converter reactor. The CO conversion and H<sub>2</sub> efficiency were not highly sensitive to temperature changes. However, with an increase in temperature, due to the adiabatic and exothermic nature of the water gas shift reactor (WGS), a significant decrease in H<sub>2</sub> efficiency and a rapid decrease in CO conversion were observed. As the temperature increased from 300 °C to 500 °C, the CO conversion decreased rapidly from 62.45% to 35.04%, while the H<sub>2</sub> efficiency decreased from 67.08% to 63.23%. This indicates the preference for operating an exothermic reactor at high temperatures.

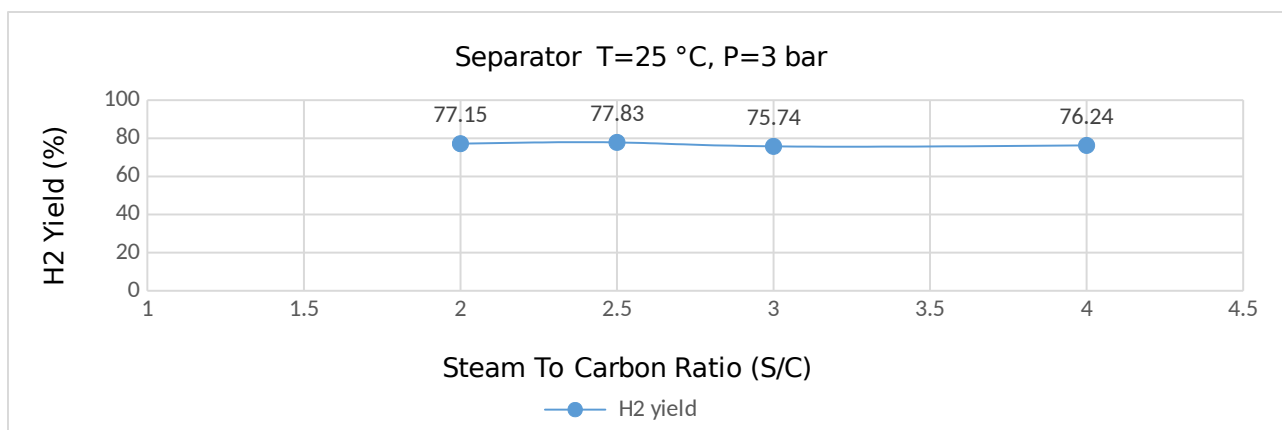


**Figure 5:** Effect of temperature on WGS reaction conversion and H<sub>2</sub> yield.

**3.5. Separator and Pressure Swing Adsorption (PSA)**

To achieve an almost pure hydrogen stream and minimize CO<sub>2</sub> and CO gas concentrations, our approach involved the simultaneous operation of

two units. The parameters of these units, guided by the Peng Robinson fluid package's principles, were optimized. Initially, the separator was employed to eliminate excess H<sub>2</sub>O, followed by the PSA unit, which effectively removed waste gases containing

CO, CO<sub>2</sub>, minimal H<sub>2</sub>O, and CH<sub>4</sub>, resulting in the production of 100% pure H<sub>2</sub>.

### 3.6. Separator

The first step that needs to be performed before sending the product from the WGS reactor to the PSA unit is the removal of unwanted water in the

PSA unit. Accordingly, the product from the converter reactor is cooled down to atmospheric temperature in a cooler before being sent to the separator, where the water is completely separated and removed. The separator operates at 25 °C and 3 atm, and the results are presented in Table 2 and Figure 6.

**Table 2:** Separation of components in the Separator and removal of unwanted water.

Components	Separator feed	Condensate	PSA
CO	0.0527	0.0	0.0612
CO <sub>2</sub>	0.1281	0.0002	0.1468
H <sub>2</sub> O	0.1468	0.9998	0.0102
CH <sub>4</sub>	0.0015	0.0	0.0017
H <sub>2</sub>	0.6708	0.0	0.7783
	1	1	1

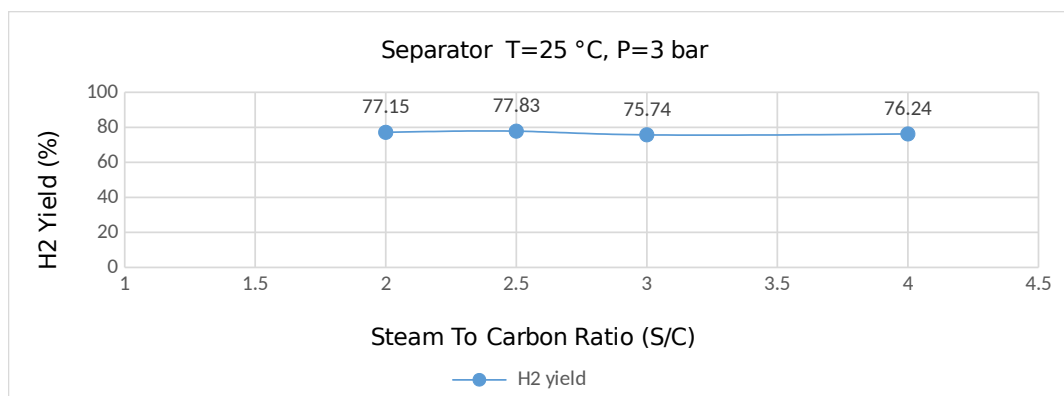


**Figure 6:** Product output in terms of the percentage of H<sub>2</sub> content after removing unwanted water in the separator for different steam-to-carbon ratios (S/C).

### 3.7. Pressure Swing Adsorption (PSA) Unit

Pressure Swing Adsorption (PSA) technology uses Carbon Molecular Sieve (CMS) columns to separate compressed air. The vessels operating on the principle of PSA are filled with CMS granules, which are a special adsorption material. In this case, a Component Splitter Reactor is used instead of PSA columns (simulated as continuous active operation in Aspen HYSYS V12 software) in various applications such as fuel cells, refineries involving hydrogenation (hydrocarbon cracking, petroleum gases, gasoline, jet fuel, gas oil, diesel, fuel oil, asphalt, etc.), petrochemicals (hydrocracking, steam

reforming (pyrolysis), isomerization, hydrogenation, etc.). The main objective of this study, particularly, is to obtain 100% pure hydrogen for use in fuel cells. The results, as provided in Table 2 show the processed gas that has been converted and separated from water entering the PSA unit. The outcome of the process is illustrated in Figure 7. In this unit, as shown in Figure 8, non-hydrogen gases (H<sub>2</sub>O, CO, CO<sub>2</sub>, and CH<sub>4</sub>) present in the process gas are separated to purify hydrogen. Output data from the PSA unit obtained through the simulation is shown in Table 2. The PSA unit operates at 25°C, 3 bar, and in an adiabatic condition.

**Table 2:** Output data from the PSA unit obtained through Aspen HYSYS v12 simulation.

Components	Feed (PSA)	PSA (tail gases)	PSA (product)
CO	0.0612	0.1894	0.0
CO <sub>2</sub>	0.1468	0.4603	0.0
H <sub>2</sub> O	0.0102	0.0317	0.0
CH <sub>4</sub>	0.0017	0.0052	0.0
H <sub>2</sub>	0.7783	0.3133	1.0
Total	1	1	1

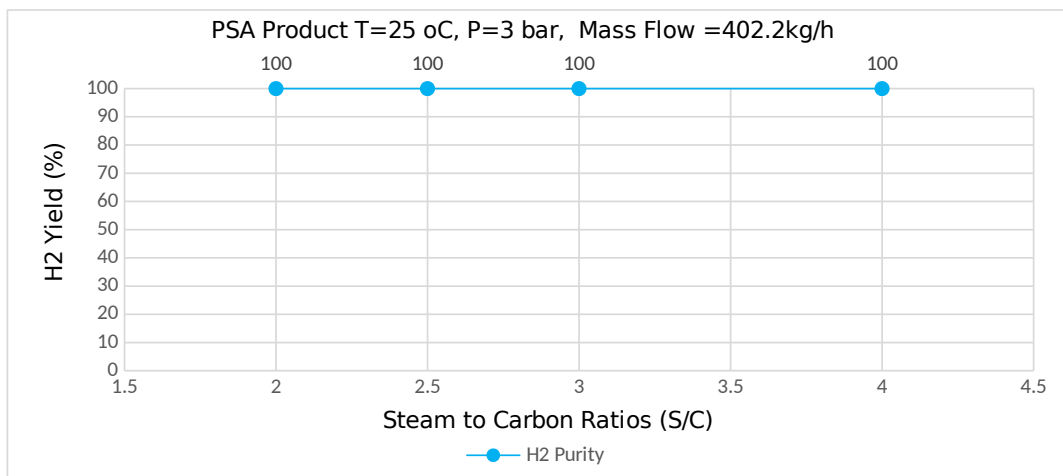


**Figure 7:** PSA unit product output and purity of the product (100% pure H<sub>2</sub>) for different steam-to-carbon ratios (S/C).

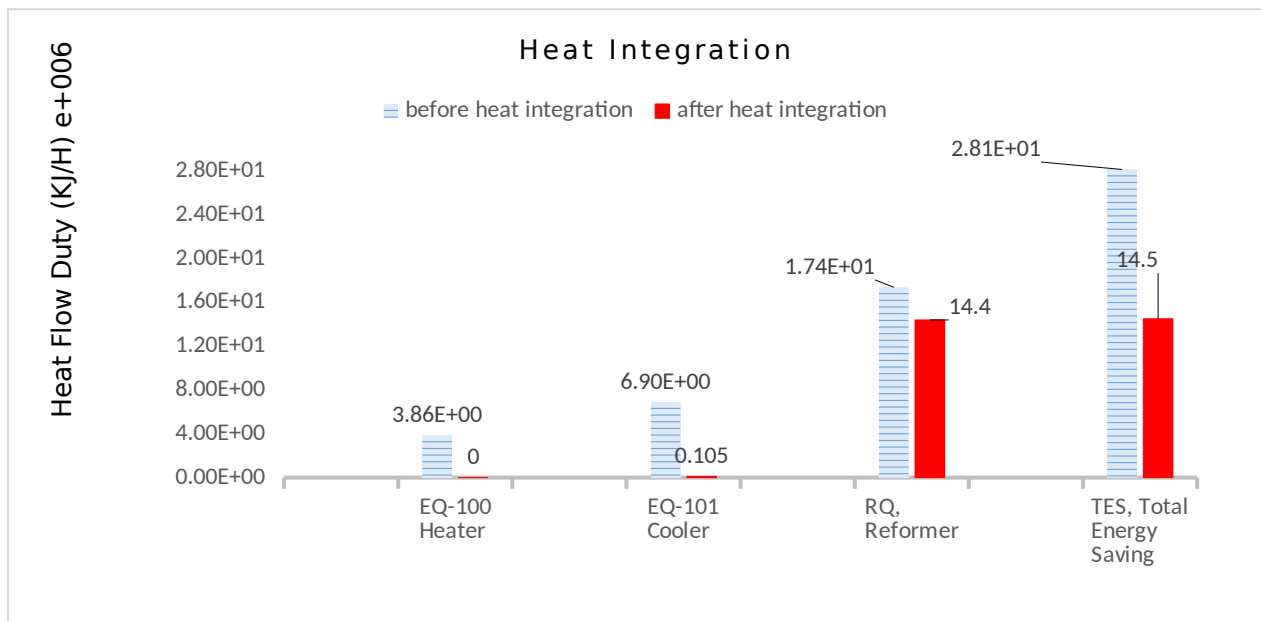


**Figure 8:** Tail gas output from the PSA unit for different steam-to-carbon ratios (S/C) (tail gas content).

**3.8. Process Heat Duty And Cooling Cost Optimization**

The reactors and miscellaneous heat duty were calculated through HYSYS by fixing as input parameters the working temperatures in the reactors and the output stream temperatures of the coolers and the heater. The obtained results are shown in Table 3.

Cooling and heating capacity play a significant role in the operational cost of this system. Therefore, it would be beneficial to save on these high-cost expenses by optimizing heat consumption or reducing cooling capacity.

**3.9. Heat Integration**

In this context, an improved process was developed in Aspen HYSYS v12 as shown in Figure 9, and certain heat exchangers were placed at key points. As a result, the waste heat exiting the reformer in heat exchanger 1 was recovered by replacing the heater with an exchanger (UA = 3.855e+06 kJ/h). The feed going to the reformer was heated by exchanging heat in heat exchanger 1, resulting in significant energy savings. At the outlet of heat exchanger 1 (E-100), the feed was cooled down to 310°C in heat exchanger 2 (UA = 3.147e+05 kJ/h) and then sent to the E-101 cooler. In the E-101 cooler, the feed for the WGS reactor was further cooled down to 300°C. The results of this optimization are shown in Figure 9, Table 4, Table 5, and Figure 10.

**Table 3:** Hysys simulation heat duties for reactors, cooler, and heaters.

Unit	Energy stream	Duty (kJ/h)
Heater	EQ-100	3.855e + 006
Reformer	Reformer Q	1.738e +007
Cooler	EQ-101	6.895e +006
WGS	WGS -Q	0.0 (adiabatic)
Cooler	EQ-102	6.336e + 006
PSA	CS- Q	0.0

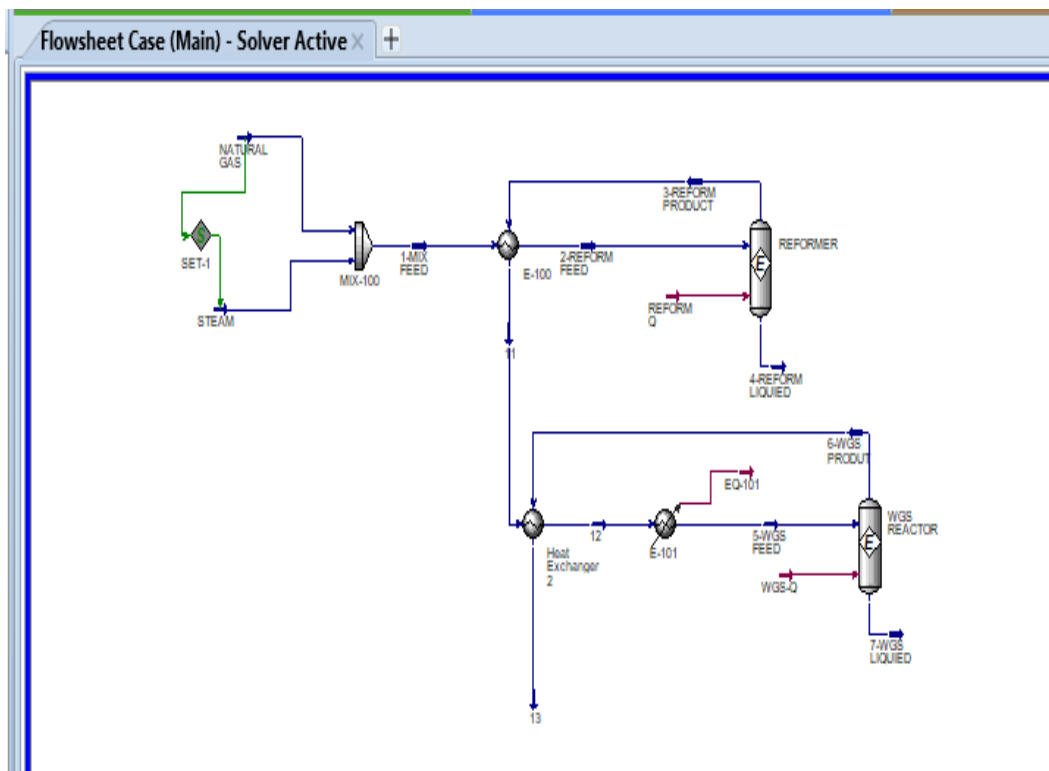


**Figure 9:** Steam methane reforming process Aspen HYSYS V12 simulation after heat integration.



**Table 4:** Heat flows for the cooler, heater, and reactors in Aspen HYSYS simulation (before heat integration).

Units	Energy stream	Heat Duty (kJ/h)
Heart	EQ-100	3.855e+006
Reformer	R- Q	1.738e+007
Cooler	EQ-101	6.895e+006
WGS	WGS-Q	0.0

**Table 5:** Heat flows for the cooler, heater, and reactors in Aspen HYSYS simulation (after heat integration).

Units	Energy stream	Heat Duty (kJ/h)
Heater	EQ-100	0.0
Reformer	R-Q	1.414e+007
Cooler	EQ-101	0.105e+006
WGS	WGS-Q	0.0

The important parameters; temperature, pressure, and hydrogen production yield in this study was compared with a similar study and was shown in Table 6:

**Table 6:** Comparison of similar works and this study.

Parameter	Our study	Similar Study
Temperature (°C)	Reformer: 900°C WGS Reactor: 300°C	Reformer: 800°C WGS Reactor: 200°C
Pressure	Pressure (atm):5	Pressure (atm):3
Hydrogen Production Yield	77.83%	product and waste parts are not specified
Waste gas	100% pure H <sub>2</sub>  22.17% H <sub>2</sub> CH <sub>4</sub> CO CO <sub>2</sub> H <sub>2</sub> O	H <sub>2</sub> : 98.719% CH <sub>4</sub> :0.185% CO:0.212% H <sub>2</sub> O:0.884%
Using area	fuel cells, petroleum refining, natural gas refineries, and petrochemical processes.	PEMFC
Reference		(Ihoeghian et al., n.d.)

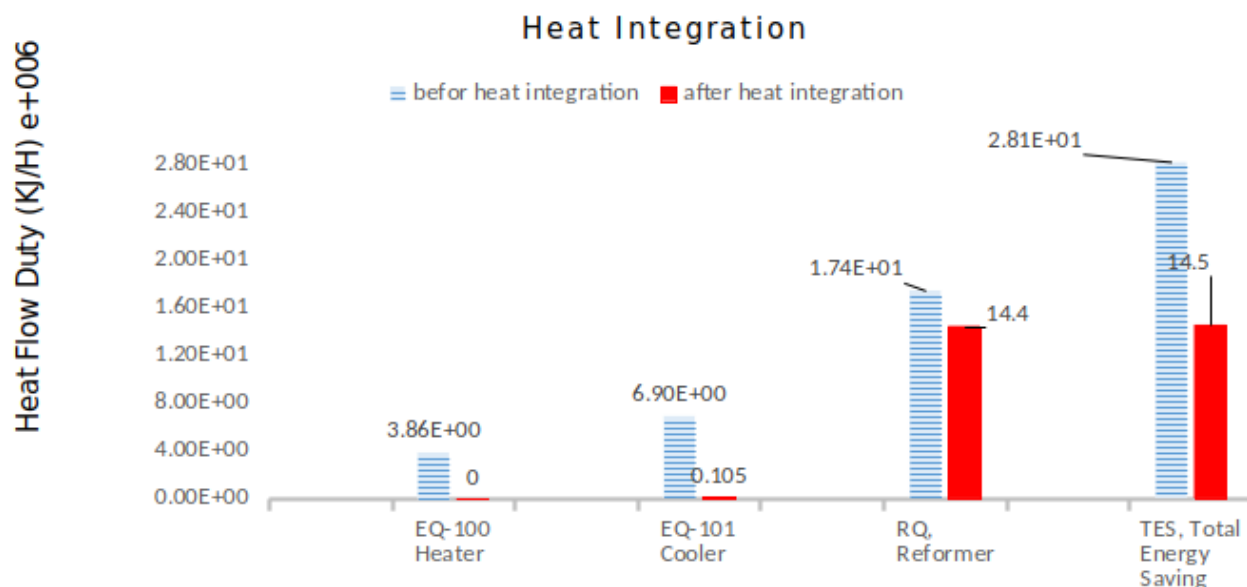


**Figure 10:** Aspen HYSYS simulation of the heat integration before and after the integration of the heater and cooler heat exchangers (achieving 51.6% energy savings after integration). Total Energy Savings (TES).

#### 4. CONCLUSION

A simulation and optimization study of an industrial natural gas steam reforming process was conducted to meet the high-purity H<sub>2</sub> production requirements for various applications such as fuel cells, petrochemicals, refineries, and many other industrial applications. All parameters were optimized to successfully operate the complete process, including hydrogen production units (reformer, water gas shift reactor) and purification units (separator and PSA). An optimization study was performed to control the steam reforming conversion process, aiming to control the final hydrogen yield and purity. The hydrogen molar flow rate was calculated using Aspen HYSYS V12 software. Furthermore, at the end of the process, the product efficiency was 77.83%, and 402.2 kg/h of 100% pure hydrogen was obtained, equivalent to 3,523.272 MT/year. Some of the hydrogen quantities from the production area and at the end of the process were mixed with other gases in the waste gas outlet of the PSA unit. It is beneficial to recover and separate hydrogen from waste gases, as it has high energy and economic value. As a result of the careful optimization of process parameters, a significant amount of 402.2 kg/h of 100% pure hydrogen was achieved, and there was a 51.6% energy savings in the heating and cooling units of the process. In conclusion, this study successfully conducted a simulation of a natural gas reforming system design capable of economically producing high-purity hydrogen for use in fuel cells. The produced hydrogen can also be utilized in various industrial applications. Similar studies present a simulation and optimization study of an industrial natural gas steam reforming process for hydrogen production to meet the refinery and petrochemical demands in Lebanon, using Aspen HYSYS software

(Madon et al., 2015). All parameters were optimized to successfully operate the complete process, including hydrogen production units (reformer reactor, high-temperature shift reactor HTS, and low-temperature shift reactor LTS) and purification units (absorber and methanation) (Riachi, 2021). Optimum hydrogen production (87.404 MT/year) was achieved and fixed. The temperatures in the reformer and shift reactors (HTS & LTS) were maintained at 900 °C, 500 °C, and 7 atm pressure, with a steam-to-carbon ratio (S/C) of 4. Furthermore, approximately 99% of the unwanted CO<sub>2</sub> and CO gases were removed in the purification process, resulting in a hydrogen purity of 98%. When used as a combustion fuel, hydrogen reduces greenhouse gas emissions. This study encompasses the steady-state simulation and optimization of steam methane reforming for hydrogen production from natural gas (methane) using Aspen HYSYS v8.6. With a steam/methane flow ratio of 2.5, the reformer temperature and pressure were set at 800 °C and 3 bar, respectively. The water gas shift reactor temperature was 200 °C, and the hydrogen purity achieved was 97% (Ding & Alpay, 2000). To conclude the cost-effectiveness and energy efficiency of the Steam Methane Reforming (SMR) process by natural gas compared to alternative hydrogen production methods, such as electrolysis or solar-based approaches, can vary depending on several factors. However, according to the International Energy Agency (IEA), the levelized cost of hydrogen production by energy source and technology in 2019 and 2050. The efficiency of SMR without carbon capture and storage (CCS) is estimated to be 76% in 2019 and 2050. The levelized cost of hydrogen production using SMR without CCS is projected to be USD 910/kW H<sub>2</sub> in 2019 and 2050. The efficiency of electrolysis using low-carbon electricity is estimated to be 64% in

2019 and 74% in 2050. The levelized cost of hydrogen production using electrolysis is projected to be USD 872/kW in 2019 and USD 269/kW in 2050 (iea.org, nrel.com). Solar-based approaches hydrogen production methods, such as solar water splitting or photoelectrochemical (PEC) cells, are highly dependent on location and available sunlight. Initial capital costs can be high, but operational costs can be low if abundant sunlight is available. These approaches can be energy-efficient when ample solar energy is harnessed. Efficiency can vary depending on the specific technology and system design. It's important to note that these figures are global averages and can vary depending on regional factors, technological advancements, and economies of scale. Additionally, the cost-effectiveness and energy efficiency of different hydrogen production methods can be influenced by factors such as the availability and cost of natural gas, renewable energy sources, carbon capture technologies, and government policies.

## 5. REFERENCES

- Alves, H. J., Bley Junior, C., Niklevicz, R. R., Frigo, E. P., Frigo, M. S., & Coimbra-Araújo, C. H. (2013). Overview of hydrogen production technologies from biogas and the applications in fuel cells. In *International Journal of Hydrogen Energy* (Vol. 38, Issue 13, pp. 5215-5225). <https://doi.org/10.1016/j.ijhydene.2013.02.057>
- Cherbanski R, Molga E., (2018). Sorption-enhanced steam methane reforming (SE-SMR) a review: reactor types, catalyst adsorbent characterization, process modeling. *Chem Process Eng* 2018;39(4):427e48. <https://doi.org/10.24425/122961>.
- Ding, Y., & Alpay, E. (2000). Adsorption-enhanced steam-methane reforming. In *Chemical Engineering Science*, 55 (18), 3929-3940.
- Dejong, M., Reinders, A.(2009). Optimizing a steam-methane reformer for hydrogen production. *International Journal of Hydrogen Energy*
- El-Shafie, M., Kambara, S., & Hayakawa, Y. (2019). Hydrogen Production Technologies Overview. *Journal of Power and Energy Engineering*, 07(01), 107-154. <https://doi.org/10.4236/jpee.2019.71007>
- Goswami, D. Y., Mirabal, S. T., Goel, N., & Ingley, H. A. (2003). A Review of Hydrogen Production Technologies. In *ASME 2003 1st International Conference on Fuel Cell Science, Engineering and Technology, FUELCELL 2003* (pp. 61-74). <https://doi.org/10.1115/FUELCELL2003-1701>
- Global Hydrogen Review 2021. (2021). In *Global Hydrogen Review 2021*. <https://doi.org/10.1787/39351842-en>
- Ihoeghian N.D., et al.(2018). STEADY-STATE SIMULATION AND OPTIMIZATION OF HYDROGEN PRODUCTION BY STEAM REFORMING OF NATURAL GAS Design of bio reactor View project Simulation of the Fluid catalytic cracking using aspen hysys View project. *Journal of Nigerian association*.
- Leonzio G., (2018). Methanol synthesis: optimal solution for better efficiency of the process. *Processes* 2018;6(3):20. <https://doi.org/10.3390/pr6030020>.
- Lemus, R. G., & Martínez Duart, J. M. (2010). Updated hydrogen production costs and parities for conventional and renewable technologies. In *International Journal of Hydrogen Energy* (Vol. 35, Issue 9, pp. 3929-3936). <https://doi.org/10.1016/j.ijhydene.2010.02.034>
- Madon, R. H., Osman, S. A., Mustaffa, N., & Fawzi, M. (2015). Akademia Baru Review of Yield Intensification on Steam Methane Reforming through Micro Reactor and Rare Earth Catalyst. In *Journal of Advanced Review on Scientific Research*, 7 (1), 32-37.
- Mokheimer E, Hussain MI, Ahmed S,Habib MA, Al-Qutub A., (2015).On the modeling of steam methane reforming. *J Energy ResourTechnol* 2014;137(1):012001. <https://doi.org/10.1115/1.4027962>.
- Olateju II, Gibson-Dick C, Egede SCO, Giwa A., (2017). Process development for hydrogen production via water-gas shift reaction using Aspen HYSYS. *Int J Eng Res Afr* 2017;30:144e53. <https://doi.org/10.4028/www.scientific.net/JER A.30.144>.
- Ramachandran, R., & Menon, R. K. (1998). An overview of industrial uses of hydrogen. In *International Journal of Hydrogen Energy* (Vol. 23, Issue 7, pp. 593-598). [https://doi.org/10.1016/s0360-3199\(97\)00112-2](https://doi.org/10.1016/s0360-3199(97)00112-2)
- Riachi, B., El Hajj Chehade, A. M., Daher, E. A., Assaf, J. C., & Hamd, W. (2020). Simulation and optimization of hydrogen production by steam reforming of natural gas for refining and petrochemical demands in Lebanon. *International Journal of Hydrogen Energy*, 45 (58), 1-12.
- Sarkarzadeh M, Farsi M, Rahimpour MR., (2019). Modeling and optimization of an industrial hydrogen unit in a crude oil refinery. *Int J Hydrogen Energy* 2019;44(21):10415e26. <https://doi.org/10.1016/j.ijhydene.2019.02.206>
- Speight JG., (2011). Handbook of industrial hydrocarbon processes. In: Speight JG, editor. Boston: Gulf Professional Publishing is an imprint of Elsevier; 2011.
- Vozniuk, O., Tanchoux, N., Millet, J. M., Albonetti, S., Di Renzo, F., & Cavani, F. (2019). Spinel Mixed Oxides for Chemical-Loop Reforming: From Solid State to Potential Application. In *Studies in Surface Science and Catalysis* (Vol. 178, pp. 281-302). <https://doi.org/10.1016/B978-0-444-64127-4.00014-8>